A&A 620, A140 (2018)
https://doi.org/10.1051/0004-6361/201834105
© ESO 2018

Astronomy & Astrophysics

C-GOALS

II. *Chandra* observations of the lower luminosity sample of nearby luminous infrared galaxies in GOALS

N. Torres-Albà[1], K. Iwasawa[1,2], T. Díaz-Santos[3], V. Charmandaris[4,5], C. Ricci[3,6,7], J. K. Chu[8], D. B. Sanders[9], L. Armus[10], L. Barcos-Muñoz[11,12], A. S. Evans[11,13], J. H. Howell[10], H. Inami[14], S. T. Linden[13], A. M. Medling[15,16], G. C. Privon[17], V. U[18], and I. Yoon[11]

[1] Institut de Ciències del Cosmos (ICCUB), Universitat de Barcelona (IEEC-UB), Martí i Franquès, 1, 08028 Barcelona, Spain
e-mail: ntorresalba@icc.ub.edu
[2] ICREA, Pg. Lluís Companys 23, 08010 Barcelona, Spain
[3] Núcleo de Astronomía de la Facultad de Ingeniería y Ciencias, Universidad Diego Portales, Av. Ejército Libertador 441, Santiago, Chile
[4] Institute for Astronomy, Astrophysics, Space Applications & Remote Sensing, National Observatory of Athens, 15236 Penteli, Greece
[5] University of Crete, Department of Physics, 71003 Heraklion, Greece
[6] Kavli Institute for Astronomy and Astrophysics, Peking University, 100871 Beijing, PR China
[7] Chinese Academy of Sciences South America Center for Astronomy, Camino El Observatorio 1515, Las Condes, Santiago, Chile
[8] Gemini North Observatory, 670 N. A'ohoku Place, Hilo, HI 96720, USA
[9] Institute for Astronomy, University of Hawaii, 2680 Woodlawn Drive, Honolulu, HI 96822, USA
[10] Infrared Processing and Analysis Center, MC 314-6, Caltech, 1200 E. California Blvd., Pasadena, CA 91125, USA
[11] National Radio Astronomy Observatory, 520 Edgemont Road, Charlottesville, VA 22903, USA
[12] Joint ALMA Observatory, Alonso de Córdova 3107, Vitacura, Santiago, Chile
[13] Department of Astronomy, University of Virginia, PO Box 400325, Charlottesville, VA 22904, USA
[14] Univ Lyon, Univ Lyon1, ENS de Lyon, CNRS, Centre de Recherche Astrophysique de Lyon (CRAL) UMR5574, 69230 Saint Genis-Laval, France
[15] Cahill Center for Astronomy and Astrophysics, California Institute of Technology, MS 249-17, Pasadena, CA 91125, USA
[16] Research School of Astronomy & Astrophysics, Australian National University, ACT 2611 Canberra, Australia
[17] Department of Astronomy, University of Florida, 211 Bryant Space Sciences Center, Gainesville, FL 32611, USA
[18] Department of Physics and Astronomy, 4129 Frederick Reines Hall, University of California, Irvine, CA 92697, USA

Received 18 August 2018 / Accepted 2 October 2018

ABSTRACT

We analyze *Chandra* X-ray observatory data for a sample of 63 luminous infrared galaxies (LIRGs), sampling the lower-infrared luminosity range of the Great Observatories All-Sky LIRG survey (GOALS), which includes the most luminous infrared selected galaxies in the local Universe. X-rays are detected for 84 individual galaxies within the 63 systems, for which arcsecond resolution X-ray images, fluxes, infrared and X-ray luminosities, spectra and radial profiles are presented. Using X-ray and mid-infrared (MIR) selection criteria, we find AGN in (31 ± 5)% of the galaxy sample, compared to the (38 ± 6)% previously found for GOALS galaxies with higher infrared luminosities (C-GOALS I). Using MIR data, we find that (59 ± 9)% of the X-ray selected AGN in the full C-GOALS sample do not contribute significantly to the bolometric luminosity of the host galaxy. Dual AGN are detected in two systems, implying a dual AGN fraction in systems that contain at least one AGN of (29 ± 14)%, compared to the (11 ± 10)% found for the C-GOALS I sample. Through analysis of radial profiles, we derive that most sources, and almost all AGN, in the sample are compact, with half of the soft X-ray emission generated within the inner ~1 kpc. For most galaxies, the soft X-ray sizes of the sources are comparable to those of the MIR emission. We also find that the hard X-ray faintness previously reported for the bright C-GOALS I sources is also observed in the brightest LIRGs within the sample, with $L_{\rm FIR} > 8 \times 10^{10}\,L_{\odot}$.

Key words. infrared: galaxies – X-rays: galaxies – galaxies: active – galaxies: starburst

1. Introduction

Luminous and ultra-luminous infrared galaxies (LIRGs and ULIRGs) are galaxies with infrared (IR) luminosities exceeding $10^{11}\,L_{\odot}$ and $10^{12}\,L_{\odot}$, respectively. LIRGs and ULIRGs are normally found to be gas-rich galaxy mergers, as tidal torques can funnel material from kpc scales to the innermost regions of the galaxy and trigger intense star formation and/or AGN activity (e.g., Hernquist 1989; Sanders 1999; Di Matteo et al. 2005), the latter more significantly so with increasing IR luminosity (e.g., Valiante et al. 2009; Petric et al. 2011; Alonso-Herrero et al. 2012).

These objects, common at redshifts 1−3 where the peak of star formation in the Universe is observed, represent a very important stage in galaxy evolution (e.g., Casey et al. 2014). The scenario proposed by Sanders et al. (1988) and Hopkins et al. (2005), for example, indicates that after a complete obscuration phase of the merger, ULIRGs in a late stage of the interaction would later disperse or consume the gas and probably evolve into an obscured type II quasar (QSO), and eventually

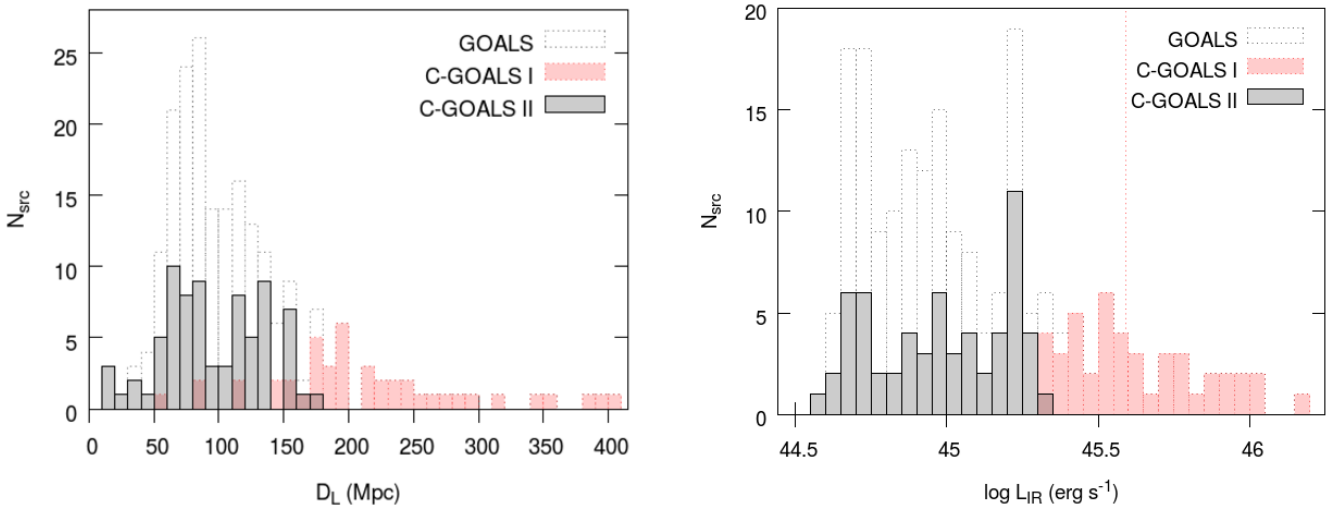

Fig. 1. Distribution of luminosity distance (*left panel*) and IR luminosity $L_{IR}(8-1000\,\mu m)$ (*right panel*) for the 44 objects of C-GOALS I (Iwasawa et al. 2011), the 63 objects of C-GOALS II, and the 201 systems of the full GOALS sample (Armus et al. 2009). The vertical dashed line represents $L_{IR} = 10^{12}\,L_{\odot}$, the boundary between LIRGs and ULIRGs.

into an exposed QSO. This process will ultimately lead to the formation of an elliptical galaxy, and accounts for the growth of the central supermassive black hole (e.g., Sanders et al. 1988; Hopkins et al. 2009).

In agreement with this scenario, recent studies of pairs of galaxies have found that the fraction of dual AGN grows with decreasing separation between companions (e.g., Ellison et al. 2011; Satyapal et al. 2014, 2017; Silverman et al. 2011; Koss et al. 2012). More specifically, in a sample of LIRGs and ULIRGs, Stierwalt et al. (2013) found an increase in the fraction of composite systems with merger stage. Satyapal et al. (2014) found larger fractions of IR-selected AGN with respect to optically selected AGN in mergers, which is likely due to the increase of obscuration. Evidence of an excess of AGN with high obscuring column densities in mergers are also found in recent works (e.g., Díaz-Santos et al. 2010; Kocevski et al. 2015; Del Moro et al. 2016; Lanzuisi et al. 2015; Ricci et al. 2017).

X-ray observations are an ideal tool for analyzing the properties of the inner regions of such obscured objects, because the gas and dust have a higher transparency than at larger wavelengths. Previous studies of small (e.g., Franceschini et al. 2003; Ptak et al. 2003; Teng et al. 2005) and larger (e.g., Teng & Veilleux 2010; Iwasawa et al. 2011; Ricci et al. 2017) samples of ULIRGs have highlighted the potential of X-rays in distinguishing the contribution of AGN and starburst and the ability to detect enshrouded AGN.

One of the recent works, C-GOALS I (*Chandra*-GOALS I, Iwasawa et al. 2011), is an X-ray study performed with the *Chandra* X-ray Observatory (*Chandra*, hereafter, Weisskopf et al. 2000) of a complete sample of LIRGs within the Great Observatories All-Sky LIRG Survey (GOALS, Armus et al. 2009). GOALS is a multi-wavelength study of the brightest IR galaxies in the local Universe, a low-redshift subsample of the 60 μm flux selected IRAS Revised Bright Galaxy Sample (RBGS, Sanders et al. 2003). The GOALS galaxies, all at $z < 0.088$, are perfect laboratories for multi-wavelength studies of LIRGs with a level of detail that only the observation of local galaxies allows. The arcsecond resolution provided by *Chandra* can offer information of individual galaxies within mergers, and help distinguish previously undetected or unresolved AGN, in particular, complementing studies of LIRGs and ULIRGs at harder X-rays (e.g. Ricci et al. 2017).

The C-GOALS I paper presents data obtained by us and others with *Chandra* and represents the X-ray component of the multi-wavelength survey for the most luminous IR GOALS sources. This work, C-GOALS II, extends the X-ray study to a subsample of the lower luminosity range of GOALS galaxies. These data were obtained during *Chandra* cycle 13 (PI: Sanders), combined with available archival data. The extension of the X-ray sample is motivated by the interest in reaching completeness in all wavelengths for the GOALS sample, and by the opportunity of comparing results derived at different IR luminosity ranges. The sample contains galaxies at earlier merger stages, contributing to the expansion of previous studies into the domain of the less luminous LIRGS. In particular, Iwasawa et al. (2011) observed a deviation in the correlation between IR and X-ray luminosities in nearby star-forming galaxies (e.g., Ranalli et al. 2003; Grimm et al. 2003; Mineo et al. 2014) for the galaxies in the C-GOALS I sample. The IR luminosities of galaxies in the C-GOALS II sample fall into the range where this change of behavior should occur, and are ideal to further study the reasons for and possible implications of such deviation.

The C-GOALS II sample is described and compared to the C-GOALS I sample in Sect. 2. The observations and data reduction are described in Sect. 3. Results, including all X-ray images, fluxes, spectra, and radial surface brightness profiles, are presented in Sect. 4, while derived properties and discussion of the X-ray and IR luminosity correlation are presented in Sect. 5. Finally, we summarize our conclusions in Sect. 6. Notes on individual objects can be found in Appendix A, and X-ray contours, detailed images in the 0.5−2 and 2−7 keV bands, along with radial surface brightness profiles for each source, can be found in Appendix B.

2. Sample

GOALS (Armus et al. 2009) is a comprehensive study of 201 of the most luminous IR-selected galaxies in the local Universe. The sample consists of 179 LIRGs and 22 ULIRGs, 85 of which are systems that contain multiple galaxies. GOALS is drawn from the IRAS RBGS (Sanders et al. 2003), with a luminosity threshold of $L_{IR} \geq 10^{11}\,L_{\odot}$. The RBGS is a complete sample of galaxies, covering the whole sky, that have IRAS 60 μm flux densities above 5.24 Jy and Galactic latitude $|b| \geq 5°$.

Table 1. Basic parameters of the objects in the C-GOALS II sample.

No.	IRAS Name	Optical ID	RA (NED) (J2000)	Dec (NED) (J2000)	z	D_L (Mpc)	$\log(L_{IR})$ ($L_\odot$)
(1)	(2)	(3)	(4)	(5)	(6)	(7)	(8)
45	F13182+3424	UGC 08387	13h 20m 35.34s	+34d 08m 22.2s	0.0233	110.0	11.73
47	F01173+1405	CGCG 436−030	01h 20m 02.72s	+14d 21m 42.9s	0.0312	134.0	11.69
49	F01484+2220	NGC 0695	01h 51m 14.24s	22d 34m 56.5s	0.0325	139.0	11.69
50	F12592+0436	CGCG 043−099	13h 01m 50.80s	+04d 20m 00.0s	0.0375	175.0	11.68
51	F11011+4107	MCG+07−23−019	11h 03m 53.20s	+40d 50m 57.0s	0.0345	158.0	11.62
52	F18329+5950	NGC 6670	18h 33m 35.91s	+59d 53m 20.2s	0.0289	129.5	11.65
53	F02512+1446	UGC 02369	02h 54m 01.78s	+14d 58m 24.9s	0.0312	136.0	11.67
54	F04315−0840	NGC 1614	04h 33m 59.85s	−08d 34m 44.0s	0.0159	67.8	11.65
56	F13497+0220	NGC 5331	13h 52m 16.29s	+02d 06m 17.0s	0.0330	155.0	11.66
57	F06076−2139	IRAS F06076−2139	06h 09m 45.81s	−21d 40m 23.7s	0.0374	165.0	11.65
60	F11231+1456	IC 2810	11h 25m 47.30s	+14d 40m 21.1s	0.0342	157.0	11.64
63	18090+0130	IRAS 18090+0130	18h 11m 35.91s	+01d 31m 41.3s	0.0342	134.0	11.65
64	F01417+1651	III Zw 035	01h 44m 30.45s	+17d 06m 05.0s	0.0274	119.0	11.64
65	F10257−4339	NGC 3256	10h 27m 51.27s	−43d 54m 13.8s	0.0094	38.9	11.64
67	F16399−0937	IRAS F16399−0937	16h 42m 40.21s	−09d 43m 14.4s	0.0270	128.0	11.63
68	F16164−0746	IRAS F16164−0746	16h 19m 11.79s	−07d 54m 02.8s	0.0272	128.0	11.62
69	F18093−5744	IC 4686/7	18h 13m 39.63s	−57d 43m 31.3s	0.0173	81.9	11.62
71	F08354+2555	NGC 2623	08h 38m 24.08s	+25d 45m 16.6s	0.0185	84.1	11.60
72	F23135+2517	IC 5298	23h 16m 00.70s	+25d 33m 24.1s	0.0274	119.0	11.60
73	20351+2521	IRAS 20351+2521	20h 37m 17.72s	+25d 31m 37.7s	0.0337	151.0	11.61
75	F16104+5235	NGC 6090	16h 11m 40.70s	+52d 27m 24.0s	0.0293	137.0	11.58
79	F13362+4831	NGC 5256	13h 38m 17.52s	+48d 16m 36.7s	0.0279	129.0	11.56
80	F03359+1523	IRAS F03359+1523	03h 38m 46.70s	+15d 32m 55.0s	0.0354	152.0	11.55
81	F04191−1855	ESO 550−IG025	04h 21m 20.02s	−18d 48m 47.6s	0.0322	135.8	11.51
82	F00085−1223	NGC 0034	00h 11m 06.55s	−12d 06m 26.3s	0.0196	84.1	11.49
83	F00506+7248	MCG+12−02−001	00h 54m 03.61s	+73d 05m 11.8s	0.0157	69.8	11.50
85	F17138−1017	IRAS F17138−1017	17h 16m 35.79s	−10d 20m 39.4s	0.0173	84.0	11.49
95	F12043−3140	ESO 440−IG058	12h 06m 51.82s	−31d 56m 53.1s	0.0232	112.0	11.43
100	F21453−3511	NGC 7130	21h 48m 19.50s	−34d 57m 04.7s	0.0162	72.7	11.42
104	F23488+1949	NGC 7771	23h 51m 24.88s	+20d 06m 42.6s	0.0143	61.2	11.40
105	F23157−0441	NGC 7592	23h 18m 22.20s	−04d 24m 57.6s	0.0244	106.0	11.40
106	F16577+5900	NGC 6286	16h 58m 31.38s	+58d 56m 10.5s	0.0183	85.7	11.37
107	F12590+2934	NGC 4922	13h 01m 24.89s	+29d 18m 40.0s	0.0236	111.0	11.38
110	F10015−0614	NGC 3110	10h 04m 02.11s	−06d 28m 29.2s	0.0169	79.5	11.37
114	F00402−2349	NGC 0232	00h 42m 45.82s	−23d 33m 40.9s	0.0227	95.2	11.44
117	F09333+4841	MCG+08−18−013	09h 36m 37.19s	+48d 28m 27.7s	0.0259	117.0	11.34
120	F15107+0724	CGCG 049−057	15h 13m 13.09s	+07d 13m 31.8s	0.0130	65.4	11.35
121	F02401−0013	NGC 1068	02h 42m 40.71s	−00d 00m 47.8s	0.0038	15.9	11.40
123	F02435+1253	UGC 02238	02h 46m 17.49s	+13d 05m 44.4s	0.0219	92.4	11.33
127	F13197−1627	MCG−03−34−064	13h 22m 24.46s	−16d 43m 42.9s	0.0165	82.2	11.28
134	F00344−3349	ESO 350−IG038	00h 36m 52.25s	−33d 33m 18.1s	0.0206	89.0	11.28
136	F23394−0353	MCG−01−60−022	23h 42m 00.85s	−03d 36m 54.6s	0.0232	100.0	11.27
141	F09437+0317	IC 0563/4	09h 46m 20.71s	+03d 03m 30.5s	0.0200	92.9	11.23
142	F13229−2934	NGC 5135	13h 25m 44.06s	−29d 50m 01.2s	0.0137	60.9	11.30
144	F13126+2453	IC 0860	13h 15m 03.53s	+24d 37m 07.9s	0.0112	56.8	11.14
147	F22132−3705	IC 5179	22h 16m 09.10s	−36d 50m 37.4s	0.0114	51.4	11.24
148	F03514+1546	CGCG 465−012	03h 54m 16.08s	+15d 55m 43.4s	0.0222	94.3	11.20
157	F12596−1529	MCG−02−33−098/9	13h 02m 19.70s	−15d 46m 03.0s	0.0159	78.7	11.17
163	F12243−0036	NGC 4418	12h 26m 54.62s	−00d 52m 39.2s	0.0073	36.5	11.19
169	F21330−3846	ESO 343−IG013	21h 36m 10.83s	−38d 32m 37.9s	0.0191	85.8	11.14
170	F06107+7822	NGC 2146	06h 18m 37.71s	+78d 21m 25.3s	0.0030	17.5	11.12
174	F14280+3126	NGC 5653	14h 30m 10.42s	+31d 12m 55.8s	0.0119	60.2	11.13
178	F12116+5448	NGC 4194	12h 14m 09.47s	+54d 31m 36.6s	0.0083	43.0	11.10
179	F23157+0618	NGC 7591	23h 18m 16.28s	+06d 35m 08.9s	0.0165	71.4	11.12
182	F00073+2538	NGC 0023	00h 09m 53.41s	+25d 55m 25.6s	0.0152	65.2	11.12
188	F23133−4251	NGC 7552	23h 16m 10.77s	−42d 35m 05.4s	0.0054	23.5	11.11
191	F04118−3207	ESO 420−G013	04h 13m 49.69s	−32d 00m 25.1s	0.0119	51.0	11.07
194	08424−3130	ESO 432−IG006	08h 44m 28.07s	−31d 41m 40.6s	0.0162	74.4	11.08
195	F05365+6921	NGC 1961	05h 42m 04.65s	+69d 22m 42.4s	0.0131	59.0	11.06
196	F23444+2911	NGC 7752/3	23h 47m 01.70s	+29d 28m 16.3s	0.0162	73.6	11.07
198	F03316−3618	NGC 1365	03h 33m 36.37s	−36d 08m 25.4s	0.0055	17.9	11.00
199	F10196+2149	NGC 3221	10h 22m 19.98s	+21d 34m 10.5s	0.0137	65.7	11.09
201	F02071−1023	NGC 0838	02h 09m 38.58s	−10d 08m 46.3s	0.0128	53.8	11.05

Notes. Column (1): Object number, also used in other tables. Column (2): Original IRAS source, where an "F" prefix indicates the Faint Source Catalog and no prefix indicates the Point Source Catalog. Column (3): Optical cross-identification, when available from NED. Columns (4)–(6): The best available right ascension (J2000), declination and heliocentric redshift from NED as of October 2008. Column (7): The luminosity distance derived by correcting the heliocentric velocity for the 3-attractor flow model of Mould et al. (2000) and adopting cosmological parameters $H_0 = 73\,\mathrm{km\,s^{-1}\,Mpc^{-2}}$, $\Omega_V = 0.73$, and $\Omega_M = 0.27$, as provided by NED. Column (8): The total (8–1000) μm luminosity in $\log_{10}$ Solar units as in (Armus et al. 2009).

Iwasawa et al. (2011) studied a subsample of GOALS, C-GOALS I (hereafter, also CGI), which is complete in the higher IR luminosity end of the GOALS sample ($\log(L_{IR}/L_{\odot})$ = 11.73−12.57). It contains 44 systems in the redshift range z = 0.010 − 0.088. The new sample, C-GOALS II (hereafter, also CGII), is an incomplete subsample of the lower luminosity section of GOALS, and includes all sources in the $\log(L_{IR}/L_{\odot})$ = 11.00 − 11.73 range with available *Chandra* data, as of January 2016. It is comprised of 63 systems, 30 of which contain multiple galaxies. The redshift range of the new sample is z = 0.003 − 0.037. The distribution of IR luminosities and distances of the two samples is shown in Fig. 1. Table 1 gives basic parameters for all the objects in the C-GOALS II sample. We note that names and positions refer to the IR detected systems. Decomposition into individual galaxies is taken into account in Sect. 4.

Figure 1 also shows the incompleteness of CGII, comparing it with the full GOALS distribution of distances and luminosities. Of the 63 systems within CGII, 31 were observed through the same proposal, which was drawn to be representative of all possible merger stages. For the remaining 32 systems, data were taken from the archive according to availability. The proposal for which observing time was awarded varies in each case, and all target different scientific goals (e.g., study of AGN, SFR, and X-ray binaries). For this reason, we do not expect our subsample to be biased toward a certain type of object, merger stage, or luminosity within the parent GOALS sample.

3. Observations and data reduction

Thirty-one systems were observed with *Chandra* in cycle 13 (PI: Sanders) with a 15 ks exposure on each target, carried out in imaging mode with the ACIS-S detector in VFAINT mode (Garmire et al. 2003). For the remaining 32 objects studied in this work, *Chandra* data were obtained from the archive. Exposure times for these targets varied from 4.88 to 58.34 ks, all taken with the ACIS-S detector in either FAINT or VFAINT mode. Table 2 shows the observation log for the whole CGII sample, as well as the total source counts in the 0.5−7 keV band for each object, obtained from the data analysis. The counts were derived for individual galaxies, and summed together when an object within the CGII sample contained more than one galaxy.

The data reduction was performed using the *Chandra* data analysis package CIAO version 4.7 (Fruscione et al. 2006), and HEASARC's FTOOLS (Blackburn et al. 1995). The cosmology adopted here is consistent with that adopted by Armus et al. (2009) and Iwasawa et al. (2011). Cosmological distances were computed by first correcting for the three-attractor flow model of Mould et al. (2000) and adopting H_0 = 70 km s^{-1} Mpc^{-1}, Ω_V = 0.72, and Ω_M = 0.28 based on the five-year WMAP results (Hinshaw et al. 2009), as provided by the NASA/IPAC Extragalactic Database (NED).

4. Results

Results of the X-ray analysis of the *Chandra* data are presented in Table A.1. For each galaxy we present the background-corrected ACIS-S X-ray soft band (S, 0.5−2 keV) count rate and X-ray hard band (H, 2−7 keV) count rate, the hardness ratio or X-ray color, estimated X-ray fluxes and luminosities in both soft and hard band, and the logarithmic ratio of each X-ray band to the IR luminosity listed in Table 1, L_{IR}(8−1000 μm). X-ray color, or hardness ratio, is computed as HR = $(H - S)/(H + S)$, using the bands defined previously.

Individual galaxies belonging to the same GOALS system (i.e., contributing to one single IRAS source) are identified by using the same GOALS number in the first column. Source names shown in the second column are used throughout this work; see Appendix A for a clarification on the identification of each component.

The hard X-ray flux (F_{HX}) listed in Table A.1 is in the 2−7 keV band, where *Chandra* is more sensitive; and the listed hard X-ray luminosities (L_{HX}) refer to the 2−10 keV band. Spectral fitting to derive the fluxes is performed in the 2−7 keV range as described in Sect. 4.4, and the fitted models are later used to estimate the luminosity up to 10 keV, in order to compare the derived results to those of previous works, in which the 2−10 keV band is used.

Although significant intrinsic absorption in dusty objects such as LIRGs is likely present, X-ray luminosities were estimated by correcting only for galactic absorption. The X-ray spectra of our galaxies are complex, containing multiple components, with different degrees of obscuration, as explained in Sect. 4.4. As the estimated absorbing column density values are heavily model dependent, we did not use them to correct the luminosities listed in Table A.1.

As mentioned in Sect. 2, many of the LIRGs in the CGII sample are composed of multiple galaxies, which are associated with a single GOALS object, as IRAS is unable to resolve them. All spatially resolved components in the *Chandra* data are presented separately, their count rates, fluxes, and luminosities were computed individually. In order to obtain the X-ray to IR ratios listed in Table A.1, the IRAS flux associated with each object must be appropriately separated into the corresponding contribution of each component. This separation was carried out according to the best possible estimate available for each source, as listed in Table 3. The most accurate estimation would be derived by obtaining the separate contribution of each component from the far-infrared (FIR) emission. When possible, this was done using *Herschel* photometric data (Chu et al. 2017). However, 14 of the multiple systems in the sample are unresolved by *Herschel*, and thus the MIR *Spitzer* MIPS 24 data were used for this purpose.

For four systems in the sample the individual components remain unresolved at MIR wavelengths, and other determinations were used, as specified in Table 3 and Appendix A.

Only objects that were detected in X-rays and contribute to at least 10% of the IR luminosity of the IRAS source were analyzed and are presented in this work. This cut means that out of the 63 GOALS systems in the sample, 84 individual galaxies are studied in CGII. No galaxy contributing <10% to the IR has a strong X-ray emission, but in cases in which the source is detected in the *Chandra* data, it is specified in Appendix A. For all galaxies in pairs that are not included in the analysis, their contribution to the IR luminosity of the bright component is taken into account.

4.1. X-ray images

We show how the X-ray radiation is related to the optical and IR emission, by comparing the 0.4−7 keV brightness contours with HST, SDSS, or IRAC images according to availability, in this order of preference. Appendix B shows X-ray contours overlaid on HST-ACS F814W (I-band) images (Evans et al. in prep.) for 27 objects, overlaid on SDSS DR-12 i-band images (Alam et al. 2015) for 18 objects and overlaid on IRAC channel 1 images (Armus et al. 2009; Mazzarella et al., in prep.) for the remaining 18 objects.

The contours are taken from a 0.4−7 keV image, smoothed using a Gaussian filter with a dispersion of 1 arcsec, with the

Table 2. *Chandra* observation log for the objects in the CGII sample.

No.	Galaxy	Obs ID	Date	Mode	Exp. Time (ks)	0.5−7.0 keV[a] (cts)	$N_{H,Gal}$[b] (10^{20} cm^{-2})
45	UGC 08387	7811	2007−02−19	VFAINT	14.07	277.9 ± 17.1	1.0
47	CGCG 436−030	15047	2012−11−24	VFAINT	13.82	168.6 ± 13.8	3.4
49	NGC 0695	15046	2013−01−01	VFAINT	14.78	312.9 ± 18.5	6.9
50	CGCG 043−099	15048	2012−11−23	VFAINT	14.78	71.9 ± 8.1	1.9
51	MCG+07−23−019	12977	2011−02−07	VFAINT	52.34	506.9 ± 26.8	1.0
52	NGC 6670	15049	2013−02−08	VFAINT	14.77	252.7 ± 16.8	3.9
53	UGC 02369	4058	2002−12−14	FAINT	9.68	120.6 ± 12.0	7.9
54	NGC 1614	15050	2012−11−21	VFAINT	15.76	800.0 ± 28.9	6.3
56	NGC 5331	15051	2013−05−12	VFAINT	14.78	121.9 ± 12.4	2.0
57	IRAS F06076−2139	15052	2012−12−12	VFAINT	14.78	52.4 ± 8.2	7.6
60	IC 2810	15053	2013−10−27	VFAINT	14.78	93.2 ± 11.7	2.5
63	IRAS 18090+0130	15054	2013−02−10	VFAINT	14.77	98.9 ± 11.3	20.2
64	III Zw 035	6855	2006−02−24	FAINT	14.98	81.4 ± 9.0	4.8
65	NGC 3256	835	2000−01−05	FAINT	27.80	8117.2 ± 102.3	9.1
67	IRAS F16399−0937	15055	2013−06−30	VFAINT	14.87	161.9 ± 14.4	13.0
68	IRAS F16164−0746	15057	2013−01−19	VFAINT	14.78	99.2 ± 11.3	11.3
69	IC 4686/7	15056	2012−11−19	VFAINT	14.48	519.7 ± 23.8	11.5
71	NGC 2623	4059	2003−01−03	FAINT	19.79	171.0 ± 14.1	3.1
72	IC 5298	15059	2013−02−04	VFAINT	14.78	222.8 ± 16.0	5.7
73	IRAS 20351+2521	15058	2012−12−13	VFAINT	13.56	146.8 ± 14.0	13.1
75	NGC 6090	6859	2006−05−14	FAINT	14.79	347.5 ± 19.3	1.6
79	NGC 5256	2044	2001−11−02	FAINT	19.69	1451.2 ± 43.5	1.7
80	IRAS F03359+1523	6856	2005−12−17	FAINT	14.76	108.2 ± 11.4	13.8
81	ESO 550−IG025	15060	2012−11−24	VFAINT	14.78	72.2 ± 10.6	3.2
82	NGC 0034	15061	2013−06−05	VFAINT	14.78	329.0 ± 19.5	2.1
83	MCG+12−02−001	15062	2012−11−22	VFAINT	14.31	311.0 ± 19.3	22.0
85	IRAS F17138−1017	15063	2013−07−12	VFAINT	14.78	207−3 ± 15.4	17.0
95	ESO 440−IG058	15064	2013−03−20	VFAINT	14.78	187.0 ± 16.1	5.6
100	NGC 7130	2188	2001−10−23	FAINT	38.64	3327.1 ± 59.3	1.9
104	NGC 7771	10397	2009−05−22	VFAINT	16.71	904.6 ± 34.6	4.0
105	NGC 7592	6860	2006−10−15	FAINT	14.99	388.7 ± 21.9	3.8
106	NGC 6286	10566	2009−09−18	FAINT	14.00	544.8 ± 27.9	1.8
107	NGC 4922	15065	2013−11−02	VFAINT	14.86	202.9 ± 17.2	0.9
110	NGC 3110	15069	2013−02−02	VFAINT	14.87	396.3 ± 22.3	3.5
114	NGC 0232	15066	2013−01−04	VFAINT	14.78	193.5 ± 15.7	1.4
117	MCG+08−18−013	15067	2013−06−03	VFAINT	13.79	101.7 ± 11.1	1.7
120	CGCG 049−057	10399	2009−04−17	VFAINT	19.06	30.2 ± 7.6	2.6
121	NGC 1068	344	2000−02−21	FAINT	47.44	100828.1 ± 326.7	2.9
123	UGC 02238	15068	2012−12−02	VFAINT	14.87	132.1 ± 13.5	8.9
127	MCG−03−34−064	7373	2006−07−31	FAINT	7.09	1029.3 ± 32.9	5.0
134	ESO 350−IG038	8175	2006−10−28	VFAINT	54.00	1794.5 ± 45.8	2.4
136	MCG−01−60−022	10570	2009−08−13	FAINT	18.90	325.4 ± 21.7	3.6
141	IC 0563/4	15070	2013−01−19	VFAINT	14.96	252.5 ± 18.9	3.8
142	NGC 5135	2187	2001−09−04	FAINT	29.30	3975.9 ± 68.0	4.9
144	IC 0860	10400	2009−03−24	VFAINT	19.15	25.9 ± 7.2	1.0
147	IC 5179	10392	2009−06−21	VFAINT	11.96	555.5 ± 32.2	1.4
148	CGCG 465−012	15071	2012−12−17	VFAINT	14.87	134.0 ± 13.4	14.8
157	MCG−02−33−098/9	15072	2013−05−08	VFAINT	14.87	141.0 ± 12.4	3.7
163	NGC 4418	4060	2003−03−10	FAINT	19.81	59.6 ± 15.3	1.9
169	ESO 343−IG013	15073	2013−06−13	VFAINT	14.78	139.6 ± 13.9	2.8
170	NGC 2146	3135	2002−11−16	FAINT	10.02	2144.2 ± 50.4	7.1
174	NGC 5653	10396	2009−04−11	VFAINT	16.52	387.1 ± 22.8	1.3
178	NGC 4194	7071	2006−09−09	FAINT	35.50	2410.3 ± 51.4	1.5
179	NGC 7591	10264	2009−07−05	FAINT	4.88	26.3 ± 6.1	5.6
182	NGC 0023	10401	2008−10−27	VFAINT	19.45	753.1 ± 31.9	3.4
188	NGC 7552	7848	2007−03−31	FAINT	5.08	832.8 ± 30.2	1.2
191	ESO 420−G013	10393	2009−05−13	VFAINT	12.42	759.0 ± 29.2	2.1
194	ESO 432−IG006	15074	2013−06−24	VFAINT	16.05	280.7 ± 20.0	19.3
195	NGC 1961	10531	2009−05−08	VFAINT	32.83	723.3 ± 40.0	8.1
196	NGC 7752/3	10569	2009−08−30	FAINT	11.99	96.0 ± 12.7	5.4
198	NGC 1365	6869	2006−04−20	FAINT	15.54	4644.2 ± 72.7	1.3
199	NGC 3221	10398	2009−03−19	VFAINT	19.03	323.5 ± 28.3	1.9
201	NGC 0838	15667	2013−07−21	VFAINT	58.34	1996.0 ± 49.6	2.6

Notes. [(a)]The source counts are background corrected and measured in the 0.5−7.0 keV band. The counts from separate components in a single system are obtained separately and then summed together. [(b)]The Galactic absorption column density is taken from the LAB HI map by Kalberla et al. (2005).

Table 3. IR fractions.

No.	Galaxy in system (1)	% (2)	Ref. (3)
47	CGCG 436−030 (W)	100	5
52	NGC 6670 (W)	62	1
53	UGC 02369 (S)	98	2
56	NGC 5331 (S)	81	1
57	IRAS F06076−2139 (N)	88	2
60	IC 2810 (NW)	68	1
63	IRAS 18090+0130 (E)	81	1
64	III Zw 035 (N)	100	5
67	IRAS F16399−0937 (N)	90	3
69	IC 4687 (N,S)*	66,22	1
75	NGC 6090 (NE)	90	4
79	NGC 5256 (SW)	63	2
80	IRAS F03359+1523 (E)	100	5
81	ESO 550−IG025 (N)	59	1
83	MCG+12−02−001 (E,W)*	90,10	2
95	ESO 440−IG058 (S)	89	1
104	NGC 7771	90	1
105	NGC 7592 (E,S)*	63,0	2
106	NGC 6286	87	1
107	NGC 4922 (N)	99	2
110	NGC 3110 (NE)	91	1
117	MCG+08−18−013 (E)	97	1
127	MCG−03−34−064	75	1
141	IC 0564	54	1
157	MCG−02−33−098/9 (W)	69	2
163	NGC 4418	99	1
169	ESO 343−IG013 (N)	78	2
179	NGC 7591	94	1
194	ESO 432−IG006 (SW)	63	1
196	NGC 7753	64	1

Notes. Column (1): Name of the galaxy (galaxies) that emits most of the IR luminosity in a double (triple) system. Column (2): Percentage of IR emission originating in the dominant component. Column (3): Reference from which the contribution to the IR luminosity is derived. 1: Derived from *Herschel* data (as in Chu et al. 2017). 2: Derived from MIPS 24 data (as in Díaz-Santos et al. 2010). 3: MIR determination from Haan et al. (2011). 4: Predicted IR emission from radio continuum in Hattori et al. (2004). 5: We refer to the notes on individual objects in Appendix A. (*)Triple-component galaxy.

exception of NGC 5135, shown in Appendix B, for which a smoothing of 0.5 arcsec was used in order to preserve the two X-ray central peaks.

Eleven contour levels were defined, divided into ten equal logarithmic intervals, in the four different surface brightness ranges shown in Table 4. "Interval 1" was used for the majority of the sample. In order to outline lower surface brightness features in some sources, 11 contour levels starting at a lower surface brightness values were taken, as "Interval 2" or "Interval 3". For a few systems, a higher lower surface brightness limit was taken in order to eliminate noisy features in the contours, defined as "Interval 4". For the bright objects NGC 1068 and NGC 1365, 21 contour levels were used instead, in order to reflect the X-ray morphology appropriately. Appendix B contains information on which optical or IR image was used to overlay the X-ray contours on, and also on the Interval that we used for X-ray contour ranges.

As the hard-band emission from all objects is generally more peaked and less intense than the soft-band emission, the contours mostly trace soft X-ray emission from the sources. For this reason, in sources for which one or more clear hard X-ray peaks are seen, these are marked with a green cross. We define a hard X-ray peak as point-source emission that clearly stands out from the rest of the photon distribution in the unsmoothed images. In cases where many point-like sources that are clearly not associated with any central source in the galaxy are present in an image, we opted not to mark them all individually. For a more detailed description of the X-ray emission in both bands, Appendix B also presents the smoothed and unsmoothed images in the 0.4−7 keV band, and smoothed images in the soft (0.5−2 keV) and hard (2−7 keV) bands, for all objects. An example of one of these images is shown in Fig. 2.

Table 4. X-ray contour ranges.

Interval	Low (1)	High (2)	Levels (3)
1	2.5×10^{-5}	7×10^{-3}	11
2	1.7×10^{-5}	7×10^{-3}	11
3	1.0×10^{-5}	7×10^{-3}	11
4	4.0×10^{-5}	7×10^{-3}	11
Galaxy			
CGCG 465-012	2.5×10^{-5}	2.0×10^{-4}	11
NGC 1068	2.5×10^{-5}	4.0×10^{-2}	21
NGC 5135	4.0×10^{-5}	1.0×10^{-2}	11
NGC 1365	2.5×10^{-5}	2.0×10^{-2}	21
NGC 0838	7.0×10^{-6}	4.0×10^{-4}	11

Notes. Columns (1) and (2): Lower and higher contour in [counts s^{-1} $arcsec^{-1}$] for the given interval, respectively. (4): Number of logarithmic contour levels.

4.2. X-ray spectra

Figure C.1 presents the X-ray spectra for all sources. Spectral data are shown separately for each object with more than one resolved component. Instead of showing the usual count rate spectra, which are data folded through the detector response, we present the *Chandra* ACIS spectra corrected for the detector response and converted into flux density units. This has the advantage of presenting the spectral properties without the need of spectral fitting, and facilitates comparison with other multi-wavelength data from GOALS. The flux density range for all spectra was set to be the same, two orders of magnitude, for consistent comparison. An example of one such spectrum is shown in Fig. 3.

This presentation introduces some uncertainty, particularly when a spectral bin is large enough, within which the detector response varies rapidly, for instance, for galaxies with only few counts. It should also be taken into account that even though these have been corrected for the detector effective area, the energy resolution of the detector is preserved, and therefore they are independent of any spectral model fitting; that is to say, they are not unfolded spectra.

It should also be noted that the spectra in Fig. C.1 are for display purposes only, and all physical quantities determined were obtained through spectral fitting of the count rate spectra, with the appropriate detector responses.

4.3. AGN selection

The AGN classification in the sample was performed using different criteria in both X-rays and IR. Any galaxy that met any of

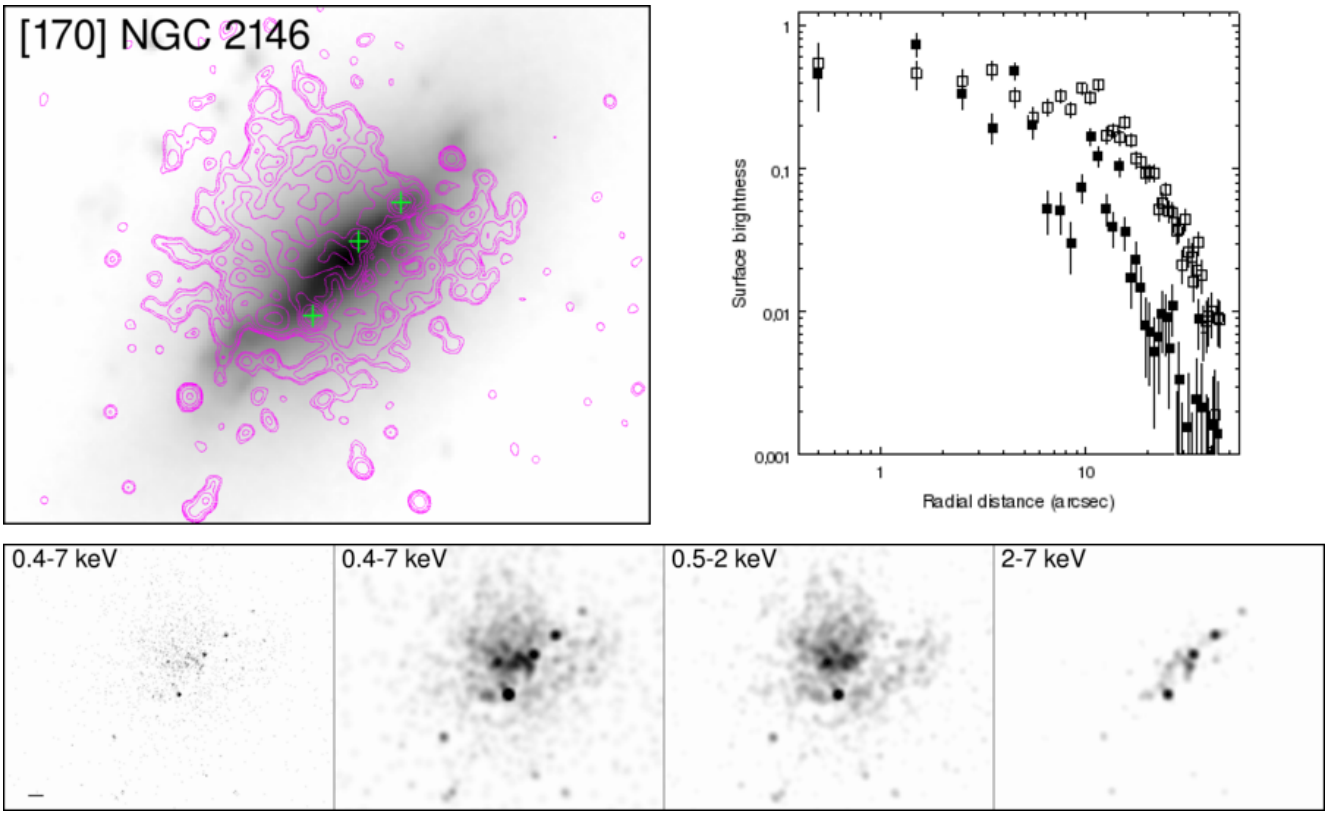

Fig. 2. X-ray images and surface brightness profiles for NGC 2146. North is up and east to the left. Similar figures for all 59 objects in the CGII sample are presented in Appendix B. *Upper left:* X-ray (0.4−7 keV) brightness contours (magenta) with marked hard X-ray peaks (green crosses) overlaid on optical/IR images. *Upper right:* Radial surface brightness profiles in the 0.5−2 keV band (open squares) and the 2−7 keV band (filled squares). Profiles have been centered using the brightness peak in the hard X-ray band, when clearly originating in the nucleus. We refer to Appendix A for ambiguous objects. *Bottom:* From left to right, unsmoothed and smoothed images in the 0.4−7 keV band, and smoothed images in the soft (0.5−2 keV) and hard (2−7 keV) bands. The pixel size is ∼0.5″ × 0.5″. The scale bar in the *bottom left* image represents 5″.

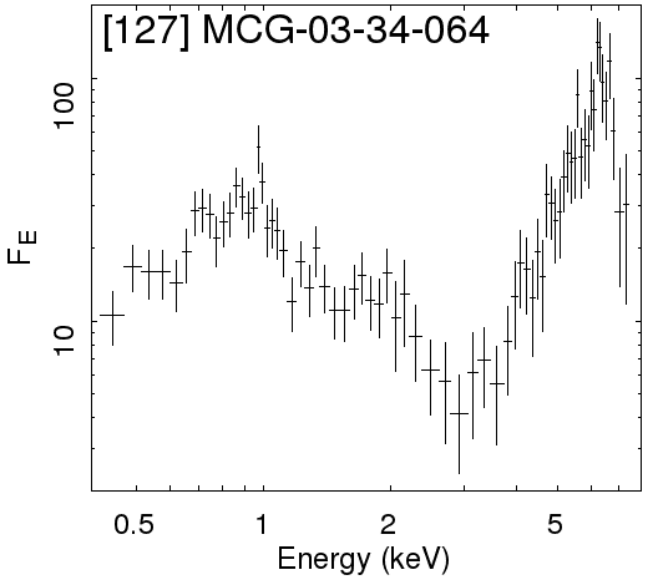

Fig. 3. X-ray flux density spectra for MCG-03-34-064, obtained from the *Chandra* ACIS. Flux density in units of 10^{-14} erg s^{-1} cm^{-2} keV^{-1}.

our selection criteria, described below, was classified as an AGN and is listed in Table 5.

The X-ray selection was performed using two different methods: an X-ray color selection, and detection of AGN spectral features.

The X-ray color, or hardness ratio, gives the relative intensity of emission in hard and soft bands (in counts). A high HR indicates strong emission above 2 keV, which is often associated with the presence of an obscured AGN, that is, column density, $N_{\rm H}$ in the range of 10^{22}−10^{24} cm^{-2}. The threshold for AGN selection was chosen as HR > −0.3, as it was for the CGI sample (see Iwasawa et al. 2011).

Figure 4 shows the hardness ratio of all sources in the sample as a function of their hard X-ray luminosity. AGN selected through all criteria described in this section are plotted with filled squares, while all absorbed AGN are marked with open circles. Most AGN in the sample have an HR below the threshold, as many are absorbed or not selected through X-rays.

Some AGN are missed by this HR selection because absorption in the nucleus is significant and soft X-ray emission coming from external starburst regions is strong. Such galaxies can still show a hard-band excess in their spectra, and if fitting them with an absorbed power-law with a fixed 1.8 photon index yielded a high enough absorbing column density, we classified them as absorbed AGN (see Sect. 4.4.2). Each of these cases is listed in Table 5 and discussed individually in Appendix A.

When absorption is even stronger, only reflected radiation can be observed in the hard band, and therefore sources appear weak, their HR being even smaller. A clear signature of a highly obscured AGN is a the detection of a strong Fe Kα line at 6.4 keV, which is also used as a criterion for AGN selection. We set a threshold of 2σ for the detection of the iron line in order to classify a source as an AGN. Sources selected through this

Table 5. Sources with an AGN signature in IR or X-rays.

No.	Galaxy	AGN_{bol} (1)	[Ne v] (2)	PAH (3)	X (4)
45	UGC 08387	0.03 ± 0.01	Y	N	N
57	IRAS F06076−2139 (S)	–	N	N	C
68	IRAS F16164−0746	0.05 ± 0.01	Y	N	C
71	NGC 2623	0.10 ± 0.03	Y	N	C
72	IC 5298	0.33 ± 0.05	Y	N	A
79	NGC 5256 (NE)	0.23 ± 0.07(u)	Y(u)	N	A
79	NGC 5256 (SW)	0.23 ± 0.07(u)	Y(u)	N	L
82	NGC 0034	0.04 ± 0.02	N	N	A
85	IRAS F17138−1017	0.07 ± 0.04	N	N	C
100	NGC 7130	0.22 ± 0.04	Y	N	LA
105	NGC 7592 (W)	0.20 ± 0.06	Y(u)	N	N
106	NGC 6286	0.11 ± 0.06	N	N	A*
107	NGC 4922 (N)	0.17 ± 0.05	Y	N	A
114	NGC 0232	0.09 ± 0.03	Y	N	N
120	CGCG 049−057	0.04 ± 0.02	N	N	C
121	NGC 1068	1.00 ± 0.01	Y	–	L
127	MCG−03−34−064	0.88 ± 0.04	Y	Y	LA
136	MCG −01−60−022	0.08 ± 0.06	N	–	CA
142	NGC 5135	0.24 ± 0.06	Y	N	L
144	IC 0860	0.06 ± 0.03	N	N	C
163	NGC 4418	0.48 ± 0.22	N	Y	N
169	ESO 343−IG013 (N)	0.09 ± 0.04	N	N	C
191	ESO 420−G013	0.25 ± 0.04	Y	N	N
194	ESO 432−IG006 (NE)	0.12 ± 0.04	N	N	A
194	ESO 432−IG006 (SW)	0.09 ± 0.05	N	N	A
198	NGC 1365	0.38 ± 0.03	N	N	CLA

Notes. Column (1): Contribution of the AGN to the bolometric luminosity of the galaxy (Díaz-Santos et al. 2017). Column (2): Detection of the [Ne v] line (Petric et al. 2011). Column (3): EW of the 6.2 μm PAH feature < 0.1 μm (Stierwalt et al. 2013). Column (4): X-ray AGN selection criteria. C: X-ray color (HR > −0.3); L: Detection of 6.4 KeV line. A: Absorbed AGN feature. Y: Source meets the criterion. N: Source does not meet the criterion. (u) Unresolved detection in a multiple system. (*)Only in the *NuSTAR* data (Ricci et al. 2016). See Appendix A for details on particular sources.

criterion are listed in Table 5, and details on the iron line fits can be found in Sect. 4.4, Table 6.

The IR selection was performed by means of the detection of the [Ne v] 14.32 μm line over kpc scales, which traces high-ionization gas. The ionization potential of [Ne v] is 96 eV, which is too high to be produced by OB stars. Therefore, detection of this line in the integrated spectra of galaxies is a good AGN indicator (see Petric et al. 2011, and references therein).

Another possible indicator is when the equivalent width of the 6.2 μm PAH feature is lower than 0.1 μm. Polycyclic aromatic hydro-carbons (PAHs) are either destroyed by the radiation originating from the AGN, or their features are diluted in the spectra by the strong MIR continuum it creates; this results in a low value of the EW (see Stierwalt et al. 2013, and references therein).

With the X-ray criteria alone, we found that 21 galaxies host an AGN. This represents (25 ± 5)% of our sample. With the addition of IR criteria, 5 other galaxies are classified as AGN, resulting in a total AGN fraction of (31 ± 5)% for the 84 individually analyzed galaxies in CGII. Galaxies selected as AGN are presented in Table 5, along with optical classifications and whether or not they meet our X-ray and IR selection criteria.

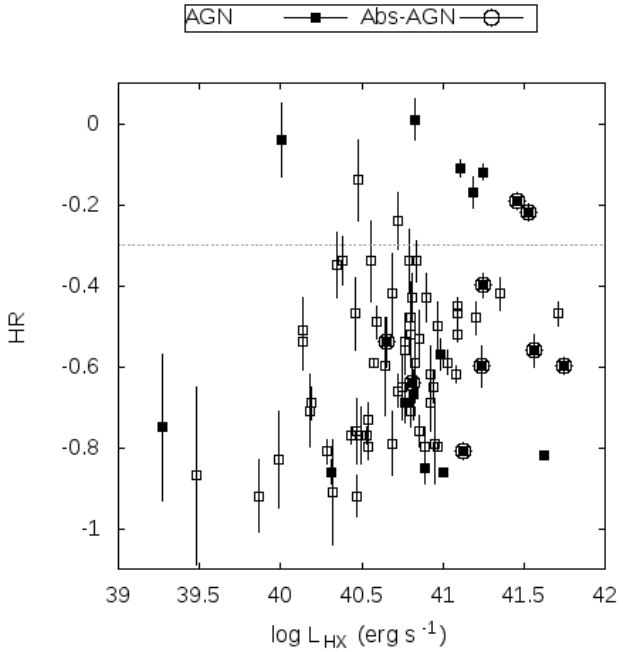

Fig. 4. Hardness ratio as a function of the 2−7 keV luminosity for all sources in the CGII sample. All AGN from Table 5 are plotted as filled squares, and those in which absorption features are fit (labeled A in the table) are marked with an open circle. The dashed line shows the −0.3 boundary, above which sources are selected as AGN (unless evidence points toward a lack of AGN presence, see Appendix A).

Two sources in the sample met the selection criteria, but we opted to not classify them as AGN, for reasons explained in Appendix A: IRAS F17138−1017 and IRAS F16399−0937 (S), which meet the HR criterion.

Table 5 also lists the contribution of the AGN to the bolometric luminosity for all sources classified as AGN. The contribution of the AGN to the MIR luminosity was derived by Díaz-Santos et al. (2017) for all GOALS galaxies, employing up to five *Spitzer*/IRS diagnostics. Applying corrections based on spectral energy distribution (SED) templates of pure starbursts and AGN sources, they derived the fractional contribution of the AGN to the overall bolometric luminosity (as in Veilleux et al. 2009).

Figure 5 shows the HR of all sources in the sample as a function of the fractional contribution of the AGN to the bolometric luminosity, AGN_{bol}. Sources with a fraction larger than 0.2 can be considered to have an energetically significant AGN. X-ray selected AGN, through any of the three criteria mentioned above, are highlighted as filled symbols. All marked AGN below the HR = −0.3 threshold show signs of obscuration, as they have been selected through any of the other two X-ray criteria. In the full C-GOALS sample, 19 of 32 X-ray selected AGN lay below AGN_{bol} < 0.2. Therefore, more than half of the AGN detected through X-rays are not easily selected through the described combination of MIR diagnostics.

4.4. X-ray spectral fitting

The 0.4−7 keV *Chandra* spectra of the CGII galaxies present similar properties to those of the CGI sample, that was analyzed by Iwasawa et al. (2011): a mostly emission-line dominated soft X-ray band, and a hard X-ray power-law. As has been discussed by these authors, both the spectral shape and the morphology of the emission (see images in Appendix B) suggest a different

Table 6. Fe Kα line fits.

No.	Galaxy	E (keV)	I (10^{-6} s^{-1} cm^{-2})	EW (keV)
79	NGC 5256 (SW)	$6.44^{+0.04}_{-0.05}$	$1.4^{+0.9}_{-0.6}$	$4.0^{+2.6}_{-1.8}$
100	NGC 7130	$6.42^{+0.03}_{-0.04}$	$3.3^{+1.6}_{-1.3}$	$0.8^{+0.4}_{-0.3}$
121	NGC 1068	$6.43^{+0.07}_{-0.04}$	$32.2^{+12.6}_{-9.0}$	$0.9^{+0.3}_{-0.3}$
127	MCG−03−34−064	$6.43^{+0.10}_{-0.08}$	$77.1^{+32.8}_{-25.4}$	$0.7^{+0.3}_{-0.2}$
142	NGC 5135	$6.41^{+0.03}_{-0.03}$	$7.2^{+2.9}_{-2.5}$	$1.1^{+0.4}_{-0.4}$
198	NGC 1365	$6.35^{+0.03}_{-0.04}$	$40.3^{+15.0}_{-14.0}$	$0.14^{+0.07}_{-0.04}$

Notes. Iron Kα Line detections with a significance of 2σ or higher. The line centroid energy is measured in the rest frame. Errors reported correspond to 1σ for one parameter of interest, leaving five parameters free.

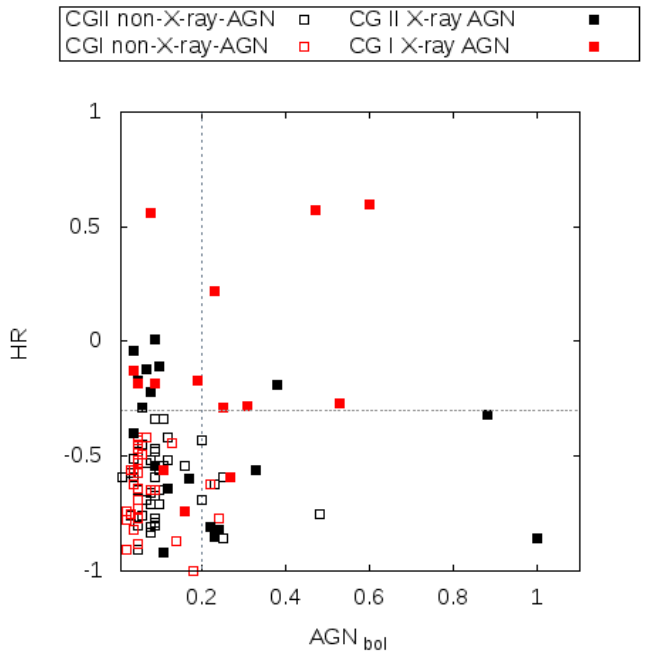

Fig. 5. Hardness ratio as a function of the fractional contribution of the AGN to the bolometric luminosity (as derived from MIR data, Díaz-Santos et al. 2017) of the source, in red for CGI sources and black for CGII. X-ray selected AGN from Table 5 are plotted as filled squares.The horizontal dashed line shows the HR = −0.3 threshold. The vertical dashed line shows the value above which the AGN is energetically significant.

origin for the soft and hard X-rays, and therefore the two were analyzed separately.

A few objects in the sample (IRAS 18090+0130 (W), IRAS F06076−2139 (S), IC 0860, and NGC 7591) were not fit because they have an excessively low count number, of the order of $\lesssim$25 cts, in the full 0.4−7 keV band. For these sources, only the count rates and HR were computed, and results on fluxes and luminosities are not presented in Table A.1.

For the majority of our sources, which have few counts, we made the fit through C statistic minimization instead of χ^2 minimization.

4.4.1. Soft band (0.4–2 keV) fitting

Starburst galaxies, when not dominated by a luminous AGN, have soft X-ray emission originating in hot interstellar gas (~0.2−1 keV), which is shock-heated by supernovae explosions and stellar winds from massive stars. Emission from hot gas can generally be fit with a standard thermal emission model, with a solar abundance pattern, for instance, *mekal* (Mewe et al. 1985; Kaastra 1992; Liedahl et al. 1995). However, in our data, such a simple model does not agree with many of the observed emission line strengths and provides an unsatisfactory fit in most cases. A better fit can be obtained either with a modified abundance pattern that is richer in α elements, or through the overlap of more than one *mekal* at different temperatures.

The hot gas within a starburst region is expected to be enriched by α elements, which are produced in core-collapse supernovae. Metal abundances should deviate from a solar pattern, as has been found for star-forming knots in nearby galaxies, such as the Antennae (Fabbiano et al. 2004). At the same time, the extended soft X-ray emitting gas is expected to be multiphase: the shocked gas swept away by a starburst wind seen at outer radii is free from absorption, while the hotter gas at inner radii may have some absorption of the interstellar medium (e.g., Strickland & Stevens 2000). A temperature gradient can be approximated at first order as two *mekal* models with different temperatures. One model would fit the most external, colder gas component (at $T = T_1$), which is located far away from the nucleus, and therefore is less strongly absorbed by the interstellar material. The other model would fit the inner, hotter gas (at $T = T_2$), which is obscured by the denser material in the central region of the galaxy.

Ideally, the data should be modeled using more than one *mekal* component, with different temperatures and absorbing column densities, and with non-solar metal abundances. However, given the quality of the data, this would imply severe overfitting. As we are interested in probing the level of obscuration in the C-GOALS sources, we opted to model the data using two *mekal* models as defined above, which both have solar abundance patterns.

The results obtained through this fitting, the parameters of which are listed in Table A.2, show that it is possible to satisfactorily fit the sources with high enough number counts using this model, which is to be expected if part of the emission truly originates in a denser, inner region. However, we note that this model is not clearly superior to a single *mekal* component with non-solar abundances, as was used by Iwasawa et al. (2011) on the CGI sample; and that most of the analyzed sources do not have good enough data quality to determine a clear best fit between the two models.

The distributions of the obtained parameters for the full CGII sample are shown in the histograms presented in Fig. 6. The temperature associated with the colder *mekal* component (T_1) used to model the 0.5−2 keV emission of each source presents a narrower distribution than that associated with the hotter component (T_2). The distribution of T_1 has a median value of 0.38±0.03 keV and an interquartile range of 0.32−0.63 keV. The distribution of T_2 has, as expected, a higher median value of 0.97 ± 0.18. The interquartile range is 0.77−1.2 keV range, with a long tail extending up to $T_2 \sim 4.5$ keV. We note that even though the two distributions overlap (i.e., some T_1 values are higher than some T_2 values), for each single source $T_2 > T_1$.

Figure 6 also shows the distribution of column densities, N_H, absorbing the hottest *mekal* component. The median of the distribution is $(1.1 \pm 0.2) \times 10^{22}$ cm^{-2}, with an interquartile range of $(0.8-1.4) \times 10^{22}$ cm^{-2}.

A few sources, named in Sect. 4.4.2, were modeled in the full 0.4−7 keV band with a single power-law; and therefore no values for T_1, T_2, and N_H were derived for them. In addition, NGC 6285

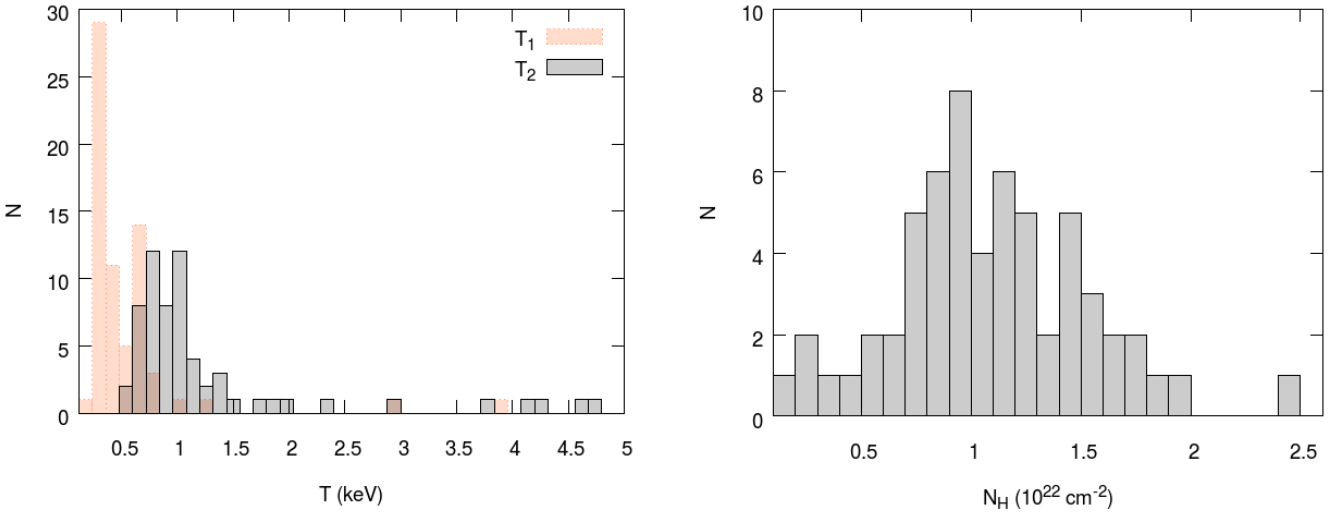

Fig. 6. *Left panel*: distribution of *mekal* model temperatures, where T_1 is the temperature of the external, colder gas component and T_2 is the temperature of the internal, hotter gas component, for the CGII sample. *Right panel*: distribution of absorbing column densities associated with the inner, hotter gas component, for the CGII sample.

and IC 2810 (SE) were fit with a single *mekal* component in the 0.4−2 keV range, and NGC 7752/3 (NE) and ESO 440-IG058 (N) were fit with a single *mekal* component in the full 2−7 keV range. These sources are not included in the histograms shown in Fig. 6, or in the averages described previously.

4.4.2. Hard band (2–7 keV) fitting

In the hard X-ray band, where the emission from hot interstellar gas and young stars significantly decreases, X-ray binaries dominate the emission in the absence of an AGN. Their emission can be fit by a simple power-law. The photon index, Γ, is the slope of a power-law model that describes a photon spectrum, defined as $dN/dE \propto E^{-\Gamma}$ photons cm^{-2} s^{-1} keV^{-1}. Derived values for Γ for all sources in the CGII sample are listed in Table A.2.

This fit was only performed for galaxies that had at least 20 cts in the 2−7 keV range. Galaxies with a lower count number were fit while imposing a fixed power-law photon index of 2 (average spectral slope found for a sample of local starburst galaxies, Ranalli et al. 2003), leaving only the model normalization as a free parameter. This limit was set in order to obtain meaningful constraints for the spectral slope. It is lower than the one fixed for the CGI sample (50 cts) since many of the sources in the current sample are much fainter, as expected given their lower IR luminosities.

A few objects within the sample show a clear, steep flux increase at energies ≥3−4 keV (see, e.g., MCG−03−34−064 in Fig. C.1), which is a sign of the presence of an absorbed AGN (see, e.g., Turner & Miller 2009). In such cases, which all have a count number higher than 20 cts, we fit an absorbed power-law imposing a fixed photon index of 1.8 (a typically expected value for the photon index of an AGN, see, e.g., Nandra & Pounds 1994). This left the absorbing column density, N_H, as a free parameter. This model was preferred when the fit yielded values $N_H \gtrsim 10^{23}$ cm^{-2}, and it was statistically better than a simple power-law fit. In such cases, we classified the source as an absorbed AGN.

A few sources in the sample (NGC 5331 (N), IRAS F16399−0937 (S), ESO 550−IG025 (S), MCG+12−02−001 (W), CGCG 049−057, UGC 02238, NGC 4418, and ESO 343−IG013 (N) and (S)) are clearly best-fit with a single power-law in the full 0.4−7 keV band, and the Γ parameter shown in Table A.2 corresponds to that fit.

4.4.3. Iron Kα lines

The Fe Kα line is a frequently used reliable diagnostic of heavily obscured AGN. As we described in Sect. 4.3, we used it as one of our X-ray AGN selection criteria. The cold iron line seen in some of the CGII sources was fit with a Gaussian model centered at 6.4 keV. Six sources in the CGII sample have such a line fit with a significance above 2σ, which is the threshold we set to consider a detection.

A more conservative and frequently used threshold to consider a line as detected in the data is a 3σ significance. If we had imposed this more restrictive criterion, only NGC 1068 and MCG−01−34−064 would have detected Fe Kα lines in the sample. The threshold was lowered because of the low signal-to-noise ratio for all sources in the CGII sample. However, we note that lowering it to 2σ does not change the fraction of selected AGN within the sample, as all sources with a line detection also meet other selection criteria. We still consider the presence of this line at 2σ to be relevant information, which can give support to other AGN determinations, and therefore included it in the analysis.

Parameters of the fit for these six sources are shown in Table 6, including the line energy, intensity, and equivalent width with respect to the continuum. The detection of these lines has been previously reported based on other X-ray observations (Koyama et al. 1989; Band et al. 1990; Mazzarella et al. 2012; Gilli et al. 1999; Levenson et al. 2002; Ricci et al. 2014; Risaliti et al. 2009).

4.5. X-ray luminosities and correlation with L_{IR}

Figure 7 shows the distribution of derived luminosities in the soft and hard band, presented in Table A.1, compared with that of those obtained for the CGI sample of Iwasawa et al. (2011). For CGII, the distributions peak at $\log(L_{SX}) \sim 40.6$ erg s^{-1} and $\log(L_{HX}) \sim 40.9$ erg s^{-1}, which is slightly lower than the peak of both bands for CGI sample, at $\log(L_X) \sim 41.1$ erg s^{-1}. The median logarithmic values for the soft- and hard-band luminosities are listed in Table 7. CGII has lower X-ray luminosity values than CGI, as expected, reflecting a correlation between IR and X-ray luminosity that is seen in both the CGI and CGII samples (see Figs. 8 and 9).

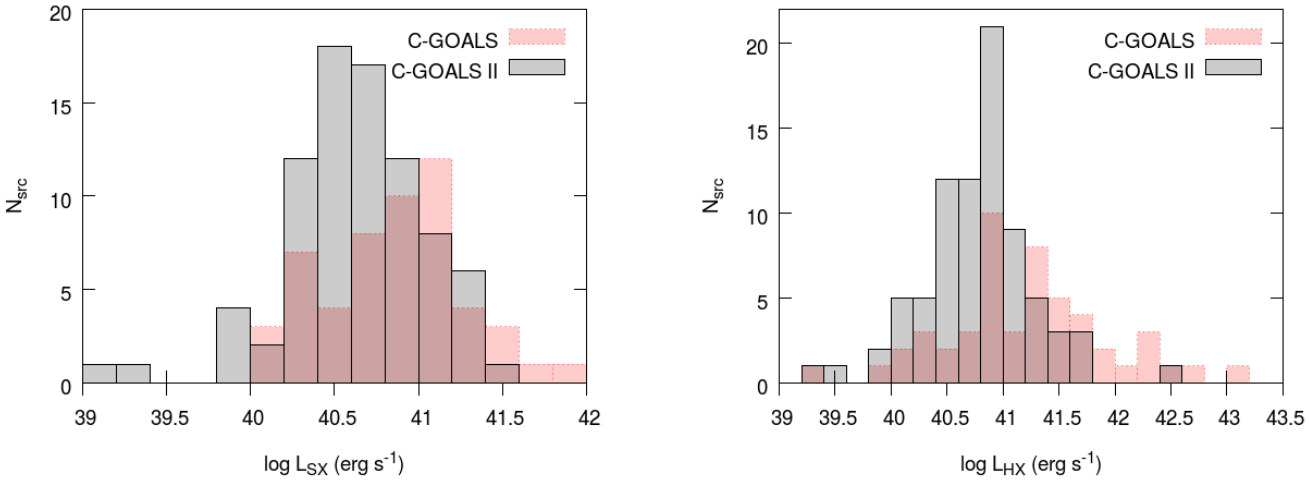

Fig. 7. Distributions of soft-band X-ray luminosity, 0.5−2 keV (*left panel*), and hard-band X-ray luminosity, 2−10 keV (*right panel*), for the individual galaxies of CGI and CGII.

Table 7. Statistical X-ray properties of the sample.

	CGI	CGII	C-GOALS
$\log(L_{SX})$	40.9 ± 0.3	40.6 ± 0.2	40.8 ± 0.4
$\log(L_{HX})$	41.2 ± 1.7	40.8 ± 0.8	40.9 ± 0.6
$\log(L_{SX}/L_{IR})$	−4.53 ± 0.34	−4.16 ± 0.42	−4.26 ± 0.48
$\log(L_{HX}/L_{IR})$	−4.40 ± 0.63	−4.04 ± 0.48	−4.17 ± 0.59
$\log(L_{SX}/L_{IR})^*$	−4.6 ± 0.1	−4.18 ± 0.35	−4.26 ± 0.45
$\log(L_{HX}/L_{IR})^*$	−4.5 ± 0.1	−4.18 ± 0.37	−4.23 ± 0.54
$\log(L_{SX}/L_{FIR})^*$	−4.44 ± 0.45	−3.82 ± 0.32	−3.96 ± 0.47
$\log(L_{HX}/L_{FIR})^*$	−4.22 ± 0.52	−3.81 ± 0.45	−3.96 ± 0.52

Notes. Median values of the distribution of soft-band and hard X-ray luminosities; and the distributions of the ratios of X-ray to IR luminosities for the C-GOALS I, C-GOALS II and full C-GOALS sample. $^{(*)}$AGN removed from the sample.

The origin of this correlation is in the presence of star formation in the galaxies. FIR luminosity measurements detect the energy absorbed by the dust of the interstellar medium from young, bright stars; and thus are a good estimator of the total star formation rate (SFR; e.g., Kennicutt 1998). In galaxies with a considerable amount of star formation, such as starburst galaxies, emission in other wavelengths can also be related to young and massive stars, such as X-ray luminosity (e.g., X-ray binaries emission and supernova remnants, SNRs). Therefore, it has been suggested that if a good correlation between X-ray luminosity and IR luminosity exists in galaxies, the SFR can be directly inferred from the X-ray luminosity. Compatible correlations have been found in previous works for local star-forming galaxies with IR luminosities lower than those of LIRGS (e.g., Ranalli et al. 2003; Grimm et al. 2003; Mineo et al. 2014).

Figure 8 shows the X-ray luminosity as a function of the IRAS IR luminosity. The data show a moderate correlation, with a typical spread of more than one order of magnitude when only sources without detected X-ray AGN presence (open squares) are considered. Sources that contain X-ray AGN typically lie above the trend, adding scatter to the correlation. Sources with multiple components are separated into their respective contributions, and plotted separately, as it has been shown that when they are plotted summed into one single source, the correlation becomes less clear (Iwasawa et al. 2009). Their total (8−1000) μm IRAS luminosity, as in Table 1, is separated into the different contributions using the percentages indicated in Table 3.

As we found in the CGI galaxies, X-ray selected AGN tend to be more luminous in X-rays than the rest of the sample, especially in the hard band. However, the values for $\log(L_X/L_{IR})$ are higher for the CGII sample than for CGI, as listed in Table 7. This result means that while our sample is less bright both in X-ray and in IR than the CGI sample, we find a higher relative X-ray to IR luminosity. Removing X-ray selected AGN from both samples gives lower ratios, which we also list.

Comparing these average values to the $\log(L_X/L_{IR}) \sim -3.7$ found by Ranalli et al. (2003) for local star-forming galaxies with lower SFR, we find a large discrepancy. However, their IR luminosity does not include the 1−40 μm range, which may contribute a non-negligible amount of power, in particular for IR-warm AGN-dominated systems. Therefore a direct comparison needs to introduce a correction. Furthermore, only at radio and FIR wavelengths are the most intense starbursts transparent (e.g., Condon 1992), so that from their detected flux the SFR can be accurately estimated.

IR luminosities derived by Ranalli et al. (2003), hereafter L_{FIR}, follow the expression

$$L_{FIR} = 1.26 \times 10^{-11}(2.58\, S_{60\mu} + S_{100\mu})\ \mathrm{erg\ s^{-1}\ cm^{-2}}, \quad (1)$$

from Helou et al. (1985).

We used this expression to derive L_{FIR} for all non-AGN objects in the CGI and CGII samples, again accounting for the contribution of multiple components following Table 3. As listed in Table 7, $\log(L_X/L_{FIR})$ is similar to −3.7 for the CGII objects, but not for the galaxies in CGI. A direct comparison between the distribution followed by objects analyzed by Ranalli et al. (2003), as well as their derived correlation, and GOALS objects is shown in Fig. 9.

The best-fit correlations derived by Ranalli et al. (2003) are

$$\log(L_{SX}) = (0.87 \pm 0.08)\log(F_{FIR}) + 2.0 \pm 3.7 \quad (2)$$

$$\log(L_{HX}) = (1.08 \pm 0.09)\log(F_{FIR}) - 7.1 \pm 4.2 \quad (3)$$

which correspond to the blue dotted lines plotted in Fig. 9.

Galaxies in the GOALS sample with $L_{FIR} \lesssim 8 \times 10^{10}\ L_\odot$ follow Eqs. (2) and (3), but those with higher L_{IR} have a systematically lower X-ray luminosity than predicted.

This behavior suggests that a better fit would be obtained with a quadratic relation in log scale. Using the least-squares

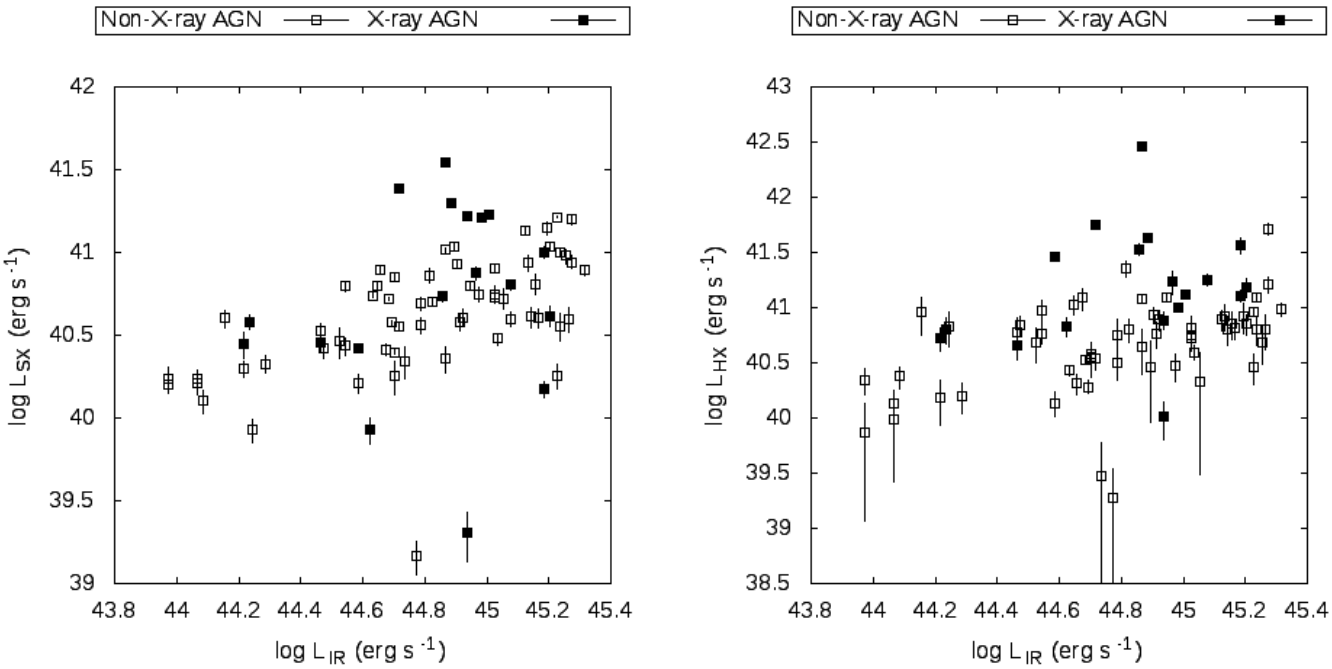

Fig. 8. Plots of soft (*left panel*, 0.5−2 keV) and hard (*right panel*, 2−10 keV) X-ray luminosity vs. IR luminosity, where the X-ray luminosity is corrected only for Galactic absorption. X-ray selected AGN, shown in Table 5, are shown in black. When multiple objects are present in a source, their IR luminosity is divided, as shown in Table 3.

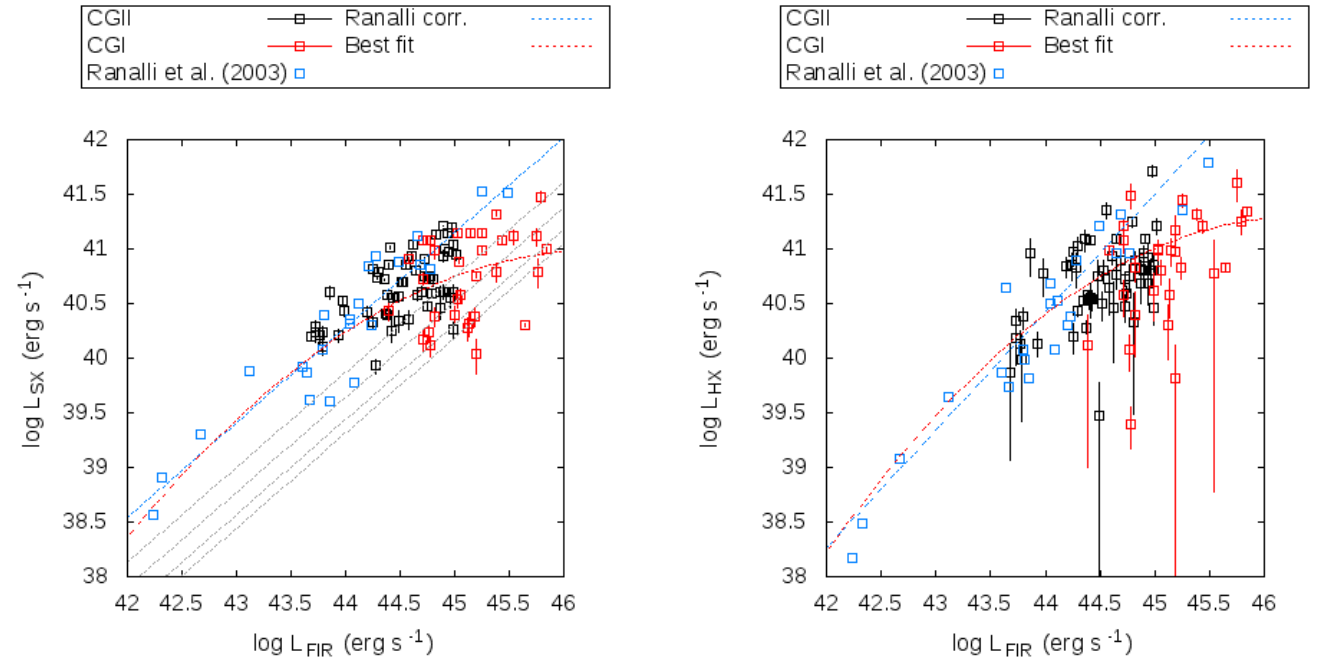

Fig. 9. Plots of soft (*left panel*, 0.5−2 keV) and hard (*right panel*, 2−10 keV) X-ray luminosity versus FIR luminosity derived as in Eq. (1), where the X-ray luminosity is corrected only for Galactic absorption. Data used by Ranalli et al. (2003), along with their derived correlation, are shown in blue. CGI and CGII data (for galaxies without an AGN) are plotted in red and black squares respectively. When multiple objects are present in a source, their IR luminosity is divided as shown in Table 3. All sources containing AGN, as listed in Table 5 or classified as AGN by Iwasawa et al. (2011) have been removed both from the plot and from the fits. The red, dashed line shows our best quadratic fit for the C-GOALS + Ranalli et al. (2003) data. Grey, dashed lines (*left panel*) show theoretical lines of obscuration for $N_{\rm H} = 0.5, 1.0, 2.0, 5.0 \times 10^{22}$ cm^{22}, as described in Sect. 4.5.

method, we obtain a best fit for the C-GOALS + Ranalli et al. (2003) data:

$$\log(L_{\rm SX}) = (-0.17 \pm 0.04)x^2 + (15 \pm 2)x + (-263 \pm 8) \quad (4)$$

$$\log(L_{\rm HX}) = (-0.17 \pm 0.06)x^2 + (15.2 \pm 2)x + (-169 \pm 10) \quad (5)$$

where $x = \log(L_{\rm FIR})$. This fit is plotted as a red dashed line in Fig. 9. Below FIR luminosities of $\sim 3 \times 10^{44}$ erg s^{-1} (i.e., $\sim 8 \times 10^{10}\, L_\odot$), the quadratic fit overlaps the linear correlation. Above this value, the X-ray luminosity increases far more slowly with FIR luminosity. This effect is stronger in soft X-rays. We note that when we fit a single power-law to

Table 8. Half-light radius

No.	Galaxy	R_H^{SX}(″)	R_H^{SX} (kpc)	No.	Galaxy	R_H^{SX}(″)	R_H^{SX} (kpc)
45	UGC 08387	2.4	1.3	104	NGC 7771	3.0	0.9
47	CGCG 436−030	2.6	1.7	104	NGC 7770	3.7	1.1
49	NGC 0695	3.7	2.5	105	NGC 7592 (E)	3.1	1.6
50	CGCG 043−099	1.2	1.0	105	NGC 7592 (W)	0.9	0.5
51	MCG+07−23−019	4.3	3.3	106	NGC 6286	7.2	3.0
52	NGC 6670 (E)	3.0	1.9	106	NGC 6285	1.7	0.7
52	NGC 6670 (W)	4.0	2.5	107	NGC 4922 (N)	<0.5	<0.3
53	UGC 02369 (S)	1.5	1.0	110	NGC 3110	9.0	3.5
54	NGC 1614	1.4	0.5	114	NGC 0232	1.5	0.7
56	NGC 5331 (N)	2.1	1.6	117	MCG+08−18−013(E)	2.3	1.3
56	NGC 5331 (S)	3.0	2.3	120	CGCG 049−057	1.1	0.3
57	IRAS F06076−2139(N)	0.7	0.6	121	NGC 1068	7.8	0.6
57	IRAS F06076−2139(S)	–	–	123	UGC 02238	4.0	1.8
60	IC 2810(NW)	1.2	0.9	127	MCG−03−34−064	<0.5	<0.2
60	IC 2810 (SE)	0.7	0.5	134	ESO 350−IG038	2.4	1.0
63	IRAS 18090+0130 (E)	2.4	1.6	136	MCG −01−60−022	4.6	2.2
63	IRAS 18090+0130(W)	<0.5	<0.3	141	IC 0564	8.0	3.6
64	III Zw 035 (S)	1.2	0.7	141	IC 0563	8.1	3.6
65	NGC 3256	7.7	1.5	142	NGC 5135	2.1	0.6
67	IRAS F16399−0937(N)	3.5	2.2	144	IC 0860	6.0	1.7
67	IRAS F16399−0937(S)	5.3	3.3	147	IC 5179	14.6	3.6
68	IRAS F16164−0746	1.5	0.9	148	CGCG 465−012	4.6	2.1
69	IC 4687	3.5	1.4	157	MCG−02−33−099	1.3	0.5
69	IC 4686	<0.5	<0.2	157	MCG−02−33−098	1.2	0.5
69	IC 4689	3.5	1.4	163	NGC 4418	2.7	0.5
71	NGC 2623	1.0	0.4	169	ESO 343−IG013 (N)	1.2	0.5
72	IC 5298	<0.5	<0.3	169	ESO 343−IG013 (S)	5.7	2.4
73	IRAS 20351+2521	4.0	2.9	170	NGC 2146	15.5	1.3
75	NGC 6090 (NE)	1.6	1.1	174	NGC 5653	9.0	2.6
75	NGC6090 (SW)	1.4	0.9	178	NGC 4194	4.2	0.9
79	NGC 5256 (NE)	0.8	0.5	179	NGC 7591	0.8	0.3
79	NGC 5256 (SW)	2.2	1.4	182	NGC 0023	3.2	1.0
80	IRAS F03359+1523(E)	1.9	1.4	188	NGC 7552	3.2	0.4
81	ESO 550−IG025 (N)	2.2	1.4	191	ESO 420−G013	1.0	0.2
81	ESO 550−IG025 (S)	1.0	0.7	194	ESO 432−IG006 (NE)	2.3	0.8
82	NGC 0034	1.3	0.5	194	ESO 432−IG006 (SW)	2.5	0.9
83	MCG+12−02−001 (E)	2.1	0.7	195	NGC 1961	8.4	2.4
83	MCG+12−02−001 (W)	2.3	0.8	196	NGC 7752/3 (NE)	0.8	0.3
85	IRAS F17138−1017	2.8	1.1	196	NGC 7752/3 (SW)	5.6	2.0
95	ESO 440−IG058 (N)	0.6	0.3	198	NGC 1365	7.0	0.6
95	ESO 440−IG058 (S)	3.8	2.1	199	NGC 3221	13.2	4.2
100	NGC 7130	<0.5	<0.2	201	NGC 0838	5.1	1.3

Notes. Radius up to which half of the source counts in the 0.5−2 keV band are emitted, for the 84 galaxies analyzed within the CGII sample.

the full data sample, we did not recover a relation that was compatible, within the errors, with Eq. (2). A power-law fit also yielded a larger χ^2 value than the fits given by Eqs. (4) and (5).

As soft X-rays are easily absorbed by moderate column densities, we show the effect that obscuration could have on the Ranalli et al. (2003) correlation. In order to do so, we took an average spectrum that is characteristic of the galaxies within our sample: a double-component *mekal* model with temperatures $T_1 = 0.38$ and $T_2 = 0.97$, the median values derived from our soft X-ray analysis. According to our model, the inner component of $T = T_2$ can have considerable absorption, and fitting yields values in the range $N_H = 0.1{-}2.5 \times 10^{22}$ cm^{-2}. We assumed different column densities, $N_H = 0.5, 1.0, 2.0, 5.0 \times 10^{22}$ cm^{22}, and absorbed the hotter component. We used the model to calculate the decrease in flux caused by the different column densities, and considering that the linear correlation derived by Ranalli et al. (2003) has no intrinsic absorption, we plot the "absorbed" equivalent correlations in Fig. 9. $N_H = 5.0 \times 10^{22}$ cm^{-2} absorbs more than 99% of the emission of the inner component in the 0.5−2 keV range, meaning that higher column densities would result in no change in the emission, that is, only the emission of the outer, unabsorbed component remains.

4.6. Radial profiles

Radial profiles for all sources (except for IRAS F06076−2139 (S), for which not enough counts are detected in the *Chandra* data) were characterized in two different ways. In the first

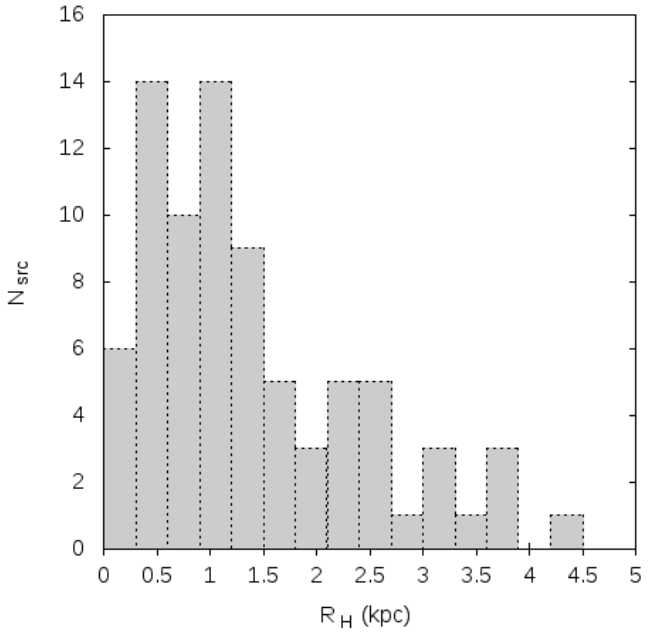

Fig. 10. Histogram of half-light radii for the sources in the CGII sample.

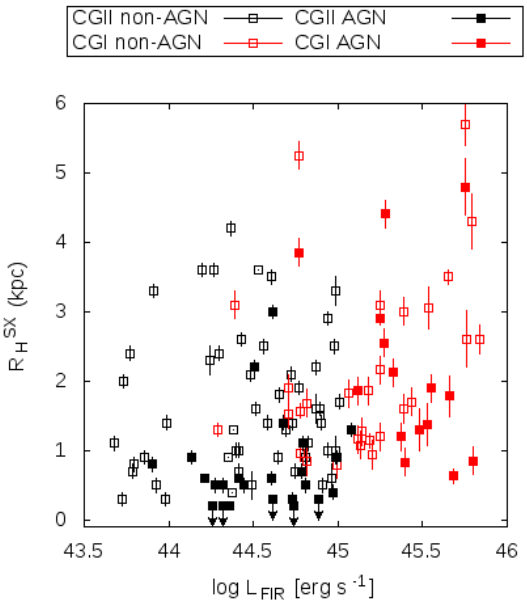

Fig. 11. Half-light radius as a function of FIR luminosity (as in Eq. (1)) for galaxies within the CGII (black) and CGI (red) sample. Sources without an AGN are plotted as open squares, while sources with an AGN are plotted as filled squares.

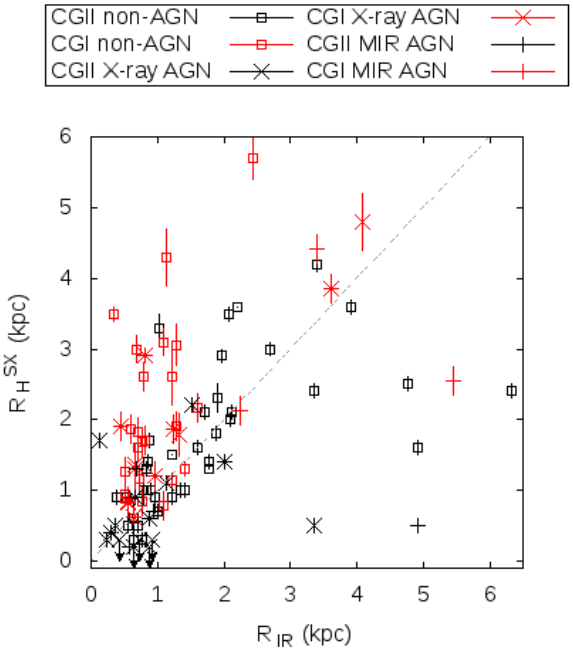

Fig. 12. Soft X-ray half-light radius as a function of 70 μm FIR radius, taken from Díaz-Santos et al. (2017). CGI data are shown in red, and CGII data in black. X-ray selected AGN and MIR selected AGN (as specified in Table 5) are plotted separately. The dashed line shows $R_{\rm IR} = R_{\rm H}^{\rm SX}$, and is not a fit to the data. Eleven systems within the whole C-GOALS sample are resolved into individual galaxies in X-rays but not at 70 μm, and are thus not plotted.

method, we computed the soft X-ray half-light radius ($R_{\rm H}^{\rm SX}$) for the 0.5−2 keV band as the radius within which half of the total number of counts is emitted. In the second method, surface brightness profiles were computed and provided in Appendix B, also shown in Fig. 2 for NGC 2146. These profiles were computed in the soft 0.5−2 keV band, shown as open squares, and the hard 2−7 keV band, shown as filled squares.

Profiles were centered using the hard X-ray peak that corresponds to the nucleus of the galaxy, which typically corresponds to the near-infrared nucleus. When no clear central emission in the (2−7) keV band was detected, the profiles were centered using IR images. For all galaxies whose radial profiles were centered using IR images, a comment has been added in Appendix A.

The values for $R_{\rm H}^{\rm SX}$, both in arcsec and in kpc, are provided in Table 8. While this value can give an idea of the size of the central more intensely emitting region of a galaxy, we note that for sources without an extensive diffuse emission (e.g., NGC 3221, which is mostly composed of point-sources), it might not have a physical meaning. Other sources show non-axisymmetric morphology, most likely associated with extended starburst winds (e.g., UGC 08387, NGC 6286 (SE), NGC 2146, NGC 4194, NGC 1365, and NGC 0838). See Appendix B for detailed images of the morphology of the X-ray emission in all sources

Because of the pixel size of the *Chandra* CCD, the smallest radius within which counts can be computed is limited to 0.5″. Very compact sources can have more than half of their detected counts within this region, making the estimation of $R_{\rm H}^{\rm SX}$ impossible. This is the case for six of our sources, for which an upper limit is provided. It would also be the case for the vast majority of sources when the hard band emission were considered, which is the reason we do not provide values of $R_{\rm H}^{\rm HX}$.

Figure 10 shows a histogram of all half-light radii presented in Table 8. Sources with only upper limits derived are included, as they all fall below $R_{\rm H}^{\rm SX} = 0.3$ kpc, which is the bin size. The distribution of $R_{\rm H}^{\rm SX}$ has a median of 1.0 ± 0.1 kpc, with an interquartile range of 0.5−1.9 kpc. This shows that most sources within CGII have a compact X-ray distribution, with half of the emission being generated within the inner ∼1 kpc. VLA 33 GHz studies of the 22 brightest LIRGs and ULIRGs in the C-GOALS sample find half-light radii below 1.7 kpc for all sources, meaning that the emission is also compact in other wavelengths (Barcos-Muñoz et al. 2017).

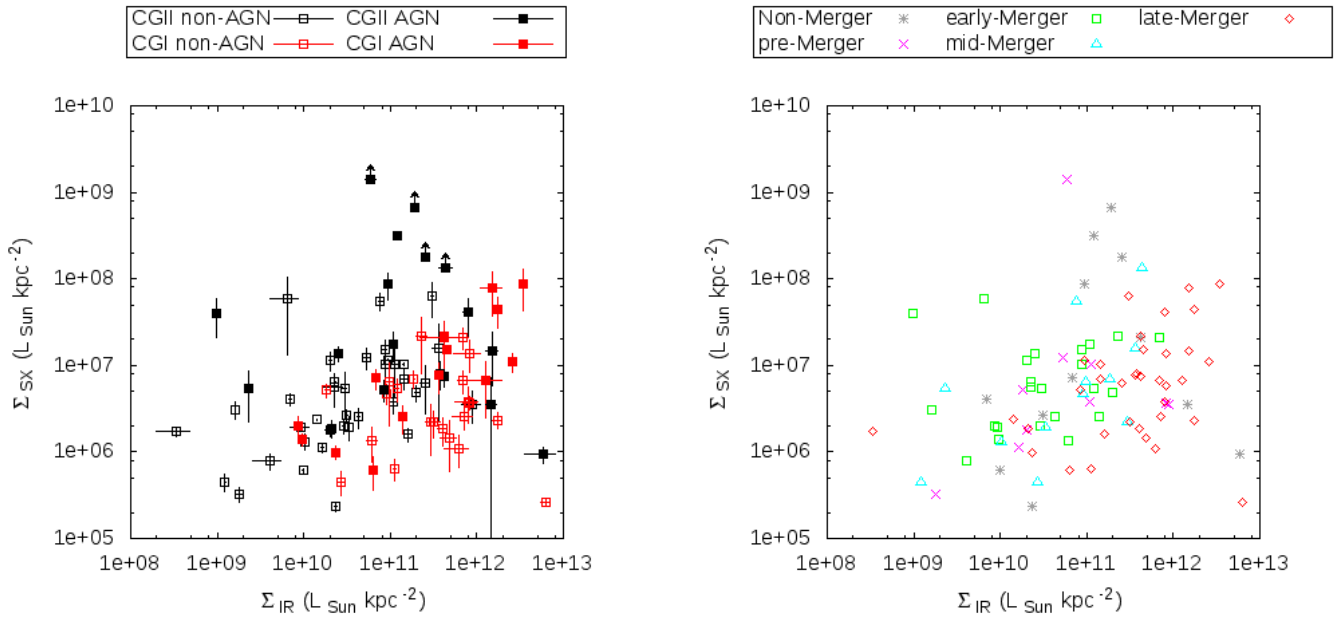

Fig. 13. Plots of X-ray luminosity surface density vs. IR luminosity surface density. *Left panel*: red data correspond to CGI sources, and black data corresponds to CGII sources. AGN are highlighted as filled symbols. *Right panel*: sources in the full C-GOALS sample are plotted as different symbols according to merger stage, as derived by Stierwalt et al. (2013). 11 systems within the whole C-GOALS sample are resolved into individual galaxies in X-rays but not at 70 μm, and are thus not plotted.

All values of $R_{\rm H}^{\rm SX}$ are upper limits, as any amount of obscuration in the sources (likely important in most, as seen in Fig. 9), which is concentrated in the inner regions, will result in an apparent decrease of compactness.

Figure 11 shows the distribution of half-light radii as a function of the FIR luminosity. The size of the most intensely X-ray emitting region shows no clear correlation with the overall IR luminosity, although CGI sources tend to have higher X-ray radii. Within the CGII sample, sources that contain an AGN, as listed in Table 5, plotted as filled squares, tend to be compact. (83 ± 7)% of them have $R_{\rm H}^{\rm SX} \leq 1$ kpc. This is in agreement with previous results from a study of the extended MIR emission in GOALS using *Spitzer*/IRS spectroscopy, where it was found that progressively more AGN-dominated galaxies tend to show more compact MIR emission (Díaz-Santos et al. 2010).

Figure 12 shows a comparison between $R_{\rm H}^{\rm SX}$ and the IR radius at 70 μm taken from Díaz-Santos et al. (2017) for all C-GOALS sources. Most sources in the sample are placed close to the $R_{\rm IR} = R_{\rm H}^{\rm SX}$ line. CGI sources tend to have a larger X-ray half-light radius for a given characteristic IR radius than CGII sources.

Outliers with very compact soft X-ray emission but a large IR radius are X-ray selected AGN ESO 343−IG013 (N) and IR selected AGN NGC 7592 (W). Both sources show clear strong hard X-ray peaks in the nucleus (see images in Appendix B). Another extreme outlier is IRAS F12112+0305, with $R_{\rm H}^{\rm SX} = 5.7 \pm 0.3$ kpc but much more compact IR emission.

4.7. Luminosity surface density

Using the luminosities listed in Table A.1 and the $R_{\rm H}^{\rm SX}$ in Table 8, we derived luminosity surface densities for all sources in the C-GOALS sample, as $\Sigma_{\rm SX} = L_{\rm SX}/\pi(R_{\rm H}^{\rm SX})^2$. $\Sigma_{\rm IR}$ is derived using 70 μm radii from Díaz-Santos et al. (2017).

Figure 13 shows $\Sigma_{\rm SX}$ as a function of $\Sigma_{\rm IR}$. The X-ray surface density tends to increase with IR surface density, although the correlation is broader than the one existing between luminosities.

Table 9. Merger stage.

	CGI	CGII	C-GOALS
Non-merger	4%	18%	12%
Pre-merger	4%	14%	10%
early-stage merger	30%	31%	30%
mid-stage merger	17%	18%	18%
late-stage merger	44%	18%	27%

Notes. Percentage of sources classified as different merger stages by Stierwalt et al. (2013) for the C-GOALS I, C-GOALS II and full C-GOALS sample.

The left plot highlights AGN as filled symbols and separates the CGI and CGII samples. CGI sources, brighter in the IR, tend to have lower $\Sigma_{\rm SX}$ for a given $\Sigma_{\rm IR}$. Within a given sample, sources with AGN tend to have a larger $\Sigma_{\rm SX}$, which is to be expected because they are both brighter in X-rays and also more compact. Figure 13 also shows, on the right, the same figure but highlighting the merger stage of the sources in the sample. Information on the merger stage is taken from Stierwalt et al. (2013), derived from visual inspection of IRAC 3.6 μm (Channel 1) images. Classification is non-merger, pre-merger (galaxy pairs prior to a first encounter), early-stage merger (post first-encounter with galaxy disks still symmetric and intact, but with signs of tidal tails), mid-stage merger (showing amorphous disks, tidal tails, and other signs of merger activity), and late-stage merger (two nuclei in a common envelope). Sources in late-stage mergers tend to have higher $\Sigma_{\rm IR}$, but lower $\Sigma_{\rm SX}$ for the same $\Sigma_{\rm IR}$.

The percentages of merger stages in the sample are listed in Table 9. Many CGI sources are late mergers, hence their higher IR luminosity. This is also visible in Fig. 13, as CGI and late mergers have the same behavior with respect to the rest of the sources in the sample.

5. Discussion

5.1. X-ray to IR luminosity relation

The X-ray to IR luminosity (or SFR) correlation has been studied in numerous previous works (e.g., Fabbiano & Trinchieri 1985; Fabbiano et al. 1988; Fabbiano 1989; Bauer et al. 2002; Grimm et al. 2003; Ranalli et al. 2003; Gilfanov et al. 2004; Persic & Rephaeli 2007; Mineo et al. 2014). For soft X-rays, it originates in starburst-wind shock-heated gas. For hard X-rays (2−10 keV), the relation is thought to originate in high mass X-ray binaries (HMXB), which are end products of star formation. At low SFRs, that is, for local starburst galaxies with $L_{\rm IR} \ll 10^{11}\,L_{\odot}$, low-mass X-ray binaries (LMXBs) can significantly contribute to the X-ray luminosity. The luminosity from LMXBs correlates with galaxy stellar mass ($M_{\star}$), and this dependence must be considered, along with the contribution of SFR (e.g., Colbert et al. 2004; Gilfanov 2004; Lehmer et al. 2008, 2010).

Figure 9 shows a comparison between C-GOALS data and the correlation derived by Ranalli et al. (2003) for a sample of nearby starbursting galaxies. Works that include the LMXB contribution at low luminosities show a slight decrease in the slope at the high-luminosity end. Therefore, their correlation can be used as a point-of-reference against which to plot the LIRG and ULIRG data, although a rigorous comparison would require including all previously mentioned works and is beyond the scope of this work.

It is clear that at higher IR luminosities the correlation breaks down in an apparent deficit of X-ray flux, more extreme in the 0.5−2 keV band. This has been observed since the inclusion of the C-GOALS ULIRGs and high-luminosity LIRGs into the described correlations (e.g., Iwasawa et al. 2009, 2011; Lehmer et al. 2010). The inclusion of our CGII data provides more information on the transition between low-IR-luminosity galaxies and ULIRGs.

This underluminosity, or X-ray quietness, is explained in many works as an effect of obscuration. LIRGs and ULIRGs have extremely high concentrations of gas and dust in their inner regions, resulting in compact starbursts. High gas column densities can easily absorb soft X-rays, and in the most extreme cases, even hard X-rays.

Galaxies in the CGII sample, which are less IR-luminous than those in the CGI sample, are generally found in less-advanced mergers (see Table 9). The concentrations of gas and dust in the inner regions of the galaxies are higher in the more advanced mergers (e.g., Ricci et al. 2017), implying that the contribution of obscuration is stronger at higher IR luminosities. From an IR point of view, Díaz-Santos et al. (2010) observed that late-stage mergers are much more compact, which also indicates larger column densities.

5.1.1. Soft X-ray faintness

As shown in Fig. 9, the obscuring column densities necessary to dim the soft X-ray emission in most of the sources are compatible with those derived from the two-component model, plotted in Fig. 6 and listed in Table A.2. The derived values of $N_{\rm H}$ are lower limits, as any gas phase with higher obscuration contributes less significantly to the X-ray emission, or is even completely absorbed, and therefore cannot be fit.

Our spectral model is based on the existence of two distinct phases in the galaxy interstellar medium (ISM). Emission is likely to come from a complex phase-continuum of gas, and thus individual estimates of properties based on the spectral fitting should be taken with caution (see, e.g., Strickland & Stevens 2000, for a discussion). However, the simple two-phase model is the most complex we can fit given our data, and it shows that the column densities can at least explain the data.

Figure 13 shows lower $\Sigma_{\rm SX}$ for CGI galaxies, which reflects both their X-ray faintness and larger soft X-ray sizes (Fig. 12). We defined the size of the emission as the half-light radius, meaning that larger sizes indicate a less compact source. This implies that the faintness most likely originates in the center of the source. As CGI galaxies are in more advanced merger stages and should have higher column densities, this is likely to be an effect of obscuration. Another likely contribution to the larger soft X-ray sizes are the strongest starbursts in CGI galaxies, which generate larger soft X-ray nebulae.

We note that the *Chandra* resolution is much better than that of *Spitzer*, which should be taken into account in any direct comparison between characteristic sizes or luminosity surface densities. Higher resolution should imply a tendency toward deriving higher compactness, while Fig. 12 shows the opposite: X-ray sizes are generally similar, or even larger than IR sizes. However, we do not know what the IR emission would look like at similar resolutions. This difference between the datasets could explain the presence of outliers below the $R_{\rm IR} = R_{\rm H}^{\rm SX}$ line, and add to the dispersion of the data. Future observations with the *James Webb* Space Telescope (JWST) would allow for better comparison.

In conclusion, the soft X-ray faintness, and therefore the quadratic best-fit curve given by Eq. (4), can be explained through obscuration, as the necessary column densities are present in the galaxies within the C-GOALS sample.

5.1.2. Hard X-ray faintness

Attributing to extinction the observed faintness in hard X-rays requires much higher gas column densities. While it is clear that more IR-luminous sources (i.e., late-stage mergers) are generally more heavily obscured (e.g., Ricci et al. 2017, for a GOALS subsample), the most extreme sources are ∼1−2 dex below the correlation shown in Fig. 9. This implies that between ∼90−99% of the central starburst region must be covered in medium that is dense enough to suppress even hard X-rays. To obscure the emission in the 2−8 keV band in which *Chandra* is sensitive, the necessary column densities would be of the order of $\sim 10^{24}$ cm^{-2}. Sources in the sample that are undetected by *NuSTAR* (Ricci et al. 2017) would require even higher column densities, of the order of $\sim 10^{25}$ cm^{-2}.

In order to explain the observed faintness, regions of sizes of the order of the $R_{\rm H}^{\rm SX}$ listed in Table 8 would need to be covered in the high $N_{\rm H}$ we described. A column density of 10^{25} cm^{-2} could imply H_2 masses of the order of $\sim 10^{10}$−$10^{11}\,M_{\odot}$ for a nuclear star-forming region of 500 pc of radius. It is unclear if such high gas masses are truly concentrated in the inner regions of ULIRGs in the GOALS sample, and thus if this "self-absorbed starburst" scenario is feasible.

To distinguish the origin of the faintness, Iwasawa et al. (2009) stacked spectra of non-AGN sources in CGI, recovering a high-ionization Fe K feature. This feature can be explained by the presence of an internally shocked, hot bubble that is produced by thermalizing the energy of supernovae and stellar winds (e.g., Chevalier & Clegg 1985), which, in contrast to the SNe and HMXB emission, could be visible through the obscuring material. With high SFRs, the luminosity and the spectra with strong Fe $_{\rm XXV}$ line can be reproduced (e.g., Iwasawa et al. 2005, for Arp 220). This high-ionization line could also originate

from low-density gas that is photoionized by a hidden AGN (e.g., Antonucci & Miller 1985; Krolik & Kallman 1987), and it has been observed as the dominant Fe K feature in some Compton-thick AGN (e.g., Nandra & Iwasawa 2007; Braito et al. 2009).

Therefore, another explanation for the X-ray faintness could be the presence of a completely obscured AGN in the nucleus of these galaxies. This AGN would contribute to the IR emission, but would escape X-ray detection. While the column densities needed to cover the AGN are as high as those needed to self-absorb a starburst, the obscured region would be much smaller. This would imply much lower masses, that are easily found in the nuclei of GOALS galaxies. The scenario of hidden AGN versus extremely compact starburst has been previously discussed for some of the C-GOALS sources that show a higher X-ray faintness. Cases such as Arp 220 (e.g., Scoville et al. 2017; Barcos-Muñoz et al. 2018) or NGC 4418 (e.g., Costagliola et al. 2013, 2015) are compatible with both scenarios. However, it is worth noting that the hidden-AGN scenario requires the presence of an AGN with significant IR emission in order to explain the X-ray faintness, which means that it is probably unlikely that MIR determinations would systematically fail to pick up their signature.

Díaz-Santos et al. (2017) suggested from interpretation of *Herschel* FIR data on the full GOALS sample that the fraction of young, massive stars per star-forming region in ULIRGs might be higher than expected. This does not imply a change in the initial mass function, but the presence of very young star-forming regions, in which most massive stars still have not disappeared (age younger than a few Myr; Inami et al. 2013). In such a case, the massive stars can contribute to the IR emission, but the number of HMXB and SNe associated with the region will be low, as they are end-products of the star formation. This would result in a lower-than-expected X-ray luminosity for a given IR luminosity. Furthermore, in such a scenario, the winds of very massive stars could generate the hot gas that explains the Fe XXV line, without the need of invoking extreme obscuration over a large population of HMXB.

In order to truly understand the origin of the X-ray faintness, further observations are needed that provide information on the obscuration within the sources (e.g., ALMA or *NuSTAR* observations), or on the unobscured SFRs (e.g., through radio observations).

5.2. AGN and double AGN fraction

In Sect. 4.3 we have shown that $(38 \pm 6)\%$ of the systems (24 of 63) within CGII contain an AGN, $(31 \pm 5)\%$ (26 of 84) of individual galaxies being classified as AGN, according to MIR and/or X-ray criteria. This fraction can be compared to the $(50 \pm 7)\%$ of the systems, or $(38 \pm 7)\%$ (21 of 55) of the analyzed individual galaxies classified by Iwasawa et al. (2011) when analyzing the more IR-luminous objects in the CGI sample. This result may indicate a slight increase of AGN presence with IR luminosity, although the fractions in the two samples are compatible within the statistical errors. Although the increase of the AGN fraction as a function of luminosity found here is not statistically significant, it is consistent with previous findings in optical and IR spectroscopy (e.g., Veilleux et al. 1995; Kim et al. 1995; Yuan et al. 2010; Stierwalt et al. 2013).

Double AGN are detected in two interacting systems, NGC 5256 and ESO 432-IG006, of the 30 multiple systems analyzed here $(7 \pm 4)\%$. In the C-GOALS sample, one double AGN system, NGC 6240, was detected out of 24 multiple systems that were analyzed $(4 \pm 4)\%$.

Theoretical estimates derived from merger simulations performed by Capelo et al. (2017), which took into account observational effects (e.g., observation angle, distance dimming of X-ray luminosity, and obscuration of gas surrounding central BH), have concluded that in a sample of major mergers hosting at least one AGN, the fraction of dual AGN should be ∼20−30%. Koss et al. (2012) studied a sample of 167 nearby ($z < 0.05$) X-ray selected AGN and found a fraction of dual AGN in multiple systems of 19.5%. When separated into major pairs (mass ratio ≥ 0.25) and minor pairs, they found 37.1% and 4.8% respectively. Other studies (e.g., Ellison et al. 2011; Satyapal et al. 2017) found a statistical excess of dual AGN that decreased with galaxy separation. Therefore, dual AGN activation is more likely in advanced merger stages.

Within CGI and CGII, the fraction of double AGN in systems that host at least one AGN is $(11 \pm 10)\%$ (1 of 9) and $(29 \pm 14)\%$ (2 of 7) respectively. The fraction found in CGII falls well within the ranges found in the two previously described works, while the dual AGN fraction in CGI is just barely compatible within the errors. Moreover, CGI galaxies are generally found in more advanced merger stages (see Table 9), meaning that according to predictions, their dual AGN fraction should be closer to the mentioned 37.1%, and not to the lower 20%.

The lack of dual AGN in the CGI sample could be explained with heavy obscuration, which is expected to be important for these sources, as discussed in the previous section. Compton-thick ($N_{\rm H} > 1.5 \times 10^{24}$ cm^{-1}) AGN may be completely obscured in our *Chandra* data (e.g., Mrk 273, Iwasawa 2018), and their scattered continuum or Fe K_α lines too faint to be detected . MIR criteria can be effective in such cases, even though they may also miss the most heavily buried AGN (e.g., Snyder et al. 2013). Recent simulations by Blecha et al. (2018) found that much of the AGN lifetime is still undetected with common MIR selection criteria, even in the late stages of gas-rich major mergers. This effect is incremented for AGN that do not contribute significantly to the bolometric luminosity, especially when considering that the presence of a strong starburst can help dilute the AGN signature. Figure 5 shows up to 19 of the 32 X-ray selected AGN in C-GOALS that contribute less than 20% to the bolometric luminosity, most of which are missed by MIR selection criteria (see Table 5).

Another likely contribution to the low fraction of dual AGN found in CGI comes from the inability to resolve individual nuclei in a late-stage merger. Many CGI galaxies are found in such a stage. While *Chandra* has a high spatial resolution (∼0.5″), very closely interacting nuclei, with separations of the order of $\lesssim$200−300 pc, would remain unresolved in our sample. *Spitzer* data, also used in this work for the MIR AGN selection, have a much lower resolution, and would not resolve double AGN with even further separations.

However, as our sample sizes are small and therefore the statistical errors large, we cannot make any strong statements regarding a decreasing trend of the double AGN presence with IR luminosity.

6. Conclusions

We analyzed *Chandra*-ACIS data for a sample of 63 LIRGs and ULIRGs, composed of 84 individual galaxies (CGII). These galaxies are a low-IR-luminosity subsample of GOALS, a complete flux-limited sample of the 60 μm selected, bright galaxies in the local Universe ($z < 0.08$). Arcsecond-resolution images, spectra, and radial surface brightness profiles were presented. We compared the observations with *Spitzer* and *Herschel* data

to contrast their X-ray and IR properties. We also compared our results to those found by Iwasawa et al. (2011) for the high-IR-luminosity subsample of GOALS (CGI). We summarize our main findings below.

- Objects with an AGN signature represent $(31 \pm 5)\%$ of the CGII sample, compared to the $(38 \pm 7)\%$ reported for the CGI sample. Double AGN are detected in two interacting systems, implying that the fraction of double AGN in systems that host at least one AGN is $(29 \pm 14)\%$, in contrast to the $(11 \pm 10)\%$ found for the CGI sample.
- 19 of 32 of the X-ray selected AGN in the full C-GOALS sample (CGI+CGII) are not energetically significant, contributing less than 20% to the bolometric luminosity of the galaxy, according to MIR determinations.
- The brightest LIRGs, at $L_{\rm FIR} > 8 \times 10^{10}\,L_{\odot}$, show a hard X-ray faintness with respect to the luminosities predicted by correlations found for nearby star-forming galaxies. This behavior is accentuated for the CGI ULIRGs. Possible explanations for the sources with most extreme deviations include a self-absorbed starburst, an obscured AGN, or the presence of extremely young star-forming regions.
- The extended soft X-ray emission shows a spectrum that is consistent with thermal emission from a two-phase gas, with an inner, hotter and more heavily obscured component, and an outer, colder and unobscured component.
- According to our modeling, an obscuration of the inner component in the range of $N_{\rm H} = 1{-}5 \times 10^{22}$ cm^{-2} can explain the soft X-ray faintness for the vast majority of the sources.
- Most sources within CGII have a compact soft X-ray morphology. $(50 \pm 8)\%$ of the sources generate half of the emission within the inner ~1 kpc. This behavior is accentuated for AGN, with $(83 \pm 7)\%$ of the sources with a half-light radius below ~ 1 kpc.
- CGI sources are, in comparison, less compact, which is most likely an effect of obscuration in the inner regions.
- Most sources in CGII have similar soft X-ray and MIR sizes, although there is important dispersion in this relation.

Acknowledgements. We thank the anonymous referee for helpful comments and suggestions. We acknowledge support by the Spanish Ministerio de Economía y Competitividad (MINECO/FEDER, UE) under grants AYA2013-47447-C3-1-P and MDM-2014-0369 of ICCUB (Unidad de Excelencia "María de Maeztu"). N.T-A. acknowledges support from MINECO through FPU14/04887 grant. T.D.-S. acknowledges support from ALMA-CONICYT project 31130005 and FONDECYT regular project 1151239. G.C.P. acknowledges support from the University of Florida. This work was conducted in part at the Aspen Center for Physics, which is supported by NSF grant PHY-1607611; V.U., G.C.P, D.B.S., A.M.M., T.D-S. and A.S.E. thank the Center for its hospitality during the Astrophysics of Massive Black Holes Mergers workshop in June and July 2018. The scientific results reported in this article are based on observations made by *Chandra* X-ray Observatory, and has made use of the NASA/IPAC Extragalactic Database (NED), which is operated by the Jet Propulsion Laboratory, California Institute of Technology under contract with NASA. We acknowledge the use of the software packages CIAO and HEASoft.

References

Alam, S., Albareti, F. D., Allende Prieto, C., et al. 2015, ApJS, 219, 12
Alonso-Herrero, A., Pereira-Santaella, M., Rieke, G. H., & Rigopoulou, D. 2012, ApJ, 744, 2
Antonucci, R. R. J., & Miller, J. S. 1985, ApJ, 297, 621
Armus, L., Mazzarella, J. M., Evans, A. S., et al. 2009, PASP, 121, 559
Atek, H., Kunth, D., Hayes, M., Östlin, G., & Mas-Hesse, J. M. 2008, A&A, 488, 491
Baan, W. A., & Klöckner, H.-R. 2006, A&A, 449, 559
Band, D. L., Klein, R. I., Castor, J. I., & Nash, J. K. 1990, ApJ, 362, 90
Barcos-Muñoz, L., Leroy, A. K., Evans, A. S., et al. 2017, ApJ, 843, 117
Barcos-Muñoz, L., Aalto, S., Thompson, T. A., et al. 2018, ApJ, 853, L28
Bauer, F. E., Alexander, D. M., Brandt, W. N., et al. 2002, AJ, 124, 2351
Blackburn, J. K. 1995, in Astronomical Data Analysis Software and Systems IV, eds. R. A. Shaw, H. E. Payne, & J. J. E. Hayes, ASP Conf. Ser., 77, 367
Blecha, L., Snyder, G. F., Satyapal, S., & Ellison, S. L. 2018, MNRAS, 478, 3056
Braito, V., Reeves, J. N., Della Ceca, R., et al. 2009, A&A, 504, 53
Brightman, M., & Nandra, K. 2011, MNRAS, 413, 1206
Capelo, P. R., Dotti, M., Volonteri, M., et al. 2017, MNRAS, 469, 4437
Casey, C. M., Narayanan, D., & Cooray, A. 2014, Phys. Rep., 541, 45
Chapman, J. M., Staveley-Smith, L., Axon, D. J., et al. 1990, MNRAS, 244, 281
Chevalier, R. A., & Clegg, A. W. 1985, Nature, 317, 44
Chu, J. K., Sanders, D. B., Larson, K. L., et al. 2017, ApJS, 229, 25
Clemens, M. S., Vega, O., Bressan, A., et al. 2008, A&A, 477, 95
Colbert, E. J. M., Heckman, T. M., Ptak, A. F., Strickland, D. K., & Weaver, K. A. 2004, ApJ, 602, 231
Condon, J. J. 1992, ARA&A, 30, 575
Corbett, E. A., Norris, R. P., Heisler, C. A., et al. 2002, ApJ, 564, 650
Costagliola, F., Aalto, S., Sakamoto, K., et al. 2013, A&A, 556, A66
Costagliola, F., Sakamoto, K., Muller, S., et al. 2015, A&A, 582, A91
Del Moro, A., Alexander, D. M., Bauer, F. E., et al. 2016, MNRAS, 456, 2105
Di Matteo, T., Springel, V., & Hernquist, L. 2005, Nature, 433, 604
Díaz-Santos, T., Charmandaris, V., Armus, L., et al. 2010, ApJ, 723, 993
Díaz-Santos, T., Armus, L., Charmandaris, V., et al. 2017, ApJ, 846, 32
Dopita, M. A., Pereira, M., Kewley, L. J., & Capaccioli, M. 2002, ApJS, 143, 47
Dudik, R. P., Satyapal, S., & Marcu, D. 2009, ApJ, 691, 1501
Ellison, S. L., Patton, D. R., Mendel, J. T., & Scudder, J. M. 2011, MNRAS, 418, 2043
Evans, A. S., Vavilkin, T., Pizagno, J., et al. 2008, ApJ, 675, L69
Fabbiano, G. 1989, ARA&A, 27, 87
Fabbiano, G., & Trinchieri, G. 1985, ApJ, 296, 430
Fabbiano, G., Gioia, I. M., & Trinchieri, G. 1988, ApJ, 324, 749
Fabbiano, G., Baldi, A., King, A. R., et al. 2004, ApJ, 605, L21
Falstad, N., González-Alfonso, E., Aalto, S., et al. 2015, A&A, 580, A52
Franceschini, A., Braito, V., Persic, M., et al. 2003, MNRAS, 343, 1181
Fruscione, A., McDowell, J. C., Allen, G. E., et al. 2006, in SPIE Conf. Ser., Proc. SPIE, 6270, 62701V
Garmire, G. P., Bautz, M. W., Ford, P. G., Nousek, J. A., & Ricker, Jr., G. R. 2003, in X-Ray and Gamma-Ray Telescopes and Instruments for Astronomy, eds. J. E. Truemper, & H. D. Tananbaum, Proc. SPIE, 4851, 28
Gilfanov, M. 2004, MNRAS, 349, 146
Gilfanov, M., Grimm, H.-J., & Sunyaev, R. 2004, Nucl. Phys. B Proc. Suppl., 132, 369
Gilli, R., Comastri, A., Brunetti, G., & Setti, G. 1999, New Astron., 4, 45
Goldader, J. D., Joseph, R. D., Doyon, R., & Sanders, D. B. 1997, ApJS, 108, 449
Grimm, H.-J., Gilfanov, M., & Sunyaev, R. 2003, MNRAS, 339, 793
Haan, S., Surace, J. A., Armus, L., et al. 2011, AJ, 141, 100
Hattori, T., Yoshida, M., Ohtani, H., et al. 2004, AJ, 127, 736
Helou, G., Soifer, B. T., & Rowan-Robinson, M. 1985, ApJ, 298, L7
Hernquist, L. 1989, Nature, 340, 687
Hill, T. L., Heisler, C. A., Norris, R. P., Reynolds, J. E., & Hunstead, R. W. 2001, AJ, 121, 128
Hinshaw, G., Weiland, J. L., Hill, R. S., et al. 2009, ApJS, 180, 225
Hopkins, P. F., Bundy, K., Murray, N., et al. 2009, MNRAS, 398, 898
Hopkins, P. F., Hernquist, L., Cox, T. J., et al. 2005, ApJ, 630, 705
Howell, J. H., Mazzarella, J. M., Chan, B. H. P., et al. 2007, AJ, 134, 2086
Hutchings, J. B., Lo, E., Neff, S. G., Stanford, S. A., & Unger, S. W. 1990, AJ, 100, 60
Inami, H., Armus, L., Charmandaris, V., et al. 2013, ApJ, 777, 156
Inui, T., Matsumoto, H., Tsuru, T. G., et al. 2005, PASJ, 57, 135
Iwasawa, K., Sanders, D. B., Evans, A. S., et al. 2005, MNRAS, 357, 565
Iwasawa, K., Sanders, D. B., Evans, A. S., et al. 2009, ApJ, 695, L103
Iwasawa, K., Sanders, D. B., Teng, S. H., et al. 2011, A&A, 529, A106
Iwasawa, K., U, V., Mazzarella, J. M., , et al. 2018, A&A, 611, A71
Joy, M., & Harvey, P. M. 1987, ApJ, 315, 480
Kaaret, P., & Alonso-Herrero, A. 2008, ApJ, 682, 1020
Kaastra, J. 1992, An X-Ray Spectral Code for Optically Thin Plasmas (Internal SRON-Leiden Report, updated version 2.0)
Kalberla, P. M. W., Burton, W. B., Hartmann, D., et al. 2005, A&A, 440, 775
Kennicutt, Jr., R. C. 1998, ApJ, 498, 541
Kewley, L. J., Dopita, M. A., Sutherland, R. S., Heisler, C. A., & Trevena, J. 2001, ApJ, 556, 121
Kewley, L. J., Groves, B., Kauffmann, G., & Heckman, T. 2006, MNRAS, 372, 961
Kim, D.-C., Sanders, D. B., Veilleux, S., Mazzarella, J. M., & Soifer, B. T. 1995, ApJS, 98, 129
Kocevski, D. D., Brightman, M., Nandra, K., et al. 2015, ApJ, 814, 104
Koss, M., Mushotzky, R., Treister, E., et al. 2012, ApJ, 746, L22

Koyama, K., Inoue, H., Tanaka, Y., et al. 1989, PASJ, 41, 731
Kreckel, K., Armus, L., Groves, B., et al. 2014, ApJ, 790, 26
Krolik, J. H., & Kallman, T. R. 1987, ApJ, 320, L5
Kunth, D., Leitherer, C., Mas-Hesse, J. M., Östlin, G., & Petrosian, A. 2003, ApJ, 597, 263
Kuo, C.-Y., Lim, J., Tang, Y.-W., & Ho, P. T. P. 2008, ApJ, 679, 1047
Lahuis, F., Spoon, H. W. W., Tielens, A. G. G. M., et al. 2007, ApJ, 659, 296
Lanzuisi, G., Ranalli, P., Georgantopoulos, I., et al. 2015, A&A, 573, A137
Larson, K. L., Sanders, D. B., Barnes, J. E., et al. 2016, ApJ, 825, 128
Lehmer, B. D., Brandt, W. N., Alexander, D. M., et al. 2008, ApJ, 681, 1163
Lehmer, B. D., Alexander, D. M., Bauer, F. E., et al. 2010, ApJ, 724, 559
Levenson, N. A., Krolik, J. H., Życki, P. T., et al. 2002, ApJ, 573, L81
Levenson, N. A., Weaver, K. A., Heckman, T. M., Awaki, H., & Terashima, Y. 2005, ApJ, 618, 167
Liedahl, D. A., Osterheld, A. L., & Goldstein, W. H. 1995, ApJ, 438, L115
Lipovetsky, V. A., Neizvestny, S. I., & Neizvestnaya, O. M. 1988, Soobshcheniya Spetsial'noj Astrofizicheskoj Observatorii, 55, 5
Lira, P., Ward, M., Zezas, A., Alonso-Herrero, A., & Ueno, S. 2002, MNRAS, 330, 259
Lonsdale, C. J., Smith, H. J., & Lonsdale, C. J. 1993, ApJ, 405, L9
Luangtip, W., Roberts, T. P., Mineo, S., et al. 2015, MNRAS, 446, 470
Magdziarz, P., & Zdziarski, A. A. 1995, MNRAS, 273, 837
Maia, M. A. G., Suzuki, J. A., da Costa, L. N., Willmer, C. N. A., & Rite, C. 1996, A&AS, 117, 487
Maiolino, R., Comastri, A., Gilli, R., et al. 2003, MNRAS, 344, L59
Mazzarella, J. M., Iwasawa, K., Vavilkin, T., et al. 2012, AJ, 144, 125
Meléndez, M., Heckman, T. M., Martínez-Paredes, M., Kraemer, S. B., & Mendoza, C. 2014, MNRAS, 443, 1358
Mewe, R., Gronenschild, E. H. B. M., & van den Oord, G. H. J. 1985, A&AS, 62, 197
Mineo, S., Gilfanov, M., Lehmer, B. D., Morrison, G. E., & Sunyaev, R. 2014, MNRAS, 437, 1698
Mirabel, I. F., & Sanders, D. B. 1988, ApJ, 335, 104
Moorwood, A. F. M., & Oliva, E. 1994, ApJ, 429, 602
Mould, J. R., Huchra, J. P., Freedman, W. L., et al. 2000, ApJ, 529, 786
Mudd, D., Mathur, S., Guainazzi, M., et al. 2014, ApJ, 787, 40
Nandra, K., & Iwasawa, K. 2007, MNRAS, 382, L1
Nandra, K., & Pounds, K. A. 1994, MNRAS, 268, 405
Norris, R. P., & Forbes, D. A. 1995, ApJ, 446, 594
Oda, S., Ueda, Y., Tanimoto, A., & Ricci, C. 2018, ApJ, 855, 79
O'Sullivan, E., Zezas, A., Vrtilek, J. M., et al. 2014, ApJ, 793, 73
Parra, R., Conway, J. E., Aalto, S., et al. 2010, ApJ, 720, 555
Pereira-Santaella, M., Alonso-Herrero, A., Colina, L., et al. 2015a, A&A, 577, A78
Pereira-Santaella, M., Colina, L., Alonso-Herrero, A., et al. 2015b, MNRAS, 454, 3679
Persic, M., & Rephaeli, Y. 2007, A&A, 463, 481
Petric, A. O., Armus, L., Howell, J., et al. 2011, ApJ, 730, 28
Ptak, A., Heckman, T., Levenson, N. A., Weaver, K., & Strickland, D. 2003, ApJ, 592, 782
Ranalli, P., Comastri, A., & Setti, G. 2003, A&A, 399, 39
Ricci, C., Ueda, Y., Paltani, S., et al. 2014, MNRAS, 441, 3622
Ricci, C., Bauer, F. E., Treister, E., et al. 2016, ApJ, 819, 4
Ricci, C., Bauer, F. E., Treister, E., et al. 2017, MNRAS, 468, 1273
Risaliti, G., Gilli, R., Maiolino, R., & Salvati, M. 2000, A&A, 357, 13
Risaliti, G., Elvis, M., Fabbiano, G., Baldi, A., & Zezas, A. 2005, ApJ, 623, L93
Risaliti, G., Elvis, M., Fabbiano, G., et al. 2007, ApJ, 659, L111
Risaliti, G., Miniutti, G., Elvis, M., et al. 2009, ApJ, 696, 160
Romero-Cañizales, C., Pérez-Torres, M. A., Alberdi, A., et al. 2012, A&A, 543, A72
Romero-Cañizales, C., Alberdi, A., Ricci, C., et al. 2017, MNRAS, 467, 2504
Roussel, H., Helou, G., Beck, R., et al. 2003, ApJ, 593, 733
Rudnick, G., Rix, H.-W., & Kennicutt, Jr., R. C. 2000, ApJ, 538, 569
Sales, D. A., Robinson, A., Axon, D. J., et al. 2015, ApJ, 799, 25
Sanders, D. B. 1999, Ap&SS, 266, 331
Sanders, D. B., Soifer, B. T., Elias, J. H., et al. 1988, ApJ, 325, 74
Sanders, D. B., Mazzarella, J. M., Kim, D.-C., Surace, J. A., & Soifer, B. T. 2003, AJ, 126, 1607
Satyapal, S., Ellison, S. L., McAlpine, W., et al. 2014, MNRAS, 441, 1297
Satyapal, S., Secrest, N. J., Ricci, C., et al. 2017, ApJ, 848, 126
Scoville, N., Murchikova, L., Walter, F., et al. 2017, ApJ, 836, 66
Shalyapina, L. V., Moiseev, A. V., Yakovleva, V. A., Hagen-Thorn, V. A., & Burenkov, A. N. 2004, Astron. Lett., 30, 1
Shu, X. W., Wang, J. X., Jiang, P., Fan, L. L., & Wang, T. G. 2007, ApJ, 657, 167
Silverman, J. D., Kampczyk, P., Jahnke, K., et al. 2011, ApJ, 743, 2
Singh, V., Risaliti, G., Braito, V., & Shastri, P. 2012, MNRAS, 419, 2089
Smith, D. A., Herter, T., Haynes, M. P., Beichman, C. A., & Gautier, III., T. N. 1996, ApJS, 104, 217
Snyder, G. F., Hayward, C. C., Sajina, A., et al. 2013, ApJ, 768, 168
Stierwalt, S., Armus, L., Surace, J. A., et al. 2013, ApJS, 206, 1
Strickland, D. K., & Stevens, I. R. 2000, MNRAS, 314, 511
Surace, J. A., Sanders, D. B., & Mazzarella, J. M. 2004, AJ, 127, 3235
Teng, S. H., & Veilleux, S. 2010, ApJ, 725, 1848
Teng, S. H., Wilson, A. S., Veilleux, S., et al. 2005, ApJ, 633, 664
Terashima, Y., Hirata, Y., Awaki, H., et al. 2015, ApJ, 814, 11
Turner, T. J., & Miller, L. 2009, A&ARv, 17, 47
Turner, M. J. L., Reeves, J. N., Ponman, T. J., et al. 2001, A&A, 365, L110
Valiante, E., Lutz, D., Sturm, E., Genzel, R., & Chapin, E. L. 2009, ApJ, 701, 1814
Vega, O., Clemens, M. S., Bressan, A., et al. 2008, A&A, 484, 631
Veilleux, S., Kim, D.-C., Sanders, D. B., Mazzarella, J. M., & Soifer, B. T. 1995, ApJS, 98, 171
Veilleux, S., Kim, D.-C., & Sanders, D. B. 1999, ApJ, 522, 113
Veilleux, S., Rupke, D. S. N., Kim, D.-C., et al. 2009, ApJS, 182, 628
Wang, J., Fabbiano, G., Elvis, M., et al. 2009, ApJ, 694, 718
Weisskopf, M. C., Tananbaum, H. D., Van Speybroeck, L. P., & O'Dell, S. L. 2000, in X-Ray Optics, Instruments, and Missions III, eds. J. E. Truemper, & B. Aschenbach, Proc. SPIE, 4012, 2
West, R. M. 1976, A&A, 46, 327
Xu, C. K., Cao, C., Lu, N., et al. 2015, ApJ, 799, 11
Yeghiazaryan, A. A., Nazaryan, T. A., & Hakobyan, A. A. 2016, A&A, 37, A1
Yuan, T.-T., Kewley, L. J., & Sanders, D. B. 2010, ApJ, 709, 884
Zhou, Z.-M., Wu, H., Huang, L., et al. 2014, Res. Astron. Astrophys., 14, 1393
Zink, E. C., Lester, D. F., Doppmann, G., & Harvey, P. M. 2000, ApJS, 131, 413

Appendix A: Notes on individual objects

Table A.1. X-ray spectral properties for the sample.

No.	Galaxy	SX (1)	HX (2)	HR (3)	F_{SX} (4)	F_{HX} (5)	L_{SX} (6)	L_{HX} (7)	SX/IR (8)	HX/IR (9)
45	UGC 08387	15.47 ± 1.06	4.28 ± 0.59	−0.57 ± 0.04	5.29	5.57	7.79	9.71	−4.44	−4.33
47	CGCG 436−030	9.01 ± 0.84	3.18 ± 0.54	−0.48 ± 0.04	3.78	5.48	8.75	16.07	−4.33	−4.07
49	NGC 0695	15.58 ± 1.06	5.59 ± 0.66	−0.47 ± 0.03	6.00	11.63	15.78	51.19	−4.08	−3.57
50	CGCG 043−099	2.60 ± 0.44	0.92 ± 0.32	−0.48 ± 0.09	1.07	1.35	3.98	6.39	−4.67	−4.46
51	MCG+07−23−019	8.51 ± 0.45	1.17 ± 0.24	−0.76 ± 0.04	3.55	1.93	10.91	7.10	−4.17	−4.35
52	NGC 6670 (E)	5.76 ± 0.64	1.21 ± 0.35	−0.65 ± 0.08	2.58	2.15	5.60	5.56	−4.27	−4.27
52	NGC 6670 (W)	7.21 ± 0.72	2.93 ± 0.50	−0.42 ± 0.04	3.31	6.18	7.24	22.73	−3.95	−3.45
53	UGC 02369 (S)	11.16 ± 1.14	1.30 ± 0.48	−0.79 ± 0.08	3.71	1.71	9.53	4.90	−4.28	−4.57
54	NGC 1614	38.57 ± 1.59	12.19 ± 0.91	−0.52 ± 0.02	16.62	18.51	10.03	12.36	−4.23	−4.14
56	NGC 5331 (N)	1.79 ± 0.38	0.73 ± 0.26	−0.42 ± 0.10	0.95	1.31	2.89	4.86	−4.06	−3.84
56	NGC 5331 (S)	4.37 ± 0.59	1.36 ± 0.36	−0.53 ± 0.07	2.13	1.97	6.46	7.10	−4.35	−4.30
57	IRAS F06076−2139(N)	1.96 ± 0.37	0.97 ± 0.27	−0.34 ± 0.08	0.93	1.48	3.60	6.26	−4.68	−4.44
57	IRAS F06076−2139(S)	0.37 ± 0.17	0.35 ± 0.17	−0.03 ± 0.17	–[a]	–[a]	–[a]	–[a]	–[a]	–[a]
60	IC 2810(NW)	3.61 ± 0.50	0.18 ± 0.15	−0.91 ± 0.13	1.67	0.55	4.27	2.10	−4.33	−4.73
60	IC 2810 (SE)	1.75 ± 0.39	0.12 ± 0.19	−0.87 ± 0.22	0.70	0.01	2.20	0.30	−4.39	−5.26
63	IRAS 18090+0130 (E)	4.01 ± 0.55	1.27 ± 0.36	−0.52 ± 0.08	1.59	2.50	4.08	6.39	−4.53	−4.34
63	IRAS 18090+0130(W)	1.08 ± 0.30	0.33 ± 0.23	−0.54 ± 0.18	–[a]	–[a]	–[a]	–[a]	–[a]	–[a]
64	III Zw 035 (N)	2.34 ± 0.41	0.84 ± 0.26	−0.47 ± 0.09	0.96	1.32	1.81	2.89	−4.97	−4.76
65	NGC 3256	263.36 ± 3.28	28.62 ± 1.67	−0.80 ± 0.01	77.43	43.02	16.29	9.21	−4.01	−4.26
67	IRAS F16399−0937(N)	4.02 ± 0.53	1.6 ± 0.34	−0.43 ± 0.06	1.79	2.52	4.03	6.45	−4.56	−4.36
67	IRAS F16399−0937(S)	2.06 ± 0.38	1.25 ± 0.31	−0.24 ± 0.07	1.00	2.07	2.79	5.30	−3.77	−3.49
68	IRAS F16164−0746	3.91 ± 0.55	2.8 ± 0.52	−0.17 ± 0.04	1.84	6.61	4.12	15.38	−4.59	−4.02
69	IC 4687	20.68 ± 1.21	4.27 ± 0.59	−0.66 ± 0.04	8.60	5.97	7.97	5.30	−4.11	−4.30
69	IC 4686	4.87 ± 0.59	0.90 ± 0.28	−0.69 ± 0.09	2.07	1.49	2.12	1.56	−3.95	−4.09
69	IC 4689	5.17 ± 0.63	0.00 ± 0.21	−1.00 ± 0.14	2.45	–[a]	2.72	–[a]	−4.11	–[a]
71	NGC 2623	4.79 ± 0.52	3.85 ± 0.49	−0.11 ± 0.02	1.74	7.93	1.49	12.85	−5.01	−4.08
72	IC 5298	11.76 ± 0.92	3.31 ± 0.56	−0.56 ± 0.04	5.17	9.66	10.03	36.65	−4.18	−3.62
73	IRAS 20351+2521	9.14 ± 0.89	1.69 ± 0.52	−0.69 ± 0.07	3.93	2.55	14.02	8.33	−4.05	−4.27
75	NGC 6090 (NE)	16.71 ± 1.07	1.84 ± 0.37	−0.80 ± 0.05	5.89	2.88	13.63	7.81	−3.99	−4.23
75	NGC6090 (SW)	4.68 ± 0.57	0.56 ± 0.21	−0.79 ± 0.10	1.71	3.11	4.00	9.01	−3.55	−3.20
79	NGC 5256 (NE)	32.39 ± 1.31	7.97 ± 0.69	−0.60 ± 0.02	11.62	18.06	24.23	55.81	−3.33	−2.97
79	NGC 5256 (SW)	20.47 ± 1.02	1.7 ± 0.32	−0.85 ± 0.04	7.98	3.30	16.56	7.72	−3.72	−4.05
80	IRAS F03359+1523(E)	5.92 ± 0.67	1.41 ± 0.38	−0.62 ± 0.07	2.22	2.30	8.68	8.32	−4.20	−4.21
81	ESO 550−IG025 (N)	2.23 ± 0.41	0.55 ± 0.24	−0.60 ± 0.12	0.73	1.17	1.78	3.58	−4.51	−4.22
81	ESO 550−IG025 (S)	1.55 ± 0.35	0.76 ± 0.26	−0.34 ± 0.10	0.69	1.51	1.65	4.29	−4.46	−4.16
82	NGC 0034	15.58 ± 1.08	6.68 ± 0.76	−0.40 ± 0.03	7.23	12.97	6.40	17.78	−4.27	−3.83
83	MCG+12−02−001 (E)	11.12 ± 0.89	3.77 ± 0.53	−0.49 ± 0.04	4.66	5.59	3.01	3.93	−4.56	−4.44
83	MCG+12−02−001 (W)	3.02 ± 0.46	1.49 ± 0.34	−0.34 ± 0.06	1.29	2.92	1.26	2.39	−3.98	−3.71
85	IRAS F17138−1017	7.84 ± 0.76	6.19 ± 0.71	−0.12 ± 0.02	3.67	12.68	3.94	17.64	−4.48	−3.83
95	ESO 440−IG058 (N)	2.12 ± 0.38	1.02 ± 0.27	−0.35 ± 0.08	0.99	1.27	1.72	2.22	−3.74	−3.63
95	ESO 440−IG058 (S)	7.16 ± 0.70	0.97 ± 0.28	−0.76 ± 0.08	3.40	1.53	5.60	2.97	−4.23	−4.50
100	NGC 7130	78.11 ± 1.44	8 ± 0.53	−0.81 ± 0.01	25.37	13.28	16.89	13.29	−3.78	−3.88
104	NGC 7771	33.16 ± 1.54	12.55 ± 1.14	−0.45 ± 0.02	12.87	20.19	6.26	12.35	−4.15	−3.85
104	NGC 7770	8.08 ± 0.73	0.34 ± 0.29	−0.92 ± 0.09	3.15	1.27	1.59	0.74	−3.77	−4.11
105	NGC 7592 (E)	8.42 ± 0.76	1.11 ± 0.32	−0.77 ± 0.07	3.35	1.80	4.94	3.13	−4.09	−4.29
105	NGC 7592 (W)	11.29 ± 0.88	2.04 ± 0.41	−0.69 ± 0.05	4.21	3.15	6.23	5.87	−3.75	−3.78
106	NGC 6285	5.04 ± 0.64	0.45 ± 0.33	−0.83 ± 0.12	1.94	0.85	1.73	0.97	−3.83	−4.08
106	NGC 6286	32.15 ± 1.64	1.27 ± 0.87	−0.92 ± 0.05	11.96	2.58	10.93	2.92	−3.86	−4.43

Notes. Column (1): background corrected count rate in the 0.5−2 keV band in units of 10^{-3} ct s^{-1}. Column (2): background corrected count rate in the 2−7 keV band in units of 10^{-3} ct s^{-1}. Column (3): X-ray colour as defined by HR = $(H - S)/(H + S)$. Column (4): observed 0.5−2 keV band flux in units of 10^{14} erg s^{-1} cm^{-2}. Column (5): observed 2−7 keV band flux in units of 10^{14} erg s^{-1} cm^{-2}. Column (6): 0.5−2 keV band luminosity corrected for Galactic absorption in units of 10^{40} erg s^{-1}. Column (7): 2−10 keV band luminosity corrected for Galactic absorption in units of 10^{40} erg s^{-1}. Column (8): logarithmic luminosity ratio of the 0.5−2 keV and 8−1000 μm bands. Column (9): logarithmic luminosity ratio of the 2−10 keV and 8−1000 μm bands. [a] Missing values due to inability to fit X-ray spectra, not enough source counts.

Table A.1. continued.

No.	Galaxy	SX (1)	HX (2)	HR (3)	F_{SX} (4)	F_{HX} (5)	L_{SX} (6)	L_{HX} (7)	SX/IR (8)	HX/IR (9)
107	NGC 4922 (N)	10.93 ± 0.97	2.73 ± 0.62	-0.60 ± 0.05	5.00	5.93	7.49	17.28	−4.09	−3.73
110	NGC 3110	21.92 ± 1.28	4.73 ± 0.77	-0.65 ± 0.04	10.32	8.40	8.54	8.70	−3.98	−3.97
114	NGC 0232	10.91 ± 0.91	2.19 ± 0.55	-0.67 ± 0.06	4.85	4.34	5.37	6.58	−4.29	−4.21
117	MCG+08−18−013(E)	5.27 ± 0.67	2.1 ± 0.45	-0.43 ± 0.06	2.43	3.56	4.07	7.84	−4.32	−4.03
120	CGCG 049−057	0.83 ± 0.28	0.76 ± 0.29	-0.04 ± 0.09	0.37	1.26	0.20	1.02	−5.63	−4.93
121	NGC 1068	1975.11 ± 6.58	150.27 ± 2.03	-0.86 ± 0.00	503.35	223.51	16.31	10.15	−3.77	−3.98
123	UGC 02238	6.94 ± 0.74	1.94 ± 0.52	-0.56 ± 0.06	2.89	4.33	3.77	5.88	−4.34	−4.15
127	MCG−03−34−064	95.67 ± 3.73	49.5 ± 2.75	-0.32 ± 0.01	37.92	158.12	35.11	289.53	−3.32	−2.40
134	ESO 350−IG038	26.85 ± 0.73	6.38 ± 0.43	-0.62 ± 0.02	10.38	10.03	10.34	12.12	−3.85	−3.78
136	MCG−01−60−022	10.52 ± 0.84	6.7 ± 0.78	-0.22 ± 0.02	4.30	16.83	5.42	33.62	−4.12	−3.33
141	IC 0564	7.14 ± 0.77	2.45 ± 0.53	-0.50 ± 0.06	3.61	5.18	3.73	9.29	−3.97	−3.57
141	IC 0563	4.93 ± 0.64	2.36 ± 0.57	-0.34 ± 0.05	2.56	4.74	2.64	6.90	−4.05	−3.63
142	NGC 5135	123.31 ± 2.14	12.39 ± 0.9	-0.82 ± 0.01	39.38	26.95	19.69	42.37	−3.59	−3.26
144	IC 0860	0.68 ± 0.26	0.37 ± 0.27	-0.29 ± 0.17	_[a]	_[a]	_[a]	_[a]	_[a]	_[a]
147	IC 5179	39.74 ± 2.14	6.71 ± 1.62	-0.71 ± 0.04	15.51	14.38	4.99	6.35	−4.13	−4.02
148	CGCG 465−012	7.13 ± 0.77	1.52 ± 0.58	-0.65 ± 0.08	2.63	4.01	3.65	5.64	−4.22	−4.04
163	NGC 4418	2.63 ± 0.59	0.38 ± 0.32	-0.75 ± 0.18	0.87	0.91	0.15	0.19	−5.61	−5.50
157	MCG−02−33−098	2.97 ± 0.46	0.77 ± 0.26	-0.59 ± 0.10	1.39	1.21	1.11	1.16	−4.31	−3.41
157	MCG−02−33−099	4.42 ± 0.56	1.32 ± 0.33	-0.54 ± 0.07	2.19	2.25	1.76	2.15	−4.37	−4.44
169	ESO 343−IG013 (N)	2.02 ± 0.38	2.05 ± 0.38	0.01 ± 0.05	0.91	4.45	0.85	6.74	−4.70	−3.80
169	ESO 343−IG013 (S)	3.15 ± 0.47	1.02 ± 0.3	-0.51 ± 0.08	1.67	1.24	1.62	1.36	−3.86	−3.93
170	NGC 2146	170.25 ± 4.38	43.74 ± 2.47	-0.59 ± 0.01	59.70	75.77	2.50	3.76	−4.31	−4.13
174	NGC 5653	20.26 ± 1.20	3.18 ± 0.7	-0.73 ± 0.04	8.00	5.37	3.59	3.44	−4.16	−4.18
178	NGC 4194	59.99 ± 1.33	7.91 ± 0.57	-0.77 ± 0.02	22.87	12.40	5.23	3.37	−3.97	−4.16
179	NGC 7591	4.29 ± 1.01	1.09 ± 0.74	-0.59 ± 0.17	_[a]	_[a]	_[a]	_[a]	_[a]	_[a]
182	NGC 0023	34.84 ± 1.45	3.88 ± 0.77	-0.80 ± 0.03	12.89	6.04	7.12	3.47	−3.85	−4.17
188	NGC 7552	148.31 ± 5.56	15.63 ± 2.09	-0.81 ± 0.03	55.45	24.24	3.76	1.92	−4.12	−4.41
191	ESO 420−G013	56.94 ± 2.19	4.17 ± 0.83	-0.86 ± 0.03	23.59	5.81	7.86	2.04	−3.76	−4.34
194	ESO 432−IG006 (NE)	8.09 ± 0.76	1.75 ± 0.48	-0.64 ± 0.06	3.69	4.46	3.82	6.41	−3.65	−3.43
194	ESO 432−IG006 (SW)	6.04 ± 0.66	1.81 ± 0.46	-0.54 ± 0.06	2.79	4.03	2.87	4.53	−4.01	−3.81
195	NGC 1961	17.55 ± 0.89	4.48 ± 0.83	-0.59 ± 0.03	12.45	15.65	6.22	10.63	−3.85	−3.62
196	NGC 7753	15.00 ± 1.65	4.43 ± 1.67	-0.54 ± 0.07	4.52	7.75	3.36	5.88	−3.94	−3.70
196	NGC 7752	7.18 ± 0.83	1.21 ± 0.53	-0.71 ± 0.09	2.72	1.83	1.97	1.53	−3.92	−4.03
198	NGC 1365	177.35 ± 3.63	121.5 ± 2.95	-0.19 ± 0.00	66.03	374.52	2.62	28.89	−4.17	−3.12
199	NGC 3221	12.47 ± 1.08	4.53 ± 1.02	-0.47 ± 0.04	4.87	12.20	2.59	12.26	−4.26	−3.59
201	NGC 0838	30.31 ± 0.75	3.91 ± 0.39	-0.77 ± 0.02	14.91	6.50	5.50	2.70	−3.89	−4.20

Table A.2. X-ray spectral parameters for the sample.

No.	Galaxy	Γ_H (1)	N_H (2)	T_1 (3)	T_2 (4)	N_H (5)
45	UGC 08387	$2.4^{+0.6}_{-0.5}$		$0.35^{+0.29}_{-0.13}$	$0.72^{+0.21}_{-0.14}$	$1.09^{+0.21}_{-0.21}$
47	CGCG 436−030	$1.7^{+0.6}_{-0.6}$		$0.68^{+0.12}_{-0.07}$	$1.42^{+0.4}_{-0.33}$	$1.5^{+0.62}_{-0.42}$
49	NGC 0695	$0.4^{+0.4}_{-0.4}$		$0.36^{+0.10}_{-0.04}$	$1.06^{+0.16}_{-0.12}$	$1.25^{+0.2}_{-0.18}$
50	CGCG 043−099	2.0		$0.75^{+0.59}_{-0.53}$	$1.46^{+78.44}_{-0.99}$	$0.98^{+2.11}_{-0.98}$
51	MCG+07−23−019	$2.2^{+0.8}_{-0.7}$		$0.51^{+0.07}_{-0.04}$	$1.03^{+0.27}_{-0.15}$	$1.36^{+0.28}_{-0.23}$
52	NGC 6670 (E)	2.0		$0.46^{+0.11}_{-0.08}$	$0.90^{+0.16}_{-0.51}$	$1.82^{+0.42}_{-0.31}$
52	NGC 6670 (W)	$0.5^{+0.5}_{-0.6}$		$0.29^{+0.06}_{-0.06}$	$0.55^{+0.11}_{-0.15}$	$1.15^{+0.39}_{-0.26}$
53	UGC 02369 (S)	2.0		$0.54^{+0.15}_{-0.18}$	$1.12^{+0.33}_{-0.23}$	$0.78^{+0.45}_{-0.27}$
54	NGC 1614	$2.4^{+0.3}_{-0.2}$		$0.63^{+0.06}_{-0.05}$	$1.12^{+0.16}_{-0.08}$	$1.57^{+0.13}_{-0.18}$
56	NGC 5331 (N)	$2.1^{+0.7}_{-0.6}$		–[a]	–[a]	–[a]
56	NGC 5331 (S)	$2.2^{+0.8}_{-1.0}$		$0.33^{+0.07}_{-0.05}$	$1.37^{+78.53}_{-0.42}$	$1.18^{+0.57}_{-1.14}$
57	IRAS F06076−2139(N)	2.0		$0.27^{+0.39}_{-0.10}$	$0.90^{+0.84}_{-0.34}$	$0.84^{+0.64}_{-0.82}$
57	IRAS F06076−2139(S)	–[d]		–[d]	–[d]	–[d]
60	IC 2810(NW)	2.0		$0.44^{+0.07}_{-0.07}$	$1.14^{+0.27}_{-0.17}$	$0.93^{+0.19}_{-0.2}$
60	IC 2810 (SE)	2.0		$1.23^{+0.27}_{-0.27}$	–[b]	–[b]
63	IRAS 18090+0130 (E)	$2.7^{+1.0}_{-1.0}$		$0.70^{+0.36}_{-0.52}$	$4.18^{+14.52}_{-1.54}$	$0.39^{+0.56}_{-0.39}$
63	IRAS 18090+0130(W)	–[d]		–[d]	–[d]	–[d]
64	III Zw 035 (N)	2.0		$0.63^{+0.19}_{-0.32}$	$1.06^{+0.37}_{-0.29}$	$2.44^{+1.3}_{-0.77}$
65	NGC 3256	$2.6^{+0.2}_{-0.2}$		$0.40^{+0.02}_{-0.01}$	$0.84^{+0.026}_{-0.03}$	$1.04^{+0.03}_{-0.02}$
67	IRAS F16399−0937(N)	$1.6^{+1.2}_{-1.2}$		$0.33^{+0.77}_{-0.15}$	$0.97^{+0.20}_{-0.23}$	$1.44^{+3.64}_{-0.39}$
67	IRAS F16399−0937(S)	$1.8^{+0.3}_{-0.3}$		–[a]	–[a]	–[a]
68	IRAS F16164−0746	$2.8^{+1.4}_{-1.5}$		$0.71^{+0.40}_{-0.71}$	$0.90^{+0.24}_{-0.27}$	$1.68^{+0.73}_{-0.55}$
69	IC 4687	$3.4^{+0.5}_{-0.5}$		$0.96^{+0.11}_{-0.14}$	$5.84^{+23.86}_{-2.61}$	$0.17^{+0.11}_{-0.08}$
69	IC 4686	2.0		$0.49^{+0.15}_{-0.19}$	$1.11^{+0.66}_{-0.17}$	$1.58^{+0.38}_{-0.48}$
69	IC 4689	2.0		$0.34^{+0.12}_{-0.06}$	–[b]	–[b]
71	NGC 2623	$0.3^{+0.4}_{-0.4}$		$0.66^{+2.99}_{-0.28}$	$4.45^{+75.45}_{-2.22}$	$0.35^{+0.34}_{-0.23}$
72	IC 5298	1.8	$4.80^{+1.45}_{-1.34}$	$0.63^{+0.16}_{-0.49}$	$0.76^{+0.22}_{-0.15}$	$1.43^{+0.48}_{-0.39}$
73	IRAS 20351+2521	$2.3^{+1.7}_{-1.9}$		$0.60^{+0.08}_{-0.11}$	$1.37^{+0.91}_{-0.45}$	$1.03^{+0.51}_{-0.57}$
75	NGC 6090 (NE)	$2.4^{+0.7}_{-0.6}$		$0.66^{+0.07}_{-0.05}$	$1.20^{+0.21}_{-0.16}$	$1.18^{+0.28}_{-0.25}$
75	NGC6090 (SW)	2.0		$0.35^{+0.29}_{-0.09}$	$0.71^{+0.59}_{-0.39}$	$1.72^{+3.04}_{-0.41}$
79	NGC 5256 (NE)	1.8	$0.72^{+0.18}_{-0.17}$	$0.29^{+0.02}_{-0.02}$	$0.82^{+0.22}_{-0.08}$	$0.96^{+0.12}_{-0.11}$
79	NGC 5256 (SW)	$2.3^{+1.1}_{-0.9}$		$0.24^{+0.02}_{-0.05}$	$0.74^{+0.08}_{-0.08}$	$0.63^{+0.1}_{-0.1}$
80	IRAS F03359+1523(E)	2.0		$0.45^{+0.40}_{-0.16}$	$4.63^{+75.27}_{-3.69}$	$0.25^{+1.28}_{-0.25}$
81	ESO 550−IG025 (N)	2.0		$0.78^{+0.34}_{-0.27}$	$2.38^{+6.07}_{-0.95}$	$0.83^{+3.84}_{-0.83}$
81	ESO 550−IG025 (S)	$1.6^{+0.5}_{-0.5}$		–[a]	–[a]	–[a]
82	NGC 0034	1.8	$1.05^{+0.73}_{-0.71}$	$0.38^{+0.06}_{-0.05}$	$1.74^{+0.62}_{-0.34}$	$0.79^{+0.3}_{-0.32}$
83	MCG+12−02−001 (E)	$2.3^{+0.4}_{-0.4}$		$0.71^{+0.14}_{-0.12}$	$1.21^{+0.15}_{-0.22}$	$1.3^{+0.23}_{-0.18}$
83	MCG+12−02−001 (W)	$1.7^{+0.3}_{-0.3}$		–[a]	–[a]	–[a]
85	IRAS F17138−1017	$1.1^{+0.3}_{-0.3}$		$0.31^{+0.17}_{-0.07}$	$1.00^{+0.14}_{-0.13}$	$1.71^{+0.27}_{-0.24}$
95	ESO 440−IG058 (N)	–[c]		$3.91^{+8.85}_{-1.63}$	–[c]	–[c]
95	ESO 440−IG058 (S)	2.0		$0.25^{+0.08}_{-0.07}$	$0.77^{+0.14}_{-0.09}$	$0.81^{+0.17}_{-0.16}$
100	NGC 7130	1.8	$3.47^{+1.40}_{-1.84}$	$0.30^{+0.01}_{-0.01}$	$0.78^{+0.04}_{-0.03}$	$0.89^{+0.04}_{-0.05}$
104	NGC 7771	$1.6^{+0.3}_{-0.3}$		$0.52^{+0.08}_{-0.04}$	$1.04^{+0.16}_{-0.09}$	$1.7^{+0.21}_{-0.18}$
104	NGC 7770	2.0		$0.36^{+0.06}_{-0.04}$	$1.07^{+0.25}_{-0.24}$	$1.1^{+0.43}_{-0.32}$
105	NGC 7592 (E)	2.0		$0.31^{+0.04}_{-0.06}$	$0.72^{+0.14}_{-0.11}$	$1.22^{+0.3}_{-0.26}$
105	NGC 7592 (W)	$1.6^{+0.7}_{-0.8}$		$0.36^{+0.30}_{-0.12}$	$0.75^{+0.42}_{-0.27}$	$1.35^{+0.98}_{-0.54}$
106	NGC 6285	2.0		$2.96^{+3.74}_{-1.00}$	–[b]	–[b]
106	NGC 6286	2.0		$0.37^{+0.05}_{-0.08}$	$0.78^{+0.13}_{-0.16}$	$0.57^{+0.13}_{-0.13}$

Notes. Column (1): Spectral power-law slope in the 2−7 keV range. Column (2): Obscuring column density for galaxies with an absorbed AGN model fit in the 2−7 keV range, in units of 10^{23} cm^{-2}. Column (3): external *mekal* model temperature. Column (4): Internal, absorbed *mekal* model temperature. Column (5): Obscuring column density associated with the internal *mekal* model, in units of 10^{22} cm^{-2}. [a]Full spectrum fitted with a single power-law. [b]Soft band spectrum fitted with a single *mekal* component. [c]Full spectrum fitted with a single *mekal* component. [d]No fit. Values without errors are imposed, as described in Sect. 4.4.2. Errors reported correspond to 1σ for one parameter of interest, leaving 5 parameters free.

Table A.2. continued.

No.	Galaxy	Γ_H (1)	N_H (2)	T_1 (3)	T_2 (4)	N_H (5)
107	NGC 4922 (N)	1.8	$2.94^{+1.41}_{-1.15}$	$0.60^{+0.10}_{-0.35}$	$0.58^{+0.16}_{-0.08}$	$1.34^{+2.04}_{-0.35}$
110	NGC 3110	$1.7^{+0.5}_{-0.5}$		$0.34^{+0.06}_{-0.03}$	$0.89^{+0.09}_{-0.10}$	$0.95^{+0.17}_{-0.14}$
114	NGC 0232	$1.6^{+0.7}_{-0.6}$		$0.37^{+0.15}_{-0.08}$	$0.91^{+0.12}_{-0.11}$	$0.77^{+0.16}_{-0.18}$
117	MCG+08−18−013(E)	$1.8^{+0.8}_{-0.8}$		$0.43^{+2.16}_{-0.33}$	$2.93^{+8.25}_{-1.45}$	$0.63^{+0.84}_{-0.6}$
120	CGCG 049−057	$1.0^{+0.7}_{-0.6}$		$-^{(a)}$	$-^{(a)}$	$-^{(a)}$
121	NGC 1068	$2.0^{+0.1}_{-0.1}$		$0.23^{+0.00}_{-0.00}$	$0.66^{+0.01}_{-0.00}$	$0.77^{+0.01}_{-0.01}$
123	UGC 02238	$1.8^{+0.2}_{-0.2}$		$-^{(a)}$	$-^{(a)}$	$-^{(a)}$
127	MCG−03−34−064	1.8	$5.02^{+0.40}_{-0.39}$	$0.28^{+0.02}_{-0.02}$	$1.02^{+0.07}_{-0.06}$	$0.9^{+0.1}_{-0.09}$
134	ESO 350−IG038	$2.0^{+0.2}_{-0.2}$		$0.33^{+0.02}_{-0.01}$	$0.97^{+0.04}_{-0.05}$	$1.19^{+0.07}_{-0.07}$
136	MCG−01−60−022	1.8	$1.10^{+0.27}_{-0.25}$	$0.30^{+0.09}_{-0.07}$	$0.68^{+0.06}_{-0.10}$	$1.08^{+0.21}_{-0.18}$
141	IC 0564	$0.7^{+0.9}_{-0.8}$		$0.29^{+0.07}_{-0.06}$	$0.56^{+0.12}_{-0.08}$	$1.42^{+0.31}_{-0.32}$
141	IC 0563	$1.5^{+0.6}_{-0.6}$		$0.65^{+0.11}_{-0.07}$	$1.93^{+77.97}_{-0.74}$	$3.28^{+2.54}_{-2.73}$
142	NGC 5135	2.0		$0.25^{+0.02}_{-0.02}$	$0.68^{+0.09}_{-0.04}$	$0.73^{+0.06}_{-0.06}$
144	IC 0860	$-^{(d)}$		$-^{(d)}$	$-^{(d)}$	$-^{(d)}$
147	IC 5179	$1.6^{+0.5}_{-0.5}$		$0.67^{+0.06}_{-0.05}$	$4.28^{+2.38}_{-1.12}$	$0.01^{+0.04}_{-0.01}$
148	CGCG 465−012	$2.0^{+0.9}_{-1.1}$		$0.38^{+0.22}_{-0.12}$	$3.75^{+12.13}_{-2.15}$	$0.44^{+0.76}_{-0.37}$
157	MCG−02−33−098	2.0		$0.32^{+0.38}_{-0.08}$	$0.99^{+0.36}_{-0.22}$	$1.42^{+0.49}_{-0.35}$
157	MCG−02−33−099	2.0		$0.25^{+0.05}_{-0.04}$	$1.02^{+0.38}_{-0.17}$	$1.25^{+0.28}_{-0.31}$
163	NGC 4418	$1.9^{+0.5}_{-0.5}$		$-^{(a)}$	$-^{(a)}$	$-^{(a)}$
169	ESO 343−IG013 (N)	$0.9^{+0.4}_{-0.3}$		$-^{(a)}$	$-^{(a)}$	$-^{(a)}$
169	ESO 343−IG013 (S)	$2.2^{+0.5}_{-0.4}$		$-^{(a)}$	$-^{(a)}$	$-^{(a)}$
170	NGC 2146	$1.7^{+0.2}_{-0.2}$		$0.38^{+0.03}_{-0.02}$	$0.72^{+0.06}_{-0.05}$	$1.18^{+0.07}_{-0.07}$
174	NGC 5653	$1.4^{+0.8}_{-0.9}$		$0.32^{+0.03}_{-0.02}$	$0.80^{+0.15}_{-0.12}$	$0.96^{+0.18}_{-0.14}$
178	NGC 4194	$2.3^{+0.3}_{-0.3}$		$0.34^{+0.01}_{-0.01}$	$0.87^{+0.1}_{-0.04}$	$0.87^{+0.06}_{-0.06}$
179	NGC 7591	$-^{(d)}$		$-^{(d)}$	$-^{(d)}$	$-^{(d)}$
182	NGC 0023	$3.0^{+0.6}_{-0.7}$		$0.30^{+0.04}_{-0.07}$	$0.84^{+0.05}_{-0.07}$	$0.69^{+0.12}_{-0.06}$
188	NGC 7552	$2.4^{+0.4}_{-0.4}$		$0.49^{+0.04}_{-0.05}$	$0.87^{+0.1}_{-0.11}$	$1.23^{+0.15}_{-0.13}$
191	ESO 420−G013	$2.9^{+0.4}_{-0.3}$		$0.25^{+0.01}_{-0.02}$	$0.77^{+0.06}_{-0.09}$	$0.58^{+0.09}_{-0.09}$
194	ESO 432−IG006 (NE)	1.8	$4.32^{+1.96}_{-1.78}$	$0.65^{+0.10}_{-0.14}$	$0.73^{+0.89}_{-0.51}$	$1.99^{+6.05}_{-0.97}$
194	ESO 432−IG006 (SW)	1.8	$1.22^{+0.76}_{-0.81}$	$0.27^{+0.11}_{-0.07}$	$0.75^{+0.35}_{-0.15}$	$0.96^{+0.25}_{-0.2}$
195	NGC 1961	$1.0^{+0.4}_{-0.3}$		$0.64^{+0.04}_{-0.04}$	$4.70^{+5.6}_{-1.74}$	$0.23^{+0.25}_{-0.15}$
196	NGC 7753	$-^{(c)}$		$6.48^{+19.82}_{-2.70}$	$-^{(c)}$	$-^{(c)}$
196	NGC 7752	2.0		$0.49^{+0.12}_{-0.16}$	$0.70^{+0.28}_{-0.12}$	$1.46^{+0.49}_{-0.47}$
198	NGC 1365	1.8	$3.42^{+0.13}_{-0.13}$	$0.33^{+0.01}_{-0.01}$	$0.96^{+0.04}_{-0.05}$	$0.94^{+0.06}_{-0.06}$
199	NGC 3221	$0.3^{+0.6}_{-0.6}$		$0.43^{+0.16}_{-0.09}$	$0.70^{+0.15}_{-0.10}$	$1.44^{+0.3}_{-0.18}$
201	NGC 0838	$2.5^{+0.3}_{-0.3}$		$0.36^{+0.02}_{-0.03}$	$1.03^{+0.05}_{-0.06}$	$0.87^{+0.07}_{-0.07}$

[45] UGC 08387. This source meets our [Ne v] 14.32 μm line selection criterion, and is thus classified as an AGN, although there is no hint of its presence in the X-ray *Chandra* data. As described in Iwasawa et al. (2011), a soft X-ray nebulae extends perpendicular to the plane of the galaxy; this is most likely associated with a galactic-scale outflow.

Previous evidence of the AGN has come from detection of compact radio sources at mili-arcsecond resolution (e.g., Lonsdale et al. 1993; Parra et al. 2010), which Romero-Cañizales et al. (2012) attributed to various supernovae in coexistence with a low-luminosity AGN. Using VLBI data, Romero-Cañizales et al. (2017) provided evidence for a parsec-scale radio jet.

[47] CGCG 436−030. This galaxy shows three bright X-ray peaks in the soft band; only the central peak corresponds to a hard-band peak. The other two peaks, placed following the spiral arm structure in the optical images, most likely correspond to star-forming regions.

The DSS image faintly shows a bridge of material between the galaxy and a fainter galaxy ∼1′ to the east, with which it seem to be interacting (Mirabel & Sanders 1988; Zink et al. 2000). This other galaxy is not detected in the *Chandra* X-ray or the MIPS data, and is only visible in near-infrared observations such as the longest-wavelength IRAC channels. Therefore, we have not considered any contribution to the IRAS flux originating from this nearby companion.

[49] NGC 0695. This source has a rather flat spectrum in the 0.4−7 keV range. There is considerable extended emission in the soft band, and both bands present a very intense emission from the central region.

[51] MCG+07−23−019. This ring galaxy is composed of an elongated main body with double components separated by ∼5″(∼4 kpc) and an oval ring with a diameter of 16″ to the west of the main body (Hattori et al. 2004). As has been suggested by JHKL-band mapping, the nucleus of the galaxy lies between the two optical components and is heavily obscured in optical images (Joy & Harvey 1987). *Chandra* data show clear emission coming from the elongated disk of the galaxy. The X-ray emission is more intense in the center, and unobscured in the hard and soft bands. Extended soft X-ray emission around the nucleus partly follows the oval ring, most likely tracing star formation.

[52] NGC 6670. This closely interacting merger is composed of two sources, NGC 6670A (or East) and NGC 6670B (or West), separated ∼0.5′. Both galaxies contribute to the IRAS flux (Chu et al. 2017), with the western component being slightly brighter.

X-ray emission from the eastern component is mostly observed in the soft band and is concentrated around the nucleus. The western source, however, shows extended diffuse emission, particularly along the plane of the galaxy. The emission near the center is more intense in the hard and soft band at both sides of the nucleus. This morphology suggests high absorption in the innermost region. The spectrum is also suggestive of a hard excess, and a simple power-law fit results in a photon index of $\Gamma = 0.5 \pm 0.5$. Fitting an absorbed power-law of fixed photon index $\Gamma = 1.8$ results in a moderate absorbing column density of $N_{\rm H} \sim 4 \times 10^{22}$ cm^{-2}, and no significant improvement on the fit. The X-ray luminosity of the source is $L_X \sim 10^{41}$ cm^{-2}. The excess at ∼6.4 keV, if interpreted as a possible Fe Kα line, is not significant to the 1σ level.

XMM-Newton data for both sources, resolved, in this double system were analyzed by Mudd et al. (2014), with no hint of an AGN presence detected. However, their short exposure implied a detection of ∼100 cts per source, which lower than the counts detected in our *Chandra* data.

We consider that even though we cannot rule out the possibility of the western source containing an AGN, we have no strong evidence to claim its presence.

[53] UGC 02369. This double system, separated by ∼0.4′, is clearly dominated in X-rays by the southern component, which, as shown in Table 3, is also responsible for ∼98% of the IR emission. Because the contribution to the IRAS flux originating in the northern galaxy is negligible, we do not present any results for this component. An X-ray analysis would not be possible either, as only ∼5 cts are detected for this source.

The southern source is compact in X-rays, with emission coming both from the nucleus and from a star-forming region in the spiral arm, in the south in the soft and hard bands.

[54] NGC 1614. This source has been classified as a possible obscured AGN through X-ray spectroscopy (Risaliti et al. 2000), although VLBI studies with a sensitivity limit of 0.9 mJy do not detect a compact radio core in it (Hill et al. 2001). Recent studies in subarcsecond MIR observations do not completely rule out a possible (weak) AGN scenario, but they constrain the nuclear luminosity to <5% of the overall bolometric luminosity of the galaxy (Pereira-Santaella et al. 2015b). ALMA observations do not detect the nucleus in either the CO (6-5) line emission or in the 435 μm continuum, ruling out a Compton-thick AGN with relatively high confidence (Xu et al. 2015).

This source also does not meet any of our AGN selection criteria either, and we do not see any signs of AGN presence in the *Chandra* spectrum.

Emission in the hard and soft band is peaked in the nucleus, and the soft-band emission also shows elongated extension in the E–W direction, as opposed to the optical edge-on disk, which is elongated toward the N–S direction. Intense star formation, very compact in the nucleus, is the most likely origin of the X-ray emission.

[56] NGC 5331. Both galaxies in this system, separated by ∼0.4′, contribute to the IRAS flux, although the southern component is responsible for ∼80% of the emission, as shown in Table 3. However, since their X-ray luminosity is similar, the northern galaxy has a much higher logarithmic ratio (HX/IR) = −3.84 (as defined in Table A.1). This value is close to the expected ratio given the correlation derived by Ranalli et al. (2003), but higher than the characteristic X-ray faintness of the GOALS sample.

[57] IRAS F06076−2139. This closely interacting merger is clearly dominated by the northern source in IR and X-rays. However, with only ∼10 cts, the southern source meets our HR criterion for AGN selection (HR = -0.03 ± 0.17). The spectrum also shows an increase in flux toward higher energies, despite the significant error bars. Only the hardness ratio is computed as part of the analysis of this source, because of the low number of counts. For the same reason, a radial profile is not provided for this component.

The northern source comes close to meeting the same AGN selection criteria, with HR = -0.34 ± 0.08. The spectrum might indicate an excess in the hard band, although an absorbed power-law fit with a fixed photon index of 1.8 yields a column density of only $N_{\rm H} \sim 1.9 \times 10^{22}$ cm^{-2}. With a full-band X-ray luminosity of $L_{\rm X} \sim 10^{41}$ erg s^{-1}, and fitting statistics also favoring a non-absorbed power-law, we opt not to consider this source an AGN.

[60] IC 2810. Both galaxies in this system, separated by ∼1.1′, contribute to the IRAS flux as shown in Table 3, with the northwestern source contributing ∼70% of the IR luminosity.

[63] IRAS 18090+0130. Both galaxies in this system, separated by ∼1.3′, contribute to the IRAS flux, with the eastern component being responsible for ∼80% of the emission. The western

component has a low X-ray flux and not enough counts to provide reliable data for any analysis further than computing a hardness ratio.

[64] III Zw 035. This closely interacting double system is completely unresolved in the *Herschel* and MIPS images we used to derive the contribution of each galaxy into the IRAS source, as shown in Table 3. However, Chapman et al. (1990) reported that the majority of the radio continuum (and also probably FIR) emission originates in the northern galaxy. High angular resolution radio continuum observations from (Barcos-Muñoz et al. 2017) indicate that the northern component is the most compact source of the brightest and closest ULIRGs from the GOALS sample, while the authors did not detect the southern component at 33 GHz. The IRAC channel 1–4 images (at 3.6, 4.5, 5.8 and 8.0 μm) show that the northern source clearly dominates and the southern source fades with increasing wavelength. Thus, we assign a contribution to the IRAS flux of 100% to the northern source.

Because of the lack of IRAS flux originating in the southern component, we do not present results for its X-ray analysis in this work, and we did not consider it a source within our sample. The total X-ray counts for this galaxy are ∼25 cts in the full 0.5−7 keV range, which does not allow for a detailed X-ray analysis either, although a simple power-law fit gives an estimated $L_{\rm X} \sim 2 \times 10^{40}$ erg s^{-1}. However, while the soft-band X-ray flux is dominated by the northern source, the hard-band X-ray flux is very similar for both, and the southern source is optically classified as a Seyfert 2 (Yuan et al. 2010). It is then possible that the northern source is responsible for the high IRAS flux, most likely having a burst of star formation, while the NIR and MIR contribution from the southern source might be due to an AGN.

[65] NGC 3256. This source is assumed to be in an advanced merger stage, with a northern brighter component (the central peak) and a southern component at about ∼10″, elongated in the E−W direction. The possibility of this being a merging obscured companion galaxy was first suggested by Moorwood & Oliva (1994), and radio observations by Norris & Forbes (1995) supported this theory by detecting two equally bright knots. However, high-resolution MIR imaging shows that the northern peak is ∼20 times brighter than the southern region, suggesting that most of the star formation in the galaxy originates there (Lira et al. 2002). The authors also found the northern peak to be brighter in X-rays in *Chandra* data. The images shown in this work mark the two hard-band peaks reported by them, the southern clearly falling in an obscured region, with dimmer soft-band emission.

The very advanced merger stage of this source makes it hard to determine how much of the surrounding extended emission was initially associated with any of the cores. Therefore, we analyzed it as a single source in order to avoid introducing errors into the determination of its IR and X-ray emission.

[67] IRAS F16399−0937. This closely interacting pair is unresolved in *Herschel* and MIPS data, although Haan et al. (2011) derived that most of the MIR emission (>90%) comes from the northern source. We used this value to correct for the fraction contributed to the IRAS flux by each galaxy.

The northern source shows two intense hard X-ray peaks, both corresponding to soft X-ray emitting regions, the more southern of which is the nucleus. The other, as well as the less-intense knots seen in both sources, probably correspond to star-forming regions. The spectrum of this source shows an excess at >4 keV, with a few hard counts coming from the nuclear region. Fitting an absorbed power-law with a photon index of 1.8 yields an absorbing column density of $N_{\rm H} \sim 2 \times 10^{23}$ cm^{-2}, although an unabsorbed power-law of photon index ∼1.6 is an equally good fit. With a net count number of ∼23 cts, we cannot confidently classify this source as an AGN.

Sales et al. (2015) also considered the possibility that the northern source might contain an embedded AGN, fitting the 0.435−500 μm SED with a model that includes an AGN torus component. The fit suggests an AGN with bolometric luminosity $L_{\rm bol} \sim 10^{44}$ erg s^{-1}, although the spectrum is also consistent with shocks ($v \sim 100-200$ km s^{-1}). This bolometric luminosity would imply a fraction $L_{\rm X}^{\rm AGN} \sim 10^{42} - 10^{43}$ erg s^{-1}, much higher than the $L_{\rm X} = 10^{41}$ erg s^{-1} detected in the *Chandra* data.

The southern source does not have a clear center in X-rays or MIR and FIR, and so the center for the radial profile was determined using the brightest region in the optical HST image. Because the source is clearly elongated, annuli centered on the eastern edge will include photons from the northern source, and to avoid interference, we removed it from the computation of radial profiles. This component meets our HR AGN selection criterion, although the image in Appendix B shows that no strong hard X-ray peak comes from the nucleus of the source; the origin of the hard counts is concentrated in two point-sources west of the nucleus. Therefore, we did not classify this source as an AGN.

[68] IRAS F16164–0746. This source meets two of our AGN selection criteria, the HR and the [Ne v] line, and is also classified as an optical Seyfert 2 in Yuan et al. (2010). The X-ray source is elongated in the soft band, in the direction perpendicular to the disk of the galaxy, which could be interpreted as an outflow. There is also a secondary point source ∼3″ from the nucleus, in the soft and hard band, without any obvious overlap with a star-forming knot. With an associated X-ray luminosity in the 2−10 keV range of $\sim 3 \times 10^{40}$ erg s^{-1}, it could be classified as a ULX.

[69] IC 4686/7. This source is part of a triple merger system, formed by IC 4687 in the north, which closely interacts with the central galaxy, IC 4686, at ∼0.5′, and IC 4689 ∼1′ south of IC 4686 (West 1976). All three galaxies contribute more than 10% to the IRAS flux (Chu et al. 2017), and were therefore analyzed here.

[71] NGC 2623. With a spectrum that clearly raises toward higher energies, giving a hardness ratio of HR = −0.11 ± 0.02, and also meeting the [Ne v] line criterion, this source is classified as an AGN. This source has been classified as an AGN previously in radio (Lonsdale et al. 1993) and X-rays (Maiolino et al. 2003).

Optical HST images show extended tidal tails, approximately 20−25 kpc in length, with a southern region rich in bright star clusters (Evans et al. 2008), although no X-ray emission is detected with *Chandra* in the region.

[72] IC 5298. This source is a clear absorbed AGN. It is visible in the *Chandra* spectrum presented here, and through *XMM-Newton* data analysis. When a photon index of 1.8 is assumed, a column density of $N_{\rm H} \sim 4 \times 10^{23}$ is obtained when data from both telescopes are used. A faint line at 6.4 keV is visible in the *Chandra* data, with a significance lower than 1σ. The line can be confirmed with a significance of ∼2σ from *XMM-Newton* EPIC data, with a fit that is also consistent with the derived absorbing column density. The AGN diagnostics is also confirmed through the [Ne v] line and the optical S2 classification (Veilleux et al. 1995).

[73] IRAS 20351+2521. This galaxy shows strong central emission in X-rays, originating in the nucleus, with extended emission and point-sources along the spiral arms that trace star-forming knots.

[75] NGC 6090. This closely interacting system is completely unresolved in *Herschel* and MIPS data. Therefore, we resorted to

the analysis performed by Hattori et al. (2004) to derive the contribution of each component to the IRAS flux listed in Table 3.

The northeastern source shows hard-band diffuse emission corresponding to the optical central region of the galaxy, and a peak ∼3″ north of the center. It corresponds to a particularly bright region in the optical and IR in one of the spiral arms.

The sources interact so closely that the radial profiles interfere with each other past 4−5″ from each nucleus, and have therefore been limited to this radius.

[79] NGC 5256. This closely interacting system is surrounded by diffuse soft-band emission in X-rays, part of which extends toward the northern direction, following a blue tidal stream seen in optical images. Between the two sources, a slightly curved excess is visible, which can be interpreted as a shock between colliding winds from both galaxies (see Mazzarella et al. 2012). This excess is the reason that the radial profile in Appendix B for the NE source shows an increase in soft-band surface brightness with distance at 5−6″.

This source has been detected in the [Ne v] line at kiloparsec scales, meeting our AGN selection criteria. However, because the two nuclei are located ver close to each other, it is not possible to know which (or if both) is responsible for this emission. The two optical classifications we used (Veilleux et al. 1995; Yuan et al. 2010) mark the NE source as a Seyfert 2, and the SW source as LINER or composite. However, Mazzarella et al. (2012) reported the opposite optical classification for the sources: the NE source as LINER and the SW source as a Seyfert 2 galaxy.

Based on the X-ray spectra, the NE source can be best fit with an absorbed AGN model, fixing a spectral index of 1.8 and obtaining a column density of $N_{\rm H} \sim 8 \times 10^{22}{\rm cm}^{-2}$, which is interpreted as a mildly absorbed AGN.

The SW source shows an excess that can be fit as an iron 6.4 keV line with a confidence of ∼2.1σ, which meets one of our X-ray AGN selection criteria.

As reported by Mazzarella et al. (2012), *XMM-Newton* EPIC data only marginally resolve the two sources, and the spectrum is presented for the whole system. However, given the spectra resolved by *Chandra*, the iron line seen in the EPIC data most likely originates in the southwestern source. Their combined analysis also results in a Compton-thick classification of the south-western source.

[80] IRAS F03359+1523. Only one of the two sources in this system is observed in X-rays, the eastern source, with an elongated morphology that corresponds to the length of the edge-on disk in the optical data. The sources are unresolved in the *Herschel* data, and only one source is visible in the MIPS data, which is centered at the position of the eastern source. It is not possible to confirm whether this is due to lack of resolution, or if the western source does not contribute to the MIPS flux. However, from observing the IRAC images from channel 1 through 4 (at 3.6, 4.5, 5.8 and 8.0 μm), it is possible to see that the eastern source clearly dominates and the western source fades with increasing wavelength. Goldader et al. (1997) also described that only one source (believed to be the eastern source) is prominent at radio wavelengths. This, together with the complete lack of X-ray emission originating in this companion source, leads us to believe that the western galaxy does not contribute to the IRAS flux.

Another source, prominent in radio wavelengths, lies ∼1.5′ to the south of IRAS F03359+1523. Clemens et al. (2008) used NVSS radio data to extrapolate that this nearby galaxy could be responsible for about ∼50% of the IRAS flux. However, images at 8 and 24 microns show a weak source that fades completely at 70 micron, leading us to believe that its contribution to the FIR luminosity is most likely negligible.

[81] ESO 550–IG025. Both sources in this system, with a separation of ∼0.3′, contribute to the IRAS flux. The southern source has a rather flat spectrum, which is partly due to the contribution of the hard X-ray peak placed at about ∼4″ west of the nucleus. This source cannot be easily interpreted as the X-ray counterpart to any star-forming regions in the galaxy. If it is associated with this galaxy, its X-ray luminosity in the 2−10 keV range is of $\sim 3 \times 10^{40}$ erg s^{-1}, implying it could be classified as a ULX.

[82] NGC 0034. This source, optically classified as a Seyfert 2 (e.g., Veilleux et al. 1999; Yuan et al. 2010), has an X-ray spectrum that shows a hard band excess. Fitting an absorbed AGN with a fixed photon index of 1.8 gives an absorbing column density of $N_{\rm H} \sim 1 \times 10^{23}$ cm^{-2}. Previous analyses of *XMM-Newton* data confirmed an AGN, either through marginal detection of the Fe Kα line or by modeling an absorption or reflection component (e.g., Shu et al. 2007; Brightman & Nandra 2011).

Ricci et al. (2017) used joint data from *Chandra*, *XMM-Newton*, and *NuSTAR* and found a clear Fe Kα feature at $6.48^{+0.06}_{-0.05}$ keV. Their spectral analysis shows a heavily obscured AGN with a column density of $N_{\rm H} = 5.3 \pm 1.1 \times 10^{23}$ cm^{-2}. Their results certainly confirm the AGN, and their derived column density differs from the one derived with only *Chandra*, most likely because *Chandra* has much lower sensitivity at high energies.

[83] MCG+12−02−001. We consider this system to be composed of three individual sources: a northern component and a main pair, separated by ∼0.3′. The western source in the pair is considered an individual galaxy in close interaction with the eastern source, although it may also be an extended star-forming region. The X-ray peak at its center together with its X-ray luminosities of $L_{\rm SX} = 1.3 \times 10^{40}$ erg s^{-1} and $L_{\rm HX} = 2.4 \times 10^{40}$ erg s^{-1}, which are comparable to those of the eastern galaxy, mean that this whole system likely is a triple.

The northern source does not contribute to the IRAS flux (Díaz-Santos et al. 2010), as specified in Table 3, and therefore was not analyzed. It is detected with *Chandra*, with ∼9 cts in the full 0.5−7 keV range.

[85] IRAS F17138−1017. This source has a rather flat spectrum in X-rays, with a flux that slightly increases toward higher energies. It meets the HR criterion for AGN selection, although no [Ne v] line is observed. Fitting with an absorbed AGN model, fixing a spectral index of 1.8, a low column density of $N_{\rm H} \sim 2 \times 10^{22}{\rm cm}^{-2}$ is obtained.

Morphologically, *Chandra* data show a soft X-ray deficit at the optical center of the galaxy, that could be caused by absorption. The hard X-ray image does not show a clear emission peak, but a rather homogeneous flux around a larger circular region. X-ray contours in the HST image show very prominent dust lanes close to the nucleus of the galaxy, to which the obtained column density could belong. These dust lanes are most likely absorbing an important part of the soft-band X-ray emission, and might be responsible for the hardness of the spectrum. Based on this and the clear lack of observation of a hard-band peak in the nucleus, we opt not to classify this source as an AGN.

Ricci et al. (2017) fit a combined *Chandra* and *NuSTAR* spectrum with a simple power-law model, obtaining a photon index of ∼1.1, which is harder than the typical X-ray emission expected of a star-forming region, but still consistent with this hypothesis.

The hard-band X-ray luminosity of $L_{\rm HX} \sim 1.8 \times 10^{41}$ erg s^{-1} we derive is high, but not incompatible with being caused by a

strong starburst, as this source falls within the uncertainties of the correlation derived by Ranalli et al. (2003).

[95] ESO 440−IG058. Both galaxies, with an angular separation of ∼2′, contribute to the IRAS flux in this source, although the southern component dominates at almost ∼90% (Díaz-Santos et al. 2010). Soft X-ray emission from the southern component is extended. This is most likely an outflow with its origin in a starburst wind.

[100] NGC 7130. This galaxy shows clear extended emission in soft X-rays around a strong peak that follows the disk of the face-on optical galaxy, tracing the spiral arms. The spectrum shows a hard excess due to absorption and an iron 6.4 keV line at high energies, which could be due to absorption in the soft band, or due to reflection. A reflection component fitting, using a *pexrav* model (Magdziarz & Zdziarski 1995) results in an iron line with an equivalent width of ∼0.6 keV, which is too low for a reflection-originated line. Therefore, our data favor an absorption model, which, when a photon index of 1.8 is imposed, results in a column density of $N_{\rm H} = 3 \times 10^{23}$ cm^{-2} and an iron line equivalent width of 0.8 keV, that is detected with a significance of ∼2.5σ.

Based only on the *Chandra* data, we find it difficult to distinguish between this scenario and a Compton-thick source with an imposed photon index of $\Gamma = 0.0$, as modeled by Levenson et al. (2005). Ricci et al. (2017) confirmed the Compton-thick AGN using a combined analysis with *NuSTAR* data.

[104] NGC 7771. This galaxy is part of an interacting quartet of galaxies, along with close companion NGC 7770 at an angular distance of ∼1.1′, NGC 7771A at ∼2.8′, and NGC 7769 at ∼5.4′ (e.g., Yeghiazaryan et al. 2016).

About 90% of the IRAS flux originates in NGC 7771, with NGC 7770 being responsible for the remaining ∼10% and NGC 7769 being resolved as a separate source by IRAS. NGC 7771A is faint in the IR, remaining undetected at 8 μm and above. There is no detection for this small component in the *Chandra* data either.

Of the many point sources seen along the disk of NGC 7771, Luangtip et al. (2015) classify 4^{+4}_{-0} as ULXs.

[105] NGC 7592. This source is a closely interacting triple system, formed by two main IR and X-ray sources (East and West) and a smaller southern source. This third source, seen in the optical SDSS images, is undetected in X-rays, and does not contribute to the IRAS flux either.

There is unresolved detection of the [Ne v] line for this triple source that meets our AGN selection criterion. However, as the western source is classified as an optical Seyfert 2, it is likely that it is the origin of the IR line. The spectrum of the western source shows an excess between 6−7 keV, originating in the nucleus, that can be fitted as a Gaussian line with an energy of $6.7^{0.1}_{-0.3}$ keV. The significance of this line is at the 1σ level, and thus we did not use this hint as a selection criterion. Given the uncertainties, however, a 6.4 keV line cannot be ruled out completely, especially when combined with the continuum.

The western source presents very compact X-ray emission, as derived from its radial profile, compared to its extended IR emission (as plotted in Fig. 12).

[106] NGC 6286. This source interacts with NGC 6285, ∼1.5′ to the northwest, showing very extended tidal disruption features. Both sources contribute to the IRAS flux (Chu et al. 2017).

The X-ray spectrum of NGC 6286 shows hard excess emission above 5 keV. With fewer than 20 cts in the 5−8 keV range, the excess is difficult to fit as an absorbed AGN using only *Chandra* data. MIR studies find possible hints of an AGN (e.g., Vega et al. 2008; Dudik et al. 2009), which are confirmed by hard X-ray *NuSTAR* observations. Ricci et al. (2016) found compelling evidence of a Compton-thick, low-luminosity AGN ($N_{\rm H} \simeq (0.95-1.32) \times 10^{24}$ cm^{-2}). We thus classify this source as an AGN.

This galaxy shows a very extended soft X-ray emission, spreading perpendicular to the optical edge-on disk up to a distance of ∼5−7 kpc, depending on the direction. A super-wind outflow generated by a strong starburst has been suggested by Shalyapina et al. (2004) through detection of an increase of $[NII]\lambda6583/H_\alpha$ ratios, and an emission nebula extending up to ∼9 kpc from the galactic plane.

[107] NGC 4922. This system contains two galaxies, separated by distance of ∼0.4′; the northern source is brighter in both X-rays and IR (Díaz-Santos et al. 2010). The southern source contributes ∼1% of the IRAS flux, and therefore its analysis is not included in this work. With only ∼40 cts, all in the 0.4−2 keV range, it is also a weak X-ray source. Another source (2MASX J13012200+2920231) lies ∼1.7′ to the north, which is undetected at 8 μm and above, and most likely does not contribute to the IRAS flux.

The northern source is selected as an AGN through the [Ne v] line, and the pair (unresolved) is also classified as a Seyfert 2 in Yuan et al. (2010). Our X-ray analysis also classifies it as an absorbed AGN, with a column density of $N_{\rm H} \sim 3 \times 10^{23}$ cm^{-2} when the photon index is fixed to 1.8. An iron 6.4 keV line is faintly visible, although only at a significance of about 1σ.

Ricci et al. (2017) analyzed *NuSTAR* observations and based on their similar *Chandra* results concluded that the source detected at high energies must correspond to NGC 4922 (N), because the companion is not detected in the 2−7 keV range. They detected a prominent Fe Kα line at $6.48^{+0.07}_{-0.07}$ keV, and found that the source is Compton-thick, with $N_{\rm H} \geq 4.27 \times 10^{24}$ cm^{-2}; this is more than one order of magnitude higher than our best *Chandra* fit.

[110] NGC 3110. This source interacts with nearby galaxy MCG−01−26−013 at its southwest, separated by ∼1.8′, which is not detected in X-rays in the *Chandra* data. Both sources contribute to the IRAS flux, although ∼90% of the IR emission has its origin in NGC 3110 (Díaz-Santos et al. 2010). The companion galaxy is not analyzed because it has no significant X-ray emission and low IR luminosity, although the IRAS flux associated with NGC 3110 is corrected for the pair's contribution.

This source has diffuse soft X-ray emission along the spiral arms, which also contain strong hard X-ray peaks that are most likely associated with star-forming knots. The nucleus of the galaxy, however, does not show peaked emission in the 2−7 keV band. Because of this particular morphology, HST optical and IRAC channel 1 images were used to center the derived radial profiles.

[114] NGC 0232. This source is paired with NGC 0235, at a distance of ∼2′, which is a known Seyfert 2 galaxy. Despite having previously been classified as non-interacting, a faint tidal bridge has been observed to connect the two galaxies (Dopita et al. 2002). NGC 0235 has two nuclei and is classified as a minor interaction (Larson et al. 2016). However, as this companion galaxy is resolved by IRAS (Surace et al. 2004) as an individual source, we did not include it in our analysis.

[117] MCG+08−18−013. This galaxy is paired with MCG+08−18−012 at ∼1′ to its west. MCG+08−18−013 is clearly dominant in the IR and the origin of the IRAS flux (Chu et al. 2017). This component's X-ray emission originates from two point sources close to the nucleus of the galaxy, one of which is bright in soft-band X-rays, and could be associated with a star-forming region, and the other in hard-band X-rays. We consider this hard-band peak to originate from the nucleus of the galaxy, and used it to center the radial profiles.

MCG+08−18−013 is undetected in X-rays and therefore not included in the analysis.

[120] CGCG 049−057. This source, despite only having a total of ∼30 cts in the 0.5−7 keV band of the available *Chandra* observation, has a hardness ratio of HR = −0.04 ± 0.09, and so meets one of the X-ray AGN selection criteria. The spectrum of the source shows, despite the large error bars, a tendency to rising flux toward higher energies. The X-ray image in the 2−7 keV band shows about ∼5 cts originating from the innermost region of the source, and thus we classified it as an AGN.

Baan & Klöckner (2006) also classified it as an AGN based on radio observations. Although optical and MIR observations (e.g., Veilleux et al. 1995; Stierwalt et al. 2013; Meléndez et al. 2014) classified it as a starburst, *Herschel* spectroscopic data analyzed by Falstad et al. (2015) showed very high column densities in the nucleus ($N_{\rm H}$ = 0.3−1.0 × 10^{25} cm^{-2}), meaning that a Compton-thick AGN could be present. This would explain the X-ray weakness we observe, which has previously been reported by Lehmer et al. (2010).

[121] NGC 1068. This well-known AGN meets our selection criteria in all bands: Seyfert 2 in both of the used optical classifications, presence of the [Ne v] line in IR, and clear detection of the Fe Kα line at 6.4 keV in X-rays with a significance of ∼3.6σ. The equivalent width of the 6.2 μm PAH feature is not presented in Stierwalt et al. (2013) because the spectrograph was saturated. Howell et al. (2007) analyzed PAH and warm dust emission in NGC 1068 in detail. Their 6.2 μm images are saturated within the inner r ∼ 500 pc, although they measure an equivalent width of the PAH feature immediately outside the region of saturation of ∼0.1. This suggests that the value of the equivalent width might drop below 0.1 farther in.

Diffuse X-ray emission is clearly observed in this source, following the optical spiral arms and star-forming regions. In order to outline all features, X-ray contours to a low enough level were necessary, which also resulted in the clear contours around the saturated feature that diagonally crosses the image.

Individual point sources can be seen spread throughout the galaxy disk in the soft and hard bands; they most likely correspond to X-ray binaries. We note that we did not mark them as hard X-ray peaks in the image in Appendix B because they are numerous and clearly do not originate from a region near the nucleus of the galaxy. None of these point sources were removed in order to derive radial profiles. Luangtip et al. (2015) classified three of them as ULXs.

[123] UGC 02238. This source presents a rather diffuse emission, showing three main X-ray peaks near the nucleus, only one of which (the westernmost) is also peaked in the 2−7 keV band. However, as shown by the contours over the IRAC channel 1 image, this region is outside of the galaxy nucleus. We consider this emission to most likely originate from different intense starburst regions because no clear hard-band central peak is visible. Optical and IR imaging data show a highly disturbed disk and tidal tails, and classify this galaxy as a post-merger stage (e.g., Smith et al. 1996; Larson et al. 2016), which is consistent with the described X-ray morphology.

We fit the overall X-ray 0.5−7 keV emission of this galaxy with a single power-law. Attempts to fit a one or two component *mekal* model produced unsatisfactory results. Two strong point sources can be seen in the 2−7 keV band image presented in Appendix B, which, if associated with the galaxy, would be classified as ULXs. The point-source at the easternmost edge of the disk of the galaxy would have an estimated luminosity of ∼4 × 10^{40} erg s^{-1}, and the strong point-source immediately south of the nucleus of the galaxy would be emitting ∼1 × 10^{40} erg s^{-1} in the 2−10 keV range. However, the very low number of counts means that these are very rough estimates.

[127] MCG-03-34-064. This source has a northeastern companion at ∼1.8′, MCG−03−34−063, which is responsible for about ∼25% of the IRAS flux (Chu et al. 2017). The analysis of this companion source is not included in this work because it is undetected in the *Chandra* data. A correction to the IR luminosity for the contribution of MCG−02−34−063 has been considered for this source.

MCG-03-34-064 presents a very peaked central emission in all X-ray bands and is a clear absorbed AGN, as seen from the spectrum. Fitting with a fixed photon index of 1.8 yields an absorbing column density of $N_{\rm H}$ ∼ 5 × 10^{23} cm^{-2}. The iron Kα line at 6.4 keV is detected, with a ∼3σ significance. With an HR = −0.32 ± 0.01 our other X-ray AGN selection criterion is almost also met.

Ricci et al. (2017) performed a *NuSTAR* analysis of this source, combined with *XMM-Newton* EPIC data, and derived an absorbing column density of $N_{\rm H}$ = $5.42^{+0.07}_{-0.09}$ × 10^{23} cm^{-2}, which is compatible with our derived result within the errors. They also detected the Fe K$_\alpha$ line and a Gaussian line at $6.62^{+0.01}_{-0.01}$ keV with EW ∼ 0.2 keV, that is not detected in the *Chandra* data.

This source also meets the [Ne v] line and 6.2 μm PAH feature AGN selection criteria. Yuan et al. (2010) classified it as a star-forming galaxy, although other works classified it as a Seyfert galaxy (e.g. Lipovetsky et al. 1988; Corbett et al. 2002).

[134] ESO 350−IG038. This galaxy presents three main star-forming condensations (Kunth et al. 2003; Atek et al. 2008). Only two of these knots, the eastern and western, are clearly resolved as X-ray sources in the *Chandra* data, both presenting peaked emission in the soft and hard bands. The region is surrounded by diffuse, soft X-ray emission. These knots, separated by ∼4″, are analyzed together as the X-ray source corresponding to the IRAS source, and not separated as two individual galaxies, as there is no clear evidence of them being individual galaxy nuclei in a state of a closely interacting merger.

[136] MCG−01−60−022. This source is near galaxies MCG−01−60−021 and Mrk 0399, at ∼4.4′ interacting with the former (e.g., Dopita et al. 2002), connected through thin and long tidal bridges. The two nearby galaxies are undetected in the *Chandra* data, and are detected together as another IRAS source, resolved from MCG−01−60−022 (Díaz-Santos et al. 2010).

This source presents diffuse soft-band emission that surrounds the central X-ray peak, which has its origin in an absorbed AGN. This sources meets the HR X-ray criterion, and spectral fitting of an absorbed power-law with a fixed photon index of 1.8 yields a an absorbing column density of $N_{\rm H}$ ∼ 1 × 10^{23} cm^{-2}.

[141] IC 0563/4. This source is a double system, composed of IC 0564 in the north and IC 0563 in the south, separated by ∼1.6′. Both contribute similarly to the IRAS flux and to the overall X-ray luminosity. Morphologically, the two galaxies have faint emission that originates in the nucleus and various point-sources spread throughout the spiral disks.

IC 0563 has a hardness ratio of −0.34 ± 0.05, which exceeds our AGN selection threshold. However, the origin of the hardness (also seen as an excess at 3−5 keV in the spectrum shown in Fig. C.1) is not the nucleus of the galaxy, but a point-source located north of it. If the source is associated with the galaxy, with a roughly estimated luminosity of ∼3 × 10^{40} erg s^{-1}, it could be classified as a ULX. Interestingly, the point-source spectrum shows a faint line at ∼1.50 ± 0.03 keV, with a significance of ∼2σ. If this source is a ULX within the galaxy, this excess cannot be easily explained as an emission line. If this source is a background quasar for which we detect a redshifted 6.4 keV iron line, a high z ∼ 3.3 would be necessary. If it were an object at z = 3.3, the X-ray spectrum would suggest that its origin is in

reflected light form a Compton-thick AGN. This scenario, however, leads to an unreasonably luminous quasar.

Similarly, IC 0564 shows a spectrum with a high flux at high energies, although the error bars are significant, which is also emitted by a northern point-source. With a roughly estimated luminosity of $\sim 3 \times 10^{40}$ erg s^{-1}, it might also be classified as a ULX if it is associated with the galaxy.

Both point-sources are marked with green crosses in the images shown in Appendix B.

[142] NGC 5135. This galaxy is classified as an optical Seyfert 2 (e.g. Yuan et al. 2010), and meets our IR [Ne v] line criterion for AGN selection (Petric et al. 2011).

It shows an excess in hard X-rays, with a Fe K_α line at 6.4 keV with a $\sim 2.9\sigma$ significance, which could be the result of either absorption or a reflection component. Fitting an absorbed power-law with fixed photon index of 1.8 yields an absorbing column density of $N_{\rm H} \sim 4 \times 10^{23}$ cm^{-2}, which is not large enough to produce the equivalent width of the iron line of $EW \sim 0.9$ keV obtained through the same model. Fitting a *pexrav* model (Magdziarz & Zdziarski 1995) with a fixed photon index of 2.0 yields a plausible $EW \sim 1.1$ keV, which means that our data favor a reflection-dominated AGN. *Suzaku* observations extending up to 50 keV allow a better estimate of the absorbing column density, $\sim 2.5 \times 10^{24}$ cm^{-2}, classifying this source as Compton-thick and providing a good estimate of the strength of the reflection component (Singh et al. 2012).

Morphologically, this source presents a very extended soft-band emission, with two central X-ray peaks that are visible only when the smoothing in the image is set to 0.5″ or less. The northern peak is responsible for the iron emission line, which indicates that it is associated with the nucleus of the galaxy. The southern peak is brighter in the 0.5−2 keV band, and most likely associated with a star-formation region. Of the many point-sources seen in the full band image, up to 6^{+1}_{-2} are classified as ULXs (Luangtip et al. 2015).

[144] IC 0860. With only ∼25 cts, no X-ray analysis beyond the calculation of the HR and the extraction of the radial profile has been performed for this source. However, despite the low count-rate, this galaxy is classified as an AGN with a value of HR = −0.29 ± 0.17. The spectrum we obtained also shows a rising tendency toward higher energies. However, because of the small number of counts detected, the classification of this X-ray source remains ambiguous.

[147] IC 5179. This galaxy shows dim soft-band extended emission near the nucleus and many X-ray point-sources spread throughout the optical disk, which most likely correspond to X-ray binaries, 8^{+0}_{-3} of which are classified as ULXs (Luangtip et al. 2015). These sources cause the radial profile to seem rather irregular, especially in hard band (see Appendix B).

[148] CGCG 465−012. This galaxy is paired with UGC 02894 at its northwest, at a distance of ∼4.2′, which is resolved as a separate source by IRAS.

CGCG 465−012 shows diffuse soft X-ray emission throughout its optical disk, concentrated in the nucleus and in a northeastern region ∼5″ from it, most likely a star-forming region. The hard-band emission is very dim and not peaked.

[157] MCG−02−33−098/9. This system is composed of two very closely interacting galaxies (separated by ∼14″), with the western one contributing ∼70% of the IRAS flux (Díaz-Santos et al. 2010). Two nearby galaxies, at ∼0.7′ northwest and ∼2′ southeast, most likely do not contribute to the IRAS flux, as they are not detected in MIR wavelengths.

Terashima et al. (2015), using *XMM-Newton EPIC-PN* data, reported the detection of a faint iron line at 6.97 keV. The *Chandra* spectrum of MCG−02−33−098 shows a slight increase at ∼7 keV, which is not significant enough to claim the presence of an excess.

[163] NGC 4418. This galaxy is paired with MCG+00−32−013 at its southeast, at a distance of ∼3′. Using IR photometry, it can be determined that more than 99% of the IRAS flux originates in NGC 4418 (Chu et al. 2017), therefore this nearby galaxy was not considered in the analysis. It also meets our PAH EW selection criteria (Stierwalt et al. 2013), and thus we classified it as AGN, despite the current debate regarding its nature.

Only two central peaks can be seen in the *Chandra* data; the eastern peak is brighter in the hard band, and thus was used to center the radial profiles. However, this source is known as a possible candidate for containing a heavily obscured AGN, and it is possible that we resolved the non-absorbed emission at either side of the nucleus. While some studies in radio and IR seemed to favor a compact starburst as a central source (e.g., Roussel et al. 2003; Lahuis et al. 2007), it is at least clear that the nucleus is extremely Compton-thick and could host either an AGN or a starburst of obscuration as extreme as the one in Arp 220 (see Costagliola et al. 2013, 2015, and references therein).

[169] ESO 343−IG013. Both galaxies in this closely interacting merger, separated by only ∼0.2′, contribute to the IRAS flux, with the northern component dominant in both IR (Díaz-Santos et al. 2010) and X-rays.

The X-ray emission is diffuse in the southern source and between sources. The northern source shows a bright X-ray peak in the soft and hard bands, which meets one of our AGN selection criteria, having HR = 0.01 ± 0.05. The X-ray spectrum of this component also shows an increase in flux toward higher energies.

The radial profile of the southern source has been centered using the brightest peak in optical and IR images, which corresponds to the dimmer X-ray peak of the 0.5−7 keV image shown in Appendix B. The northern source presents very compact X-ray emission, as derived from its radial profile, compared to its extended IR emission (as plotted in Fig. 12).

[170] NGC 2146. This galaxy, most likely a post-merger object (Hutchings et al. 1990), shows very extended soft-band X-ray emission in the direction perpendicular to the plane of the optical disk, originating in a super-wind driven by the central starburst (see Kreckel et al. 2014). The hard-band emission is limited to the region encompassed by the galaxy disk, which presents a lack of soft-band emission. This lack is most likely a result of absorption in the plane of the galaxy. The radial profiles have been centered using the brightest peak in the NIR IRAC channel 1 image.

A detailed *Chandra* analysis of point sources in the galaxy, including seven ULXs, and the extended emission, can be found in Inui et al. (2005).

[174] NGC 5653. This source presents a diffuse X-ray emission along the spiral arms seen in the optical images, with a bright X-ray knot at a distance of ∼15″ from the nucleus. This knot falls on one of the spiral arms and appears very blue in optical images; it also is the strongest X-ray and IR source in the galaxy (Díaz-Santos et al. 2010). It could be argued that this source is a second galaxy, that merges with the larger NGC 5653. This source has been classified as a lopsided galaxy (Rudnick et al. 2000), which is usually assumed to be an indicator of weak tidal interaction. However, as we have no clear evidence of this and do not see a central point-source in hard X-rays, we opt to consider it a particularly active star-forming region. Luangtip et al. (2015) found 1 ± 1 ULXs in this source.

The NIR IRAC channel 1 image was used to centre the radial profile, due to the difficulty of finding a clear nucleus in the X-ray data.

[178] NGC 4194. This source, commonly known as the Medusa, is the result of a merger with very particular tidal features, as seen in optical images. The X-ray morphology of the source is also particular, showing a very extended emission in soft X-rays, especially toward the northwest, most likely indicative of a strong starburst-driven wind. Luangtip et al. (2015) find 1 ± 1 ULXs in this source, while a detailed study of all X-ray point sources was performed by Kaaret & Alonso-Herrero (2008).
[179] NGC 7591. This galaxy interacts with PGC 214933, at ∼1.8′ southwest; and a dimmer galaxy lying ∼3.6′ to the east is detected in HI (Kuo et al. 2008). PGC 214933 contributes ∼6% of the IRAS flux (Chu et al. 2017), and is undetected in the *Chandra* data.

With only ∼26 cts in the 0.5−7 keV band, no X-ray analysis beyond the calculation of the HR and the extraction of the radial profile has been performed for NGC 7591.

NGC 7591 is the only source in our sample that is optically classified as a Seyfert 2 galaxy (Yuan et al. 2010), while being classified as a LINER by Veilleux et al. (1999), and does not meet any of our AGN selection criteria. The contribution of an AGN component to the bolometric luminosity of the galaxy, as estimated by (Díaz-Santos et al. 2017), is low: $\mathrm{AGN_{bol}} = 0.09 \pm 0.02$. With a flux estimation using the CIAO tool *srcflux*, the obtained luminosity of this source in the 0.5−7 keV band is $L_X = 2.5^{+1.8}_{-1.3} \times 10^{40}$ erg s^{-1}. This X-ray luminosity is low for an AGN, and only possible for this type of source if is Compton-thick. Even though we cannot rule out this possibility, we consider that a single optical classification as Seyfert 2 is not a strong enough criterion to classify this source as an AGN.
[182] NGC 0023. This source is paired with NGC 0026, at a distance of ∼9.2′ (Hattori et al. 2004), which is far enough to guarantee no contribution to the IRAS flux.

This source shows central extended emission surrounding the nucleus, which is not a strongly peaked hard X-ray source. The source spectrum shows a lack of emission at >3 keV and a small excess at higher energies, which is not significant enough indicate an AGN. Luangtip et al. (2015) classified 2 ± 2 of the galaxy's point sources as ULXs.
[188] NGC 7552. This source shows extended soft-band X-ray emission in the inner region of the galaxy, surrounded by numerous point-sources, which most likely correspond to X-ray binaries. Of these, 2^{+3}_{-1} are classified as ULXs (Luangtip et al. 2015).
[191] ESO 420-G013. This source meets our IR [Ne v] line criterion for AGN selection, and shows a slight excess at around 6.4 keV, which is not significant enough in the *Chandra* data to confirm the presence of an X-ray AGN. Although Yuan et al. (2010) classified is as HII dominated, other optical classifications have previously pointed toward a Seyfert nature (e.g., Maia et al. 1996)
[194] ESO 432-IG006. The two galaxies in this system, separated by ∼0.5′, contribute similarly to the IRAS flux, and have significant X-ray emission. They also present signs of an absorbed AGN. Fitting such a model, with a fixed photon index of 1.8, on the northeastern source yields an absorbing column density of $N_\mathrm{H} \sim 4 \times 10^{23}$ cm^{-2}; and on the south-western source it yields $N_\mathrm{H} \sim 1 \times 10^{23}$ cm^{-2}.
[195] NGC 1961. Most of the X-ray emission of this source is concentrated on the nucleus, with a few point sources spread throughout the spiral arms. Another emission peak is found in a region about ∼20″ west of the nucleus. It is unclear whether this source truly overlaps with emission regions in IR images (IRAC channels 1−4, MIPS24/70), or has no counterpart.

The spectrum presented in Fig. C.1 includes the full region, and the hard X-ray excess originates in this outer source. Therefore, we see no spectral traces of the presence of an AGN.
[196] NGC 7752/3. This double system is composed of NGC 7752 to the southwest and NGC 7753 ∼2′ to the northeast, the latter being the dominant source in the IRAS flux (Chu et al. 2017).

X-ray emission in the northeastern source is point-like in the nucleus, with a few other point sources spread throughout the galaxy spiral arms. The X-ray best spectral fit for this source was performed using a single *mekal* component for the full spectrum, but no fit is truly satisfactory.

The southwestern source presents much more diffuse emission, with no clear central point source. The most concentrated emission in the soft band comes from a region just west of the IR nucleus of the galaxy, which is the one we used to center the radial profile. This region seems to correspond to a slight increase in IR emission in the IRAC channel 1 image, which means that it is most likely a star-forming region. (Kewley et al. 2001, 2006) used optical diagnostic diagrams to classify this source either as an AGN or the composite of AGN and starburst (Zhou et al. 2014; Pereira-Santaella et al. 2015a), although we see no X-ray signs of activity.
[198] NGC 1365. This very bright source meets all three of our X-ray AGN selection criteria, with $\mathrm{HR} = -0.19 \pm 0.00$, an absorbing column density of $N_\mathrm{H} \sim 3 \times 10^{23}$ cm^{-2} when fitting an absorbed AGN model with fixed photon index of 1.8, and a 6.4 keV iron K_α line at a significance of $\sim 2.9\sigma$. This galaxy hosts a very well-known AGN, with frequent dramatic spectral variability (e.g., Risaliti et al. 2005, 2007) that is attributable to variations in the column density along the line of sight.

The *Chandra* data show bright and extended diffuse emission in soft band, spreading along the central region of the galaxy, and a strong central point source (see, e.g., Wang et al. 2009). Luangtip et al. (2015) found 6^{+2}_{-1} ULXs in this galaxy. We have chosen to show only the central emission in the galaxy in Appendix B and not the open spiral arms around it, in order to better distinguish the X-ray morphology of the region of interest.
[199] NGC 3221. This source consists mostly of point-like sources scattered along the optical edge-on disk of the galaxy, 6^{+0}_{-1} of which are classified as ULXs (Luangtip et al. 2015). The hard-band spectrum can be fit with a power law of index $\Gamma = 0.3 \pm 0.6$, with the nucleus being a stronger hard X-ray source than the other point sources. Even though such a flat spectrum could be indicative of an obscured AGN, fitting an absorbed power-law with a fixed photon index of 1.8 yields an absorbing column density of only $N_\mathrm{H} \sim 5 \times 10^{22}$ cm^{-2}. We conclude that we cannot confirm the presence of an absorbed AGN, even though we cannot rule out the possibility either.
[201] NGC 0838. This galaxy is in a complex system. NGC 0839 is placed ∼2.4′ to the south–east, and the center of the closely interacting system formed by NGC 0833 and NGC 0835 is found at ∼4′ to its west. IRAS resolves three of these four sources; NGC 0833/0835 interact too closely to derive their fluxes separately. However, because NGC 0838 is resolved, we did not include the rest of the components of the complex system in this work.

Oda et al. (2018) analyzed 3−50 keV *NuSTAR* data of this compact group. NGC 0838 is not detected above 8 keV, showing no evidence of an obscured AGN. The conclusion that NGC 0838 is a starburst-dominated galaxy is also reached in the detailed works by O'Sullivan et al. (2014), Turner et al. (2001).

This source is very bright in X-rays and has a complex morphology of diffuse soft-band emission surrounding the nucleus, a clear example of a strong starburst wind. Of the point sources, 2^{+1}_{-0} are classified as ULXs (Luangtip et al. 2015).

Appendix B: Observations

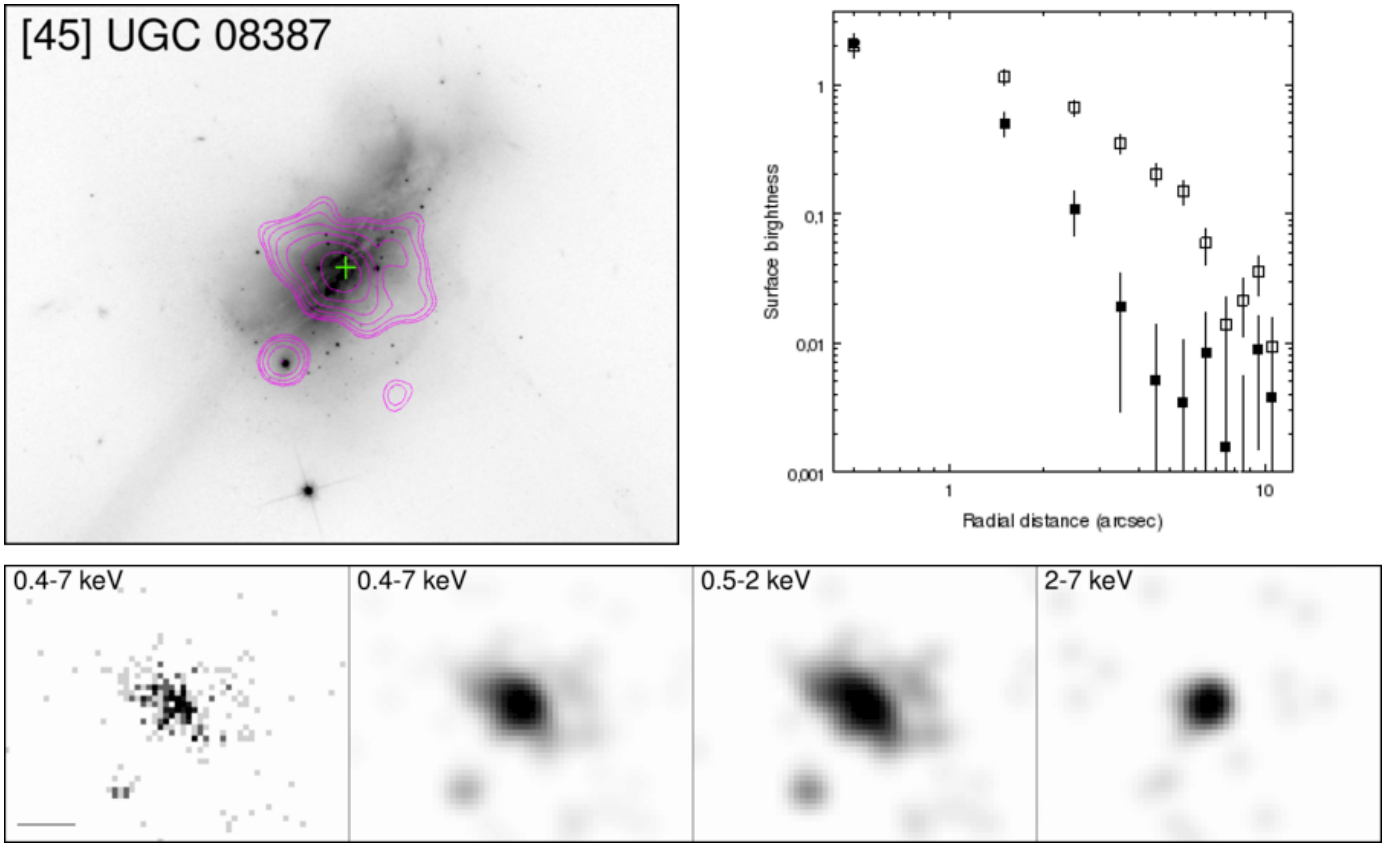

Fig. B.1. *Overlay on* HST-ACS F814W. *Contours:* Interval 1.

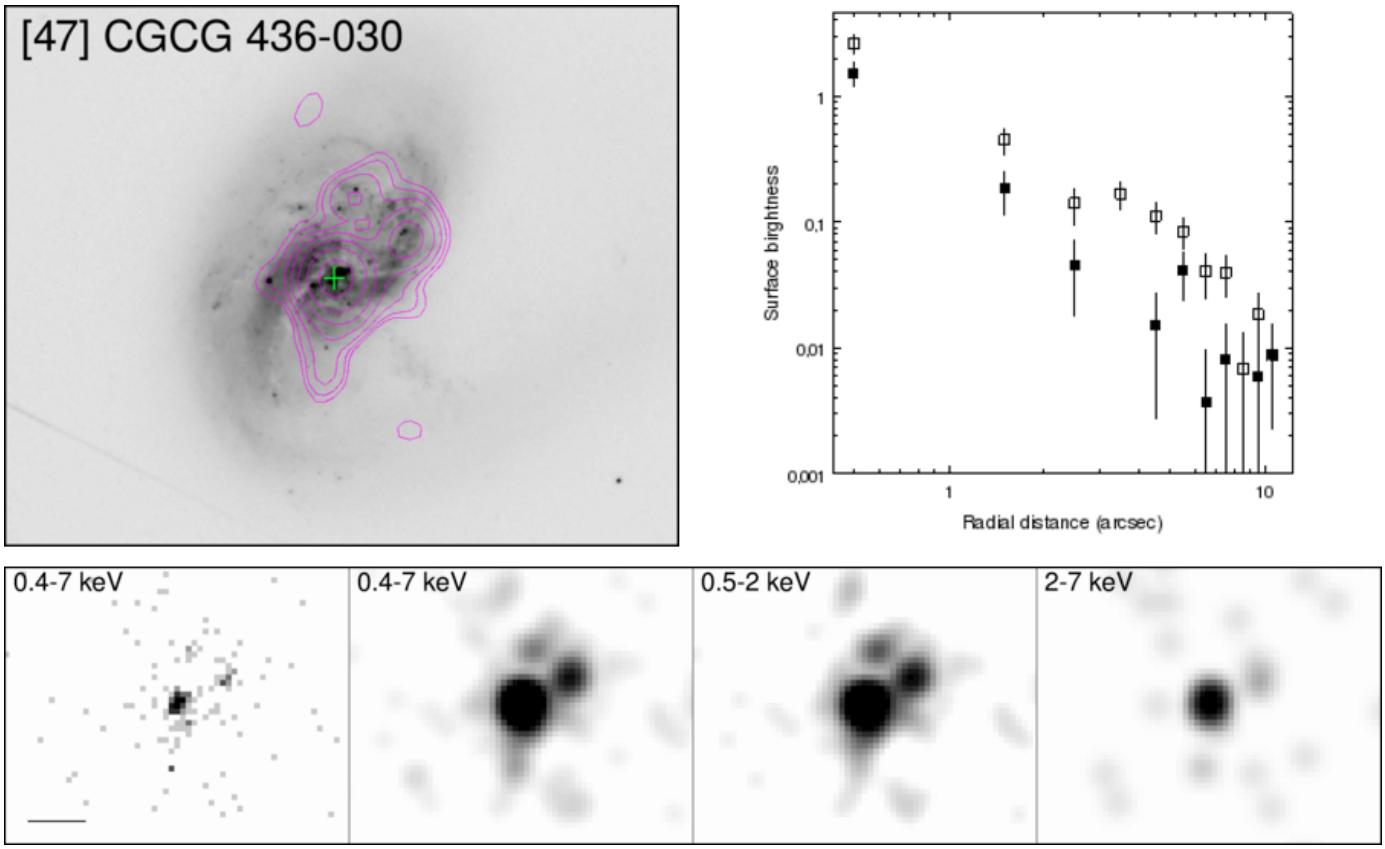

Fig. B.2. *Overlay on* HST-ACS F814W. *Contours:* Interval 1.

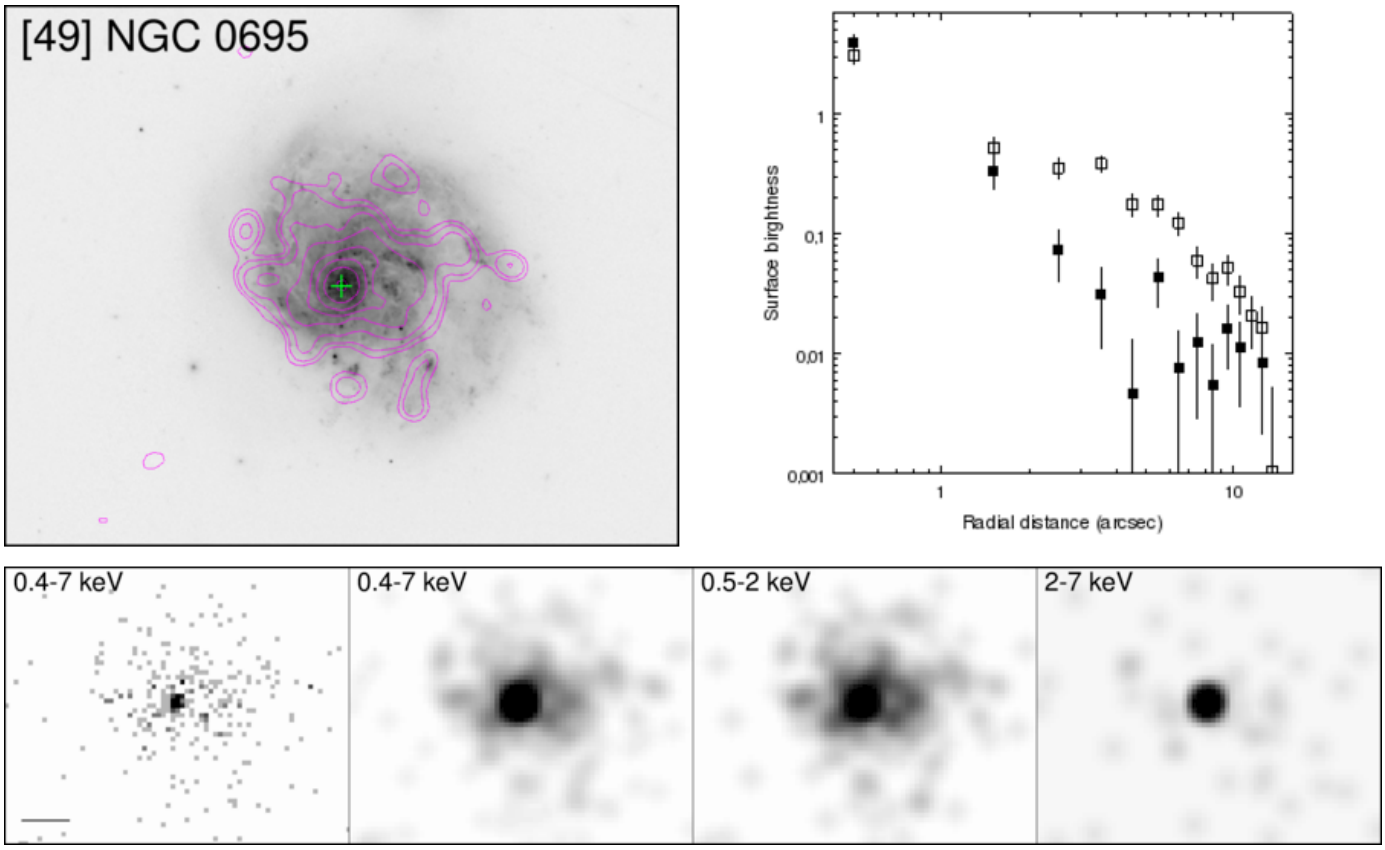

Fig. B.3. *Overlay on* HST-ACS F814W. *Contours:* Interval 1.

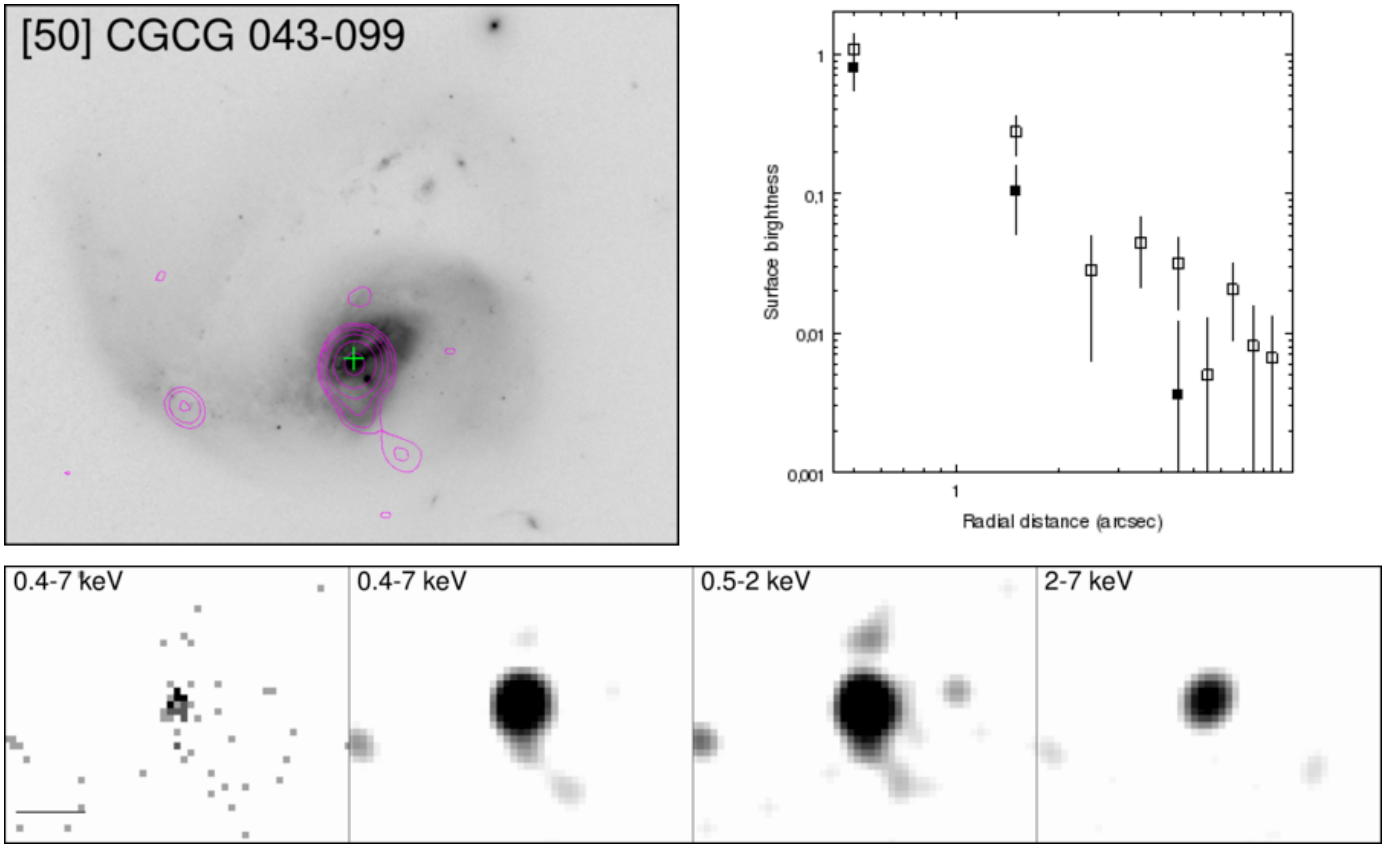

Fig. B.4. *Overlay on* HST-ACS F814W. *Contours:* Interval 1.

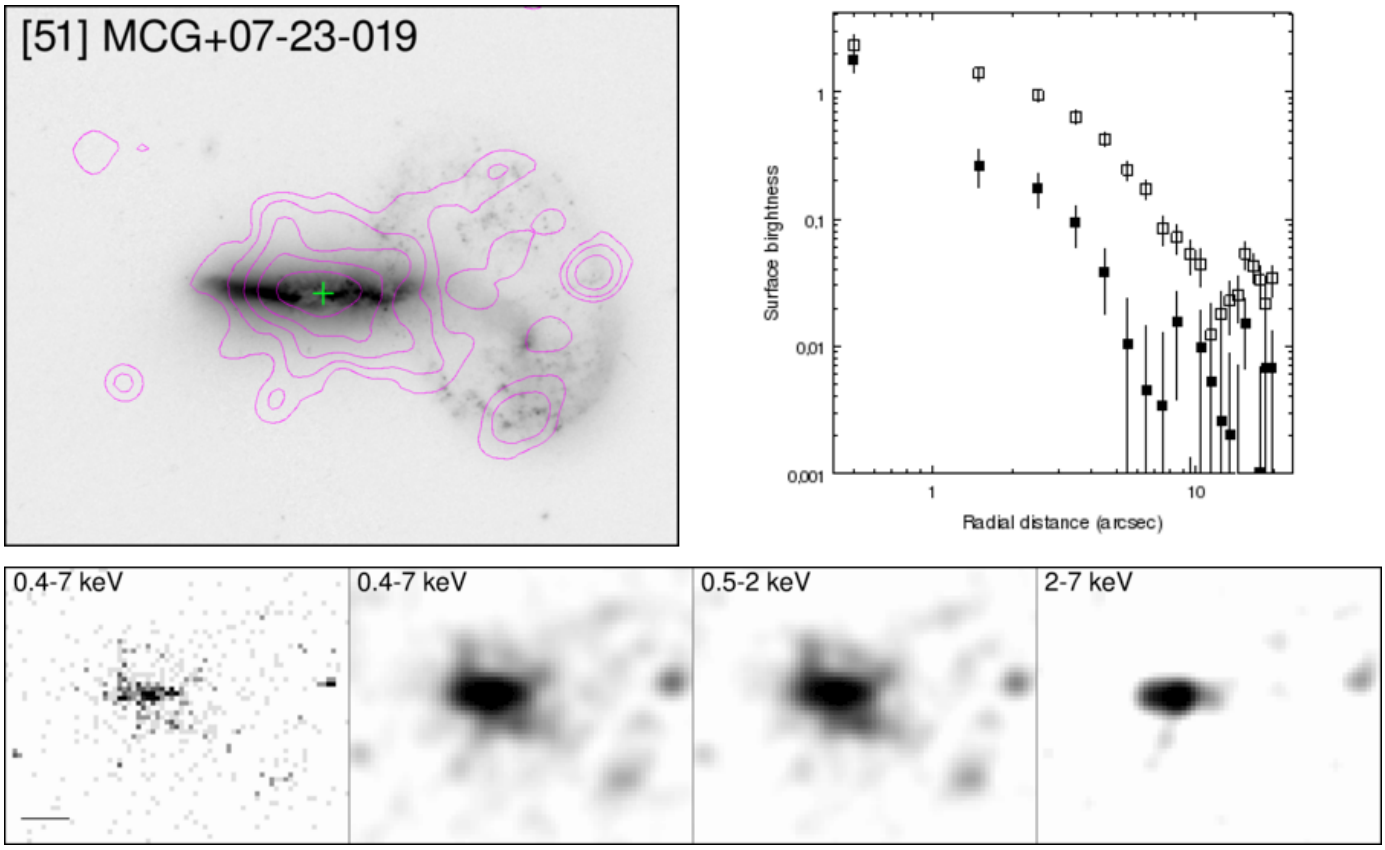

Fig. B.5. *Overlay on* HST-ACS F814W. *Contours:* Interval 3.

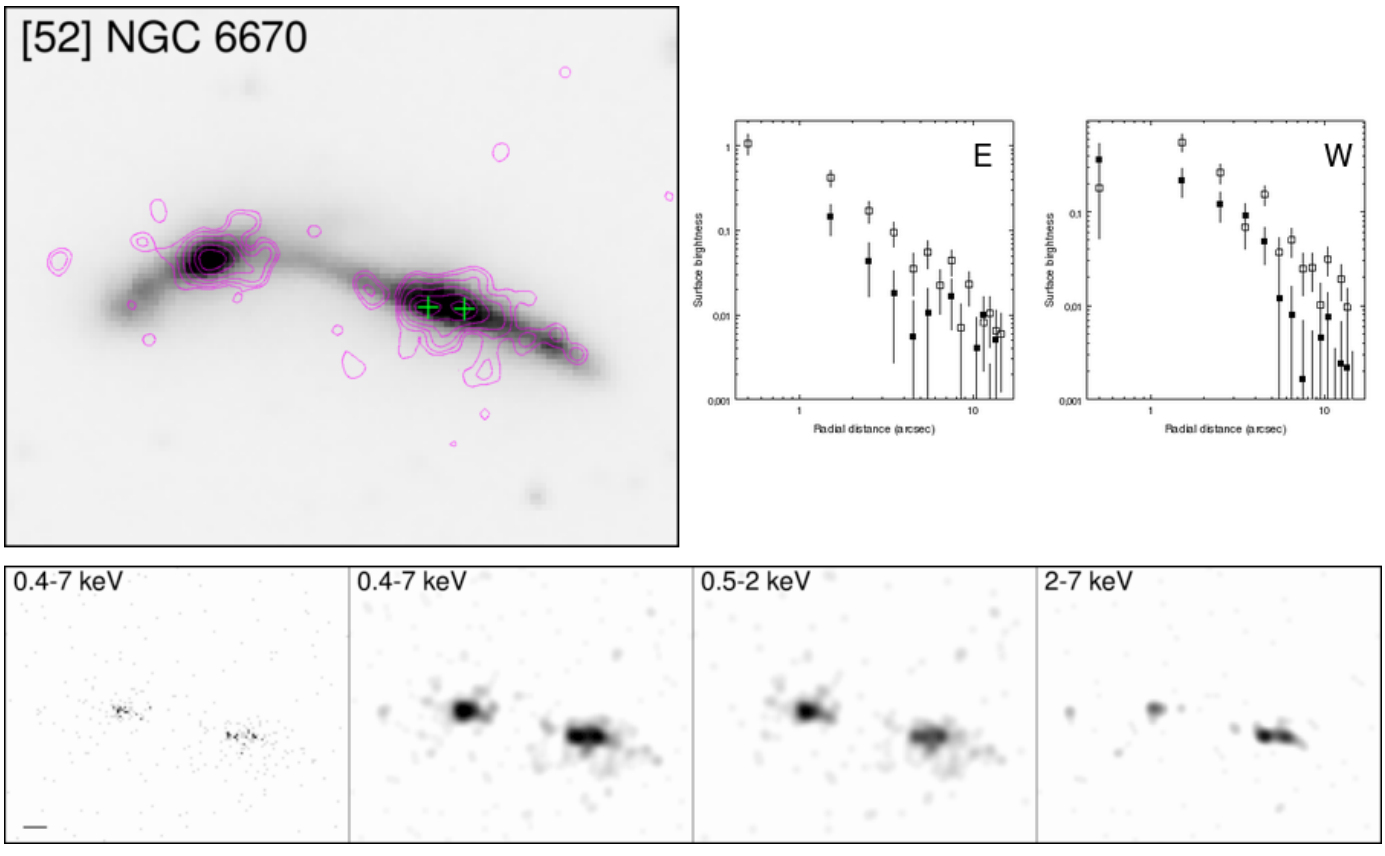

Fig. B.6. *Overlay on* HST-ACS F814W. *Contours:* Interval 1.

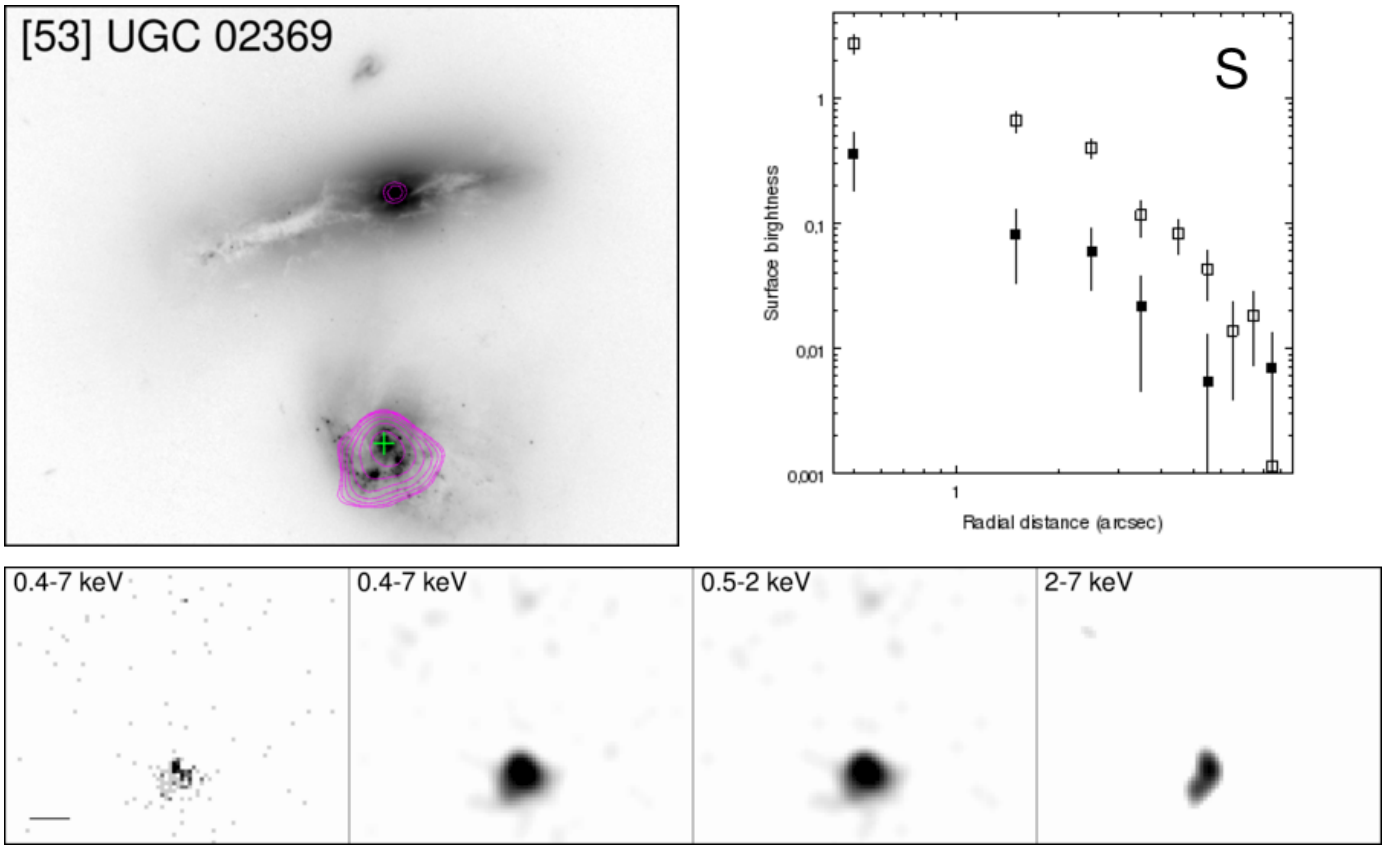

Fig. B.7. *Overlay on* HST-ACS F814W. *Contours:* Interval 4.

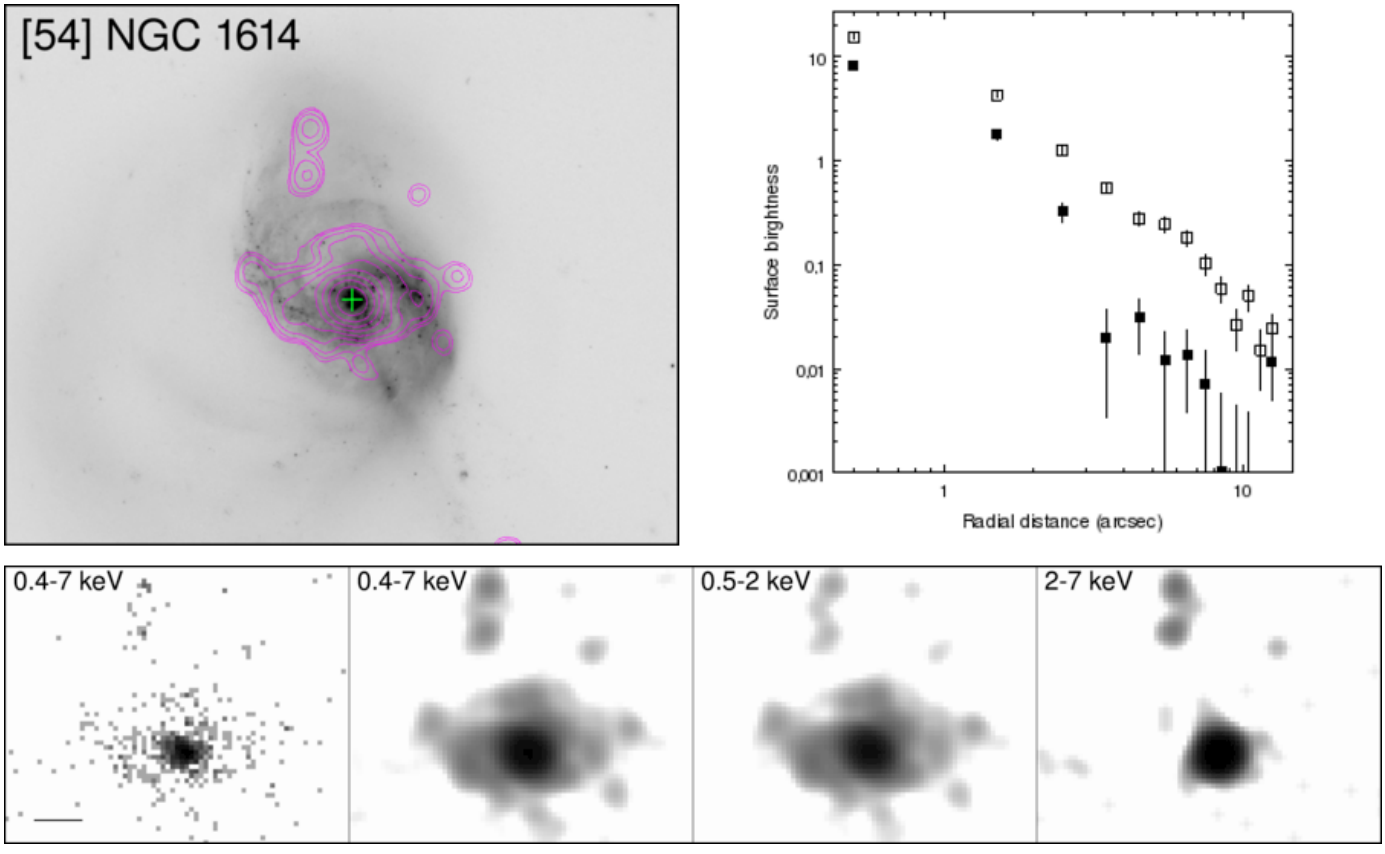

Fig. B.8. *Overlay on* HST-ACS F814W. *Contours:* Interval 1.

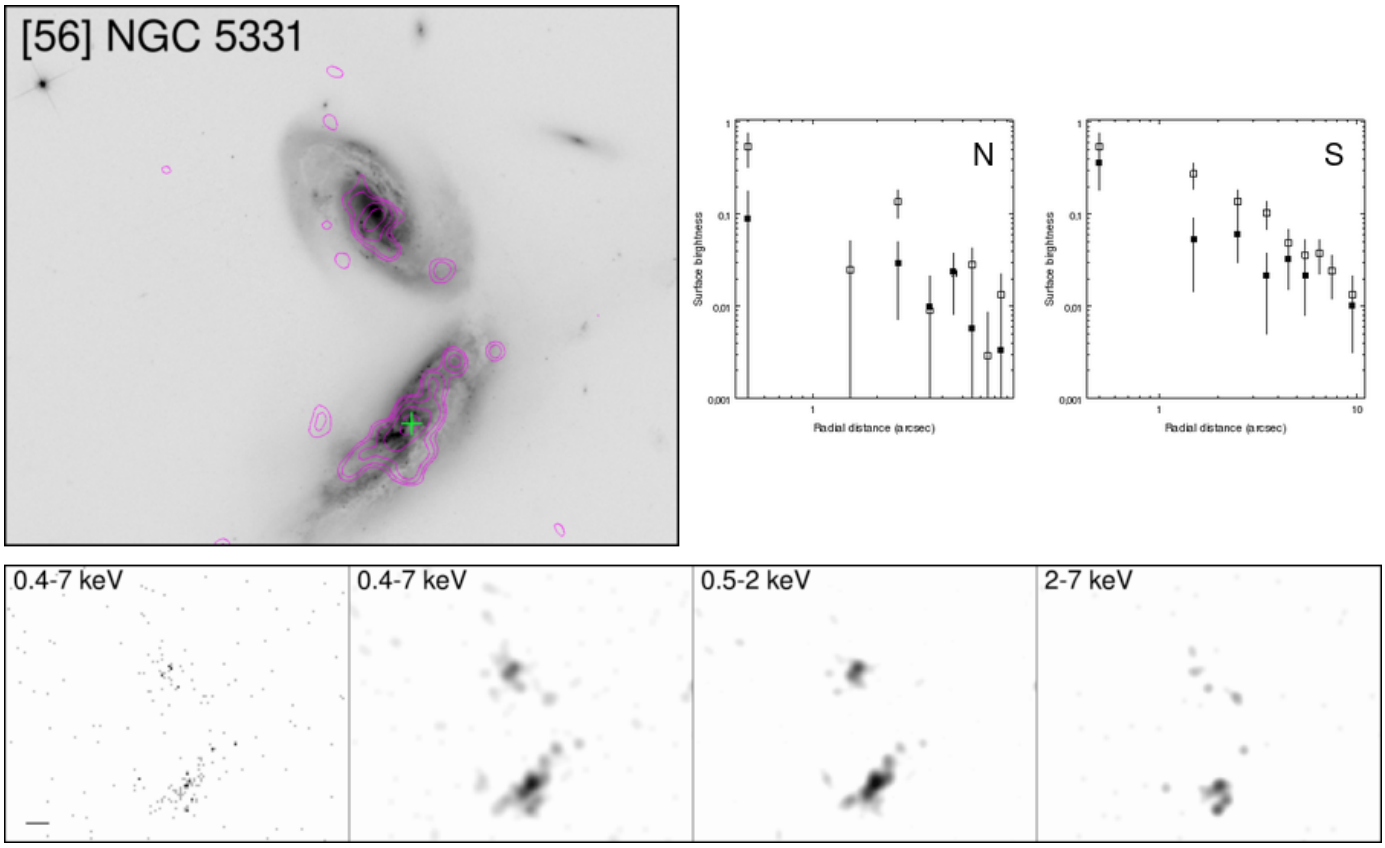

Fig. B.9. *Overlay on* HST-ACS F814W. *Contours:* Interval 2.

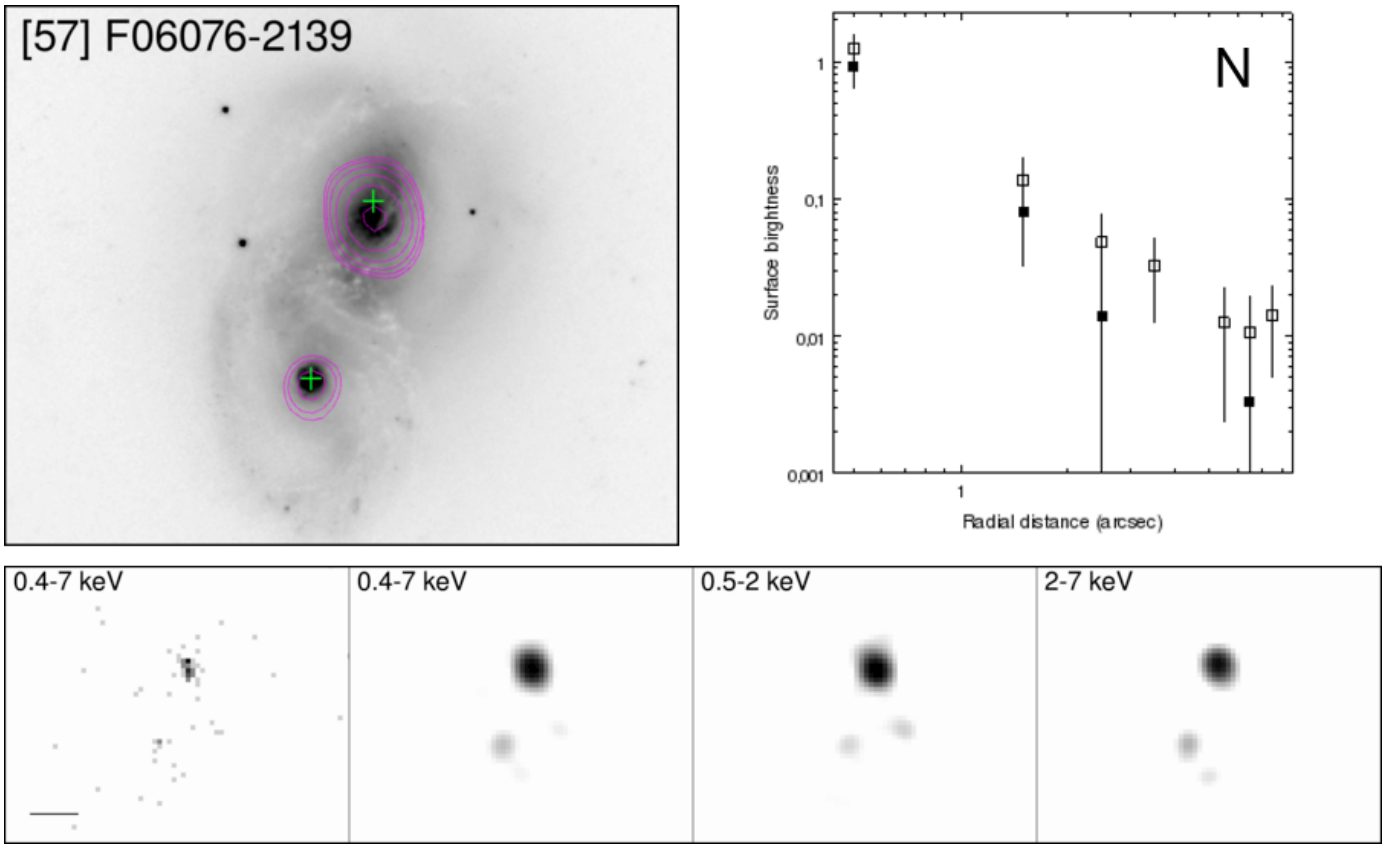

Fig. B.10. *Overlay on* HST-ACS F814W. *Contours:* Interval 1.

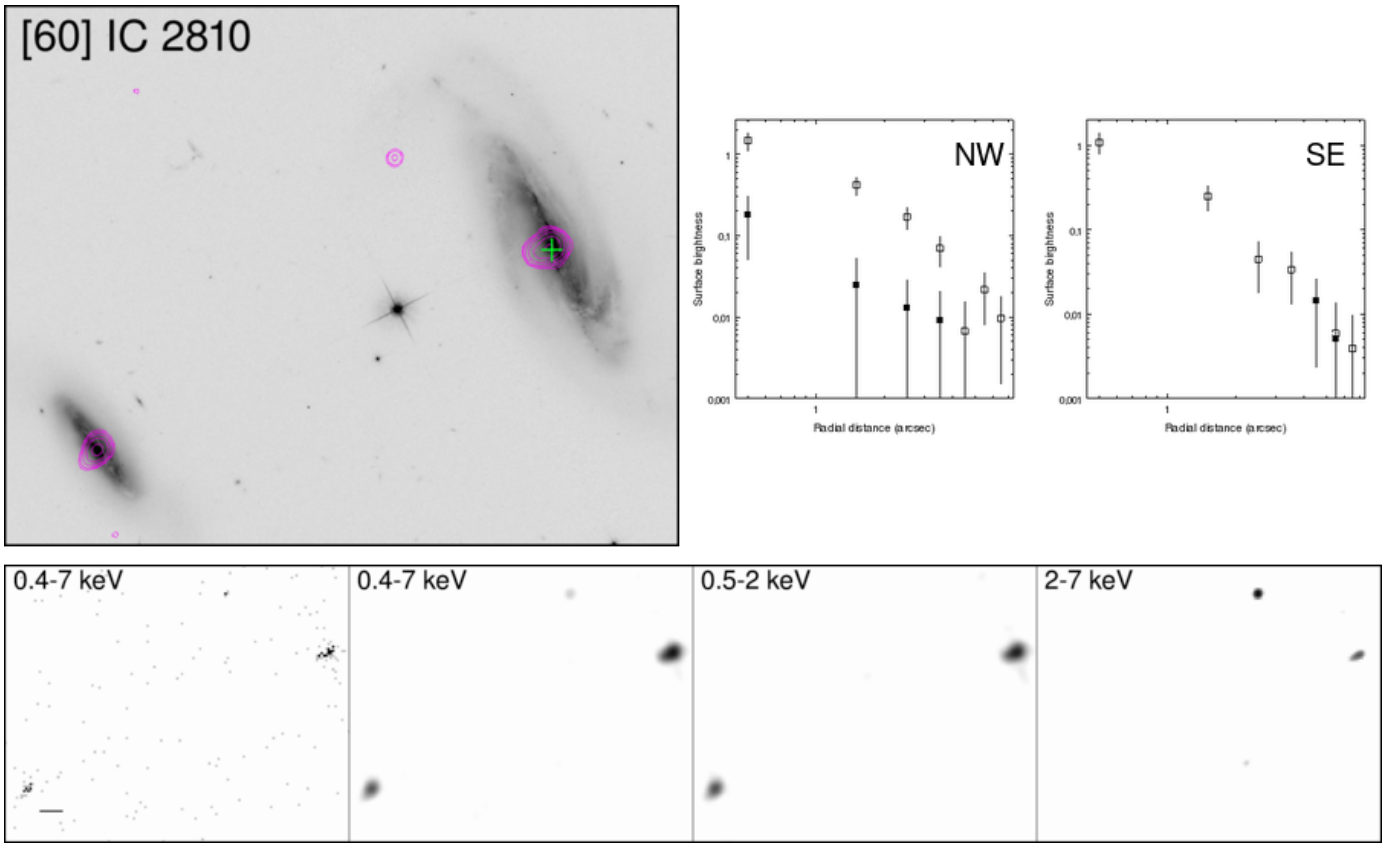

Fig. B.11. *Overlay on* HST-ACS F814W. *Contours:* Interval 1.

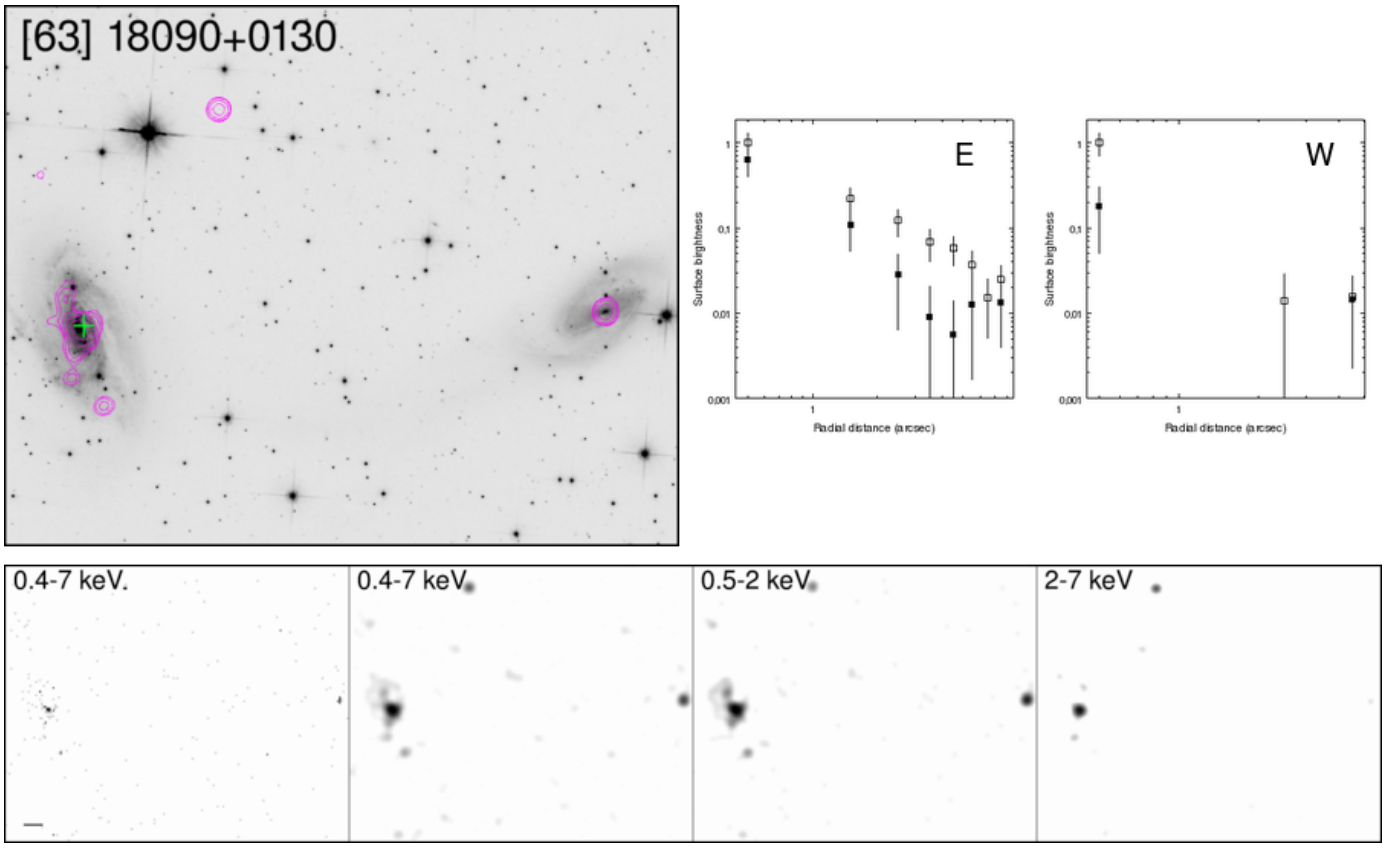

Fig. B.12. *Overlay on* HST-ACS F814W. *Contours:* Interval 1.

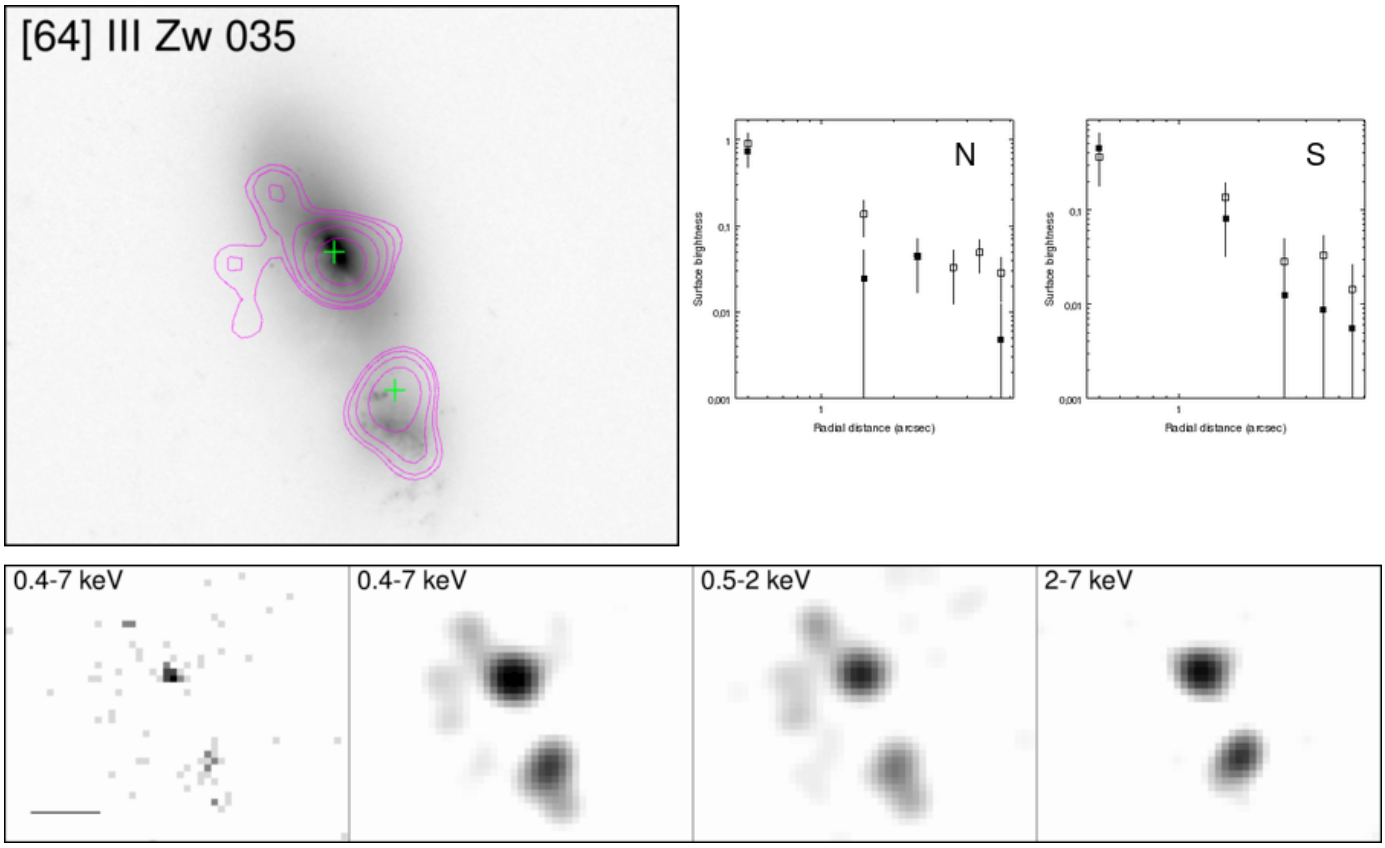

Fig. B.13. *Overlay on* HST-ACS F814W. *Contours:* Interval 1.

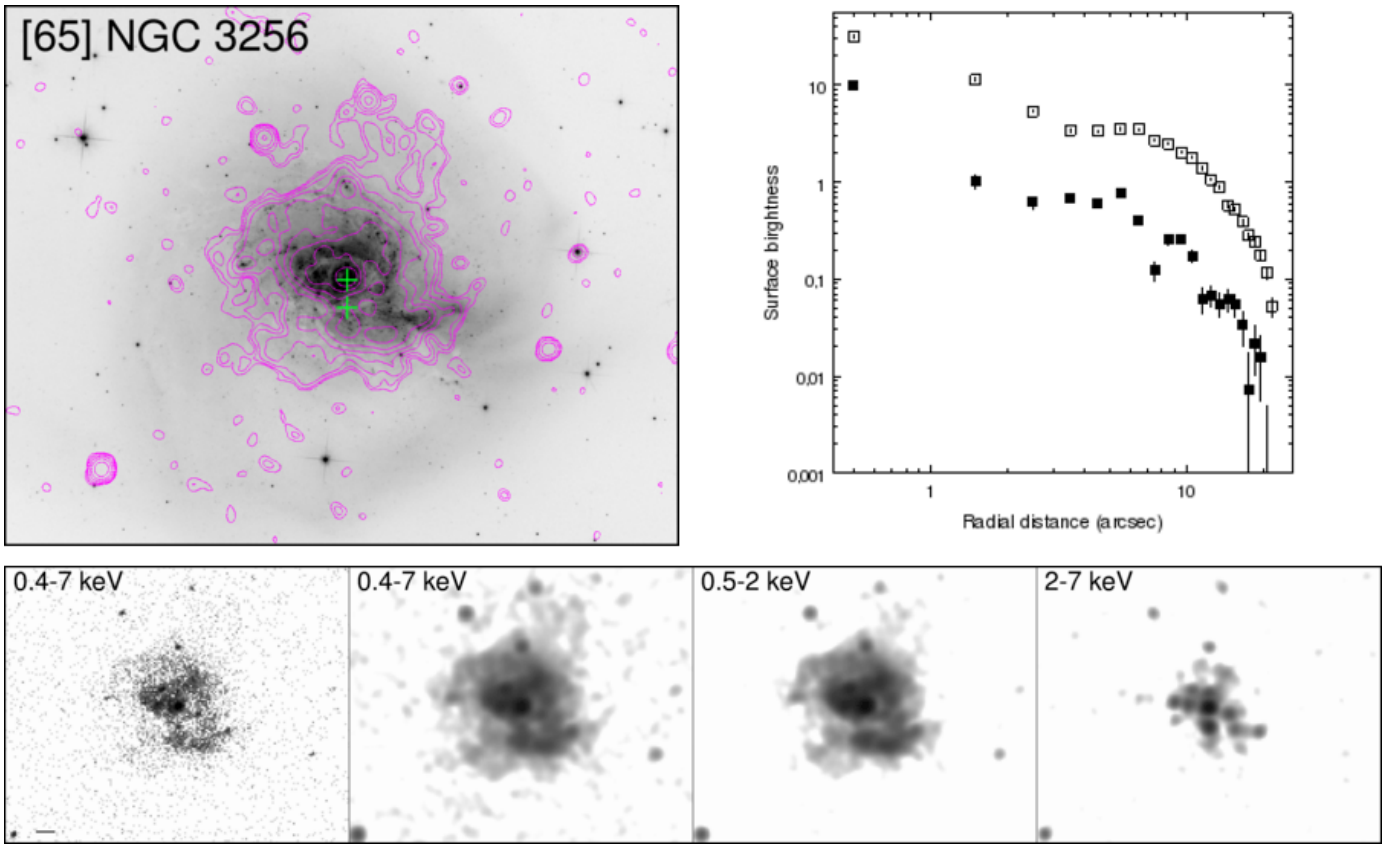

Fig. B.14. *Overlay on* HST-ACS F814W. *Contours:* Interval 1.

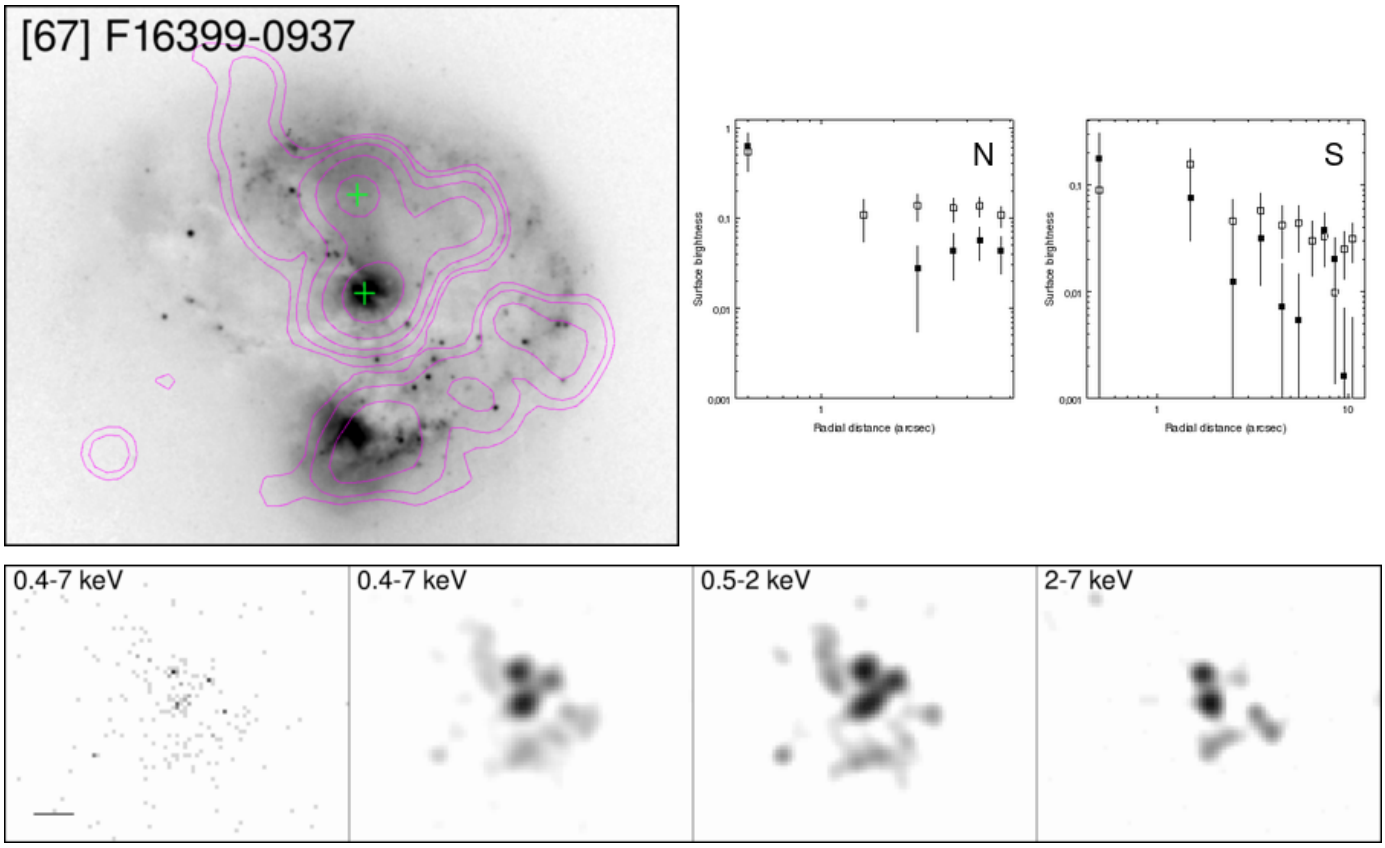

Fig. B.15. *Overlay on* HST-ACS F814W. *Contours:* Interval 1.

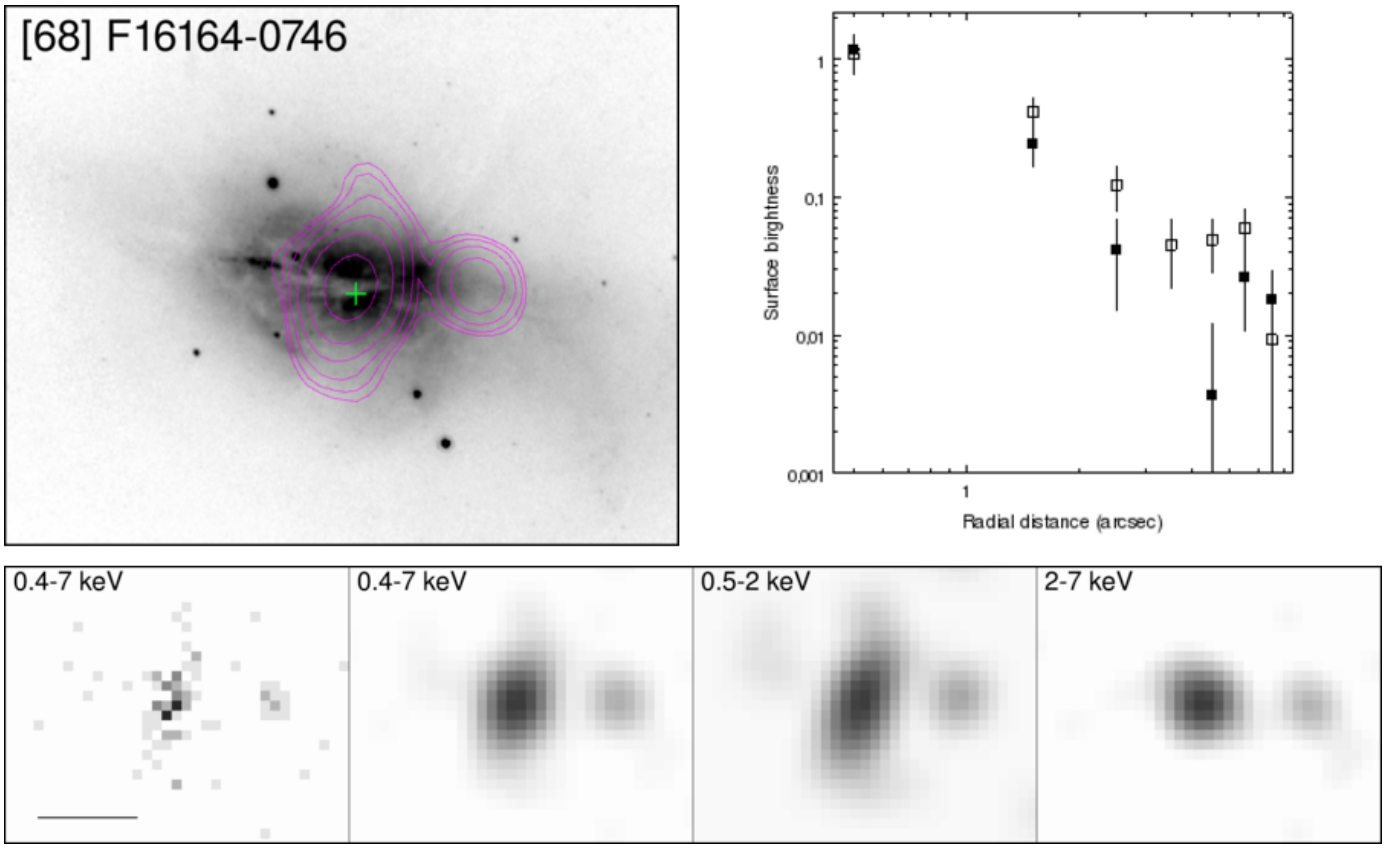

Fig. B.16. *Overlay on* HST-ACS F814W. *Contours:* Interval 1.

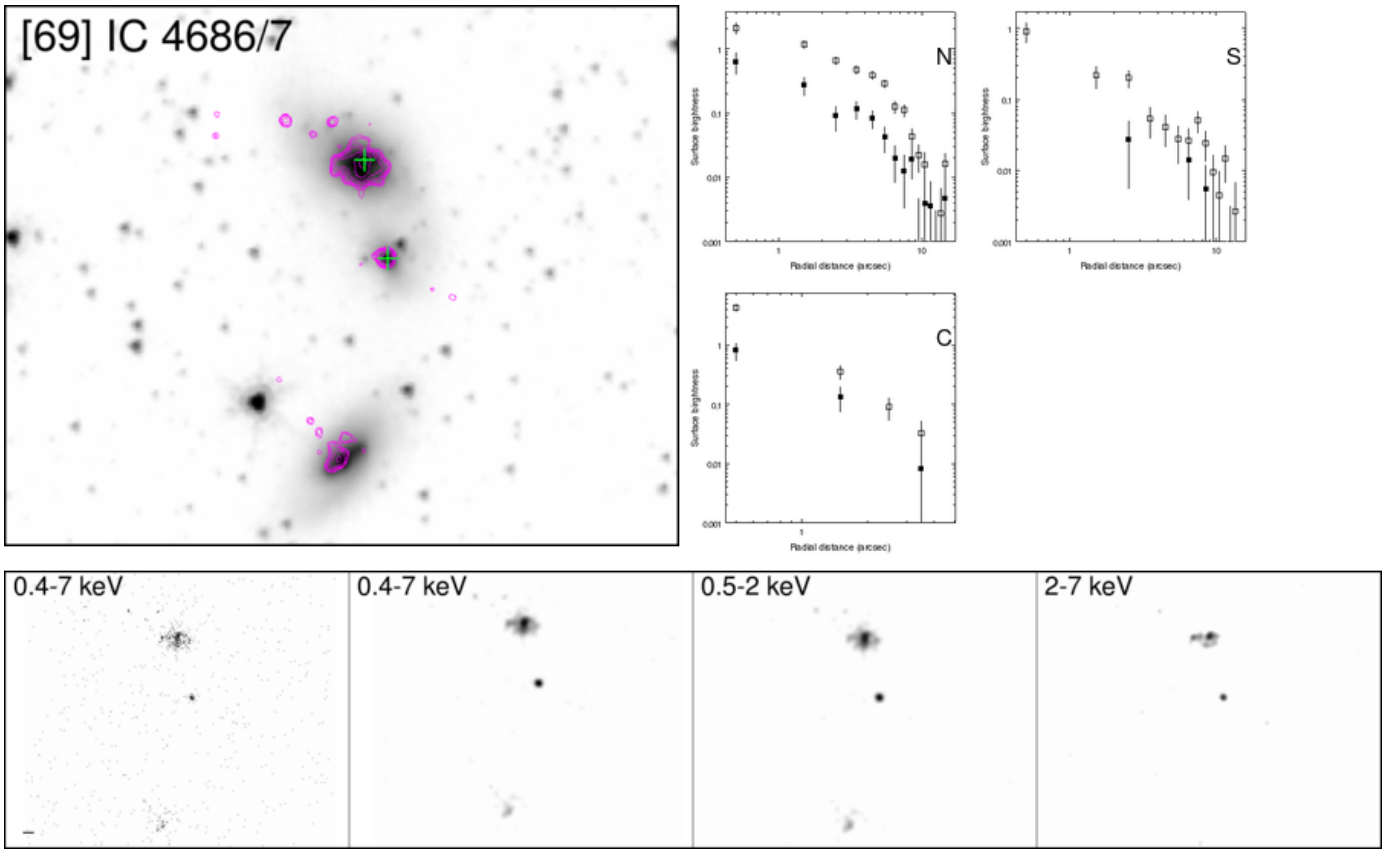

Fig. B.17. *Overlay on* HST-ACS F814W. *Contours:* Interval 1.

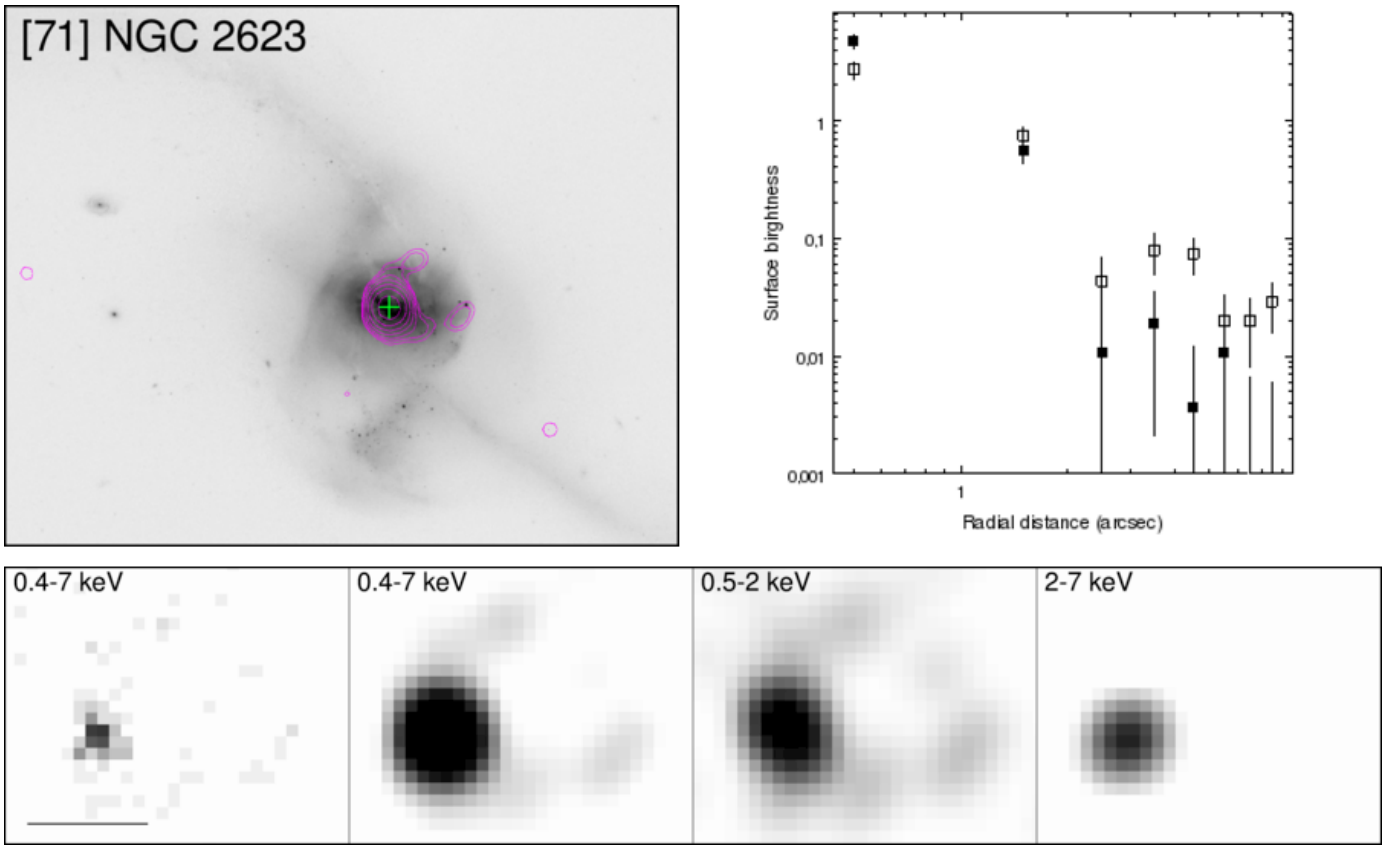

Fig. B.18. *Overlay on* HST-ACS F814W. *Contours:* Interval 1.

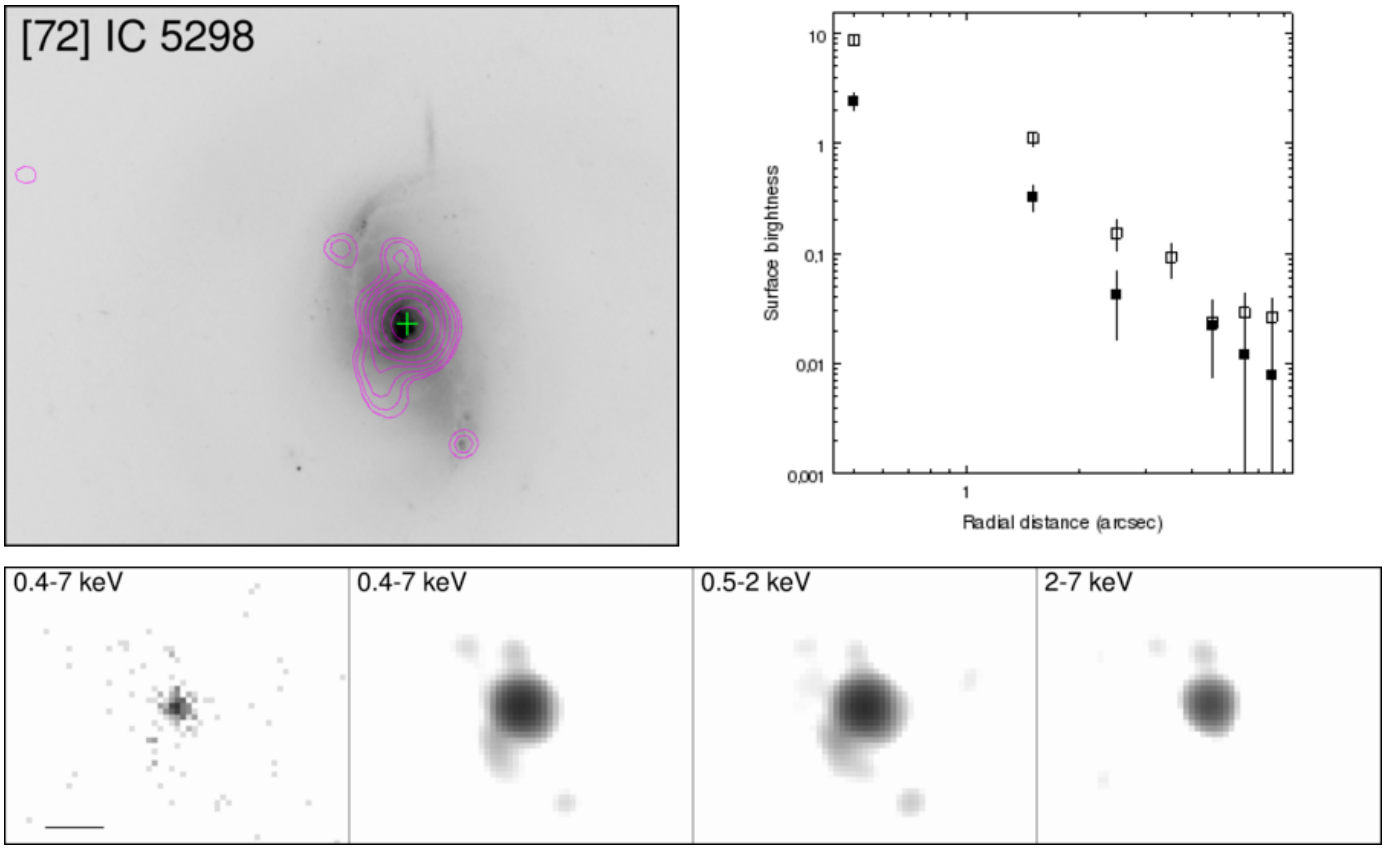

Fig. B.19. *Overlay on* HST-ACS F814W. *Contours:* Interval 1.

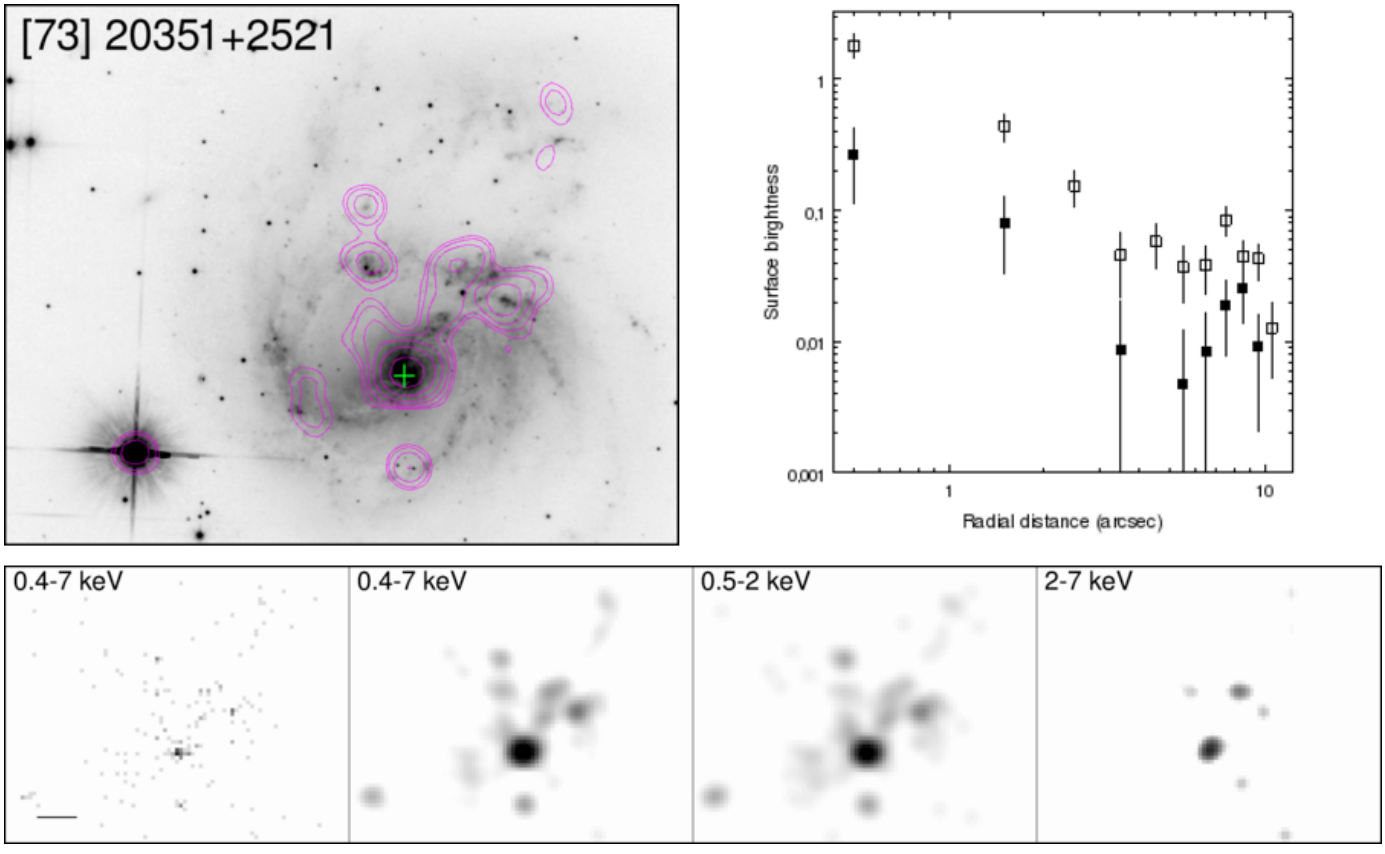

Fig. B.20. *Overlay on* HST-ACS F814W. *Contours:* Interval 1.

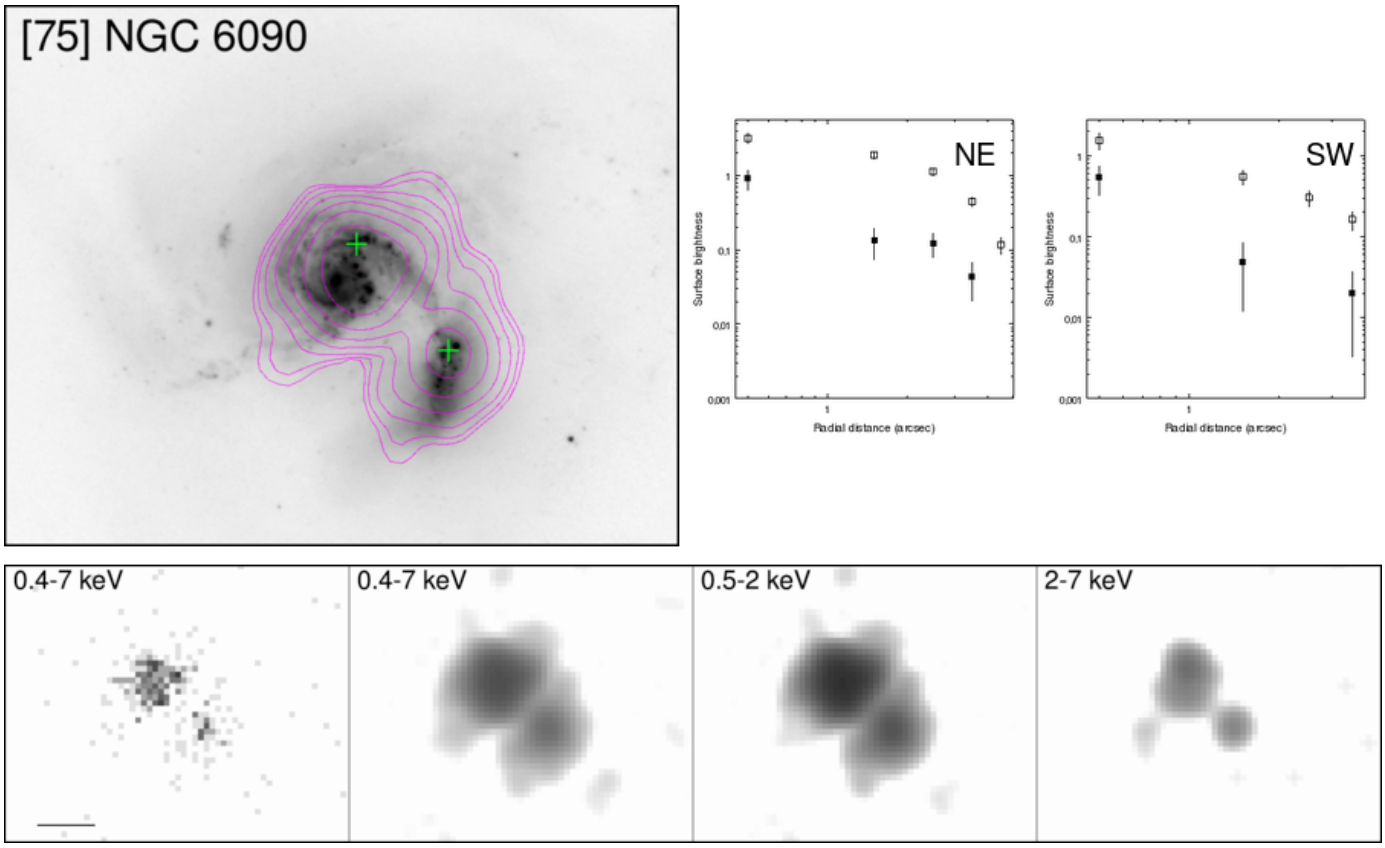

Fig. B.21. *Overlay on* HST-ACS F814W. *Contours:* Interval 1.

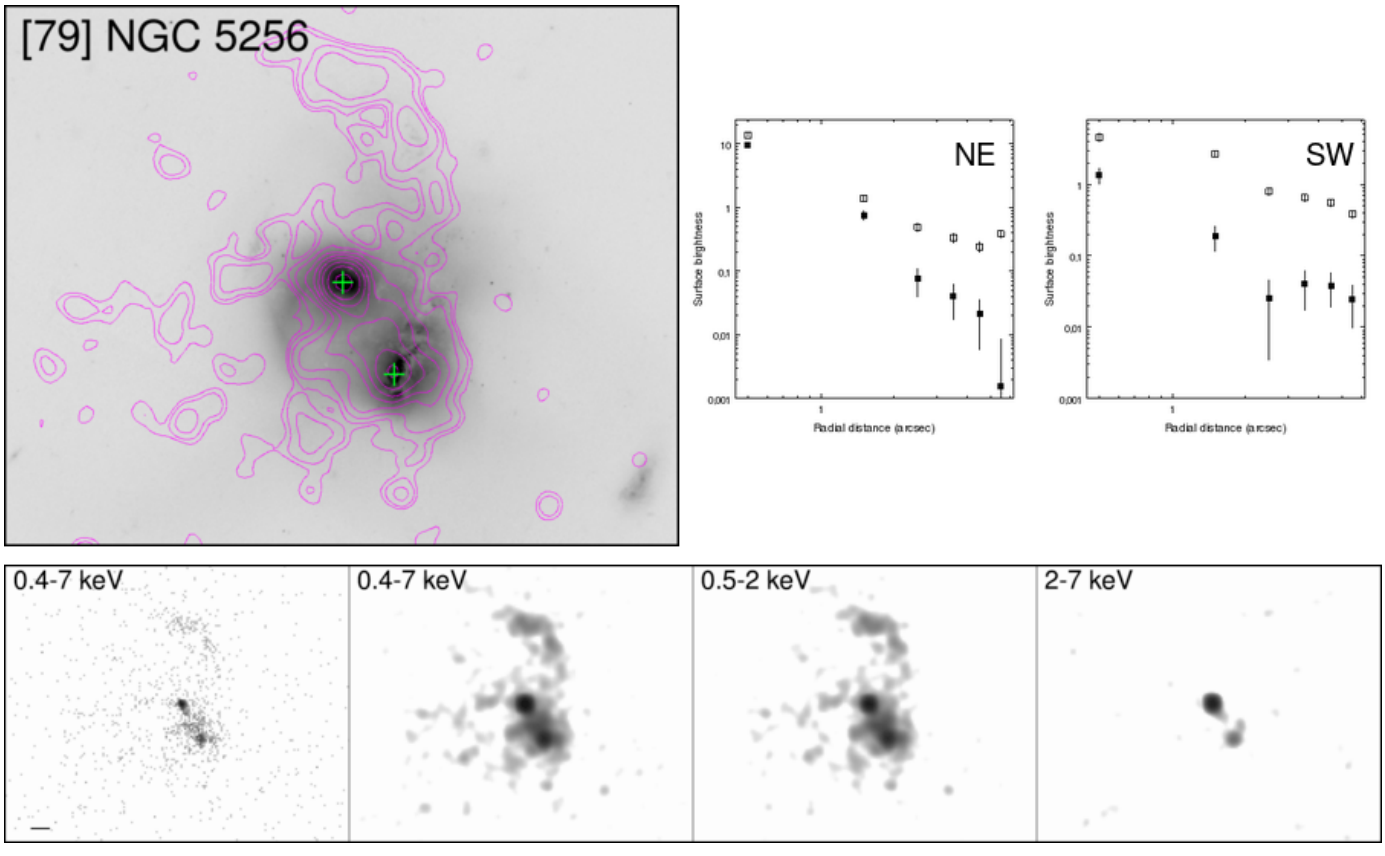

Fig. B.22. *Overlay on* HST-ACS F814W. *Contours:* Interval 2.

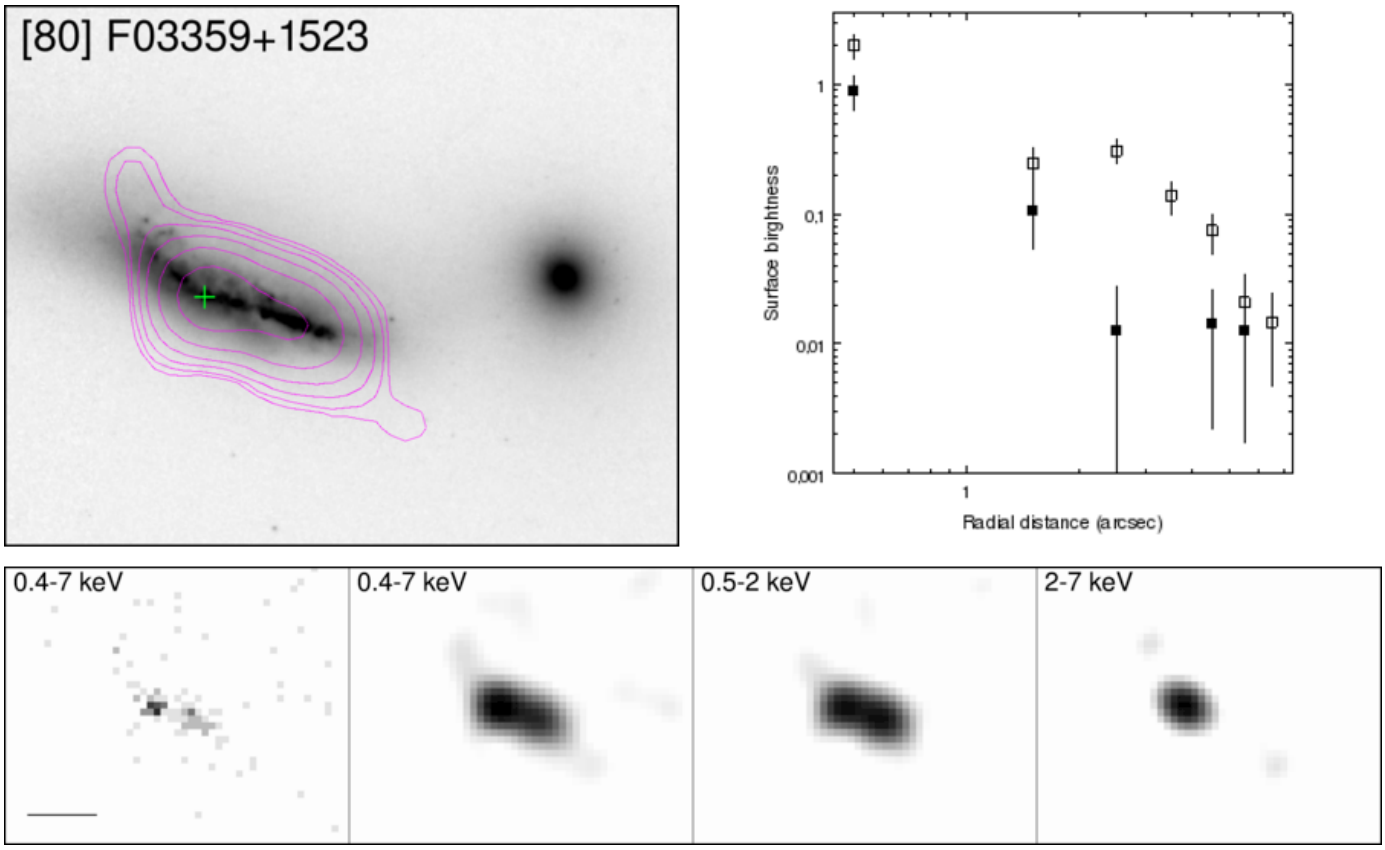

Fig. B.23. *Overlay on* HST-ACS F814W. *Contours:* Interval 1.

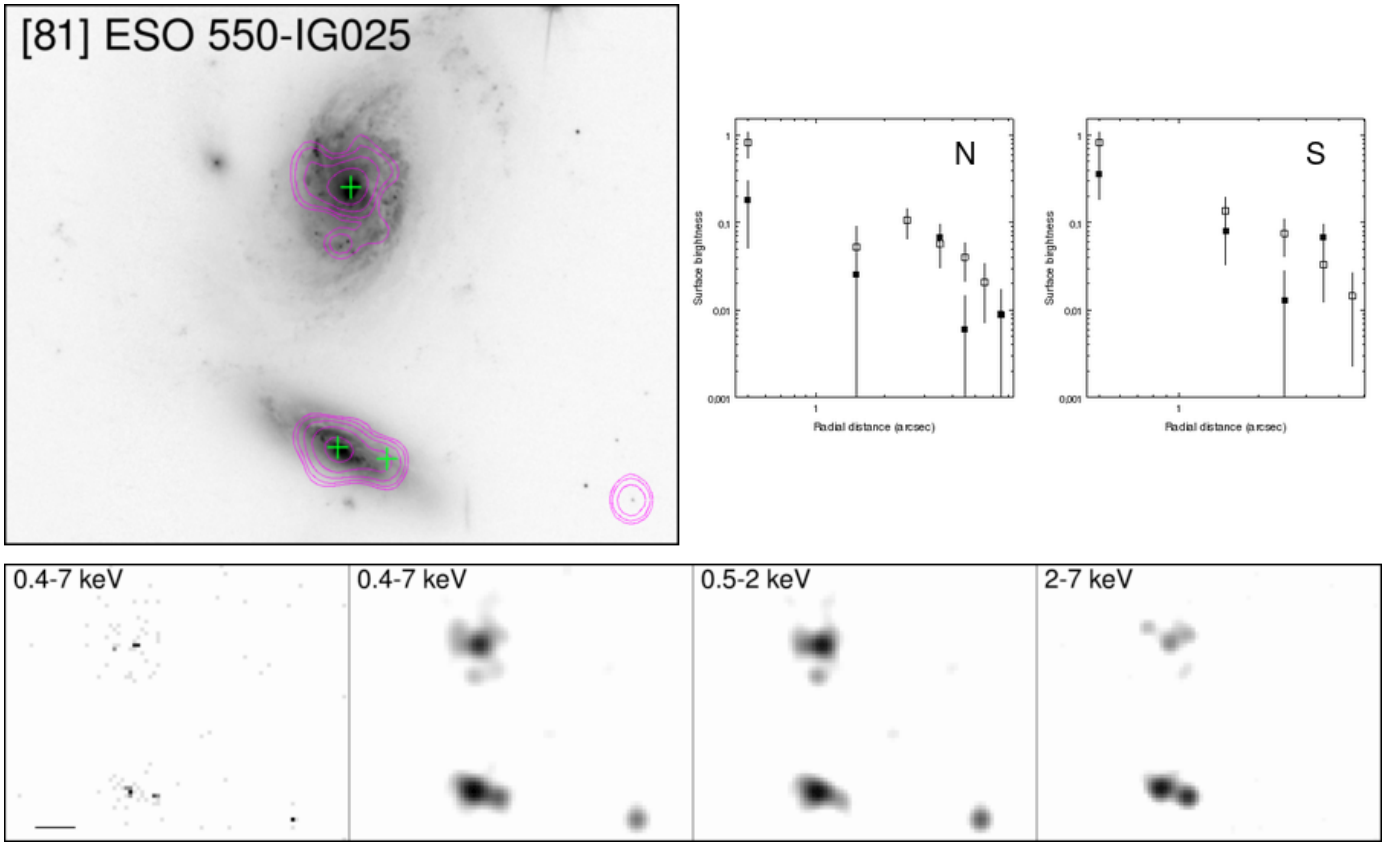

Fig. B.24. *Overlay on* HST-ACS F814W. *Contours:* Interval 1.

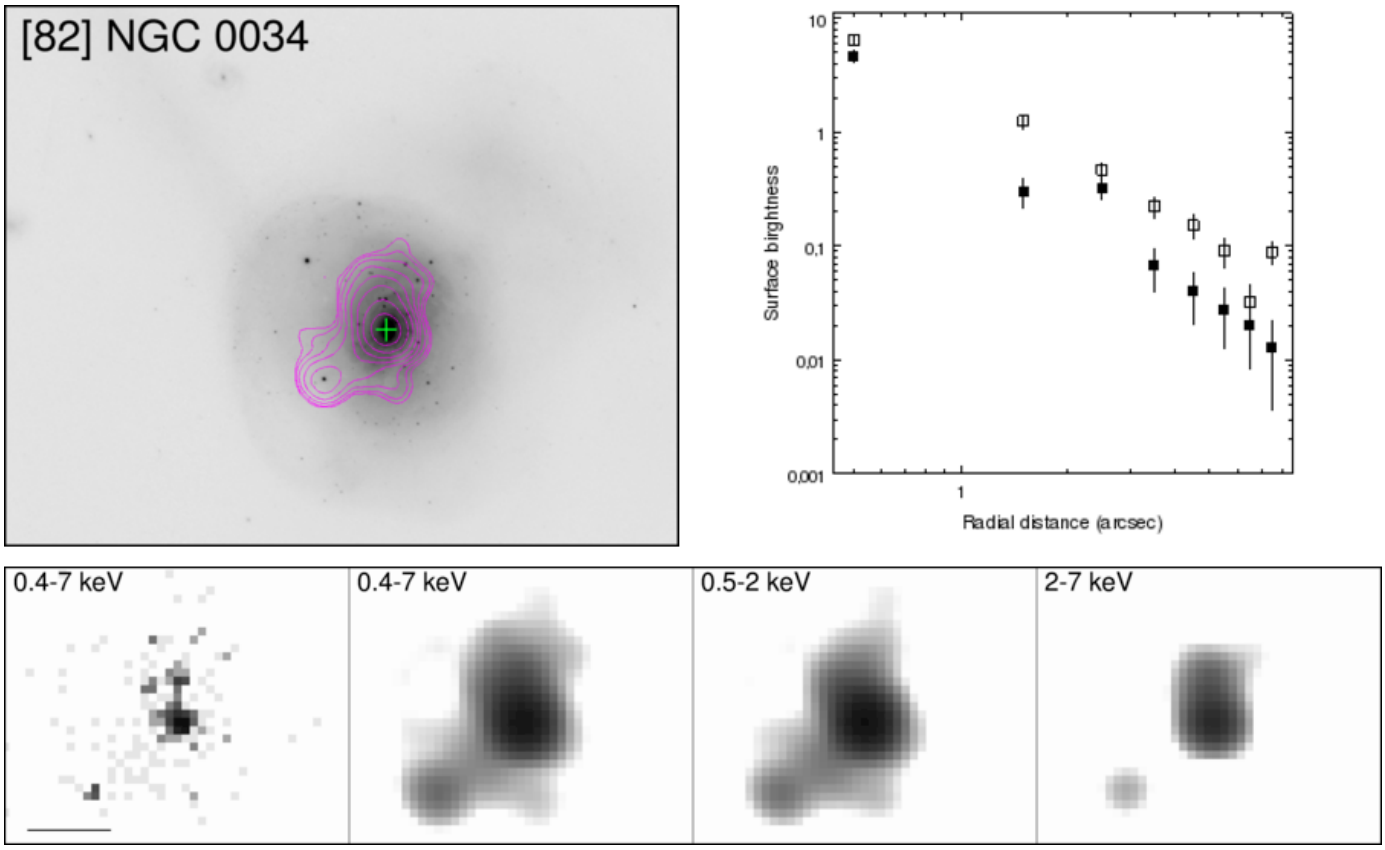

Fig. B.25. *Overlay on* HST-ACS F814W. *Contours:* Interval 1.

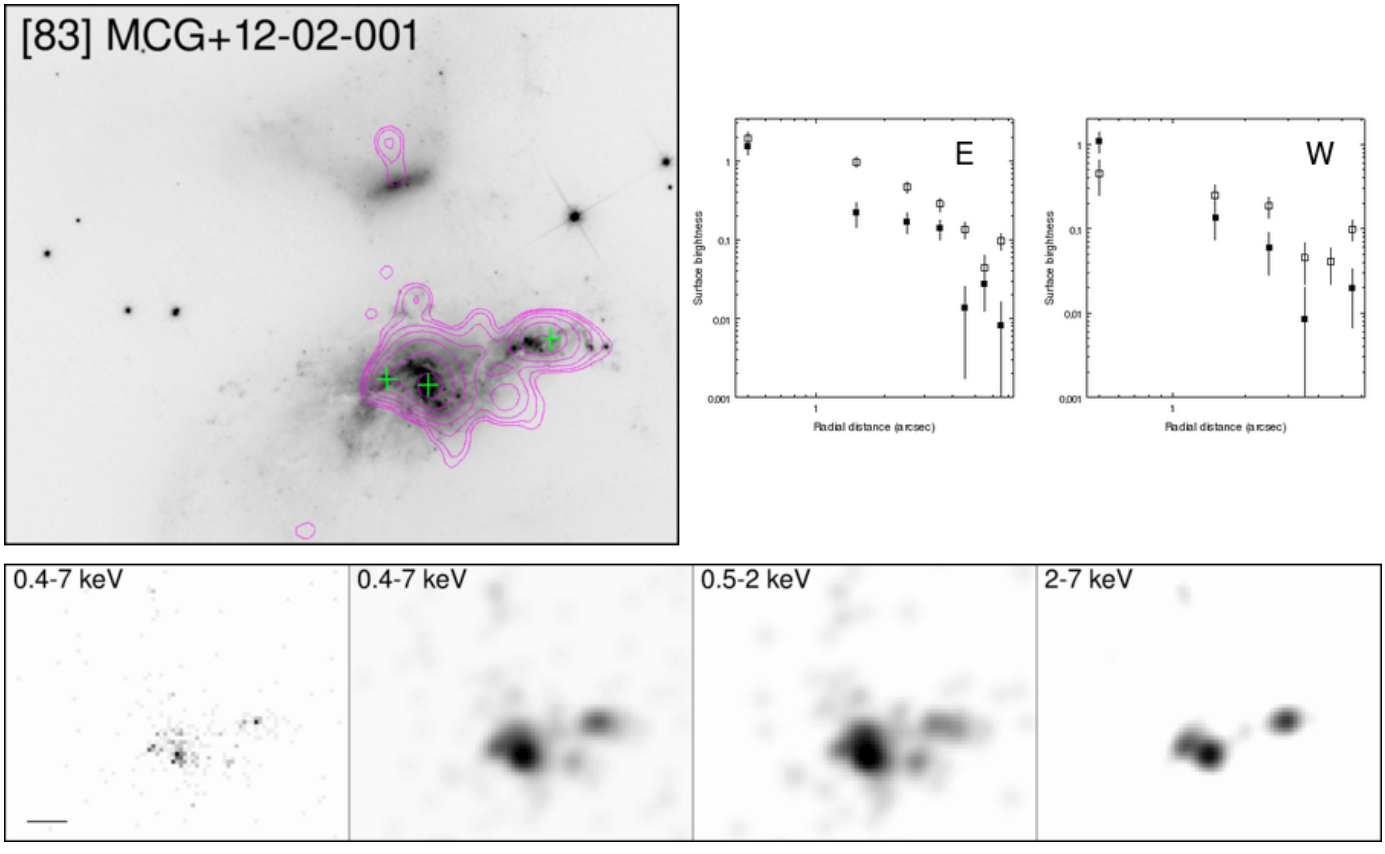

Fig. B.26. *Overlay on* HST-ACS F814W. *Contours:* Interval 1.

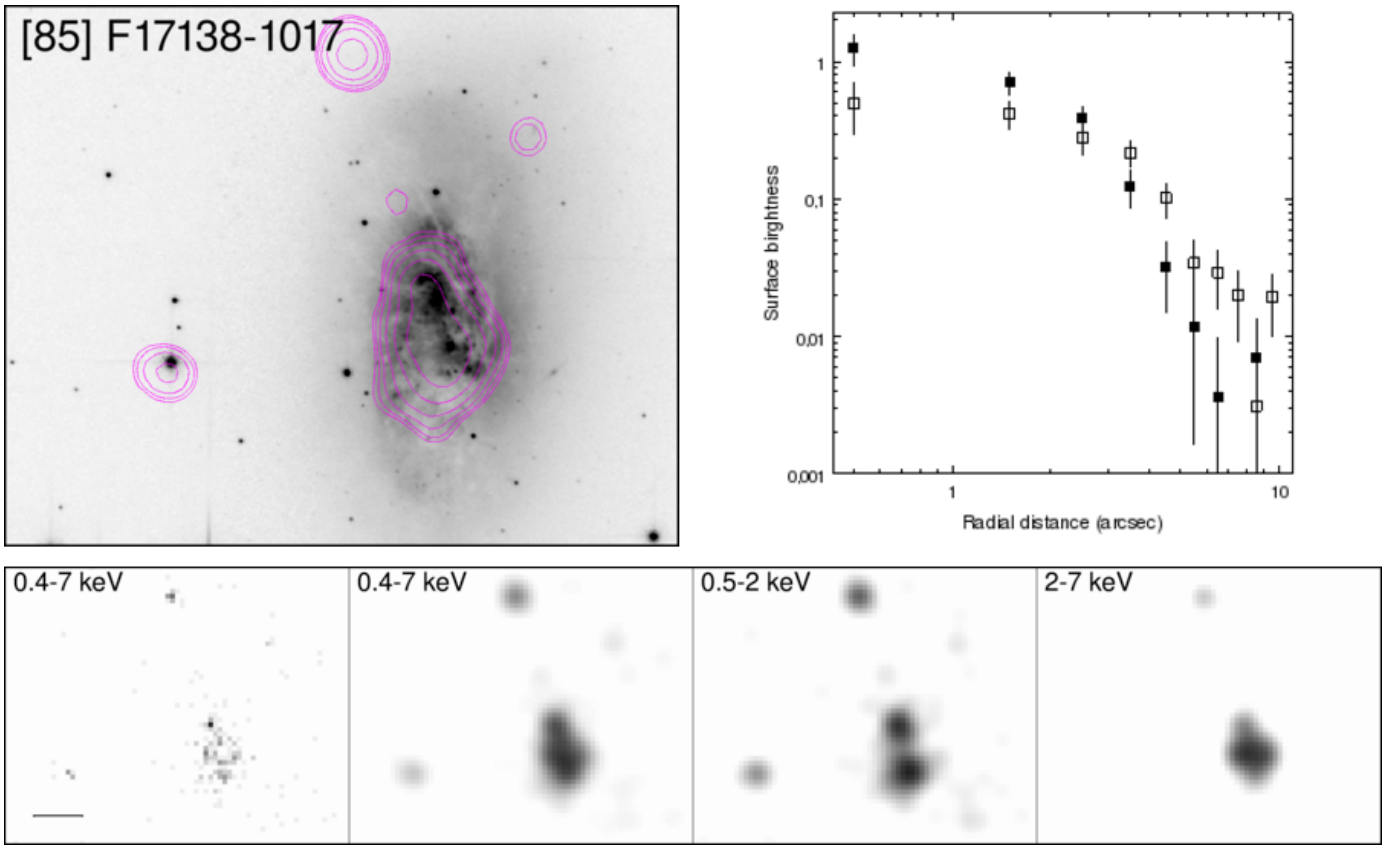

Fig. B.27. *Overlay on* HST-ACS F814W. *Contours:* Interval 1.

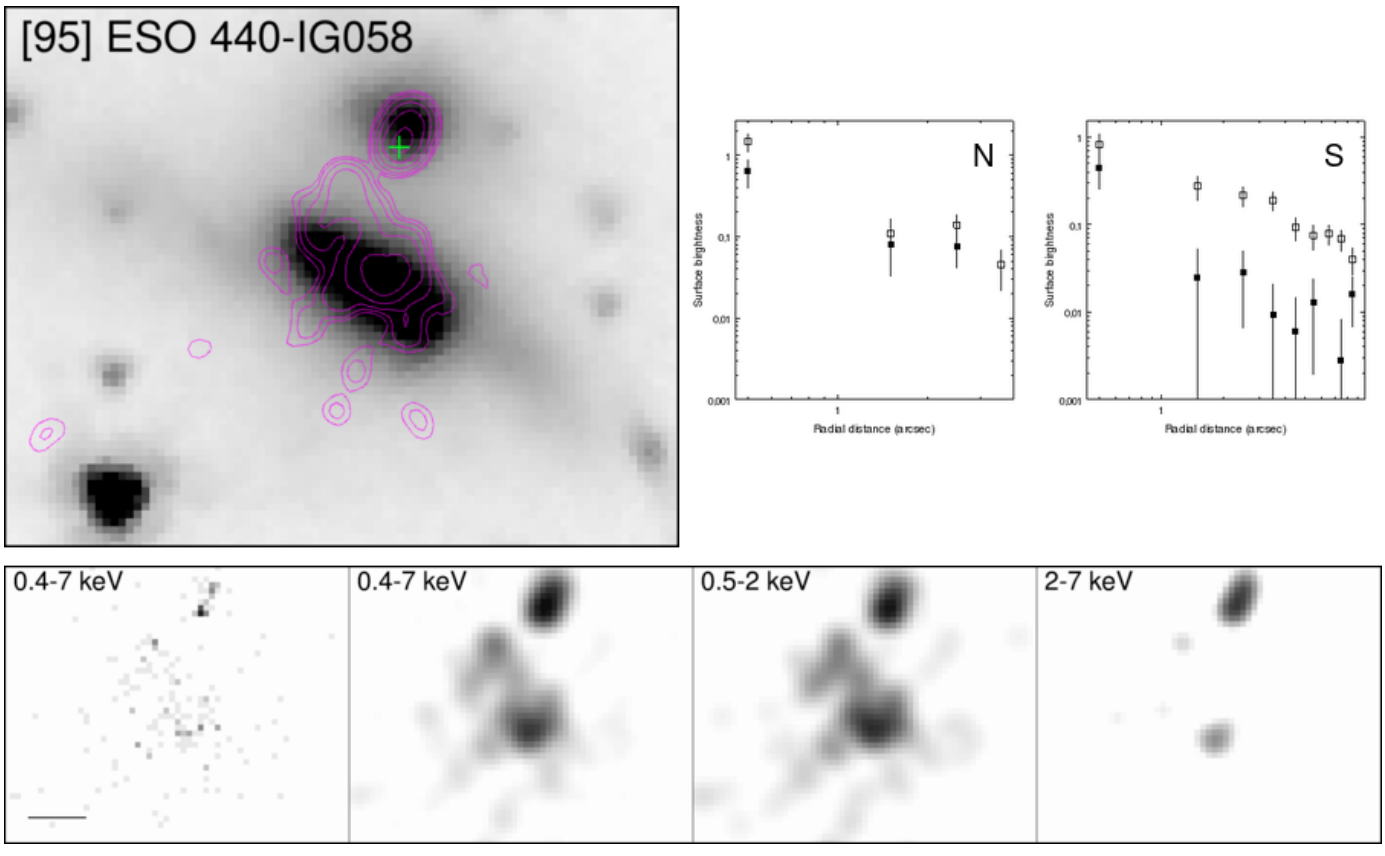

Fig. B.28. *Overlay on* IRAC channel 1. *Contours:* Interval 2.

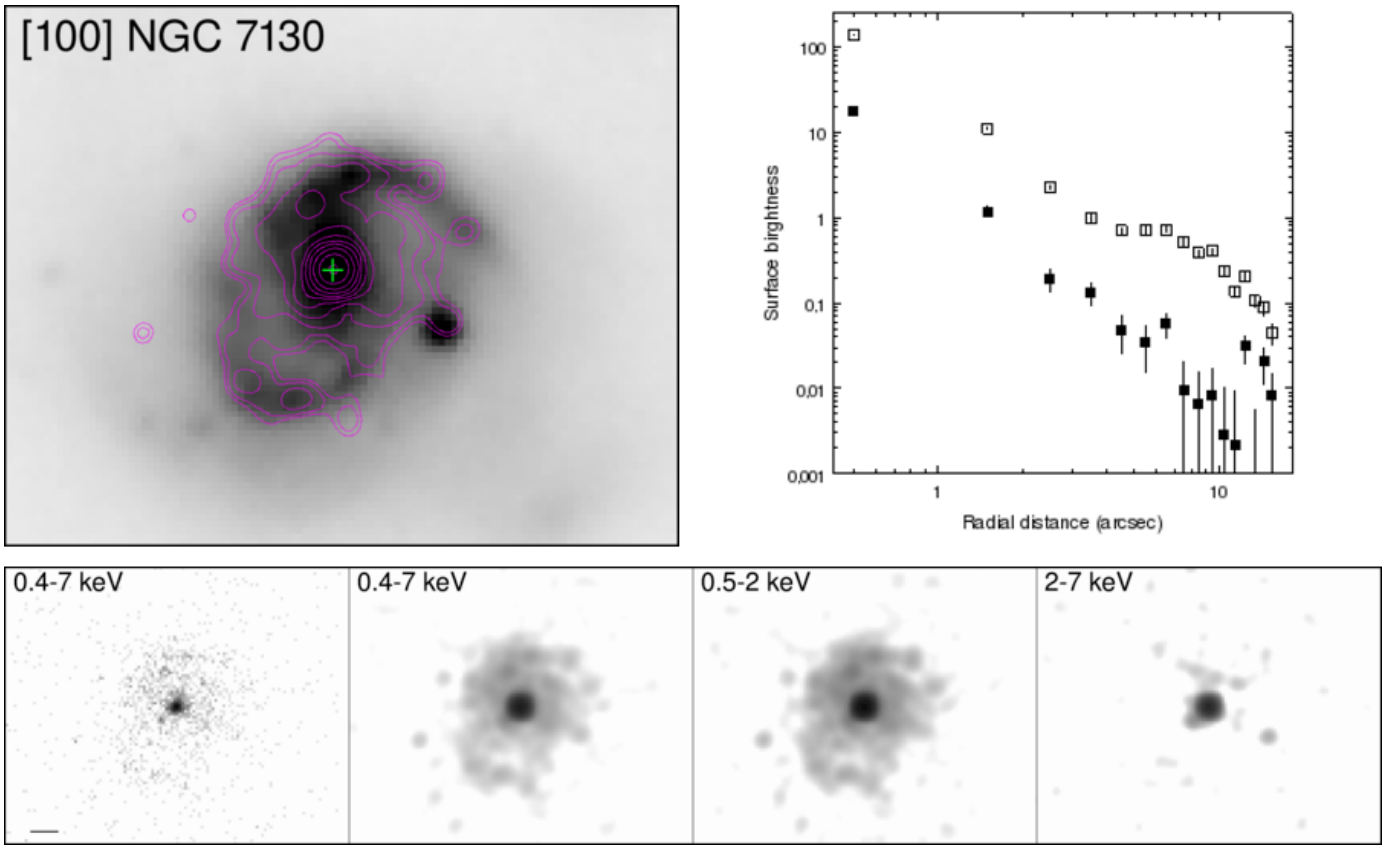

Fig. B.29. *Overlay on* IRAC channel 1. *Contours:* Interval 1.

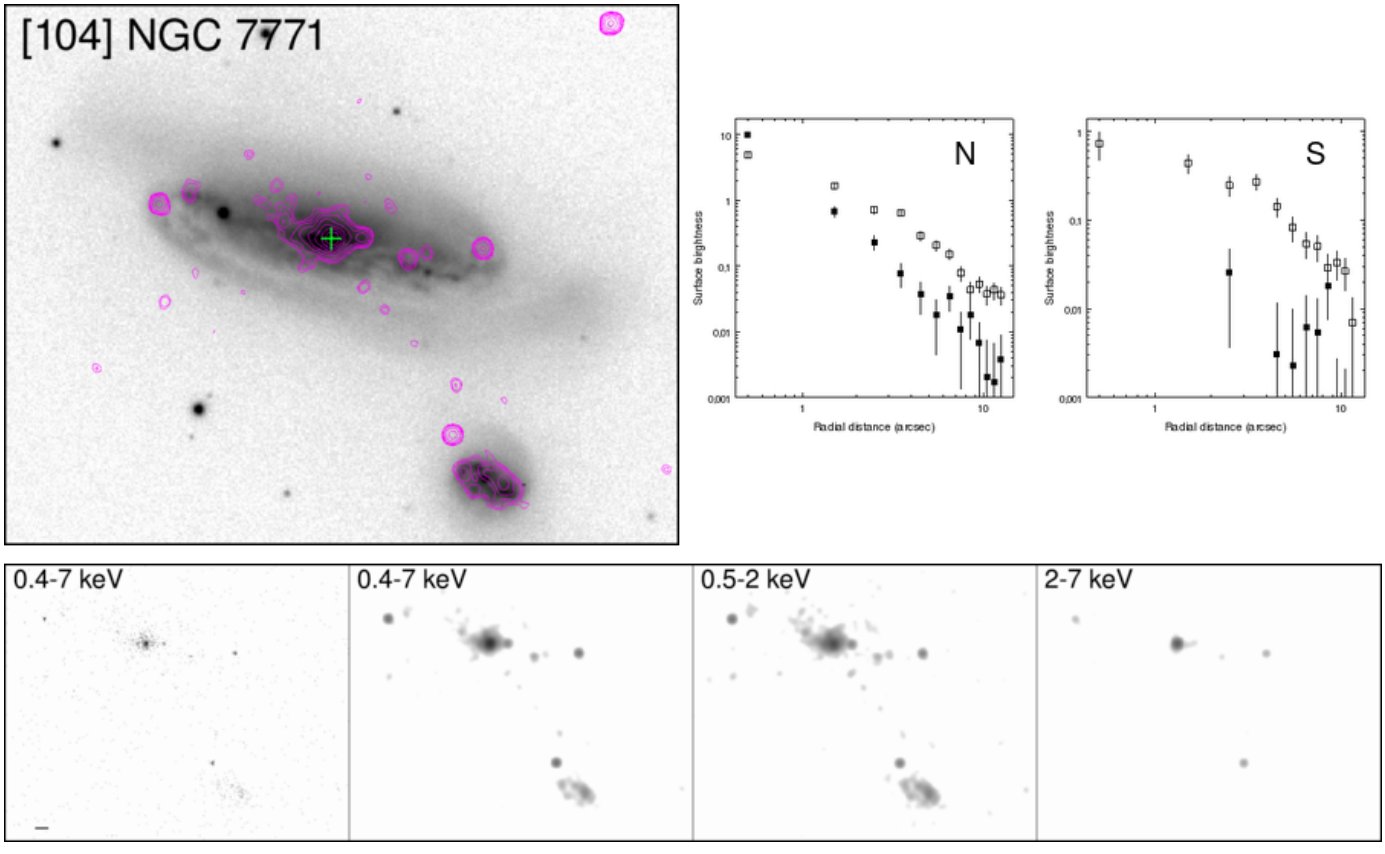

Fig. B.30. *Overlay on* SDSS DR-12 *i*-band. *Contours:* Interval 1.

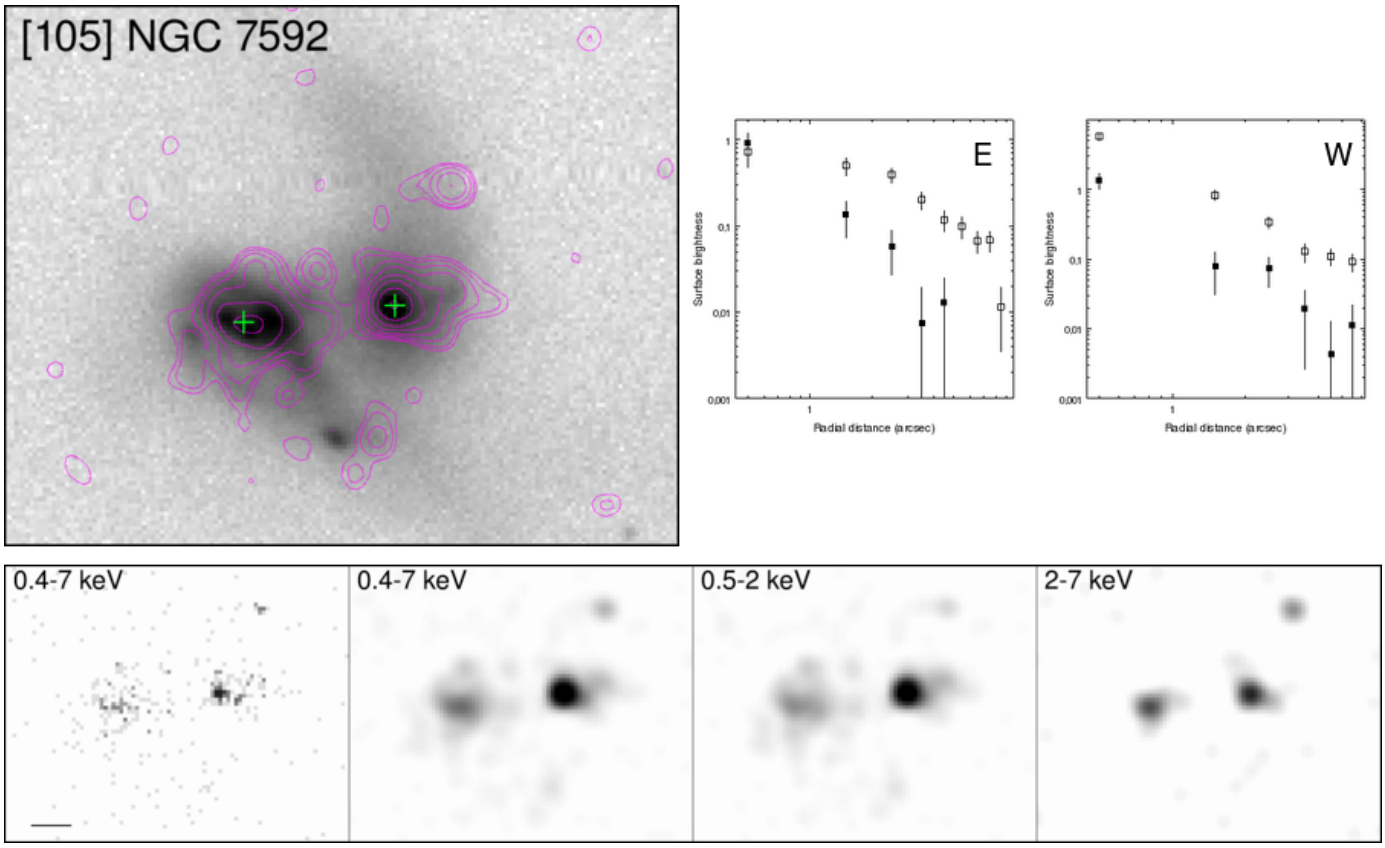

Fig. B.31. *Overlay on* SDSS DR-12 *i*-band. *Contours:* Interval 2.

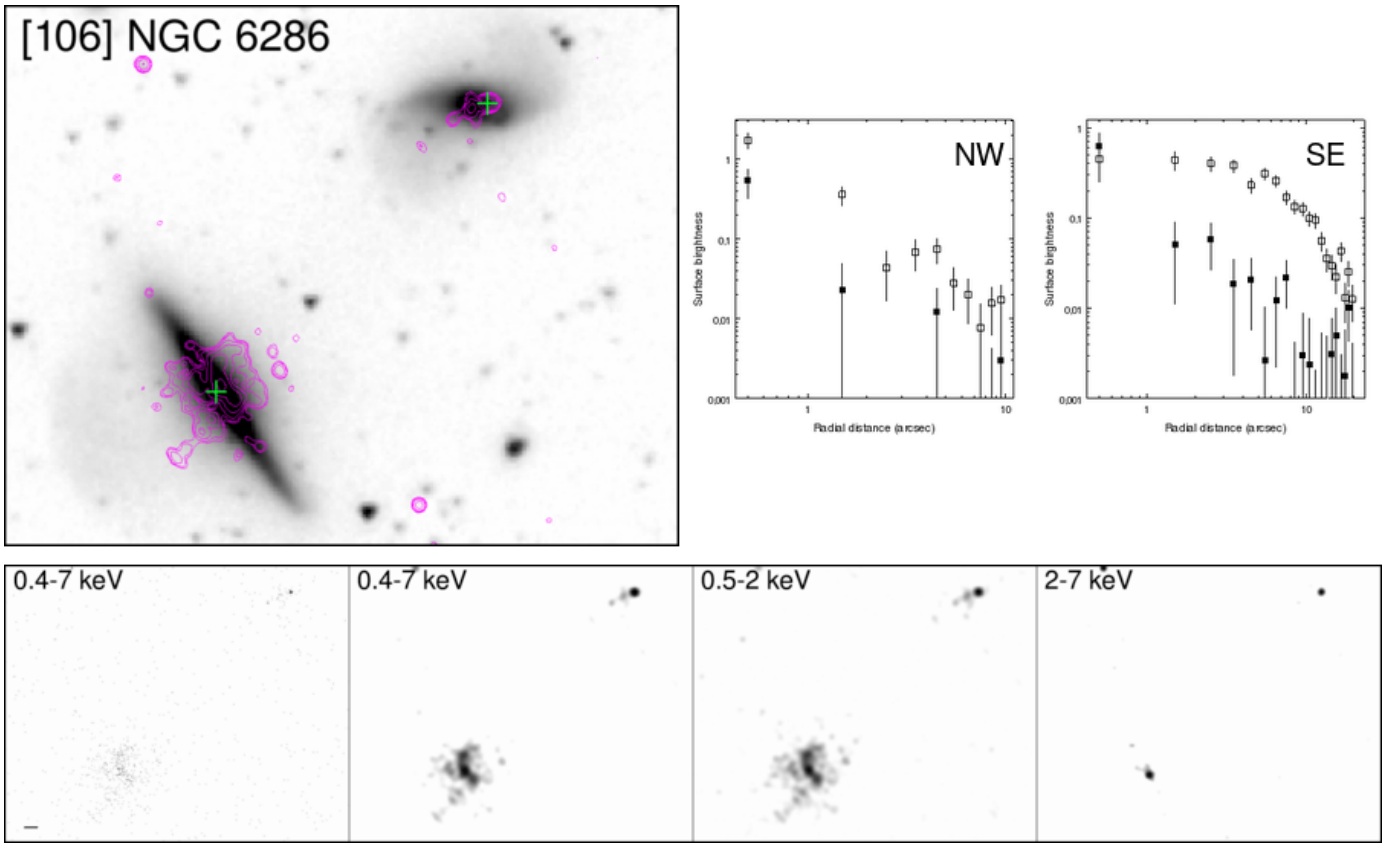

Fig. B.32. *Overlay on* IRAC channel 1. *Contours:* Interval 1.

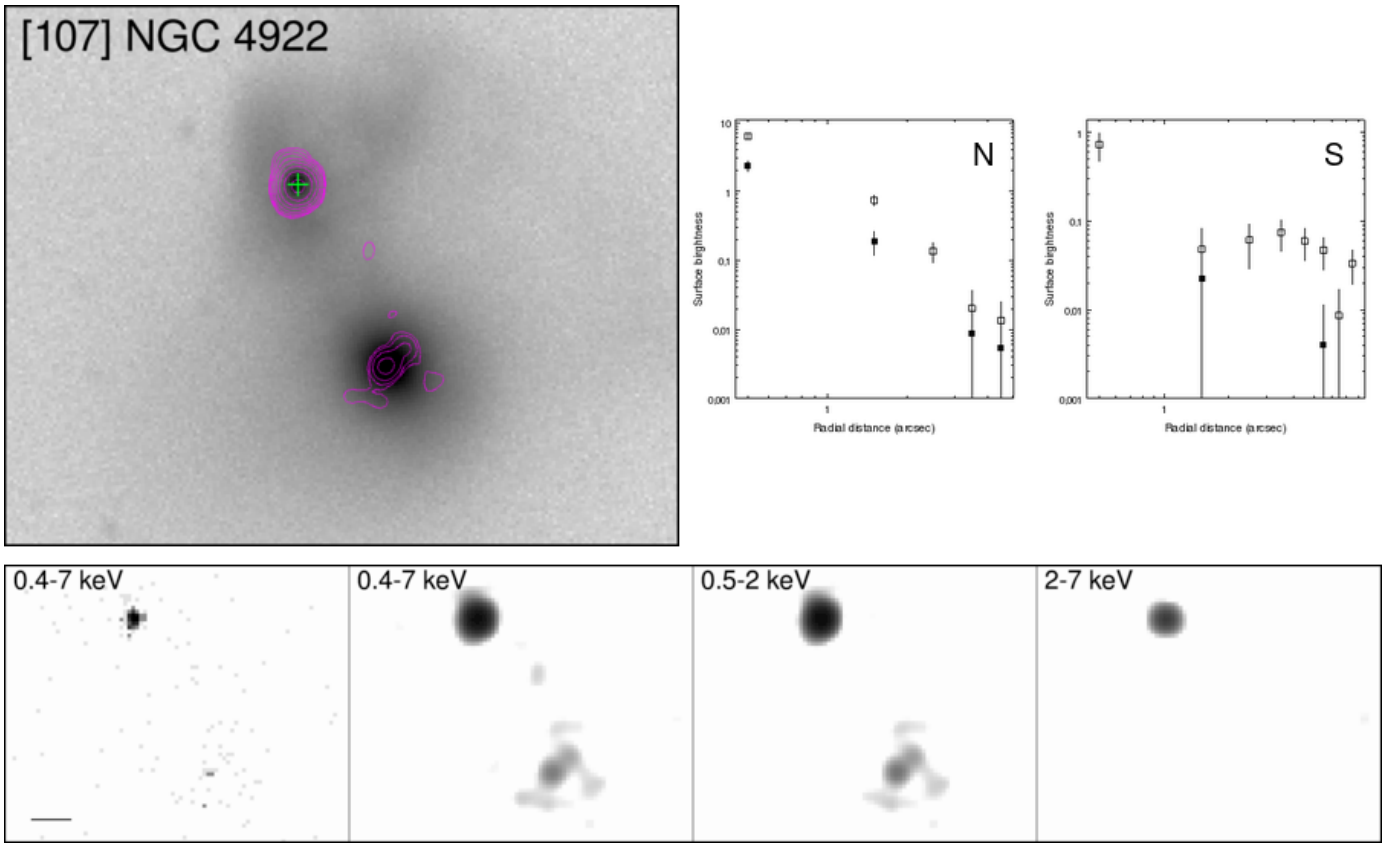

Fig. B.33. *Overlay on* SDSS DR-12 *i*-band. *Contours:* Interval 1.

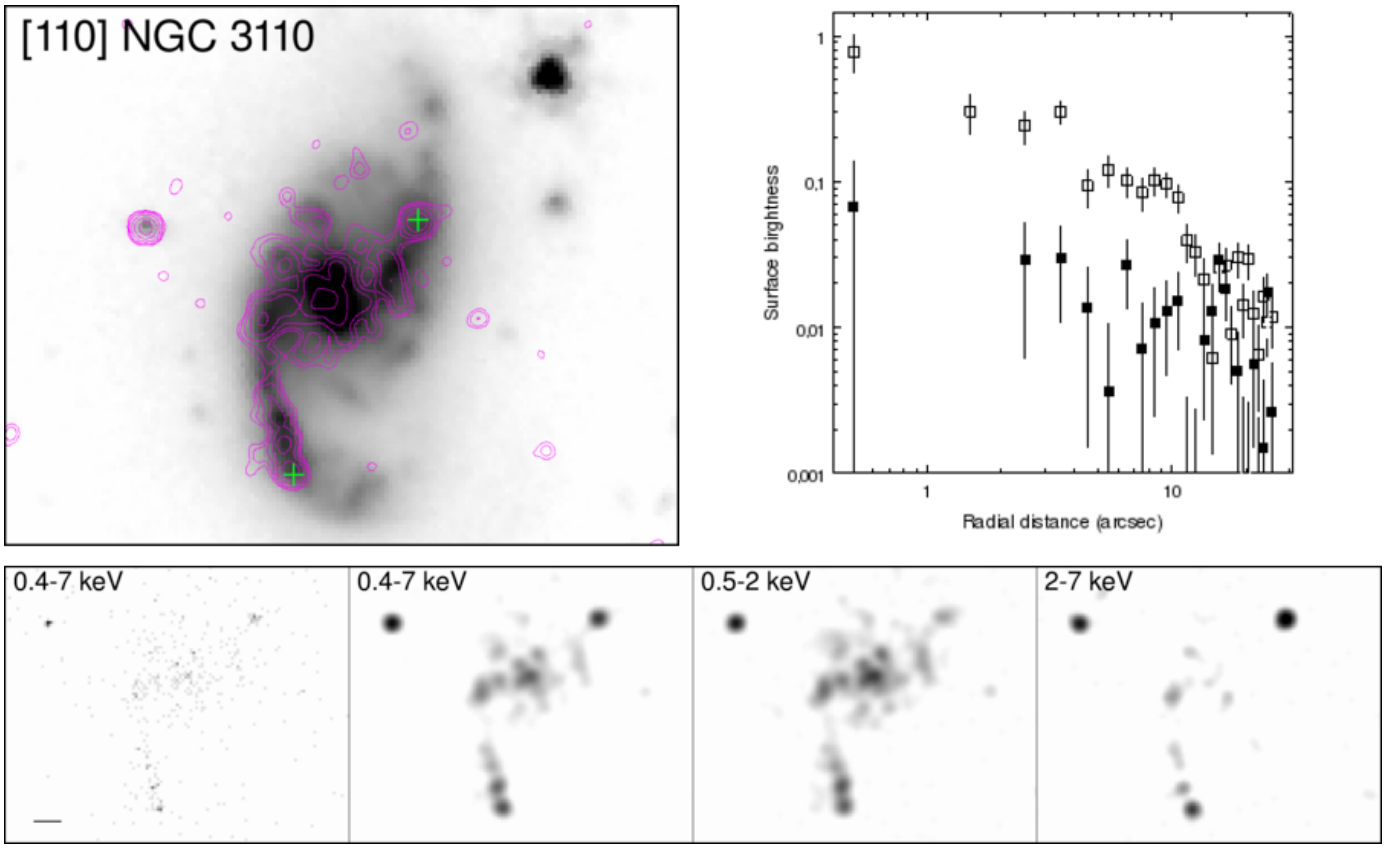

Fig. B.34. *Overlay on* IRAC channel 1. *Contours:* Interval 2.

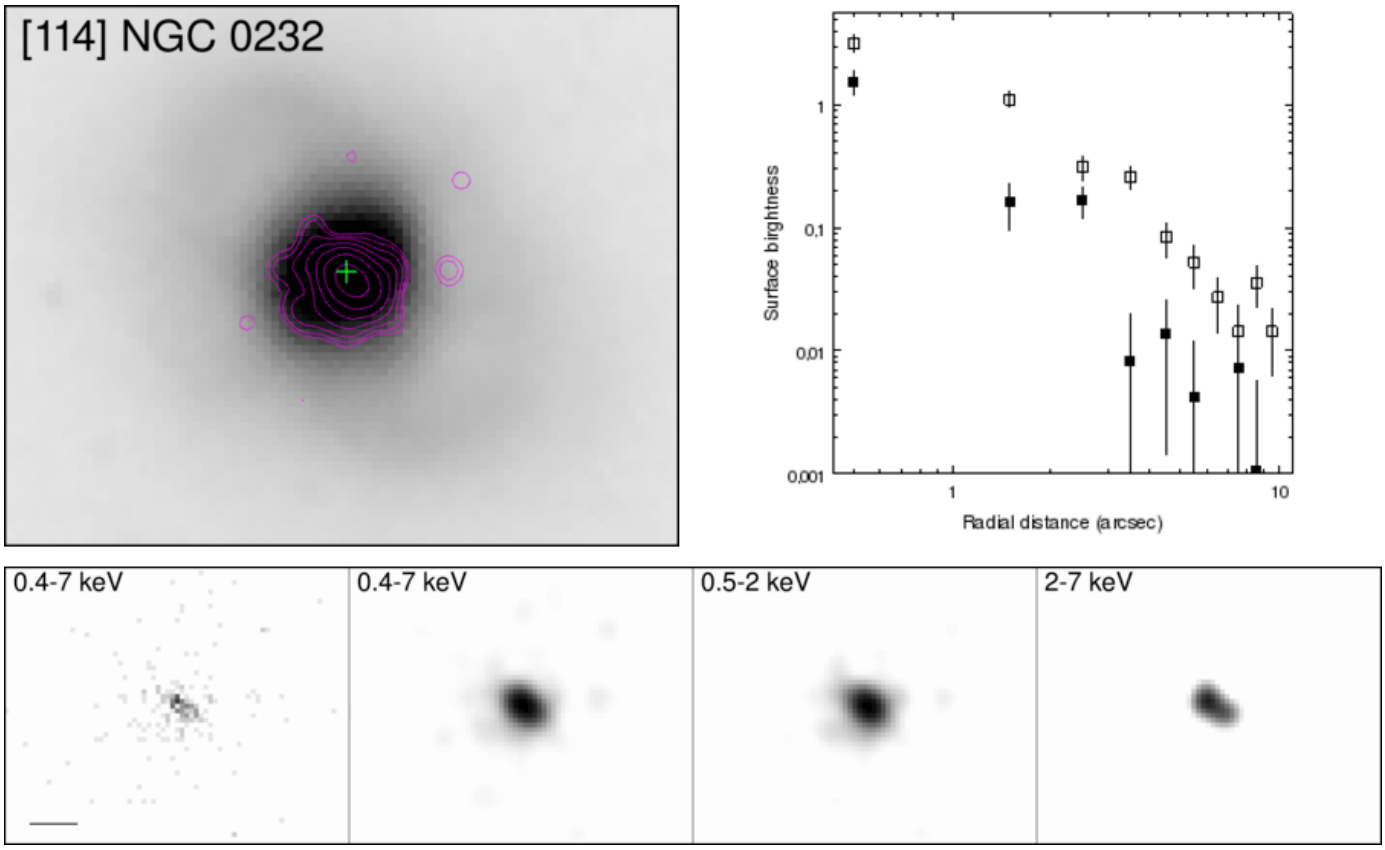

Fig. B.35. *Overlay on* IRAC channel 1. *Contours:* Interval 1.

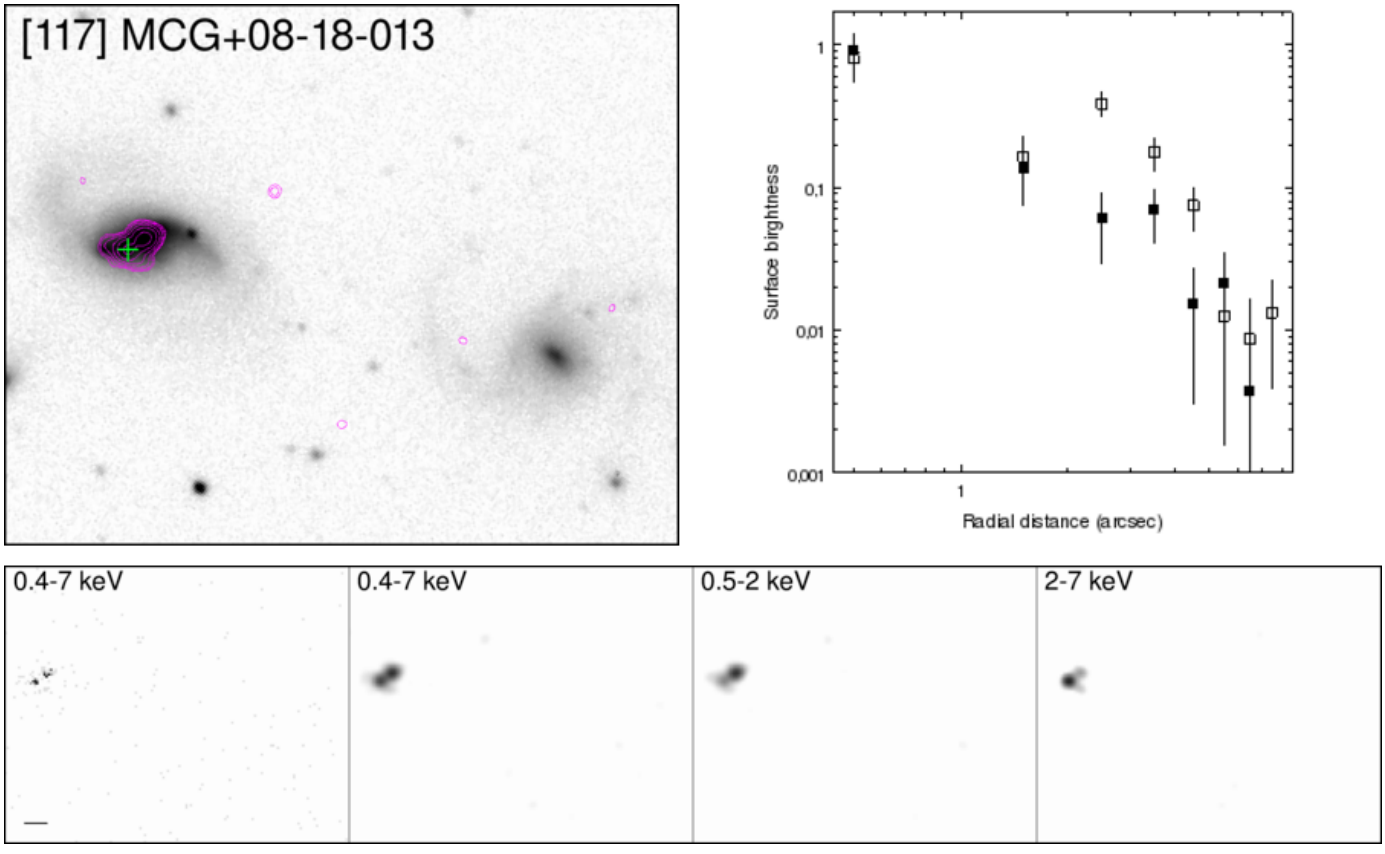

Fig. B.36. *Overlay on* SDSS DR-12 *i*-band. *Contours:* Interval 1.

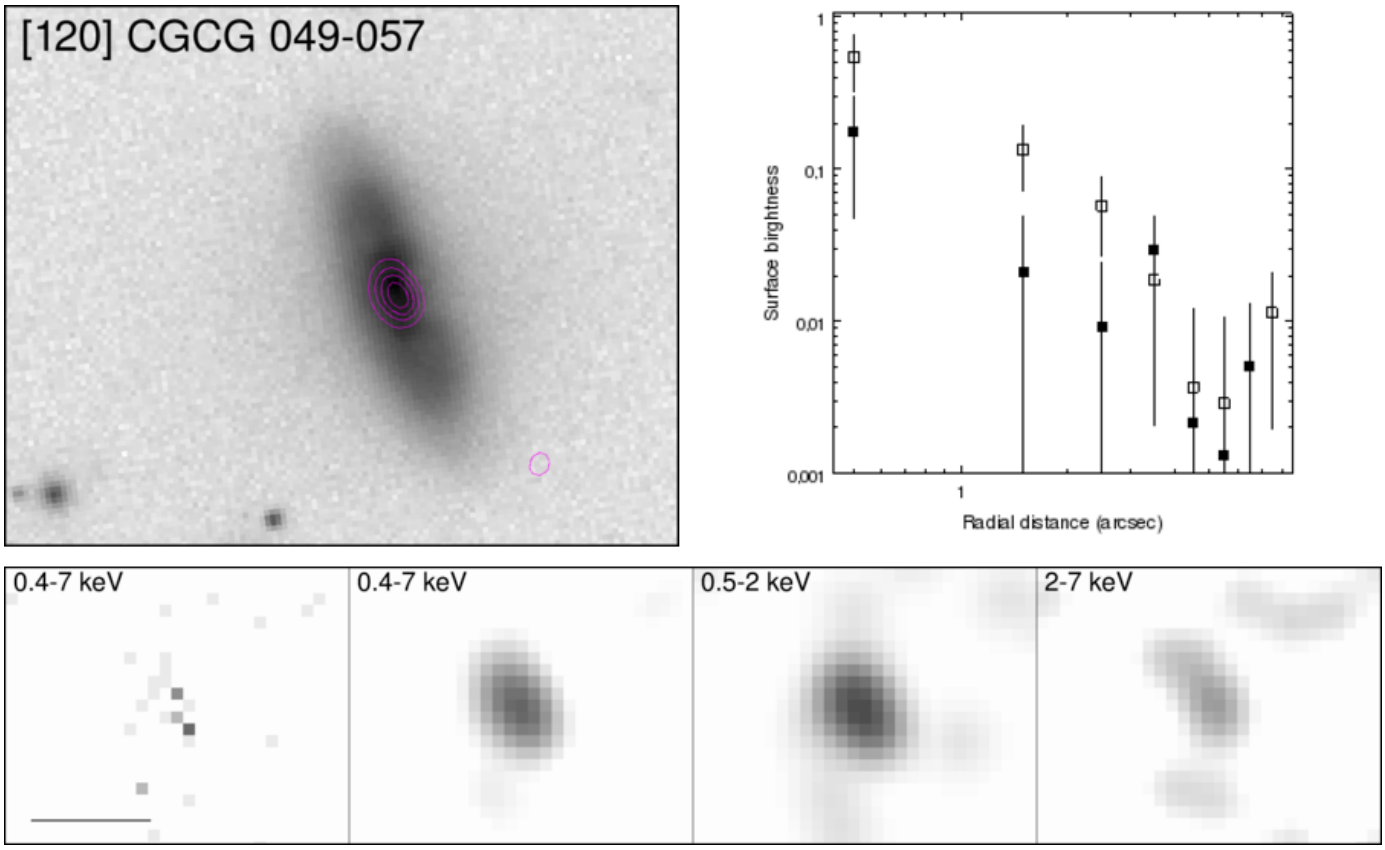

Fig. B.37. *Overlay on* SDSS DR-12 *i*-band. *Contours:* Custom.

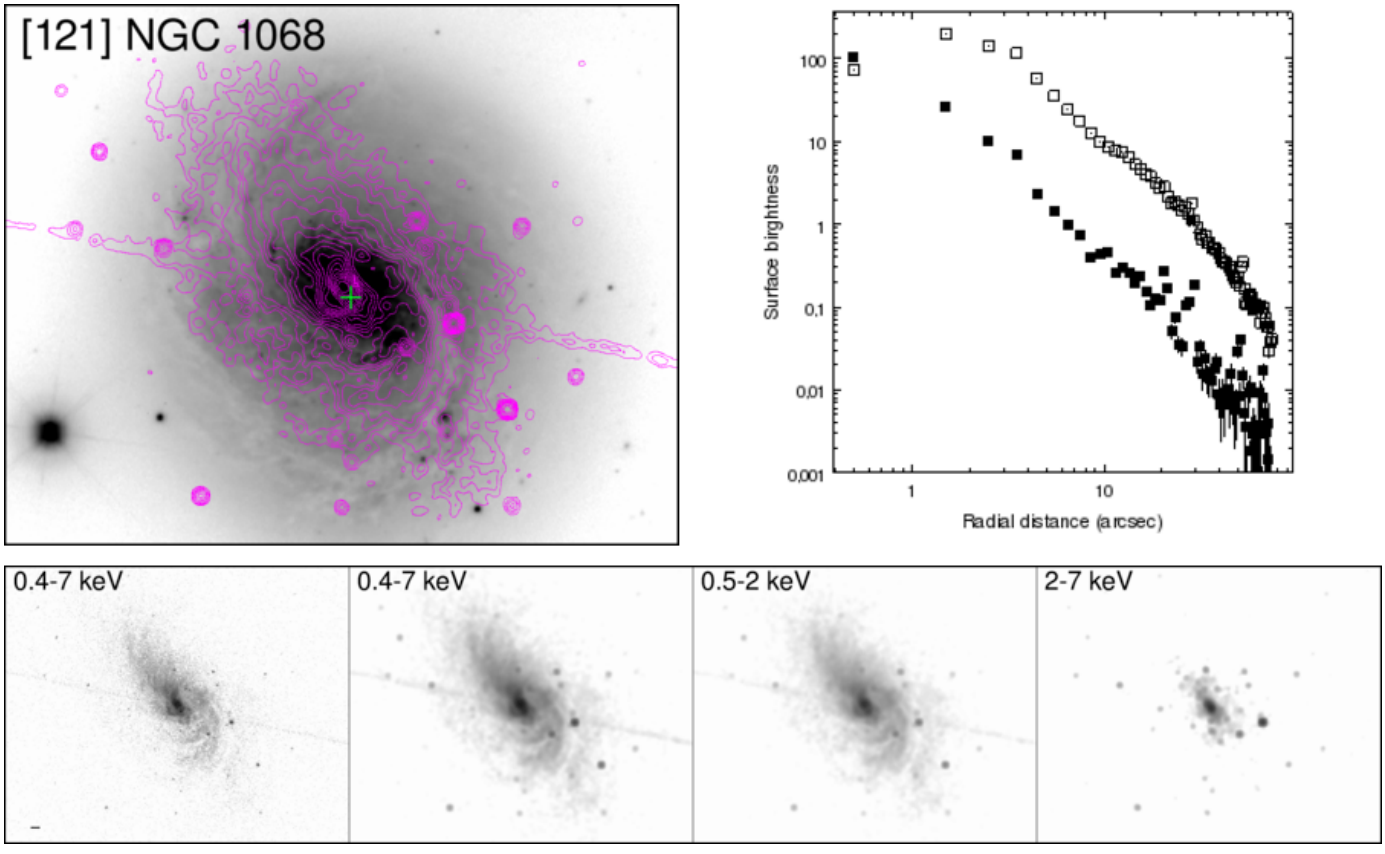

Fig. B.38. *Overlay on* SDSS DR-12 *i*-band. *Contours:* Custom.

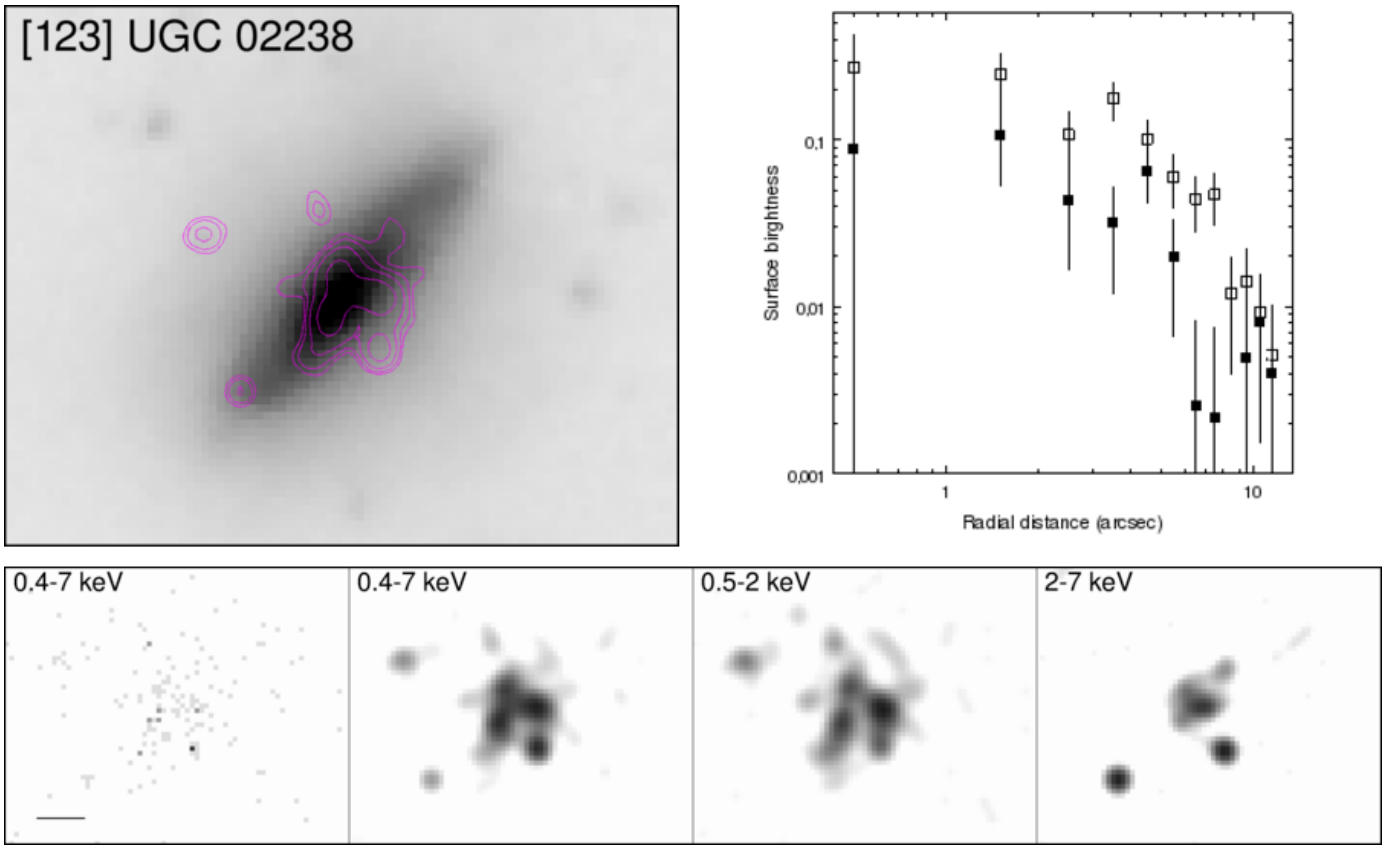

Fig. B.39. *Overlay on* IRAC channel 1. *Contours:* Interval 1.

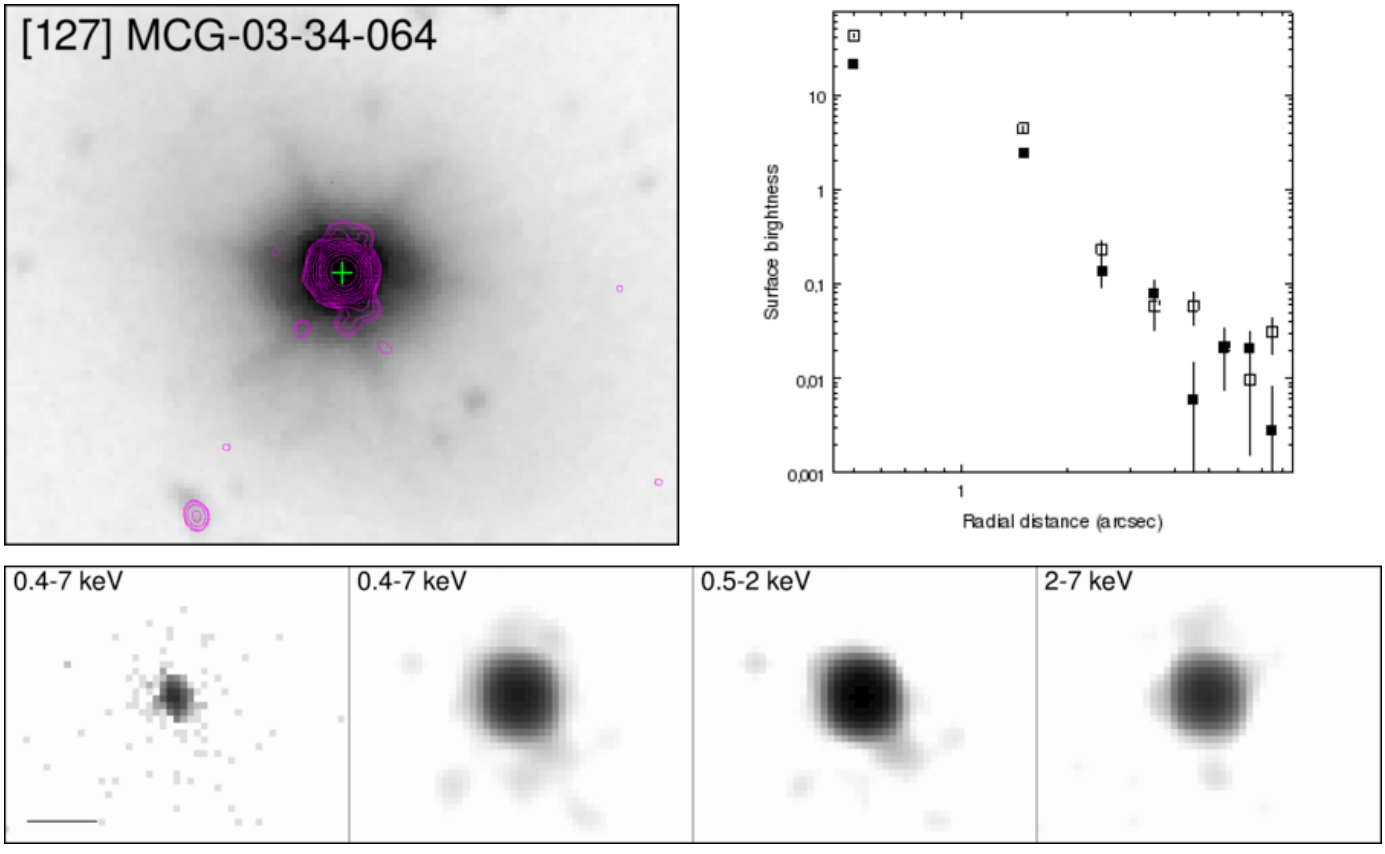

Fig. B.40. *Overlay on* IRAC channel 1. *Contours:* Interval 4.

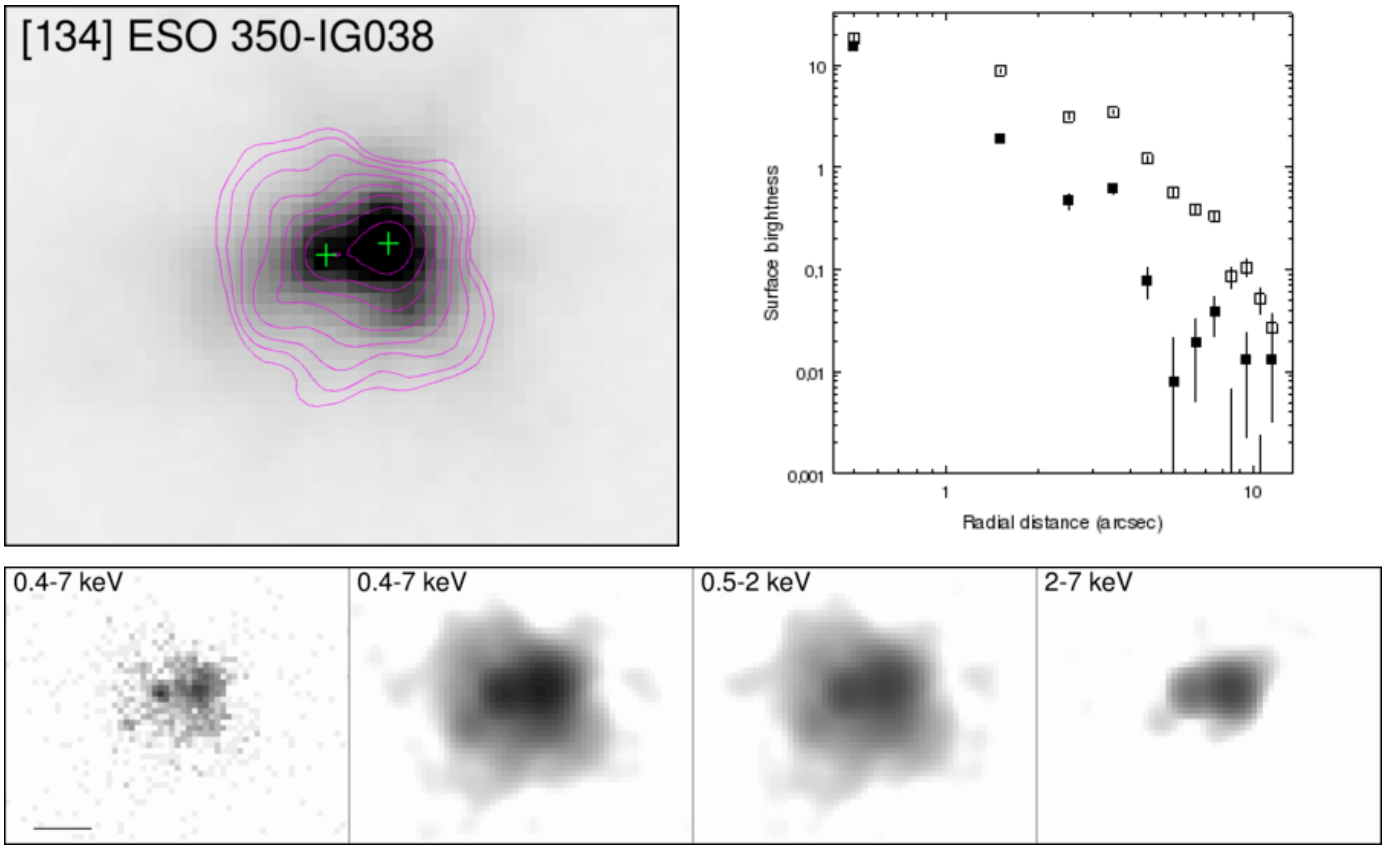

Fig. B.41. *Overlay on* IRAC channel 1. *Contours:* Interval 2.

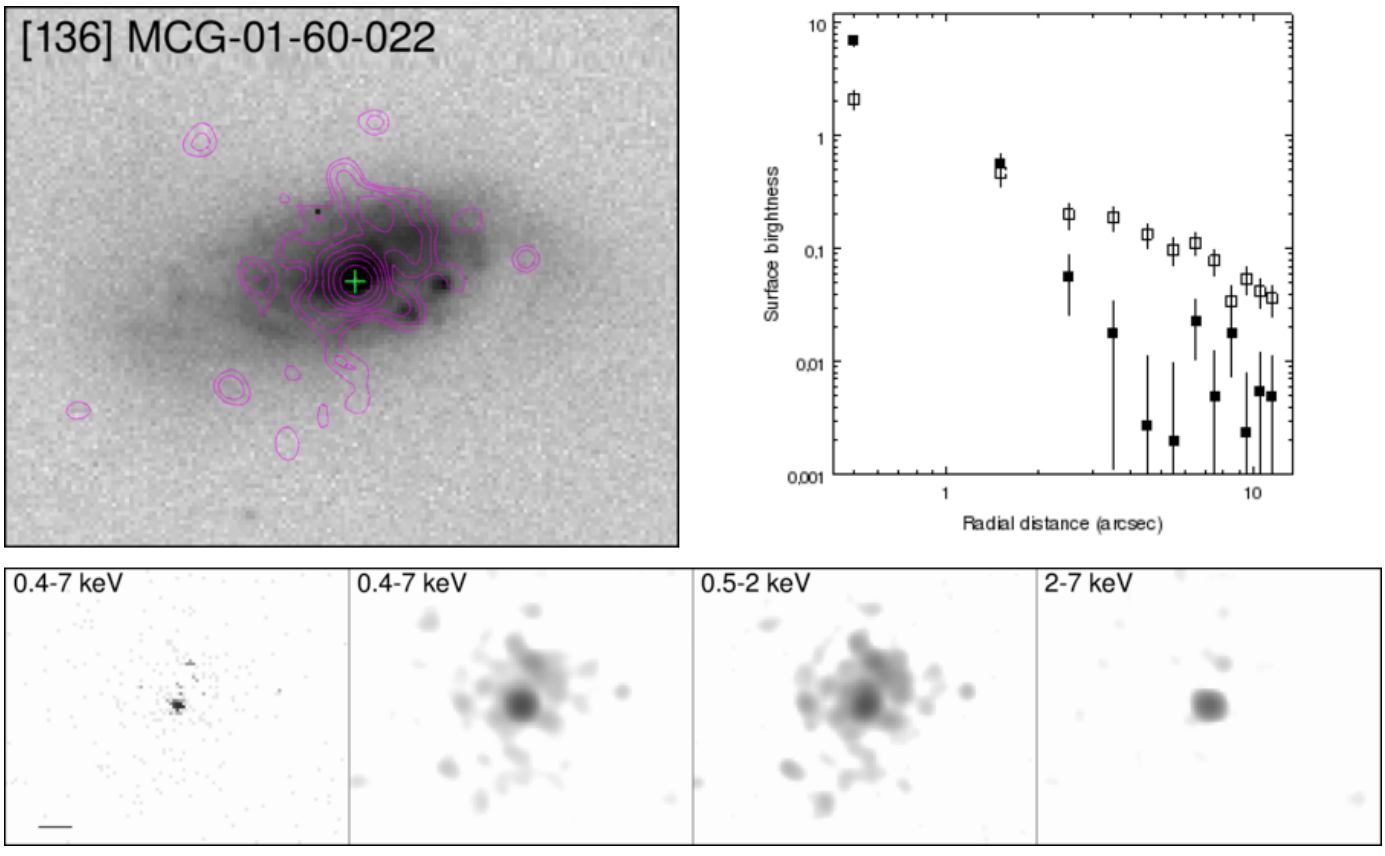

Fig. B.42. *Overlay on* SDSS DR-12 *i*-band. *Contours:* Interval 2.

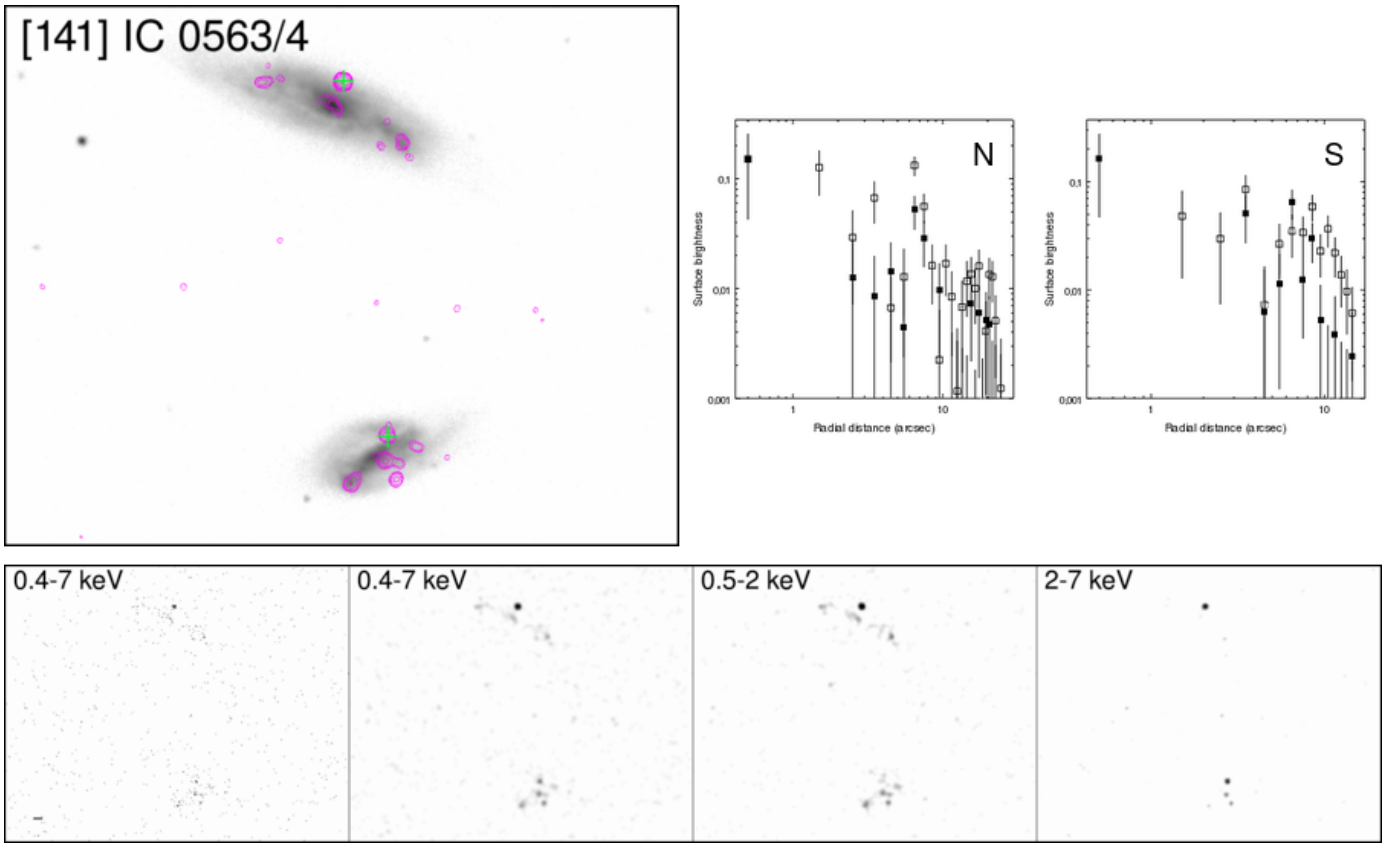

Fig. B.43. *Overlay on* SDSS DR-12 *i*-band. *Contours:* Interval 1.

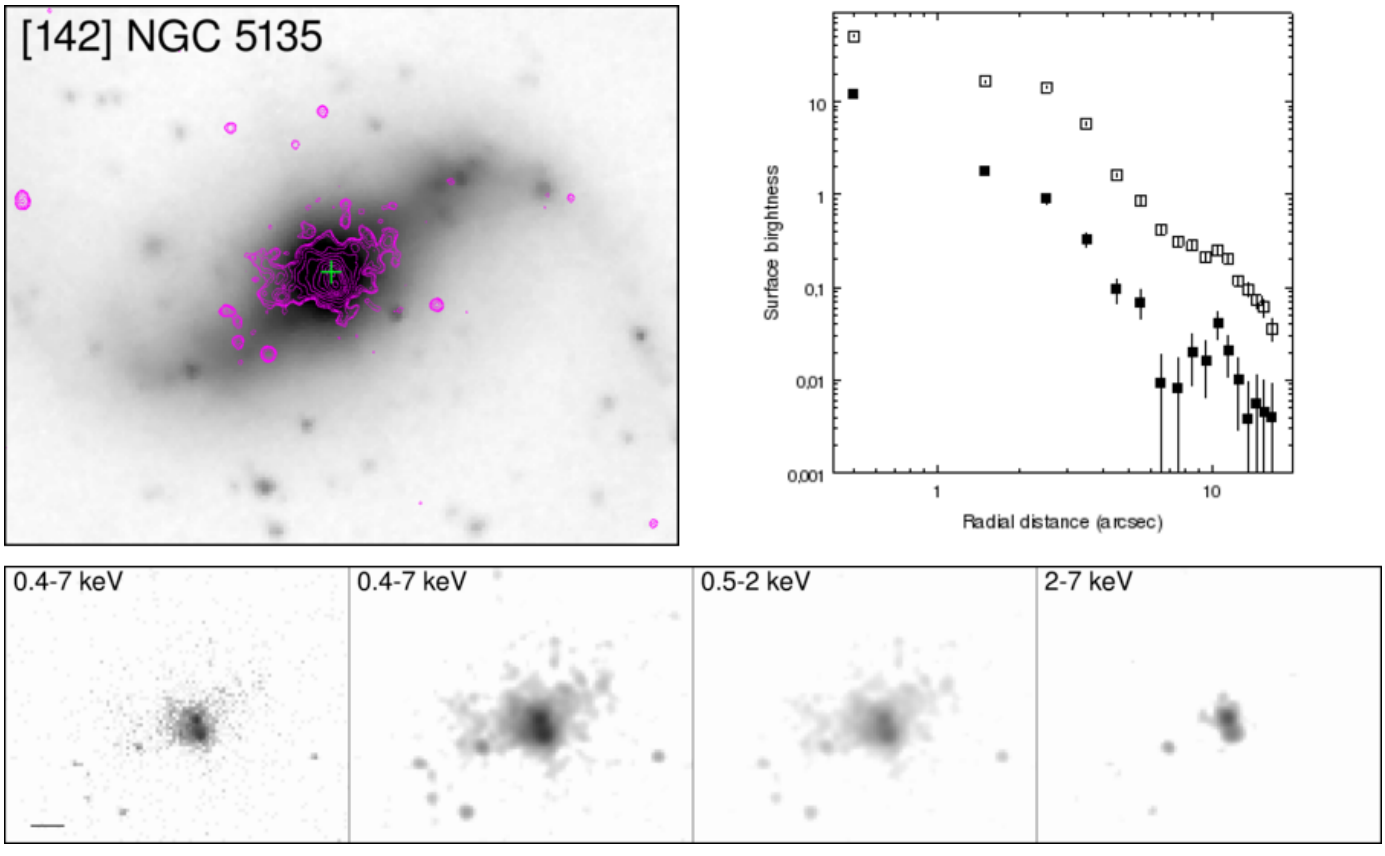

Fig. B.44. *Overlay on* IRAC channel 1. *Contours:* Custom.

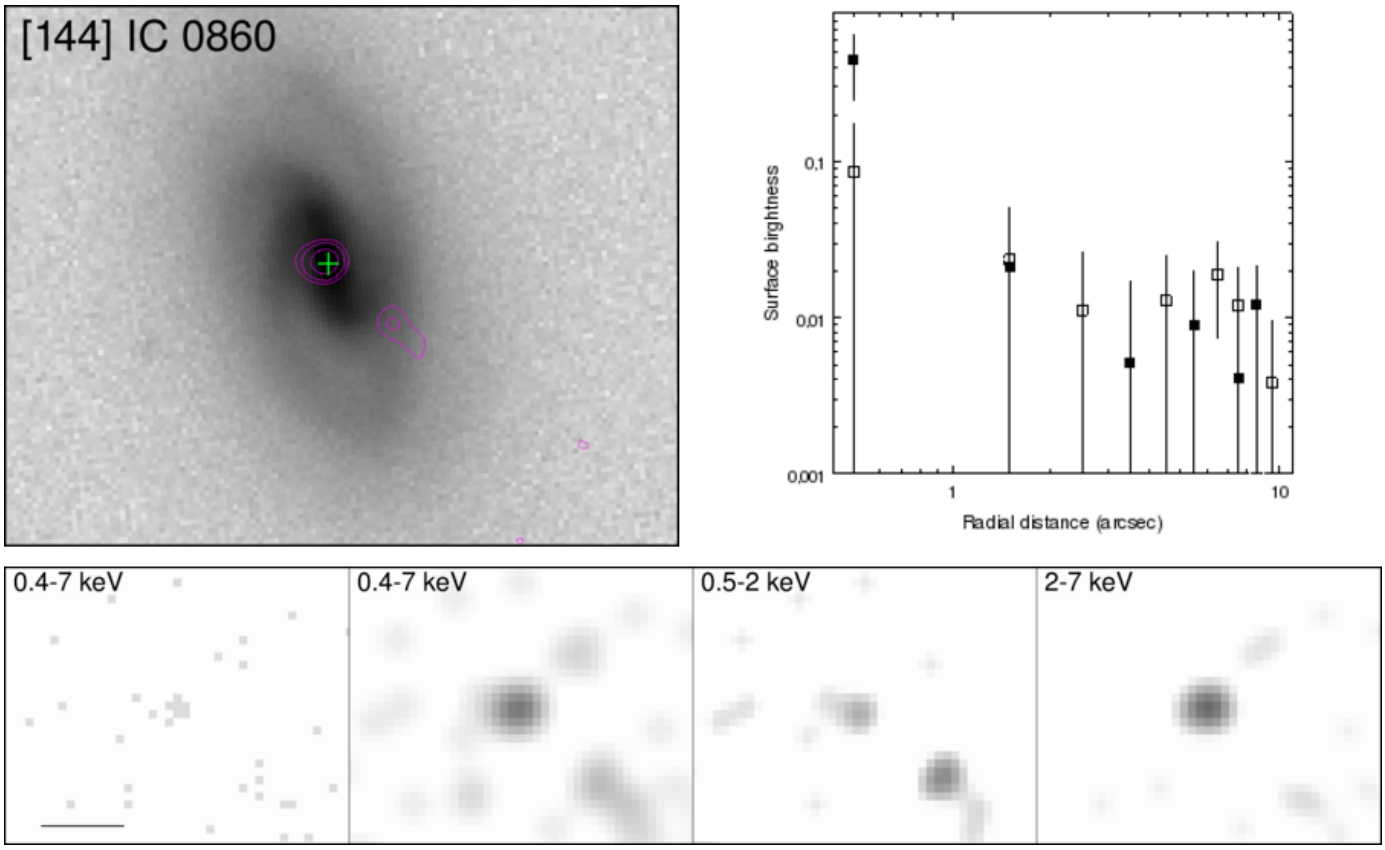

Fig. B.45. *Overlay on* SDSS DR-12 *i*-band. *Contours:* Interval 2.

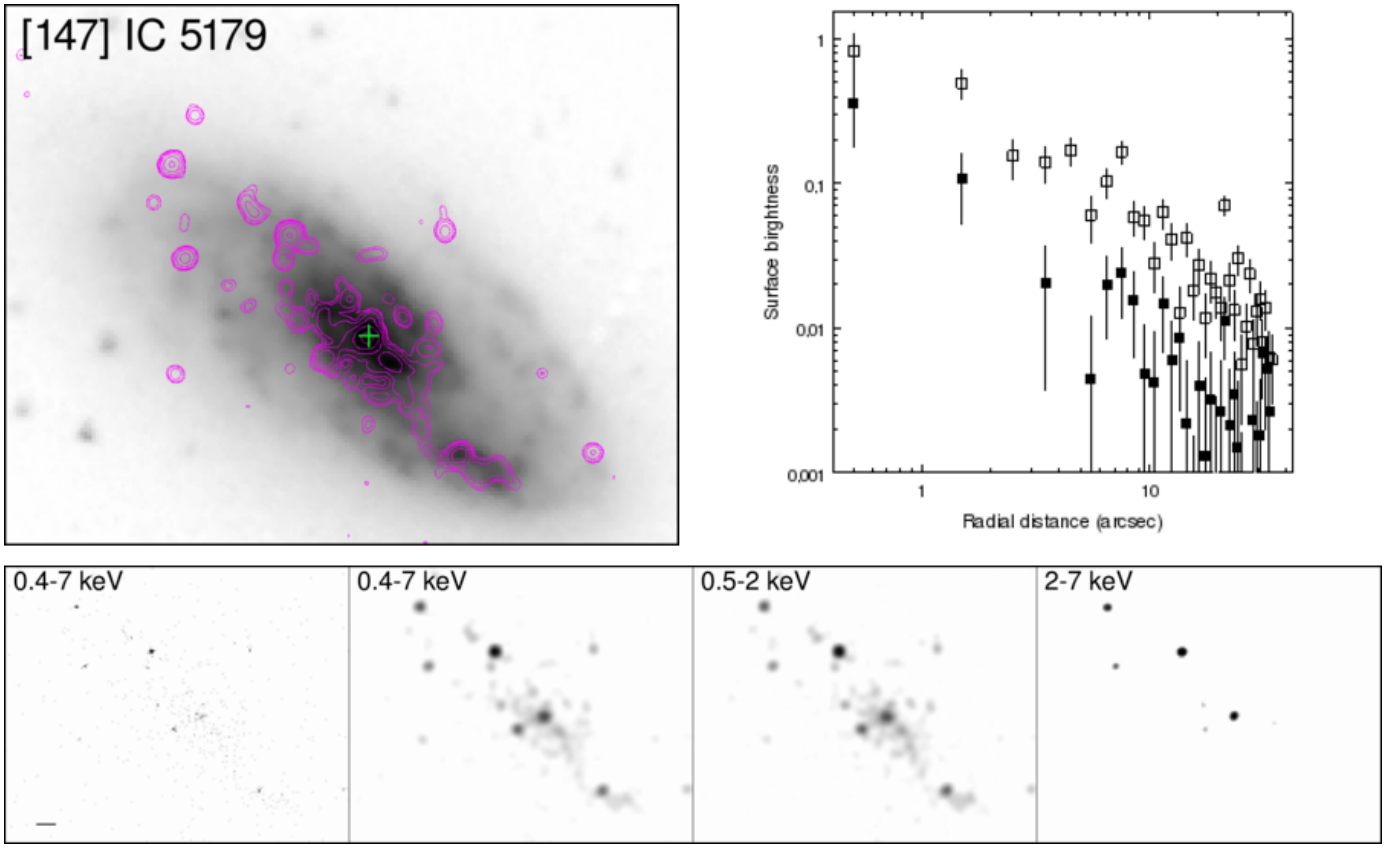

Fig. B.46. *Overlay on* IRAC channel 1. *Contours:* Interval 1.

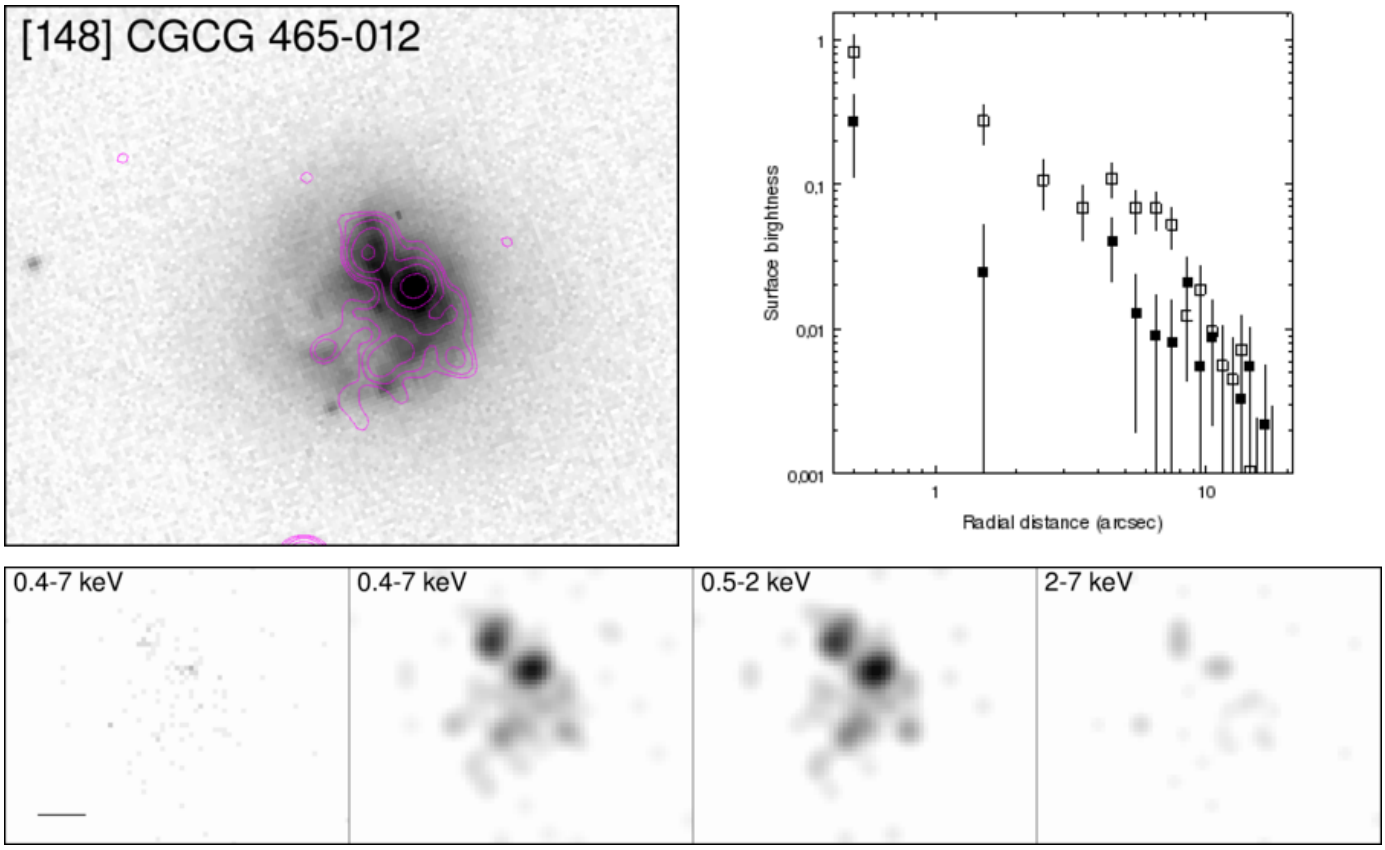

Fig. B.47. *Overlay on* SDSS DR-12 *i*-band. *Contours:* Interval 2.

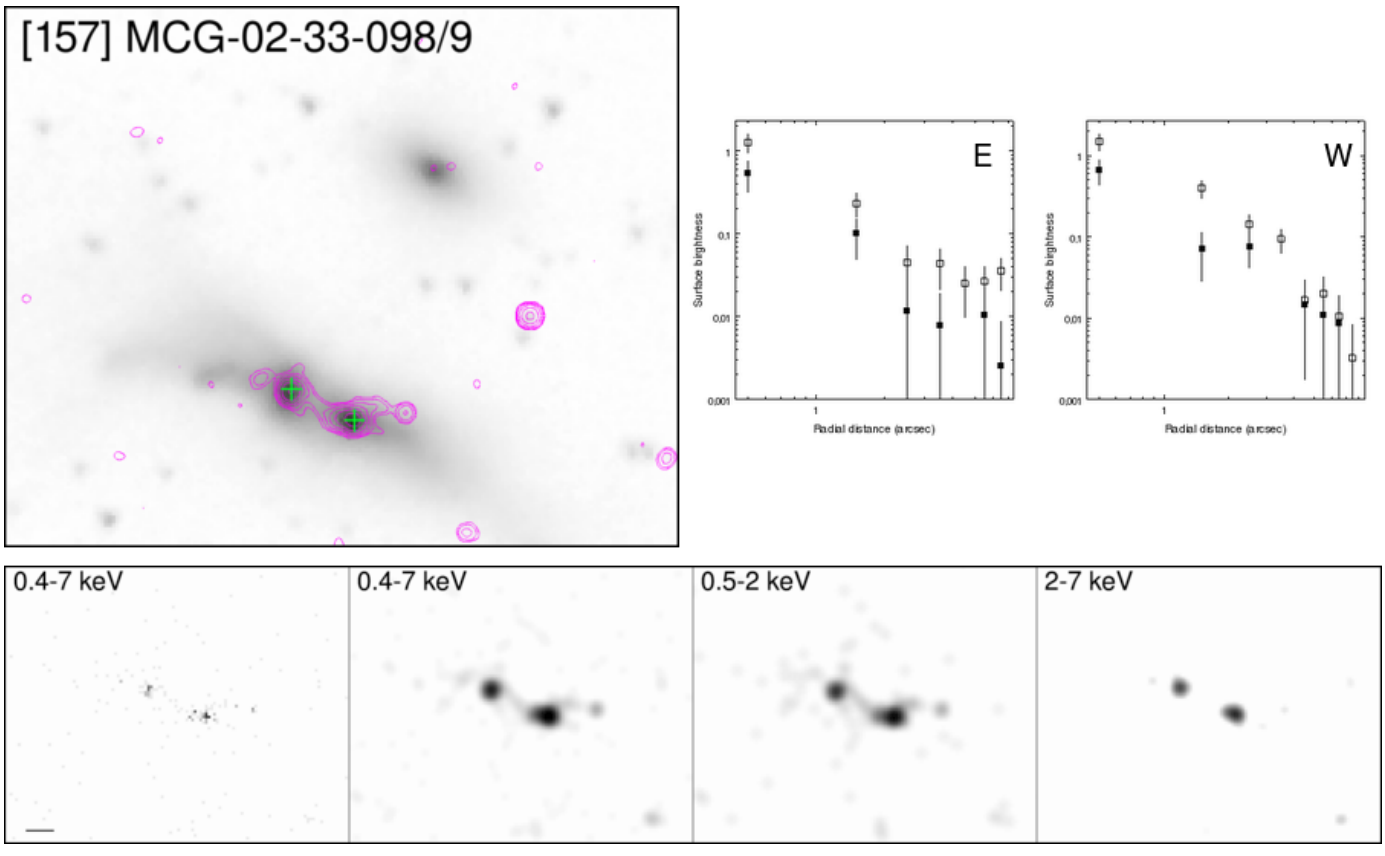

Fig. B.48. *Overlay on* IRAC channel 1. *Contours:* Interval 1.

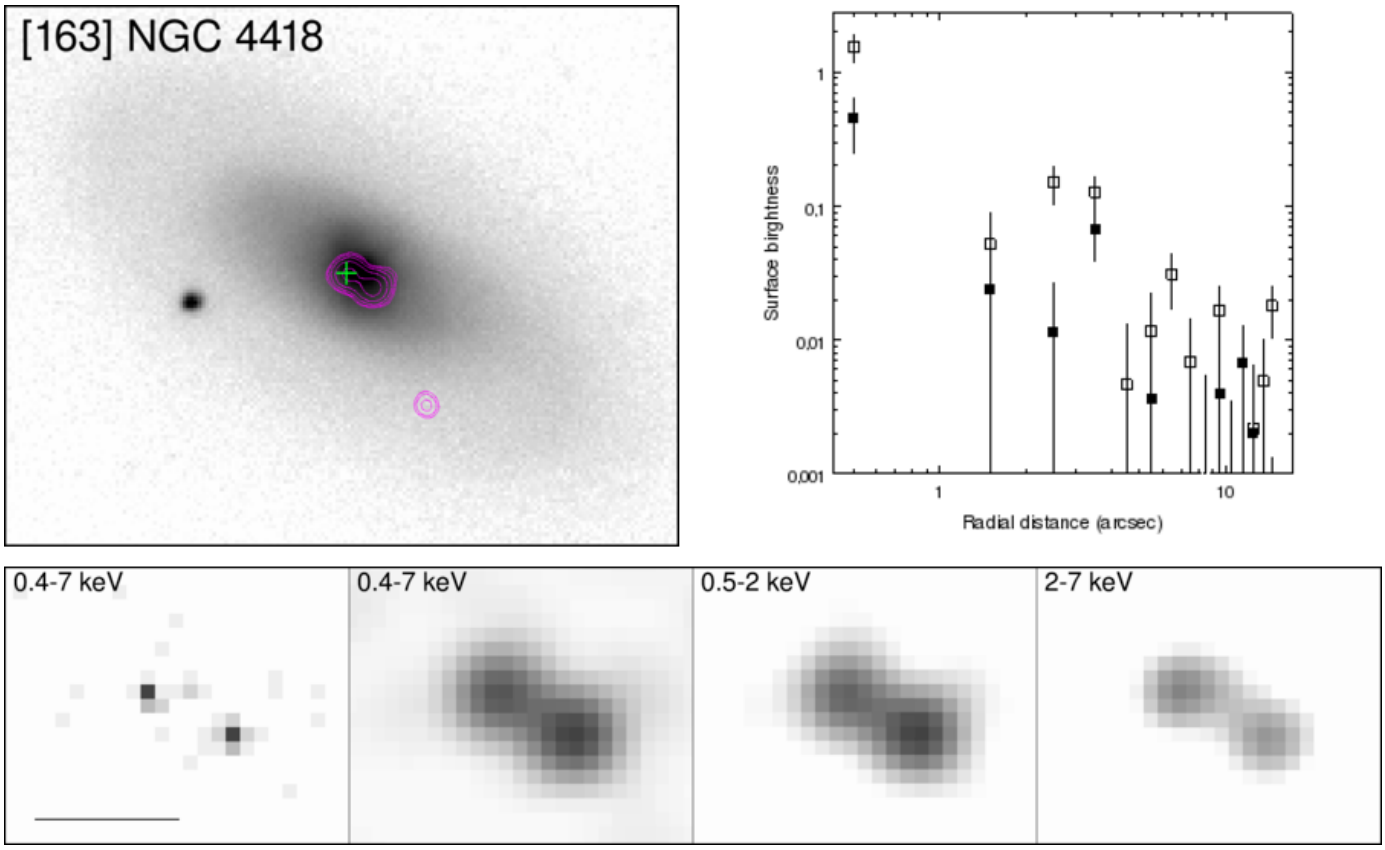

Fig. B.49. *Overlay on* SDSS DR-12 *i*-band. *Contours:* Interval 1.

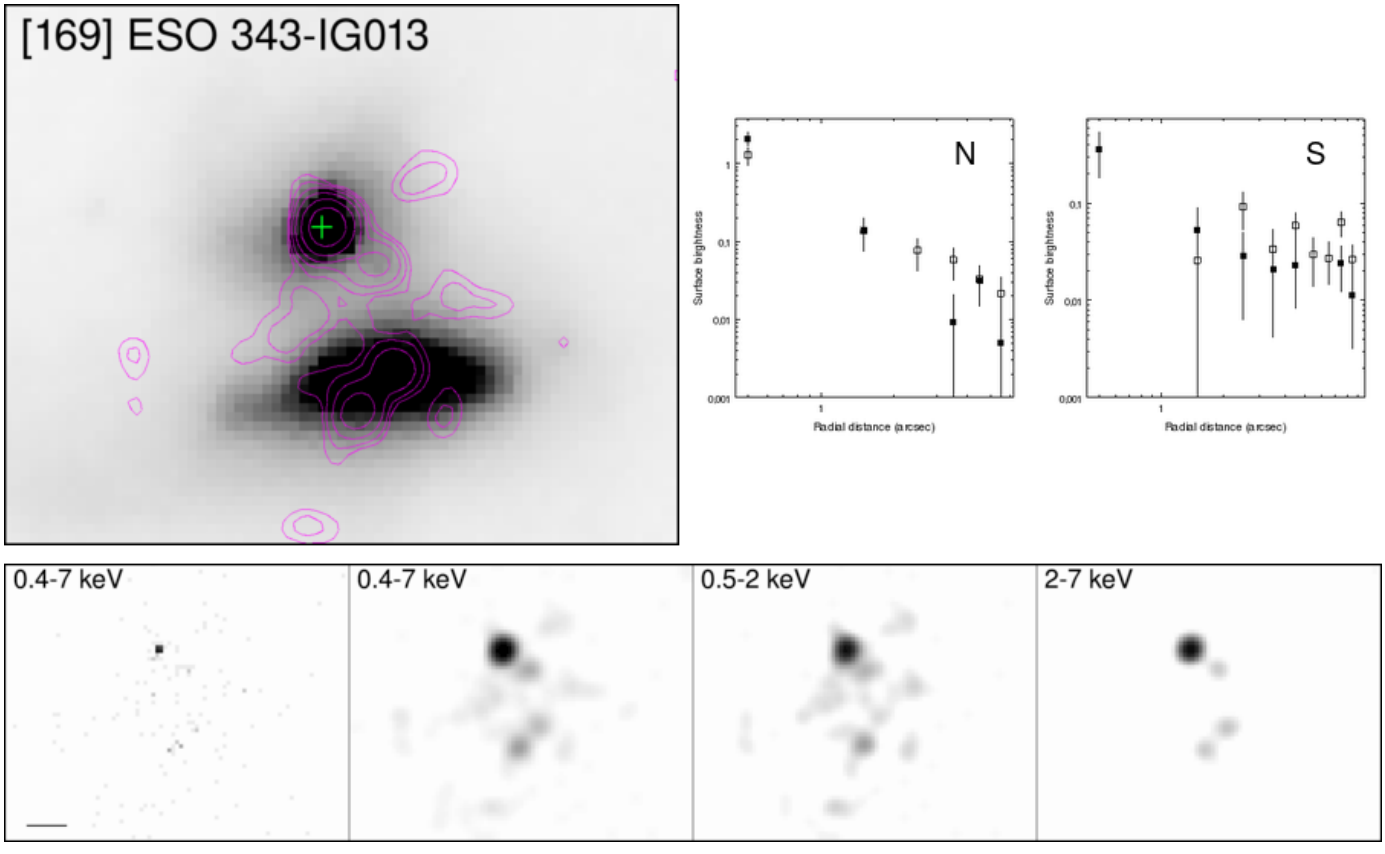

Fig. B.50. *Overlay on* IRAC channel 1. *Contours:* Interval 2.

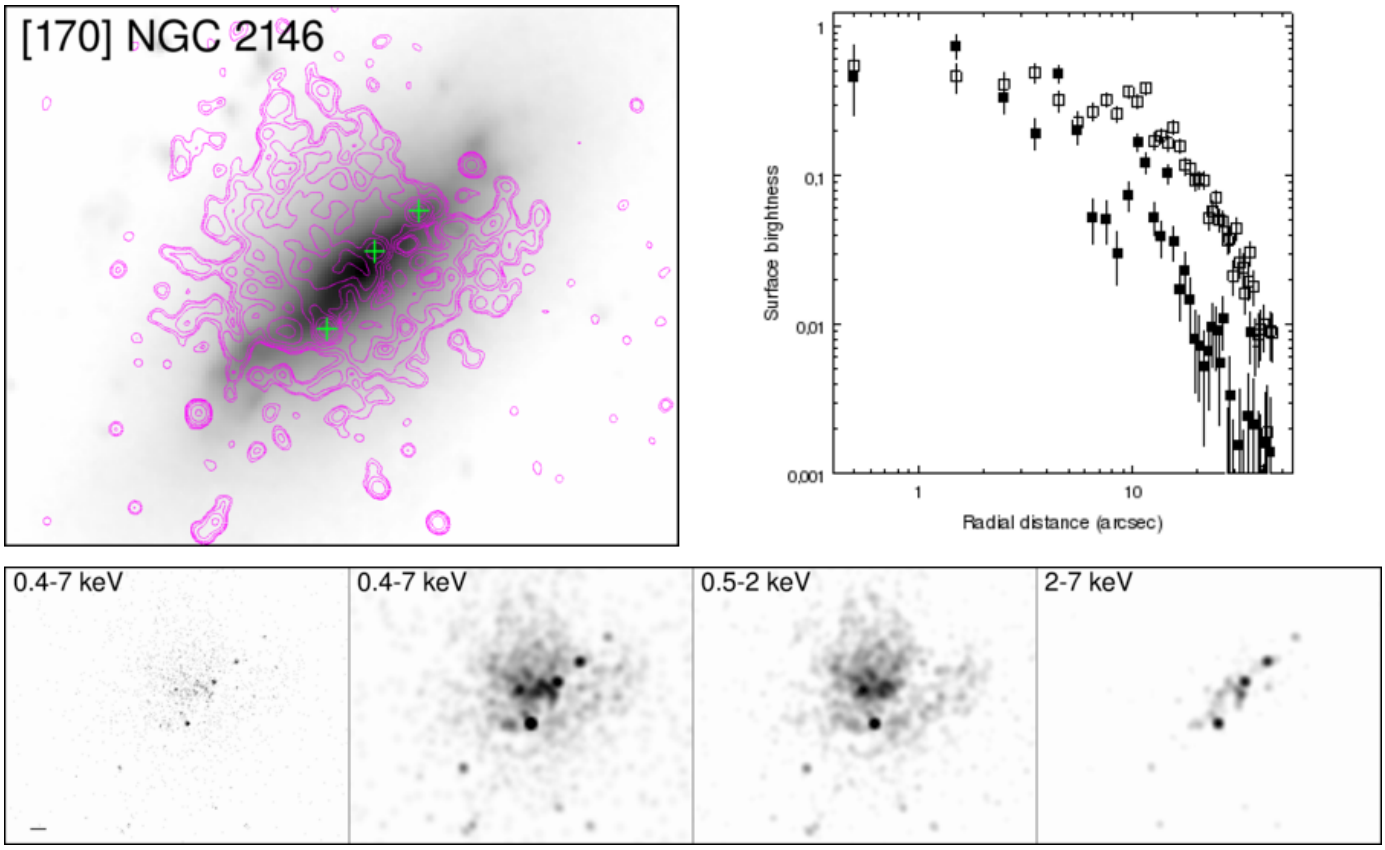

Fig. B.51. *Overlay on* IRAC channel 1. *Contours:* Interval 1.

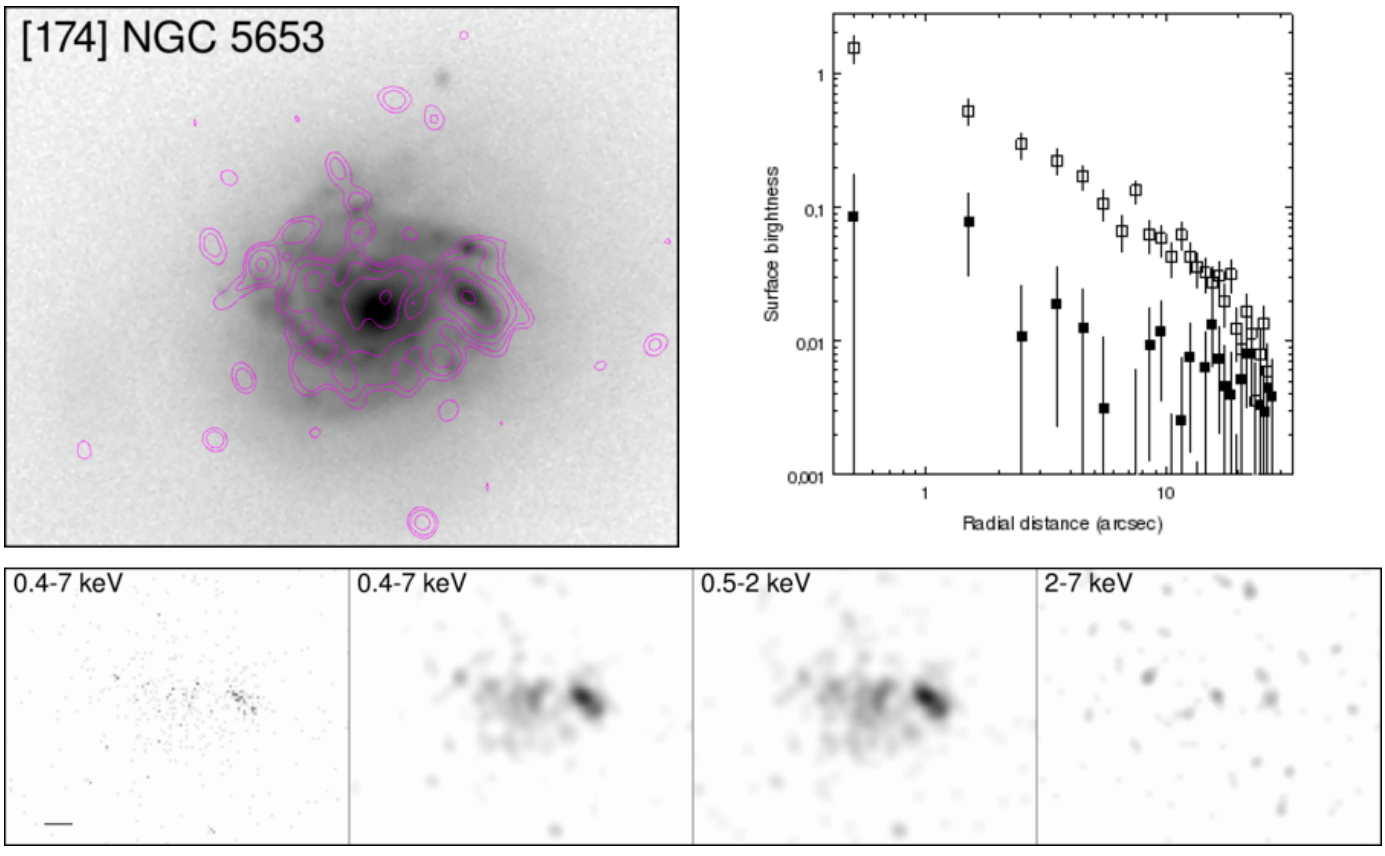

Fig. B.52. *Overlay on* SDSS DR-12 *i*-band. *Contours:* Interval 2.

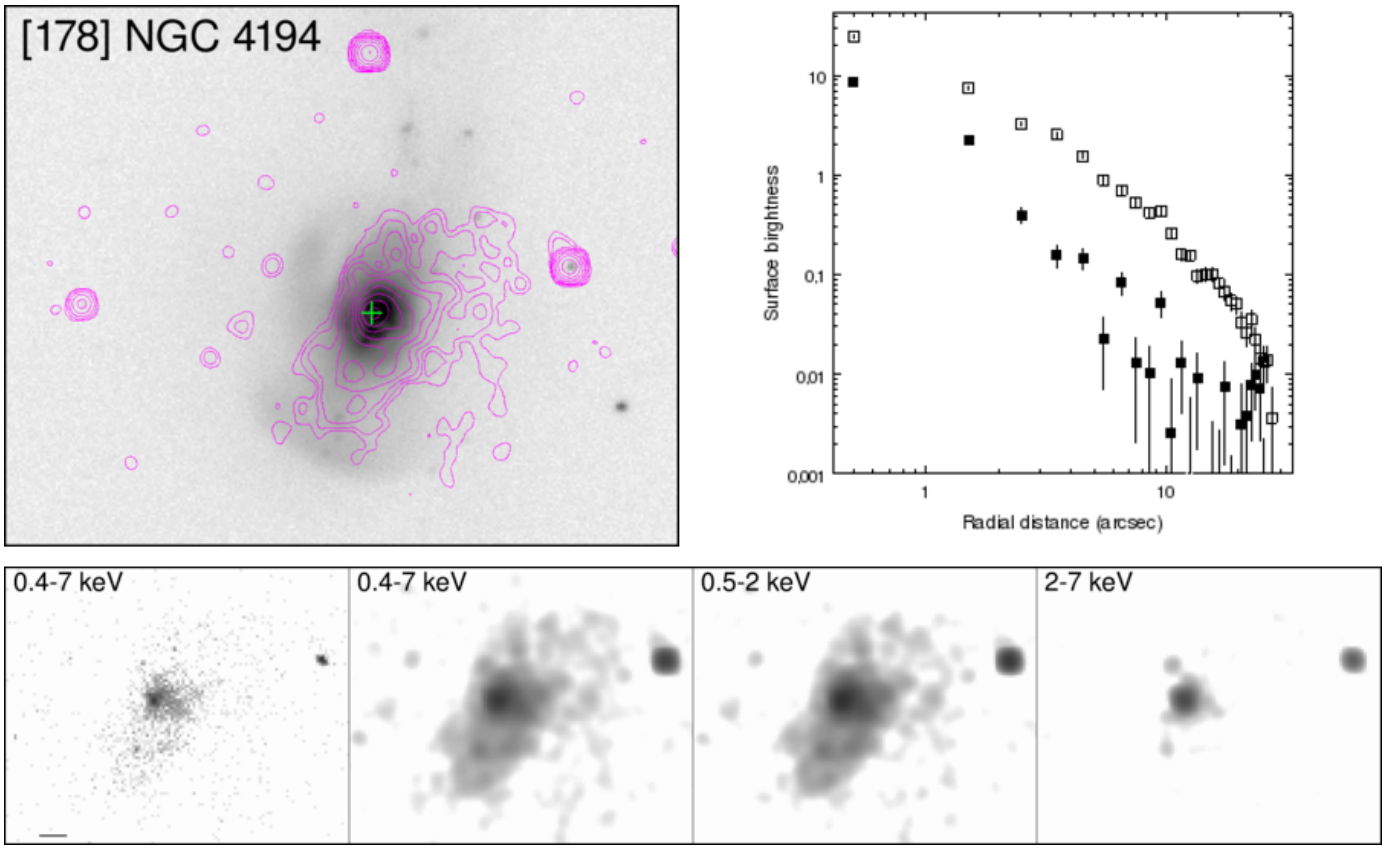

Fig. B.53. *Overlay on* SDSS DR-12 *i*-band. *Contours:* Interval 1.

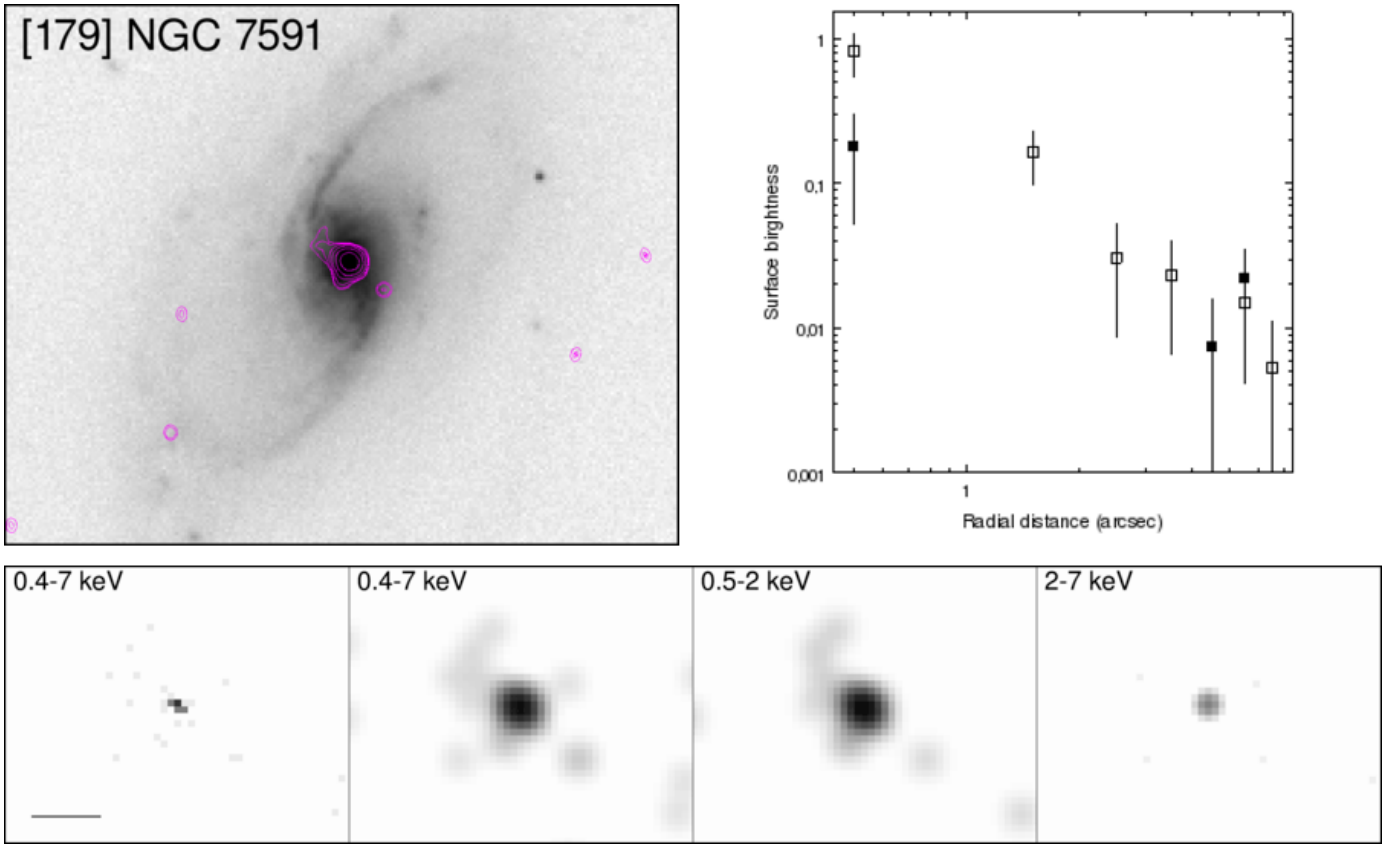

Fig. B.54. *Overlay on* SDSS DR-12 *i*-band. *Contours:* Interval 4.

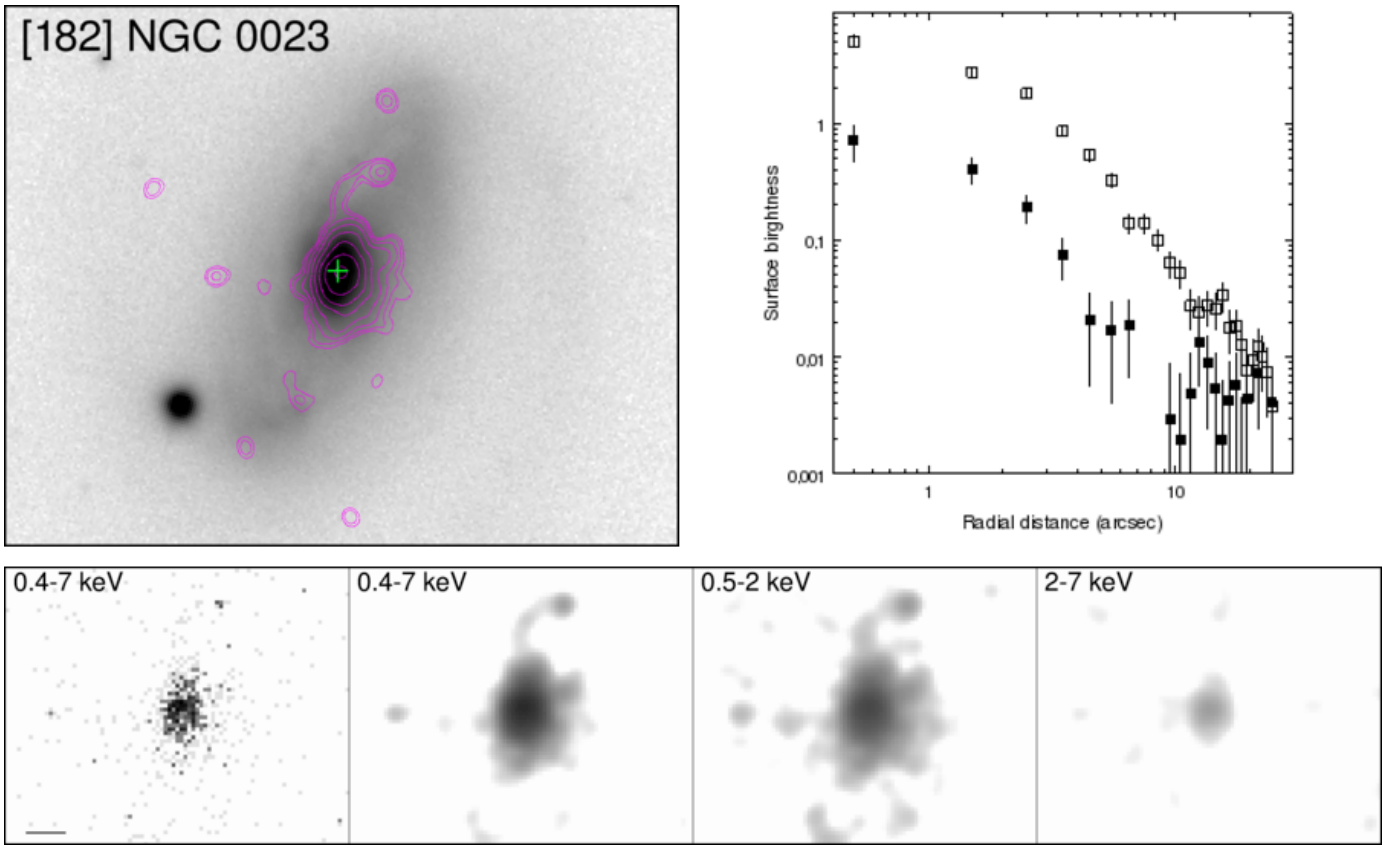

Fig. B.55. *Overlay on* SDSS DR-12 *i*-band. *Contours:* Interval 1.

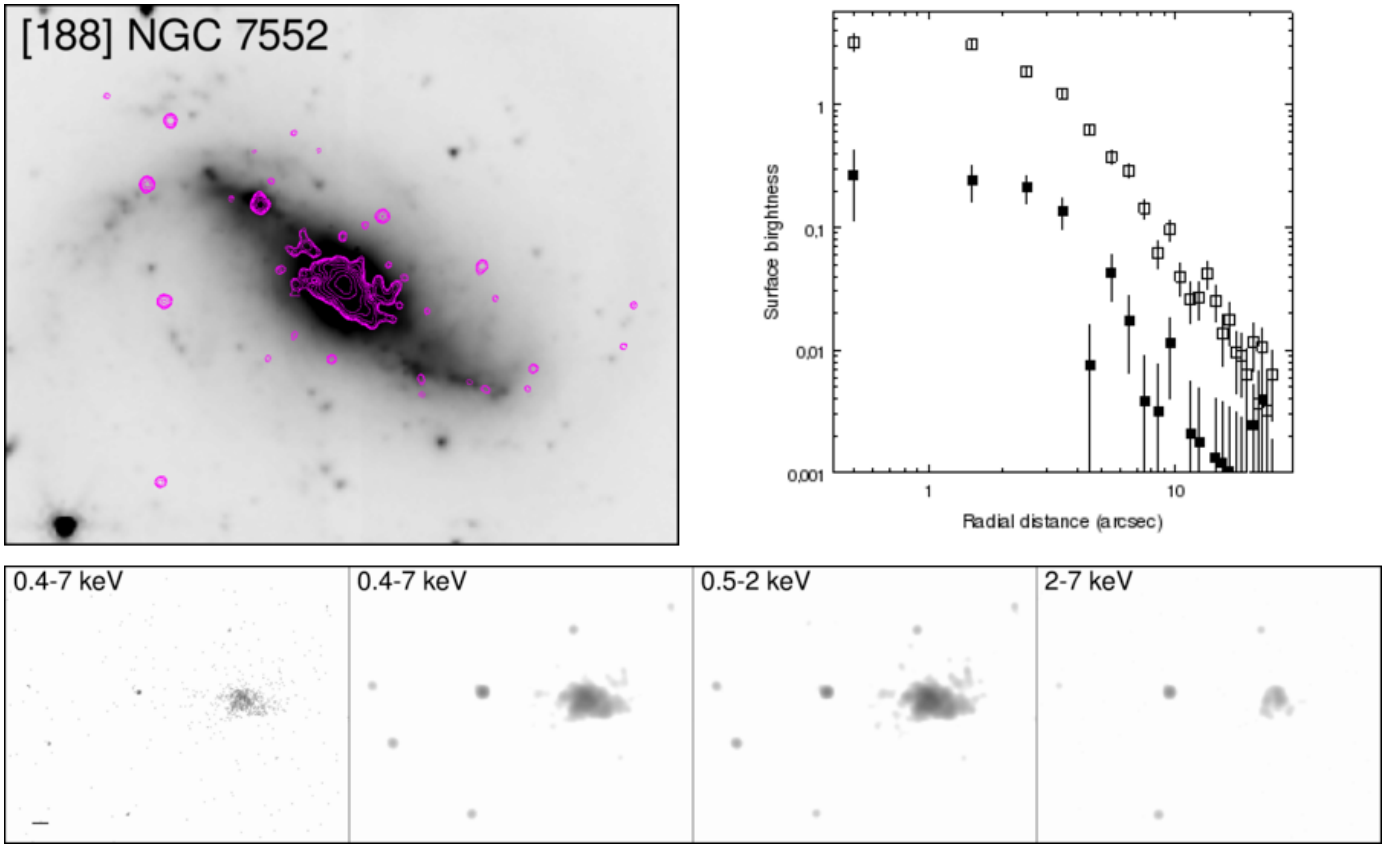

Fig. B.56. *Overlay on* IRAC channel 1. *Contours:* Interval 4.

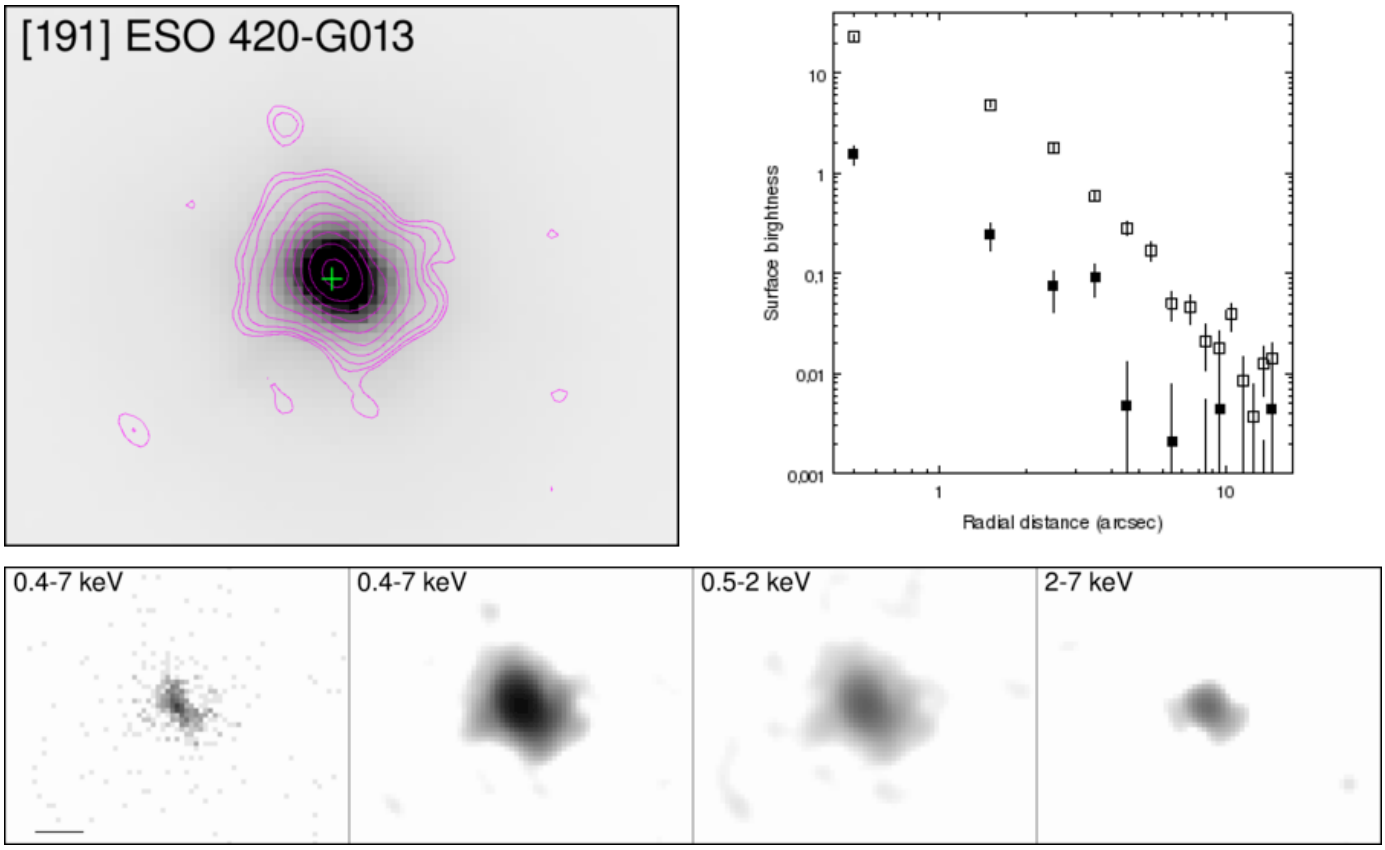

Fig. B.57. *Overlay on* IRAC channel 1. *Contours:* Interval 1.

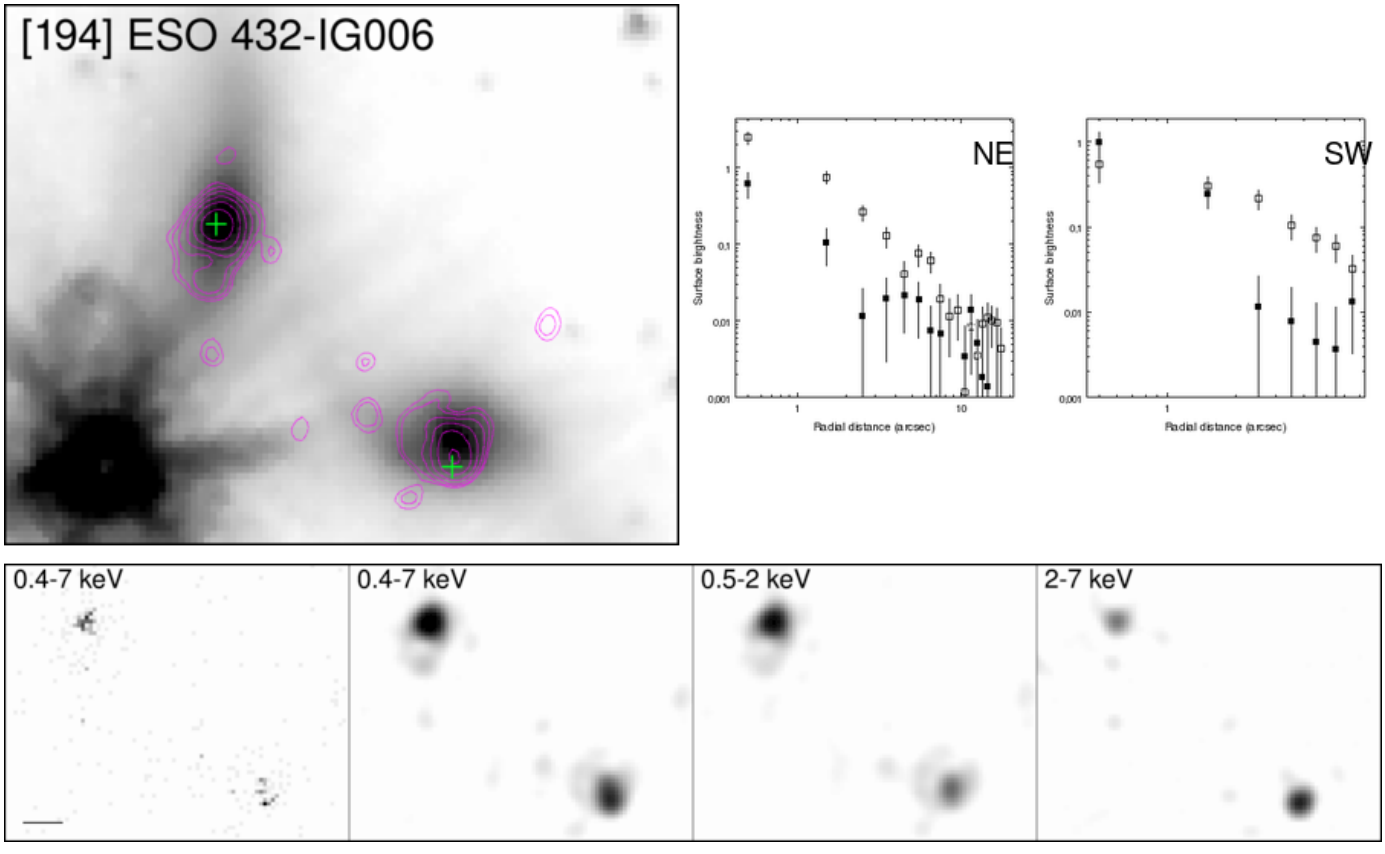

Fig. B.58. *Overlay on* IRAC channel 1. *Contours:* Interval 1.

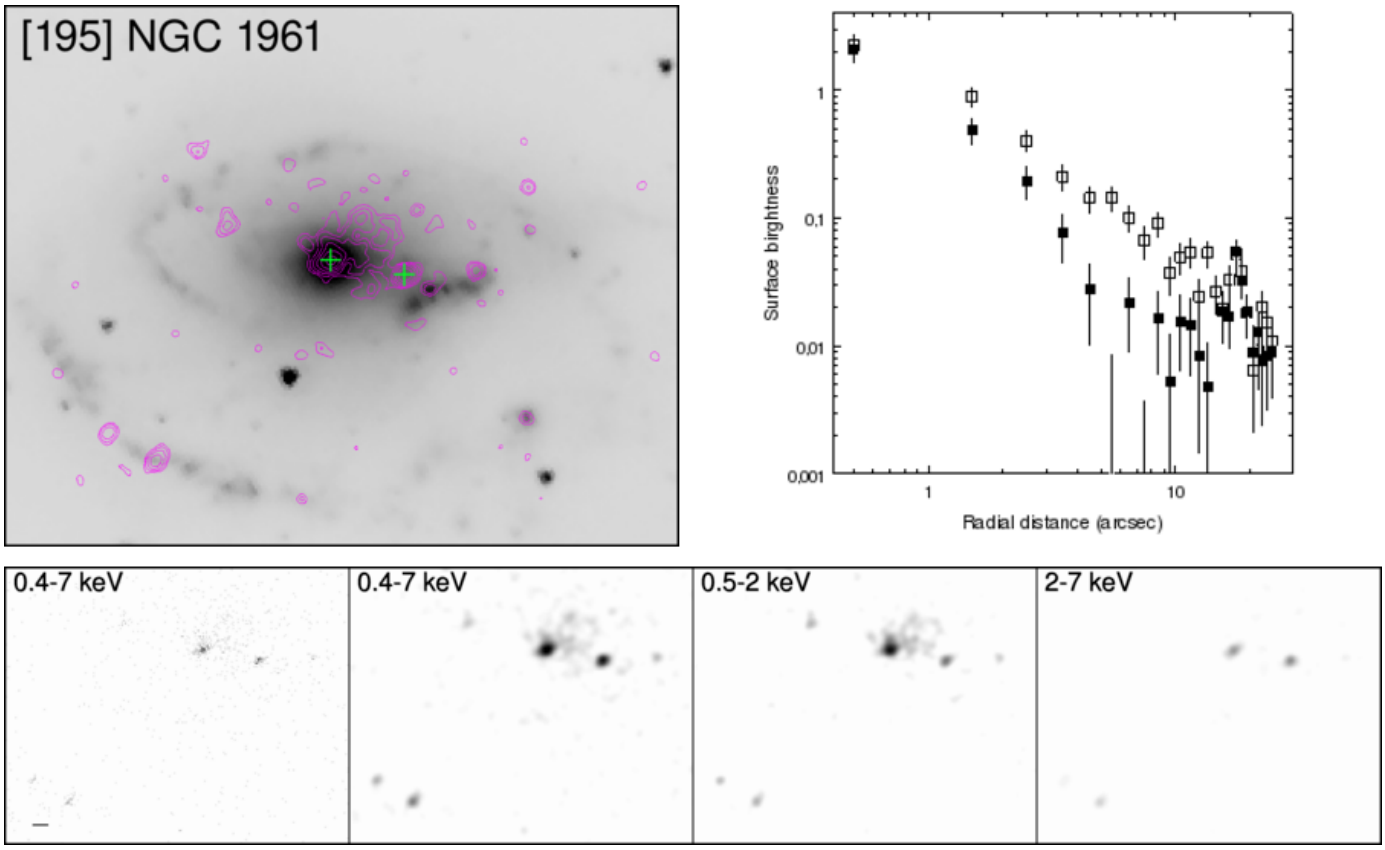

Fig. B.59. *Overlay on* IRAC channel 1. *Contours:* Interval 3

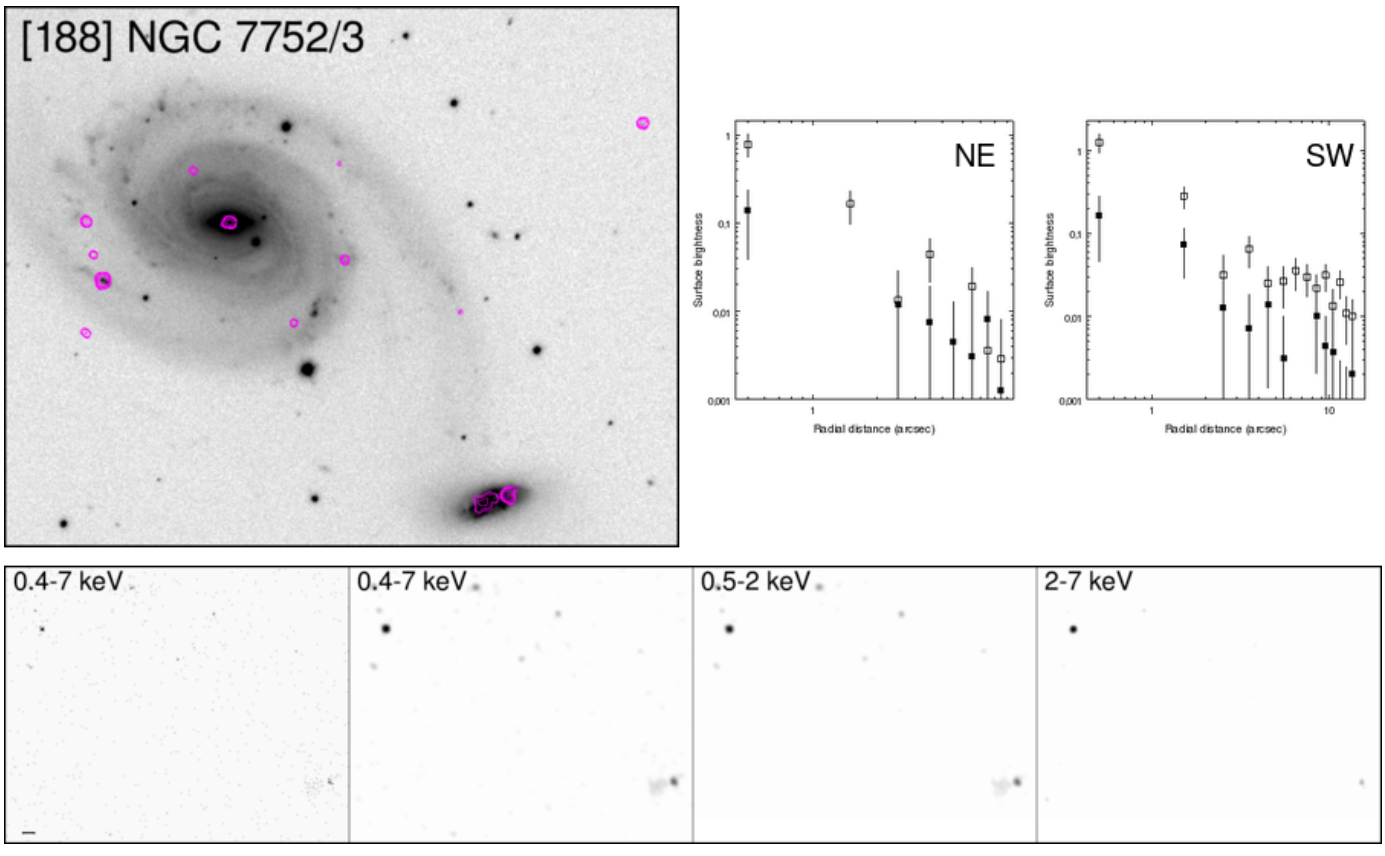

Fig. B.60. *Overlay on* SDSS DR-12 *i*-band. *Contours:* Interval 4.

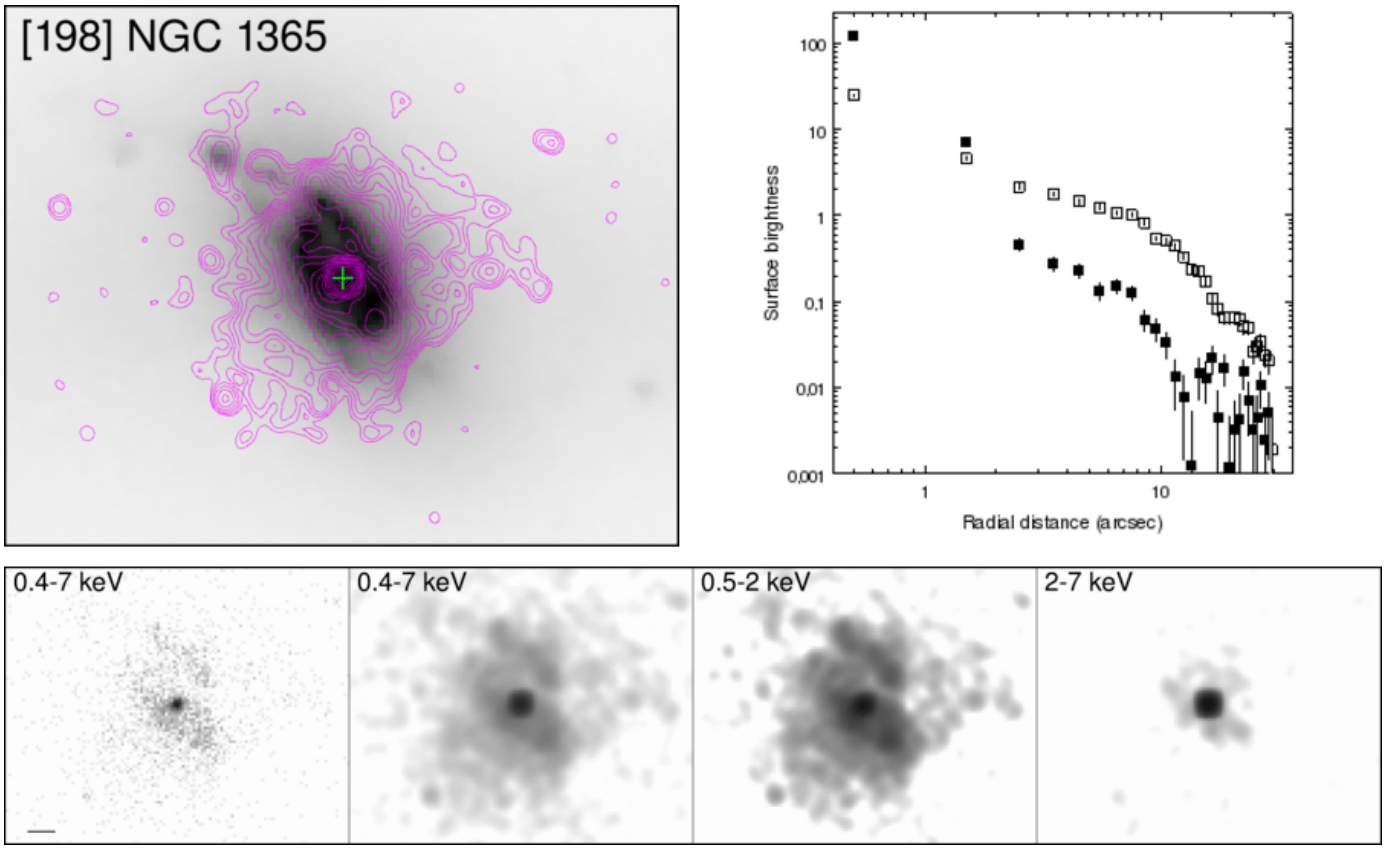

Fig. B.61. *Overlay on* IRAC channel 1. *Contours:* Custom.

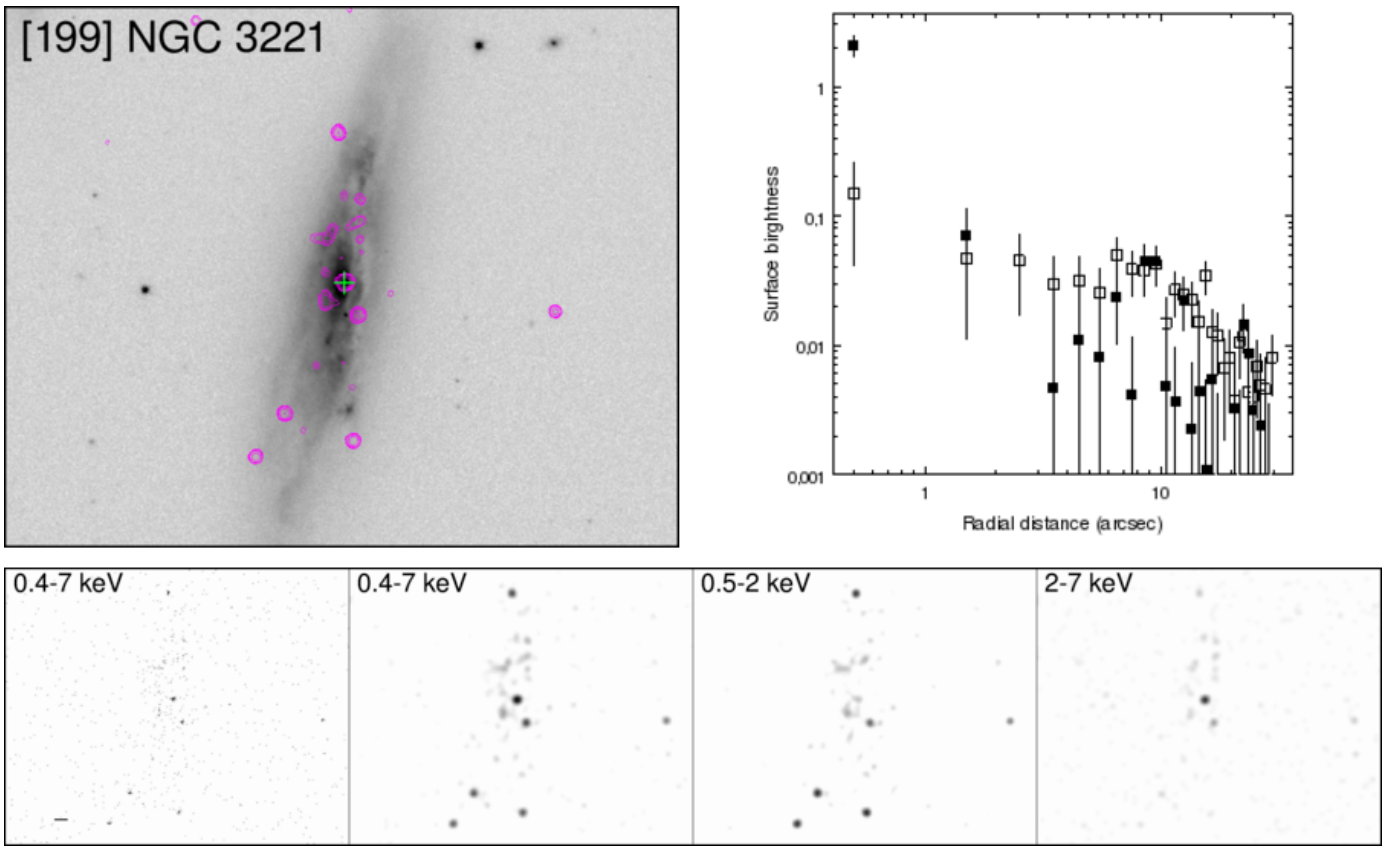

Fig. B.62. *Overlay on* SDSS DR-12 *i*-band. *Contours:* Interval 1.

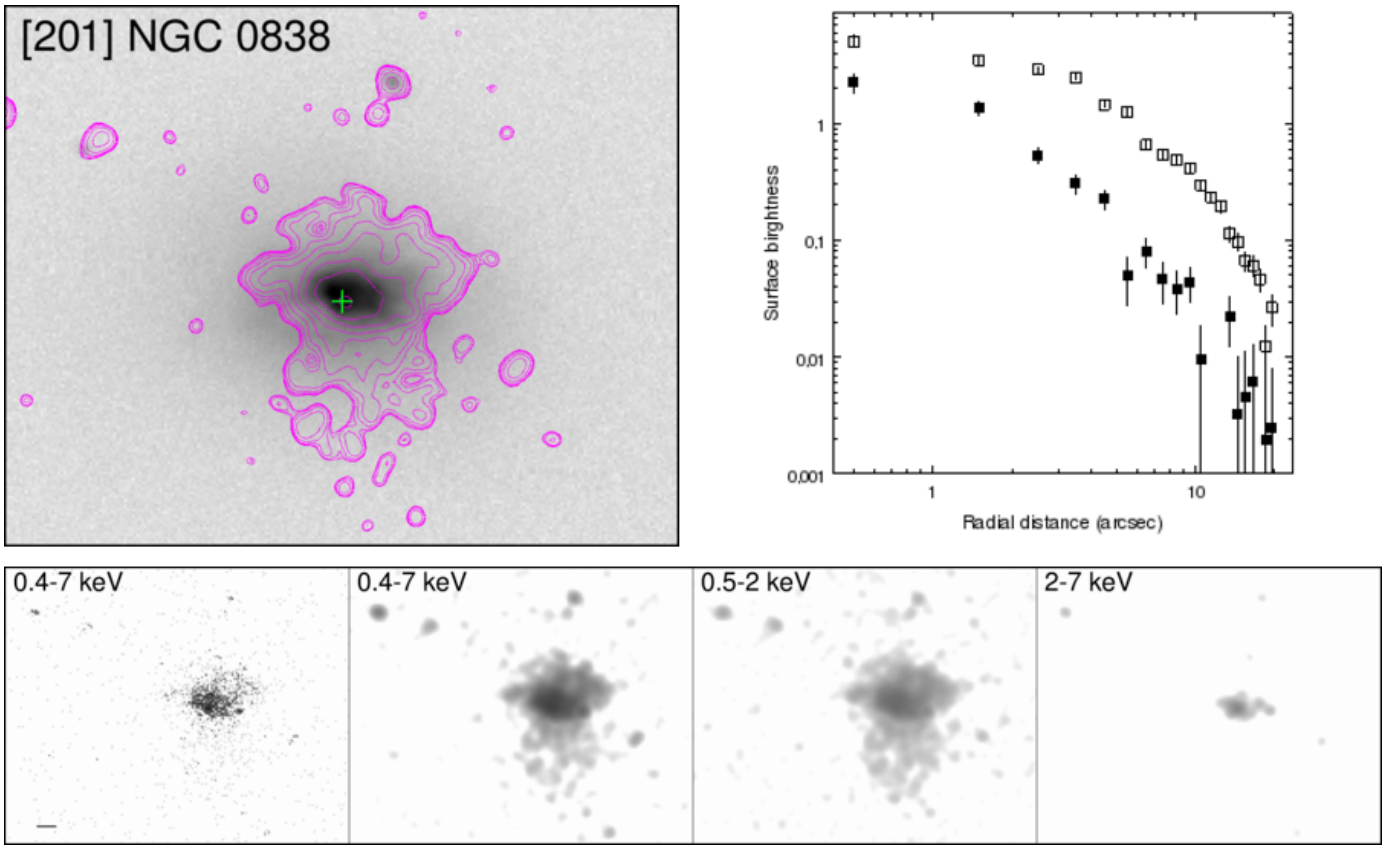

Fig. B.63. *Overlay on* SDSS DR-12 *i*-band. *Contours:* Custom.

Appendix C: X-ray spectra

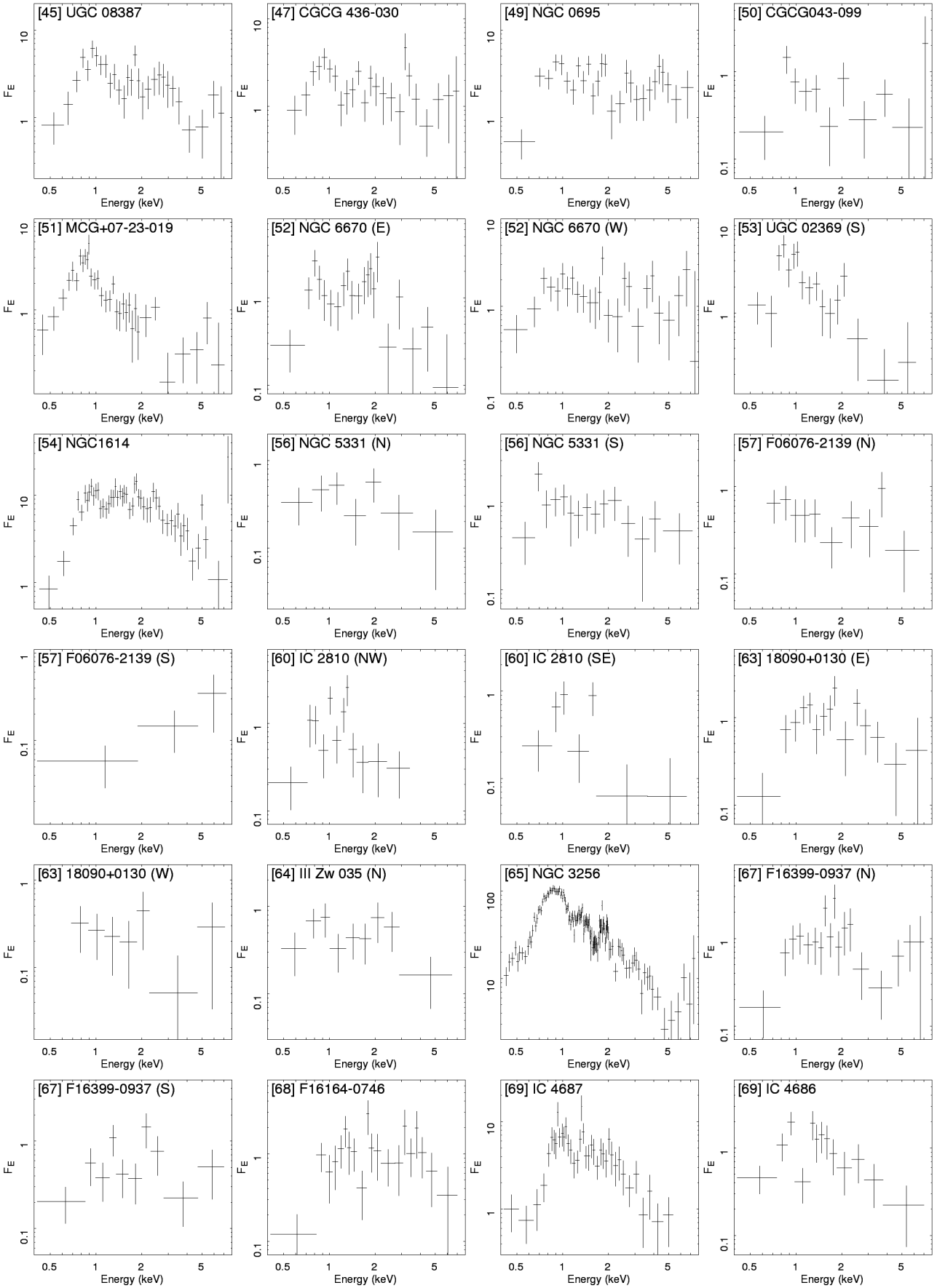

Fig. C.1. X-ray flux density spectra for the 84 individual galaxies of CGII, obtained from the *Chandra* ACIS. Flux density in units of 10^{-14} erg s^{-1} cm^{-2} keV^{-1}.

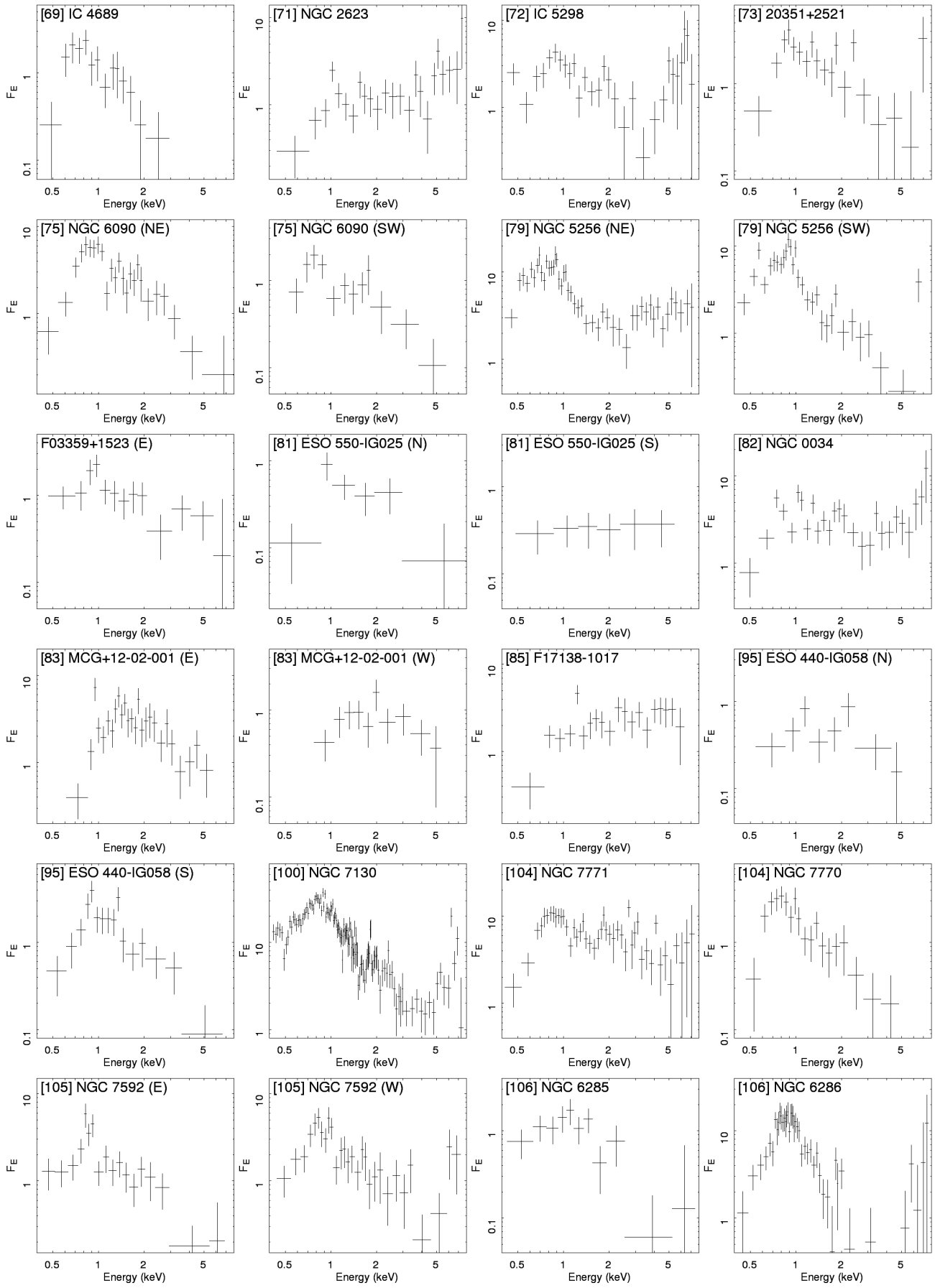

Fig. C.1. continued.

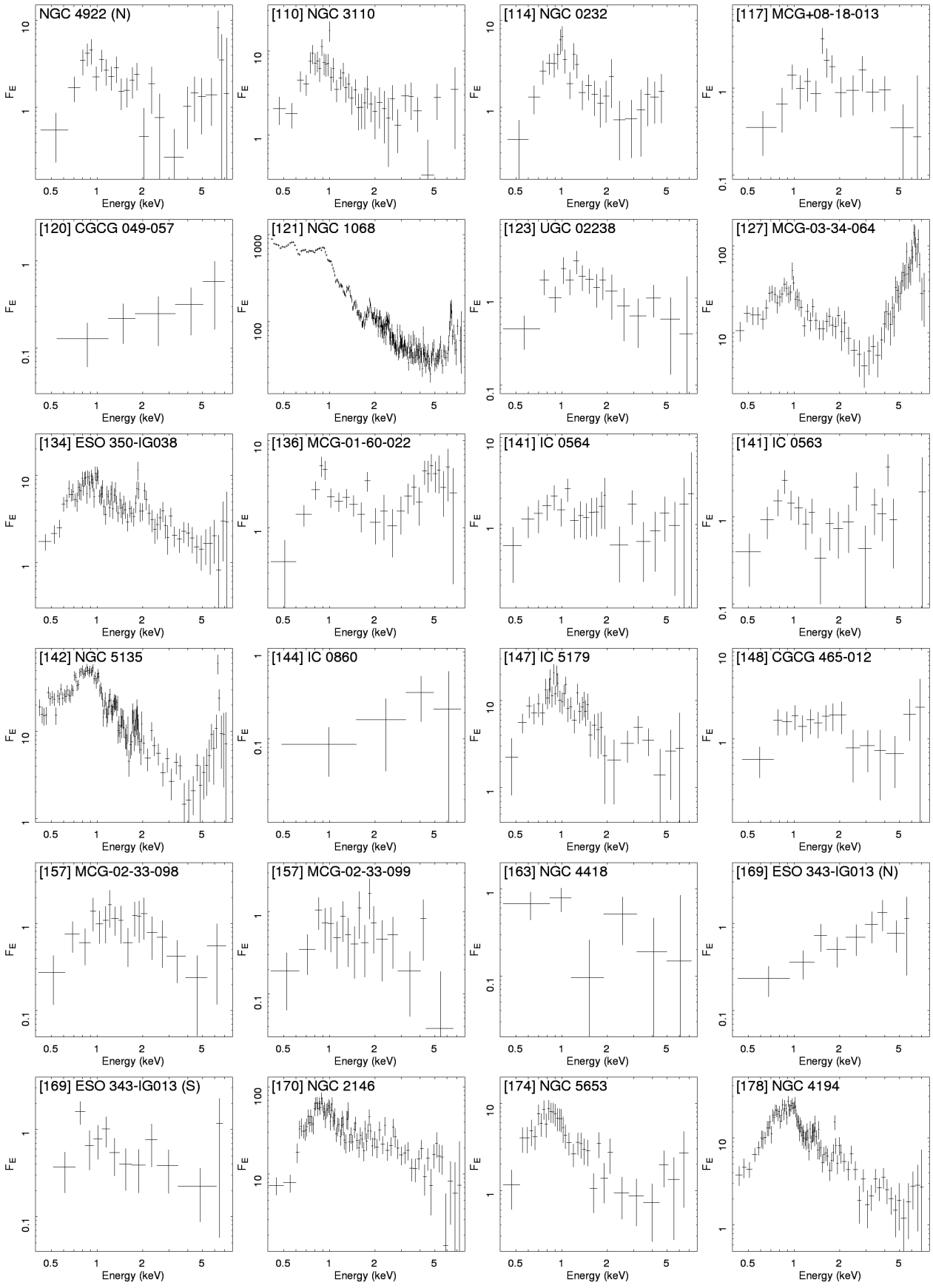

Fig. C.1: continued.

Fig. C.1. continued.

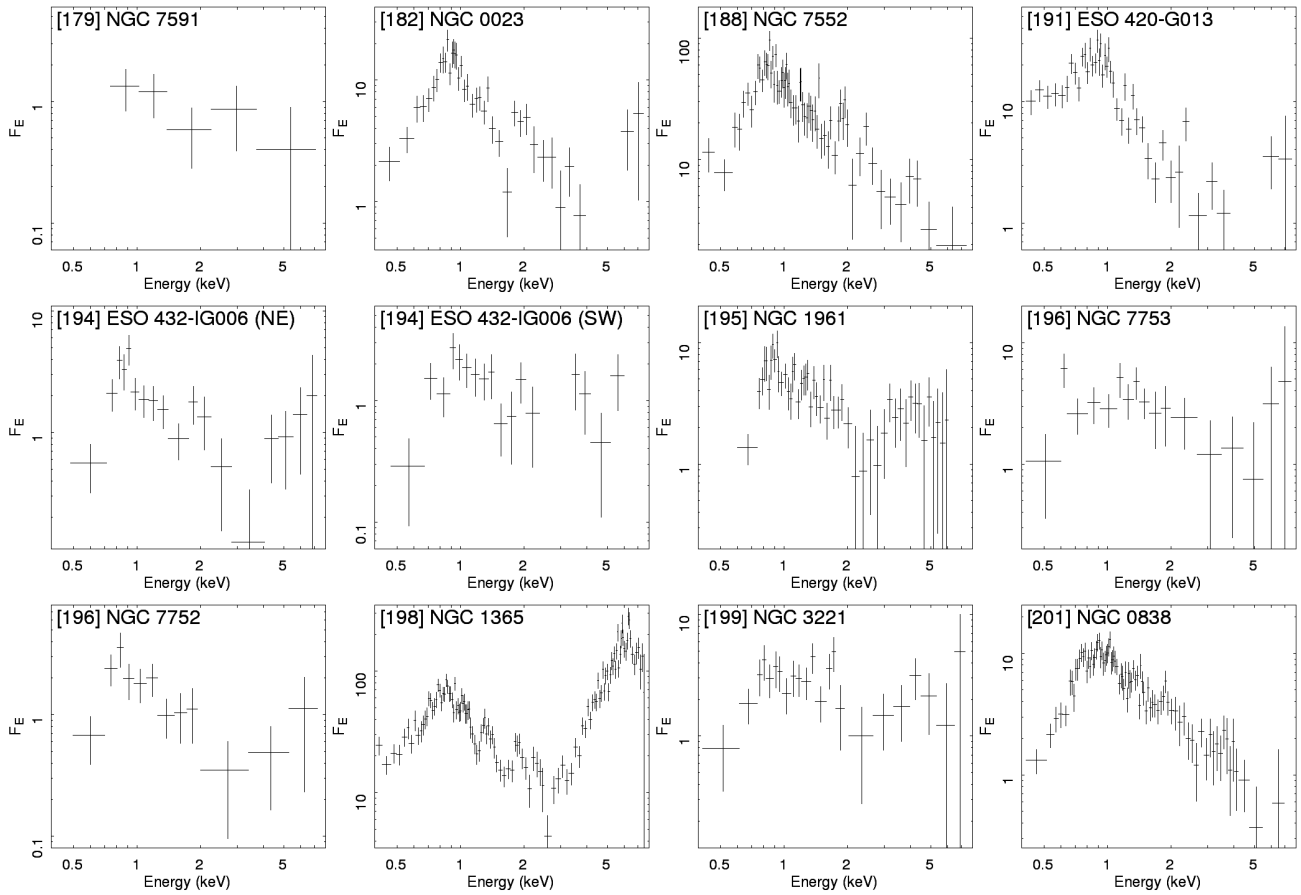

Fig. C.1. continued.